A Unified Model of Electroporation and Molecular Transport

by

Kyle Christopher Smith

B.S.E., Biomedical Engineering
Duke University, 2003

S.M., Electrical Engineering and Computer Science
Massachusetts Institute of Technology, 2006

Submitted to the Harvard-Massachusetts Institute of Technology
Division of Health Sciences and Technology
in Partial Fulfillment of the Requirements for the Degree of

Doctor of Philosophy in Biomedical and Electrical Engineering
at the
Massachusetts Institute of Technology

February 2011

Signature of Author: _____

Harvard-M.I.T. Division of Health Sciences and Technology
M.I.T. Department of Electrical Engineering and Computer Science
January 31, 2011

Certified by: _____

James C. Weaver, Ph.D.
Senior Research Scientist
Harvard-M.I.T. Division of Health Sciences and Technology
Thesis Supervisor

Accepted by: _____

Ram Sasisekharan, Ph.D.
Director, Harvard-M.I.T. Division of Health Sciences and Technology
Edward Hood Taplin Professor of Health Sciences and Technology
and Biological Engineering

A Unified Model of Electroporation and Molecular Transport

by

Kyle Christopher Smith

Submitted to the Harvard-Massachusetts Institute of Technology
Division of Health Sciences and Technology on January 31, 2011
in Partial Fulfillment of the Requirements for the Degree of
Doctor of Philosophy in Biomedical and Electrical Engineering

Abstract

Biological membranes form transient, conductive pores in response to elevated transmembrane voltage, a phenomenon termed electroporation. These pores facilitate electrical and molecular transport across cell membranes that are normally impermeable. By applying pulsed electric fields to cells, electroporation can be used to deliver nucleic acids, drugs, and other molecules into cells, making it a powerful research tool. Because of its widely demonstrated utility for in vitro applications, researchers are increasingly investigating related in vivo clinical applications of electroporation, such as gene delivery, drug delivery, and tissue ablation.

In this thesis, we describe a quantitative, mechanistic model of electroporation and concomitant molecular transport that can be used for guiding and interpreting electroporation experiments and applications. The model comprises coupled mathematical descriptions of electrical transport, electrodiffusive molecular transport, and pore dynamics. Where possible, each of these components is independently validated against experimental results in the literature. We determine the response of a discretized cell system to an applied electric pulse by assembling the discretized transport relations into a large system of nonlinear differential equations that is efficiently solved and analyzed with MATLAB.

We validate the model by replicating in silico two sets of experiments in the literature that measure electroporation-mediated transport of fluorescent probes. The model predictions of molecular uptake are in excellent agreement with these experimental measurements, for which the applied electric pulses collectively span nearly three orders of magnitude in pulse duration ($50\,\mu s - 20\,ms$) and an order of magnitude in pulse magnitude ($0.3 - 3\,kV/cm$).

The advantages of our theoretical approach are the ability to (1) analyze in silico the same quantities that are measured by experimental studies in vitro, (2) simulate electroporation dynamics that are difficult to assess experimentally, and (3) quickly screen a wide array of electric pulse waveforms for particular applications. We believe that our approach will contribute to a greater understanding of the mechanisms of electroporation and provide an in silico platform for guiding new experiments and applications.

Thesis Supervisor: James C. Weaver, Ph.D.
Title: Senior Research Scientist, Harvard-M.I.T. Division of Health Sciences and Technology

Dedicated to my family.

Acknowledgments

This thesis project was a major undertaking that spanned several years of dedicated work. I am grateful to the many people who assisted me in overcoming the challenges that I encountered along the way.

First and foremost, I thank my research advisor, Dr. James Weaver, who provided innumerable suggestions and ideas over the course of many insightful discussions. I am grateful to my thesis committee members, Dr. Mehmet Toner and Dr. Joel Voldman, for their guidance and advice. I enjoyed many interesting conversations with my colleagues in the Weaver Research Group, Dr. T. R. Gowrishankar, Dr. Axel Esser, and Reuben Son, and appreciate the many insights they provided. I also thank Ken Weaver for keeping the many computer systems essential to this project running smoothly.

The funding for this research project was primarily provided by Graduate Research Fellowships from the Whitaker Foundation, National Science Foundation, and Harvard-M.I.T. Division of Health Sciences and Technology. I am extremely grateful to these institutions for their generous contributions to my educational development.

Last, but certainly not least, I thank my family and friends for their continual support. It's hard to imagine tackling a project of this magnitude without such wonderful people to turn to when things get difficult. In particular, I thank my parents, Todd and Karen Smith, and my girlfriend, Christina Supelana.

Contents

List of Figures

List of Tables

Chapter 1

Introduction

1.1 Research Significance and Objectives

Electroporation is widely used for delivering exogenous molecules (nucleic acids, drugs, and fluorescent probes) into cells in biological research laboratories and is increasingly pursued for medical applications [1, 2]. It is most often used to transfect cultured cells in vitro, though it has also found use for a number of other more specialized experimental applications, such as transfecting retinal cells [3] and single neurons [4] in vivo and chick embryos in ovo [5].

Electroporation is fundamentally attractive because, by transiently disrupting the plasma membrane, it provides an operationally simple, effective means of facilitating the transport of a wide range of different molecules into cells. Additionally, for in vivo applications, by appropriately localizing the applied electric field, the region of tissue affected by electroporation can be controlled and limited [6–14], which is advantageous for many applications.

Following the success of in vitro electroporation in experimental applications, researchers began investigating potential electroporation-based medical therapies, currently emphasizing drug delivery, gene delivery, or electroporation alone (without drugs) to treat or ablate tissue. A number of in vivo studies have shown that electroporation can be used to treat solid tumors by greatly enhancing the delivery of nonpermeant anticancer drugs [15–17] or suicide genes [18], with both approaches leading to the destruction of the treated tissue.

Perhaps even more intriguing, recent studies have shown that electric pulses alone with very short

duration and large magnitude can induce apoptosis in cells in vitro [19–22] and in vivo [23–26], thereby leading to the destruction of treated cells or tissue without the need to introduce any drugs or genes. Rather large conventional electroporation pulses can be used to ablate tissue in a similar manner. However, this leads to necrosis rather than apoptosis [27, 28]. There is also ongoing interest in using electroporation to transfect skeletal muscle cells in vivo [29] for applications such as DNA vaccines [30] and increasing production of proteins like erythropoietin [31].

The common characteristic among all of these applications of electroporation is that they involve transmembrane transport though temporary pores. Indeed, transmembrane transport underlies not only electroporation-based applications but also the basic mechanisms of electroporation and therefore our fundamental understanding of electroporation. Much of what we know about electroporation has been determined through the analysis of measurements of electroporation-mediated electrical and molecular transport. More direct methods of observing pores appear infeasible because of the very short length scales (nanometers to micrometers) and time scales (nanoseconds to milliseconds) characteristic of electroporation and the absence of a significant contrast mechanism for imaging. With a few exceptions [32, 33], these measurements involve the collective effects of large ensembles of pores rather than single pores.

Lacking the ability to measure specific details about pores, many research studies focus on *what* results are observed and not *why* they are observed, at least not in any rigorous sense. Additionally, most electroporation studies are not quantitative, often, for example, reporting changes in relative fluorescence rather than calibrating the measurement system and reporting the total number of molecules transported. As a result, only limited comparisons can be made among the many experiments in the literature.

Accordingly, the primary objective of this research project was to develop a theoretical framework within which experimental findings can be interpreted and compared. This framework takes the form of a robust, comprehensive model integrating separate mechanisms for independent physical

phenomena, with each mechanism having an established theoretical or experimental basis. More specifically, the comprehensive, system-level model comprises separate mechanistic models for pore creation and destruction, pore expansion and contraction, and electrical and electrodiffusive molecular transport in bulk electrolyte and through pores. These mechanisms can be independently investigated and provide a means of breaking the complex process that is electroporation into simpler pieces that can be more readily characterized and validated prior to usage in a cell model. In addition, these quantitative, mechanistic models are, in essence, hypotheses. They represent preliminary, testable statements of our current understanding of electroporation.

Although a number of theoretical models have been used to describe and investigate electroporation, each has been limited in its scope or its assumptions. Some of these models have provided insights into particular aspects of electroporation, such as pore creation, but none has characterized the process of electroporation and its effects comprehensively. The system-level model presented here allows the investigation of electroporation from the onset of the applied electric pulse to the resealing of pores, throughout including the transport of molecules of interest. This enables us to make direct comparisons with measurements made in electroporation experiments, which generally evaluate transmembrane transport of tracer molecules or the transmembrane voltage and/or resistance of the membrane during and after the electric field application. Additionally, because electroporation affects biological systems by facilitating transport between cell compartments in an unregulated manner, the model enables the investigation of potential mechanisms by which electroporation leads to observed downstream biological events, such as apoptosis.

1.2 Experimental Electroporation Literature

Electroporation is very difficult to study experimentally because it involves very short length scales (nanometers to micrometers) and time scales (nanoseconds to milliseconds), and applicable measurement systems are limited in their spatial and temporal resolution. In fact, most studies do not observe pores in any direct sense. Rather, they examine secondary effects of large ensembles of pores. For example, many studies have examined the changes in fluorescence of cells electropo-

rated in the presence of fluorescent dyes [34–48]. Others have examined the transmembrane voltage of pulsed cells during or after electroporation using voltage sensitive dyes [49–52] or patch clamp techniques [53, 54]. The comprehensive electroporation model presented here will be of great use in making comprehensive sense of the wide array of available experimental data.

A useful way to approach the experimental electroporation literature is to first recognize that, in essence, all electroporation experiments measure either the direct effects that pores have on transmembrane transport or the downstream chemical or biological effects that occur as consequences of transmembrane transport. With this in mind, one can begin to form sensible hypotheses about the mechanisms of electroporation.

Downstream chemical and biological effects indicate that *something* happened, with varying degrees of sensitivity and specificity. However, these effects generally do not provide insights into the mechanisms of electroporation because they are merely observable endpoints of complex sequences of events, but they do provide a place to begin hypothesizing about potential mechanisms, and this can subsequently lead to important insights. These empirical observations are most useful when interpreted within the context of basic mechanisms.

More specifically, reported experimental studies have examined many biological and chemical effects that occur downstream of electroporation. Gene expression [55, 56] and cell death [43, 57] following conventional electroporation pulses have long been of interest because of the widespread use of electroporation to transfect cells. Studies that measure gene expression and transfection efficiency are helpful to researchers who use electroporation to transfect cells, but they do not provide much information about the electroporation processes that lead to DNA uptake. Studies of cell death are of similar utility to electroporation users. Cell death likely results from transport between cell compartments that are not supposed to communicate in an unregulated manner [2]. Experiments that quantify cell death following various pulses [43, 57] are helpful in forming hypotheses about precisely what sequence of events might lead to cell death and how they relate

to electroporation. Recent studies on the effects of submicrosecond, megavolt-per-meter electric pulses have demonstrated that these pulses can lead to downstream effects, such as apoptosis induction [19–26], that are not observed in response to more conventional electric pulses. These effects are thought to result from electroporation of organelle membranes. All of these biological and chemical events occur as the result of transmembrane transport, though the details of the relevant transport are not always immediately clear.

Experiments that directly measure transport during and after electroporation, as opposed to inferring it from downstream effects, are of much greater potential use in explaining the mechanisms of electroporation. Such studies examine either the transport of small ions or polar tracer molecules. They provide information that is essential for developing and testing quantitative models of electroporation. The experiments can be replicated in silico and the model results can then be directly compared with the experimental results.

Electroporation drastically increases the membrane conductance, thereby allowing small ions to pass through the membrane with relatively little resistance. Extremely sensitive experiments on planar membranes have actually detected the stepwise (quantized) changes in membrane conductance associated with the creation and destruction of individual pores [32]. Importantly, the sizes of the pores can be straightforwardly calculated from these stepwise changes in conductance.

Similar (but lower resolution) measurements have been made at the cell level using patch clamp techniques [53, 54]. To date, these methods have not been used to provide details about individual pores, but they have been used to measure the conductance and transmembrane voltage of the entire plasma membrane in the minutes after electroporation. The experiments have provided useful information on the rate of recovery of the plasma membrane (pore resealing), and they have also provided experimental confirmation that submicrosecond, megavolt-per-meter pulses electroporate the plasma membrane, despite numerous earlier claims to the contrary [20, 58–66].

Changes in membrane conductance can also be detected by measuring the transmembrane voltage using voltage sensitive membrane dyes [49–52]. Upon application of an electric field, the creation of pores in the plasma membrane causes a tremendous increase in the membrane conductance. This limits the peak transmembrane voltage and leads to a subsequent drop in transmembrane voltage in a process called reversible electrical breakdown. This can be measured experimentally. The transmembrane voltage has been measured for both long duration, small magnitude pulses [49–51] and short duration, large magnitude pulses [52] in several impressive experimental studies. Notably, predictions of mechanistic models of cell electroporation are consistent with these results [10, 14, 67–74].

Electroporation can also be investigated experimentally by measuring the transport of tracer molecules during and after electroporation. Some studies have measured the total uptake of fluorescent molecules at single time point after the applied electric pulse for a number of different pulses [38, 39, 43, 44, 48]. Others have measured the uptake at many time points for a few different pulses [42, 46, 47]. The most insightful and useful of these studies are those that used calibrated measurement systems [34, 38, 39, 42–44, 46, 48], enabling them to report the number of transported molecules (with some quantified error), rather than just relative fluorescence [41, 45, 47], which cannot be interpreted with a useful degree of confidence.

1.3 Theoretical Electroporation Literature

To understand why the presented electroporation model is particularly comprehensive and useful, one should first consider the previous electroporation models in the literature. These models range from simplistic to sophisticated, but each is limited in either its scope or assumptions.

The simplest models of electroporation are empirical, didactic, or descriptive models. Such models describe *what* electroporation does but do not provide details as to *how* or *why*. For example, one model describes electroporation as a process that prevents the transmembrane voltage from exceeding a threshold (1 V) [75, 76]. After the threshold is reached, the transmembrane voltage is

fixed at the threshold until the end of the pulse. Electroporation does, in fact, limit the transmembrane voltage as pore formation alters the voltage division between the membrane and electrolyte, but this sort of model representation is a gross oversimplification and cannot provide any real quantitative insights into electroporation.

Somewhat more complex are spatially distributed passive (linear) cell models [77–80]. Such models appear sophisticated because they often have membranes that are spatially distributed in 2-D or 3-D systems that "look" like a cell. The spatial sophistication of these models masks unsophisticated passive representations of cell membranes, as the electrical (and other) properties in passive models are time-invariant. However, the very reason electroporation is interesting is that the membrane properties are *not* time-invariant: in response to elevated transmembrane voltage, membranes form pores that increase the conductances of the membranes by orders of magnitude and facilitate transport. Passive models cannot account for electroporation of membranes or the tremendous changes in the electrical properties of the system that accompany electroporation [72].

The use of passive models increased with research into the effects of ultrashort pulses, and these models were (mis)used to support claims that ultrashort pulses could electroporate organelle membranes without electroporating the plasma membrane [20, 58–66]. Such claims have since been refuted [53, 54, 72, 76]. Passive models are of little use in investigating electroporation because they cannot actually make any predictions about pores (i.e., when and where pores form, how many pores form, etc.) or effects of pores, such as how pores contribute to the redistribution of electric fields or molecular transport.

Spatially distributed models that incorporate the asymptotic model of electroporation are typically similar to passive models in the sophistication of the systems used but have a membrane representation based on a mechanistic model of electroporation [10, 67–70, 72, 81]. These models allow for the formation of conductive pores in membranes as functions of the local transmembrane voltage. The pores are not dynamic, however. Rather, they are fixed at a radius of $\sim$0.8 nm until they reseal.

Asymptotic models capture approximately the electrical behavior of cells in response to applied electric fields reasonably well and predict reversible electrical breakdown and “flattening” peaks in angular transmembrane voltage profiles, both hallmarks of electroporation [49–52, 82].

In contrast to passive models, asymptotic models can make predictions about pores (i.e., when and where pores will form, how many pores will form, etc.) and the redistribution of electric fields in response to electroporation. Their predictions are particularly reasonable for short pulses, for which pores do not expand significantly [83]. However, asymptotic models are not useful for estimating molecular transport because their small, static pores artificially limit transmembrane transport to small ions.

Spatially distributed models with dynamic pores represent the most sophisticated electroporation models that have been developed to date. These models have all of the desirable properties of asymptotic models plus the added advantage that they describe the temporal evolution (expansion and contraction) of pores [13, 14, 71, 73, 74]. Importantly, models with dynamic pores have the potential to be coupled with molecular transport models to give a complete picture of the dynamics of electroporation and concomitant molecular transport that underly electroporation applications and experimental observations. Indeed, the objective of this research project was to develop just such a model.

All of the cell models described above are continuum models. That is, they assume that atom scale fluctuations can be considered sufficiently averaged temporally and spatially as to follow larger scale continuum dynamics. Discrete, molecular dynamics models of electroporation have also been developed. These models consider strongly forced interactions between atoms that have been assigned to small lipid bilayer-electrolyte systems. Molecular dynamics models have bolstered our understanding of how pores form and what they look like at the molecular level [84–94], partially validating the longstanding aqueous pore hypothesis [1]. Moving forward, they have the potential to provide important information about pore dynamics and may assist in determining parameters

for continuum models, neither of which can be easily accomplished by experimental approaches. They cannot (and will not for the foreseeable future) provide insights into the process of electroporation at the cell (or higher) level. Nonetheless, molecular dynamics models are likely to continue to generate fundamental and practical information about the mechanisms of electroporation.

1.4 Thesis Structure

The first half of this thesis describes the "building blocks" of the comprehensive cell system electroporation model. Each chapter focuses on a single aspect of the comprehensive model. Specifically:

Chapter 2: Molecular transport properties.

Chapter 3: Molecular transport (electrodiffusion) in bulk electrolyte.

Chapter 4: Ionic and molecular transport through pores.

Chapter 5: Pore energy and dynamics.

The second half of this thesis describes (1) the integration of the building blocks into a comprehensive cell electroporation model, (2) model validation, (3) general features of the responses of cells to applied electric pulses, and (4) implications of the model results. Specifically:

Chapter 6: Transmembrane transport resulting from nanosecond electric pulses.

Chapter 7: Implementation and validation of the comprehensive cell model.

Chapter 8: General features of the responses of cells to applied electric pulses.

Chapter 9: Potential mechanisms by which large magnitude pulses may induce apoptosis.

This thesis is written as a collection of eight manuscripts that will be submitted to peer-reviewed journals following thesis submission. As a result, references to other chapters appear as citations of the associated "in preparation" manuscripts.

References

[1] Weaver, J.C. and Chizmadzhev, Y.A. Theory of electroporation: A review. *Bioelectroch Bioener*, 41(2):135–160, 1996.

[2] Weaver, J.C. Electroporation of biological membranes from multicellular to nano scales. *IEEE T Dielect El In*, 10(5):754–768, 2003.

[3] Matsuda, T. and Cepko, C.L. Electroporation and RNA interference in the rodent retina in vivo and in vitro. *P Natl Acad Sci USA*, 101(1):16–22, 2004.

[4] Kitamura, K., Judkewitz, B., Kano, M., Denk, W., and Hausser, M. Targeted patch-clamp recordings and single-cell electroporation of unlabeled neurons in vivo. *Nat Methods*, 5(1):61–67, 2008.

[5] Voiculescu, O., Papanayotou, C., and Stern, C.D. Spatially and temporally controlled electroporation of early chick embryos. *Nat Protoc*, 3(3):419–426, 2008.

[6] Heller, R., Jaroszeski, M.J., Glass, L.F., Messina, J.L., Rapaport, D.P., DeConti, R.C., Fenske, N.A., Gilbert, R.A., Mir, L.M., and Reintgen, D.S. Phase I/II trial for the treatment of cutaneous and subcutaneous tumors using electrochemotherapy. *Cancer*, 77(5):964–971, 1996.

[7] Sel, D., Mazeres, S., Teissie, J., and Miklavcic, D. Finite-element modeling of needle electrodes in tissue from the perspective of frequent model computation. *IEEE T Bio-Med Eng*, 50(11):1221–32, 2003.

[8] Pliquett, U., Elez, R., Piiper, A., and Neumann, E. Electroporation of subcutaneous mouse tumors by rectangular and trapezium high voltage pulses. *Bioelectrochemistry*, 62(1):83–93, 2004.

[9] Davalos, R.V., Mir, I.L.M., and Rubinsky, B. Tissue ablation with irreversible electroporation. *Ann Biomed Eng*, 33(2):223–231, 2005.

[10] Smith, K.C. *Cell and Tissue Electroporation*. Master's thesis, Massachusetts Institute of Technology, Cambridge, Massachusetts, 2006.

[11] Heller, L.C., Jaroszeski, M.J., Coppola, D., McCray, A.N., Hickey, J., and Heller, R. Optimization of cutaneous electrically mediated plasmid DNA delivery using novel electrode. *Gene Ther*, 14(3):275–280, 2007.

[12] Sel, D., Lebar, A.M., and Miklavcic, D. Feasibility of employing model-based optimization of pulse amplitude and electrode distance for effective tumor electropermeabilization. *IEEE T Bio-Med Eng*, 54(5):773–781, 2007.

[13] Esser, A.T., Smith, K.C., Gowrishankar, T.R., and Weaver, J.C. Towards solid tumor treatment by irreversible electroporation: Intrinsic redistribution of fields and currents in tissue. *Technol Cancer Res T*, 6(4):261–273, 2007.

[14] Esser, A.T., Smith, K.C., Gowrishankar, T.R., and Weaver, J.C. Towards solid tumor treatment by nanosecond pulsed electric fields. *Technol Cancer Res T*, 8(4):289–306, 2009.

[15] Rols, M.P., Delteil, C., Golzio, M., Dumond, P., Cros, S., and Teissie, J. In vivo electrically mediated protein and gene transfer in murine melanoma. *Nat Biotechnol*, 16(2):168–171, 1998.

[16] Mir, L.M. and Orlowski, S. Mechanisms of electrochemotherapy. *Adv Drug Deliv Rev*, 35(1):107–118, 1999.

[17] Gothelf, A., Mir, L.M., and Gehl, J. Electrochemotherapy: Results of cancer treatment using enhanced delivery of bleomycin by electroporation. *Cancer Treat Rev*, 29(5):371–387, 2003.

[18] Goto, T., Nishi, T., Tamura, T., Dev, S.B., Takeshima, H., Kochi, M., Yoshizato, K., Kuratsu, J., Sakata, T., Hofmann, G.A., and Ushio, Y. Highly efficient electro-gene therapy of solid tumor by using an expression plasmid for the herpes simplex virus thymidine kinase gene. *P Natl Acad Sci USA*, 97(1):354–359, 2000.

[19] Hofmann, F., Ohnimus, H., Scheller, C., Strupp, W., Zimmermann, U., and Jassoy, C. Electric field pulses can induce apoptosis. *J Membrane Biol*, 169:103–109, 1999.

[20] Beebe, S.J., Fox, P.M., Rec, L.J., Willis, L.K., and Schoenbach, K.H. Nanosecond, high-intensity pulsed electric fields induce apoptosis in human cells. *FASEB J*, 17(9), 2003.

[21] Schoenbach, K.H., Joshi, R.P., Kolb, J.F., Chen, N.Y., Stacey, M., Blackmore, P.F., Buescher, E.S., and Beebe, S.J. Ultrashort electrical pulses open a new gateway into biological cells. *P IEEE*, 92(7):1122–1137, 2004.

[22] Hall, E.H., Schoenbach, K.H., and Beebe, S.J. Nanosecond pulsed electric fields induce apoptosis in p53-wildtype and p53-null HCT116 colon carcinoma cells. *Apoptosis*, 12(9):1721–1731, 2007.

[23] Nuccitelli, R., Pliquett, U., Chen, X.H., Ford, W., Swanson, R.J., Beebe, S.J., Kolb, J.F., and Schoenbach, K.H. Nanosecond pulsed electric fields cause melanomas to self-destruct. *Biochem Bioph Res Co*, 343:351–360, 2006.

[24] Garon, E.B., Sawcer, D., Vernier, P.T., Tang, T., Sun, Y., Marcu, L., Gundersen, M.A., and Koeffler, H.P. In vitro and in vivo evaluation and a case report of intense nanosecond pulsed electric field as a local therapy for human malignancies. *Int J Cancer*, 121(3):675–682, 2007.

[25] Nuccitelli, R., Chen, X., Pakhomov, A.G., Baldwin, W.H., Sheikh, S., Pomicter, J.L., Ren, W., Osgood, C., Swanson, R.J., Kolb, J.F., Beebe, S.J., and Schoenbach, K.H. A new pulsed electric field therapy for melanoma disrupts the tumor's blood supply and causes complete remission without recurrence. *Int J Cancer*, 125(2):438–45, 2009.

[26] Nuccitelli, R., Tran, K., Sheikh, S., Athos, B., Kreis, M., and Nuccitelli, P. Optimized nanosecond pulsed electric field therapy can cause murine malignant melanomas to self-destruct with a single treatment. *Int J Cancer*, 127(7):1727–36, 2010.

[27] Edd, J.F., Horowitz, L., Davalos, R.V., Mir, L.M., and Rubinsky, B. In vivo results of a new focal tissue ablation technique: Irreversible electroporation. *IEEE T Bio-Med Eng*, 53(7):1409–1415, 2006.

[28] Rubinsky, B., Onik, G., and Mikus, P. Irreversible electroporation: A new ablation modality–Clinical implications. *Technol Cancer Res T*, 6(1):37–48, 2007.

[29] Aihara, H. and Miyazaki, J. Gene transfer into muscle by electroporation in vivo. *Nat Biotechnol*, 16(9):867–870, 1998.

[30] Widera, G., Austin, M., Rabussay, D., Goldbeck, C., Barnett, S.W., Chen, M.C., Leung, L., Otten, G.R., Thudium, K., Selby, M.J., and Ulmer, J.B. Increased DNA vaccine delivery and immunogenicity by electroporation in vivo. *J Immunol*, 164:4635–4640, 2000.

[31] Rizzuto, G., Cappelletti, M., Maione, D., Savino, R., Lazzaro, D., Costa, P., Mathiesen, I., Cortese, R., Ciliberto, G., Laufer, R., La Monica, N., and Fattori, E. Efficient and regulated erythropoietin production by naked DNA injection and muscle electroporation. *P Natl Acad Sci USA*, 96(11):6417–6422, 1999.

[32] Melikov, K.C., Frolov, V.A., Shcherbakov, A., Samsonov, A.V., Chizmadzhev, Y.A., and Chernomordik, L.V. Voltage-induced nonconductive pre-pores and metastable single pores in unmodified planar lipid bilayer. *Biophys J*, 80(4):1829–1836, 2001.

[33] Kotulska, M. Natural fluctuations of an electropore show fractional Levy stable motion. *Biophys J*, 92(7):2412–2421, 2007.

[34] Bartoletti, D.C., Harrison, G.I., and Weaver, J.C. The number of molecules taken up by electroporated cells: Quantitative determination. *FEBS Lett*, 256(1-2):4–10, 1989.

[35] Tekle, E., Astumian, R.D., and Chock, P.B. Electro-permeabilization of cell membranes: Effect of the resting membrane potential. *Biochem Bioph Res Co*, 172(1):282–7, 1990.

[36] Tekle, E., Astumian, R.D., and Chock, P.B. Electroporation by using bipolar oscillating electric field: An improved method for DNA transfection of NIH 3T3 cells. *P Natl Acad Sci USA*, 88(10):4230–4, 1991.

[37] Glogauer, M. and McCulloch, C.A. Introduction of large molecules into viable fibroblasts by electroporation: Optimization of loading and identification of labeled cellular compartments. *Exp Cell Res*, 200(2):227–34, 1992.

[38] Prausnitz, M.R., Lau, B.S., Milano, C.D., Conner, S., Langer, R., and Weaver, J.C. A quantitative study of electroporation showing a plateau in net molecular-transport. *Biophys J*, 65(1):414–422, 1993.

[39] Prausnitz, M.R., Milano, C.D., Gimm, J.A., Langer, R., and Weaver, J.C. Quantitative study of molecular-transport due to electroporation – Uptake of bovine serum-albumin by erythrocyte-ghosts. *Biophys J*, 66(5):1522–1530, 1994.

[40] Tekle, E., Astumian, R.D., and Chock, P.B. Selective and asymmetric molecular transport across electroporated cell membranes. *P Natl Acad Sci USA*, 91(24):11512–6, 1994.

[41] Prausnitz, M.R., Corbett, J.D., Gimm, J.A., Golan, D.E., Langer, R., and Weaver, J.C. Millisecond measurement of transport during and after an electroporation pulse. *Biophys J*, 68(5):1864–1870, 1995.

[42] Djuzenova, C.S., Zimmermann, U., Frank, H., Sukhorukov, V.L., Richter, E., and Fuhr, G. Effect of medium conductivity and composition on the uptake of propidium iodide into electropermeabilized myeloma cells. *Biochim Biophys Acta*, 1284(2):143–52, 1996.

[43] Canatella, P.J., Karr, J.F., Petros, J.A., and Prausnitz, M.R. Quantitative study of electroporation-mediated molecular uptake and cell viability. *Biophys J*, 80(2):755–764, 2001.

[44] Puc, M., Kotnik, T., Mir, L.M., and Miklavcic, D. Quantitative model of small molecules uptake after in vitro cell electropermeabilization. *Bioelectrochemistry*, 60(1-2):1–10, 2003.

[45] Sun, Y., Vernier, P., Behrend, M., Wang, J., Thu, M., Gundersen, M., and Marcu, L. Fluorescence microscopy imaging of electroperturbation in mammalian cells. *J Biomed Opt*, 11(2), 2006.

[46] Kennedy, S.M., Ji, Z., Hedstrom, J.C., Booske, J.H., and Hagness, S.C. Quantification of electroporative uptake kinetics and electric field heterogeneity effects in cells. *Biophys J*, 94(12):5018–5027, 2008.

[47] Pucihar, G., Kotnik, T., Miklavcic, D., and Teissie, J. Kinetics of transmembrane transport of small molecules into electropermeabilized cells. *Biophys J*, 95(6):2837–2848, 2008.

[48] Zaharoff, D.A., Henshaw, J.W., Mossop, B., and Yuan, F. Mechanistic analysis of electroporation-induced cellular uptake of macromolecules. *Exp Biol Med*, 233(1):94–105, 2008.

[49] Kinosita, K., Ashikawa, I., Saita, N., Yoshimura, H., Itoh, H., Nagayma, K., and Ikegami, A. Electroporation of cell membrane visualized under a pulsed-laser fluorescence microscope. *Biophys J*, 53:1015–1019, 1988.

[50] Hibino, M., Shigemori, M., Itoh, H., Nagayama, K., and Kinosita, K.J. Membrane conductance of an electroporated cell analyzed by submicrosecond imaging of transmembrane potential. *Biophys J*, 59(1):209–220, 1991.

[51] Hibino, M., Itoh, H., and Kinosita, K. Time courses of cell electroporation as revealed by submicrosecond imaging of transmembrane potential. *Biophys J*, 64(6):1789–1800, 1993.

[52] Frey, W., White, J.A., Price, R.O., Blackmore, P.F., Joshi, R.P., Nuccitelli, R., Beebe, S.J., Schoenbach, K.H., and Kolb, J.F. Plasma membrane voltage changes during nanosecond pulsed electric field exposure. *Biophys J*, 90:3608–3615, 2006.

[53] Pakhomov, A.G., Shevin, R., White, J.A., Kolb, J.F., Pakhomova, O.N., Joshi, R.P., and Schoenbach, K.H. Membrane permeabilization and cell damage by ultrashort electric field shocks. *Arch Biochem Biophys*, 465(1):109–118, 2007.

[54] Pakhomov, A.G., Kolb, J.F., White, J.A., Joshi, R.P., Xiao, S., and Schoenbach, K.H. Long-lasting plasma membrane permeabilization in mammalian cells by nanosecond pulsed electric field (nsPEF). *Bioelectromagnetics*, 28(8):655–663, 2007.

[55] Satkauskas, S., Bureau, M.F., Puc, M., Mahfoudi, A., Scherman, D., Miklavcic, D., and Mir, L.M. Mechanisms of in vivo DNA electrotransfer: Respective contributions of cell electropermeabilization and DNA electrophoresis. *Mol Ther*, 5(2):133–140, 2002.

[56] Cemazar, M., Golzio, M., Sersa, G., Hojman, P., Kranjc, S., Mesojednik, S., Rols, M., and Teissie, J. Control by pulse parameters of DNA electrotransfer into solid tumors in mice. *Gene Ther*, 2009.

[57] Krassowska, W., Nanda, G.S., Austin, M.B., Dev, S.B., and Rabussay, D.P. Viability of cancer cells exposed to pulsed electric fields: The role of pulse charge. *Ann Biomed Eng*, 31(1):80–90, 2003.

[58] Schoenbach, K.H., Beebe, S.J., and Buescher, E.S. Intracellular effect of ultrashort electrical pulses. *Bioelectromagnetics*, 22(6):440–448, 2001.

[59] Beebe, S.J., Fox, P.M., Rec, L.J., Somers, K., Stark, R.H., and Schoenbach, K.H. Nanosecond pulsed electric field (nsPEF) effects on cells and tissues: Apoptosis induction and tumor growth inhibition. *IEEE T Plasma Sci*, 30(1):286–292, 2002.

[60] Beebe, S.J., White, J., Blackmore, P.F., Deng, Y.P., Somers, K., and Schoenbach, K.H. Diverse effects of nanosecond pulsed electric fields on cells and tissues. *DNA Cell Biol*, 22(12):785–796, 2003.

[61] Buescher, E.S. and Schoenbach, K.H. Effects of submicrosecond, high intensity pulsed electric fields on living cells–Intracellular electromanipulation. *IEEE T Dielect El In*, 10(5):788–794, 2003.

[62] Deng, J.D., Schoenbach, K.H., Buescher, E.S., Hair, P.S., Fox, P.M., and Beebe, S.J. The effects of intense submicrosecond electrical pulses on cells. *Biophys J*, 84(4):2709–2714, 2003.

[63] Vernier, P.T., Sun, Y.H., Marcu, L., Salemi, S., Craft, C.M., and Gundersen, M.A. Calcium bursts induced by nanosecond electric pulses. *Biochem Bioph Res Co*, 310:286–295, 2003.

[64] Chen, N.Y., Schoenbach, K.H., Kolb, J.F., Swanson, R.J., Garner, A.L., Yang, J., Joshi, R.P., and Beebe, S.J. Leukemic cell intracellular responses to nanosecond electric fields. *Biochem Bioph Res Co*, 317(2):421–427, 2004.

[65] White, J.A., Blackmore, P.F., Schoenbach, K.H., and Beebe, S.J. Stimulation of capacitative calcium entry in HL-60 cells by nanosecond pulsed electric fields. *J Biol Chem*, 279(22):22964–22972, 2004.

[66] Vernier, P.T., Sun, Y.H., Marcu, L., Craft, C.M., and Gundersen, M.A. Nanosecond pulsed electric fields perturb membrane phospholipids in T lymphoblasts. *FEBS Lett*, 572:103–108, 2004.

[67] DeBruin, K.A. and Krassowska, W. Modeling electroporation in a single cell. I. Effects of field strength and rest potential. *Biophys J*, 77(3):1213–1224, 1999.

[68] DeBruin, K.A. and Krassowska, W. Modeling electroporation in a single cell. II. Effects of ionic concentrations. *Biophys J*, 77(3):1225–1233, 1999.

[69] Smith, K.C., Neu, J.C., and Krassowska, W. Model of creation and evolution of stable electropores for DNA delivery. *Biophys J*, 86(5):2813–2826, 2004.

[70] Gowrishankar, T.R., Esser, A.T., Vasilkoski, Z., Smith, K.C., and Weaver, J.C. Microdosimetry for conventional and supra-electroporation in cells with organelles. *Biochem Bioph Res Co*, 341:1266–1276, 2006.

[71] Krassowska, W. and Filev, P.D. Modeling electroporation in a single cell. *Biophys J*, 92(2):404–417, 2007.

[72] Smith, K.C. and Weaver, J.C. Active mechanisms are needed to describe cell responses to submicrosecond, megavolt-per-meter pulses: Cell models for ultrashort pulses. *Biophys J*, 95(4):1547–1563, 2008.

[73] Esser, A.T., Smith, K.C., Gowrishankar, T.R., Vasilkoski, Z., and Weaver, J.C. Mechanisms for the intracellular manipulation of organelles by conventional electroporation. *Biophys J*, 98(11):2506–14, 2010.

[74] Talele, S., Gaynor, P., Cree, M.J., and van Ekeran, J. Modelling single cell electroporation with bipolar pulse parameters and dynamic pore radii. *J Electrostat*, 68(3):261–274, 2010.

[75] Vernier, P.T., Sun, Y.H., Marcu, L., Craft, C.M., and Gundersen, M.A. Nanoelectropulse-induced phosphatidylserine translocation. *Biophys J*, 86:4040–4048, 2004.

[76] Vernier, P.T., Sun, Y.H., and Gundersen, M.A. Nanoelectropulse-driven membrane perturbation and small molecule permeabilization. *BMC Cell Biol*, 7:37, 2006.

[77] Yao, C., Li, C., Mi, Y., Sun, C., and Mo, D. Analysis of transmembrane potentials induced by pulsed electric field with different durations based on five-shelled dielectric model of cell. In *P Ann Int IEEE EMBS*, pages 4243–4246. Shanghai, China, 2005.

[78] Kotnik, T. and Miklavcic, D. Theoretical evaluation of voltage inducement on internal membranes of biological cells exposed to electric fields. *Biophys J*, 90:480–491, 2006.

[79] Yao, C., Mo, D., Li, C., Sun, C., and Mi, Y. Study of transmembrane potentials of inner and outer membranes induced by pulsed-electric-field model and simulation. *IEEE T Plasma Sci*, 35(5):1541–1549, 2007.

[80] Yao, C., Mi, Y., Li, C., Hu, X., Chen, X., and Sun, C. Study of transmembrane potentials on cellular inner and outer membrane–Frequency response model and its filter characteristic simulation. *IEEE T Bio-Med Eng*, 55(7):1792–1799, 2008.

[81] Neu, J.C. and Krassowska, W. Asymptotic model of electroporation. *Phys Rev E*, 59(3):3471–3482, 1999.

[82] Glaser, R.W., Leikin, S.L., Chernomordik, L.V., Pastushenko, V.F., and Sokirko, A.I. Reversible electrical breakdown of lipid bilayers: Formation and evolution of pores. *Biochim Biophys Acta*, 940(2):275–287, 1988.

[83] Vasilkoski, Z., Esser, A.T., Gowrishankar, T.R., and Weaver, J.C. Membrane electroporation: The absolute rate equation and nanosecond time scale pore creation. *Phys Rev E*, 74(2), 2006.

[84] Tieleman, D.P., Leontiadou, H., Mark, A.E., and Marrink, S.J. Simulation of pore formation in lipid bilayers by mechanical stress and electric fields. *J Am Chem Soc*, 125(21):6382–6383, 2003.

[85] Tieleman, D.P. The molecular basis of electroporation. *BMC Biochem*, 5(10), 2004.

[86] Tarek, M. Membrane electroporation: A molecular dynamics simulation. *Biophys J*, 88:4045–4053, 2005.

[87] Gurtovenko, A.A. and Vattulainen, I. Pore formation coupled to ion transport through lipid membranes as induced by transmembrane ionic charge imbalance: Atomistic molecular dynamics study. *J Am Chem Soc*, 127:17570–17571, 2005.

[88] Hu, Q., Sridhara, V., Joshi, R.P., Kolb, J.F., and Schoenbach, K.H. Molecular dynamics analysis of high electric pulse effects on bilayer membranes containing DPPC and DPPS. *IEEE T Plasma Sci*, 34:1405–1411, 2006.

[89] Wohlert, J., den Otter, W.K., Edholm, O., and Briels, W.J. Free energy of a trans-membrane pore calculated from atomistic molecular dynamics simulations. *J Chem Phys*, 124, 2006.

[90] Vernier, P.T., Ziegler, M.J., Sun, Y.H., Chang, W.V., Gundersen, M.A., and Tieleman, D.P. Nanopore formation and phosphatidylserine externalization in a phospholipid bilayer at high transmembrane potential. *J Am Chem Soc*, 128:6288–6289, 2006.

[91] Vernier, P.T. and Ziegler, M.J. Nanosecond field alignment of head group and water dipoles in electroporating phospholipid bilayers. *J Phys Chem B*, 111(45):12993–12996, 2007.

[92] Leontiadou, H., Mark, A.E., and Marrink, S.J. Ion transport across transmembrane pores. *Biophys J*, 92(12):4209–4215, 2007.

[93] Bockmann, R.A., de Groot, B.L., Kakorin, S., Neumann, E., and Grubmuller, H. Kinetics, statistics, and energetics of lipid membrane electroporation studied by molecular dynamics simulations. *Biophys J*, 95(4):1837–1850, 2008.

[94] Ziegler, M.J. and Vernier, P.T. Interface water dynamics and porating electric fields for phospholipid bilayers. *J Phys Chem B*, 112(43):13588–13596, 2008.

Chapter 2

Compilation and Computation of the Size, Charge, and Diffusivity of Fluorescent Dyes and Other Small Molecules

Abstract

Quantitative descriptions of molecular transport within bulk media and through small aqueous pathways are of long-standing interest. Motivations range from fundamental mechanistic understanding to optimization of drug delivery, involving processes such as diffusive permeation, iontophoresis, and electroporation. Molecular size, charge, and diffusivity are critical input parameters in these quantitative descriptions that are often unavailable in the research literature, even for important and widely used molecules. Here, we describe in silico methods to estimate molecular size, charge, and diffusivity and provide these parameters for a number of fluorescent dyes (e.g., Alexa, Rhodamine, and propidium) and proteins (e.g., human serum albumin) that are widely used in experimental research. First, we describe methods of "measuring" molecular dimensions using software and the advantages of regarding their shape as approximately cylindrical, rather than spherical. Second, we show how software tools can be used to "titrate" molecules to determine their net charge. Third, we describe the development of molar mass- and molecular volume-based diffusivity correlations, and show how considerations of molecular shape can be used to increase the quality of these correlations. The resulting molecular charge and diffusivity estimates are in good agreement with published values. The predicted diffusivity values have a mean error of $\sim$10 % for the basic (non-shape-corrected) correlations and just $\sim$4 % for the shape-corrected correlations.

2.1 Introduction

The most fundamental parameters relevant to the transport of molecular solutes are their size, charge, and diffusivity (diffusion coefficient) [1–3]. Knowledge of these parameters is important to a wide range of experimental and theoretical studies of transport phenomena in biological systems, from intracellular transport within the cytoplasm [4, 5] to transmembrane transport through channels [6, 7] and lipidic pores [8, 9]. Additionally, quantitative characterization of transport and transport parameters is highly relevant to a range of clinical applications. Examples include iontophoresis for transdermal drug delivery [10–13], physical methods for improving gene delivery [14], and electroporation-mediated delivery of drugs [15–19] and genes [20–26] to cells.

Accurate determinations of diffusivity for many molecules of biological and experimental significance either have not been reported or are difficult to find in the research literature. The diffusivities of some molecules have only been measured with imprecise, dated methods, and the diffusivities of many others have simply never been measured at all. Moreover, some of the parameters that are available are of questionable accuracy. The widely used Rhodamine 6G, for example, was long said to have a diffusivity of $28 \times 10^{-11}\,\mathrm{m}^2/\mathrm{s}$ [27], but several recent studies [28–30] have used a range of high-precision methods and found that its value is actually in the range $41.1 \times 10^{-11} - 45.5 \times 10^{-11}\,\mathrm{m}^2/\mathrm{s}$, which is $\sim 50\,\%$ larger.

Mathematical models of transport phenomena use diffusivity, and often size and charge, as basic input parameters, and therefore the quality of the model results is limited by the quality of the input parameters (the well-known “garbage in, garbage out” problem). As a result, accurate values of these parameters for widely used molecules are of great importance.

In this study, we developed in silico methods of determining and verifying molecular size, charge, and diffusivity values. Our particular motivation was to determine the transport properties of fluorescent dyes, like propidium and yo-pro-1, that are widely used in investigations of electroporation

[8, 31–35], as well as molecular species that are widely used in biological experiments, many of them fluorescent dyes or proteins that are commonly labeled with fluorescent dyes. Several recent studies have used high-precision methods to measure diffusivity [28–30, 36], and we took advantage of this to increase the quality of our diffusivity estimates.

The methods described here, as well as the results and consolidation of useful experimental values from the research literature, should aid researchers studying biological transport.

2.2 Methods and Results

2.2.1 Molecule Selection and Structure Acquisition

Molecule Selection

Each molecule examined was selected for one of a few reasons. The first and main reason was relevance to our primary field of study, electroporation. Such molecules included ATP, bleomycin, calcein, fluorescein, lucifer yellow, propidium, yo-pro-1, cytochrome *c*, human serum albumin (HSA), bovine serum albumin (BSA), and lactalbumin, among others. The second reason for selection was the availability of recent high-precision diffusivity measurements [28–30, 36]. Such molecules included the Alexa dyes, Atto 655, Oregon Green 488, and the Rhodamine dyes. The third reason for selection was shape. Our initial results suggested a relationship between molecular shape and diffusivity. Therefore, the vital stains Congo Red and Fast Scarlet, both of which are rod-shaped and have published diffusivity values, were added to help elucidate the effect of shape on diffusivity. Finally, the ions chloride, calcium, sodium, and potassium, were selected for their importance to the functioning of biological systems and for comparison purposes.

Acquisition of Molecular Structures

The structures of the small (non-protein) molecules were obtained from the PubChem (http://pubchem.ncbi.nlm.nih.gov) and Chemical Entities of Biological Interest (ChEBI) (http://www.ebi.ac.uk/chebi) databases. When possible, the structures were downloaded in their pre-optimized 3-D conformations. When their 3-D conformations were unavailable, their 2-D conformations were

downloaded and the ChemAxon MarvinView (version 5.3.8, 2010, http://www.chemaxon.com) conformer was used to find the lowest-energy 3-D conformations for the structures.

The structures of the proteins were obtained from the Protein Data Bank (PDB) (http://www.pdb.org) in their 3-D conformations.

Table 2.1 lists all of the molecules studied here with the structure source and basic properties of each.

2.2.2 Molecular Size and Shape

Molecular Size

The molar mass M_s of each molecule studied was taken from its entry in its structure source database (Table 2.1).

UCSF Chimera [37] (version 1.4.1, 2010, http://www.cgl.ucsf.edu/chimera) was used to visualize the structures of molecules and measure their van der Waals (VDW) volumes. After loading and examining each molecule with the Chimera software, the VDW surface was added using the *Surface* tool and the molecular volume V_s was determined using the *Measure Volume and Area* tool. The molecular volume of each molecule is shown in Table 2.1.

Molecular Shape and Dimensions

UCSF Chimera was also used to assess the shapes of molecules and measure their dimensions. In general, molecules do not exhibit simple geometric shapes. Rather, they are amorphous and "lumpy". Nonetheless, for many purposes, it is sufficient to approximate the shapes of molecules as simple, well-defined geometric shapes (e.g., spheres and cylinders). We chose to approximate the molecules as cylinders because this allowed a much more precise description of molecular shape than approximating them as spheres, while still being simple enough to facilitate in silico "measurement" of the molecular dimensions.

Table 2.1: Molecular Structure Sources and Basic Properties

Molecule	Database	ID	M_s	V_s	r_s	l_s	S_s	z_s
Alexa 350	ChEBI	51744	396.3	0.3015	0.43	1.65	1.92	−1.00
Alexa 488	ChEBI	52953	532.5	0.4046	0.67	1.44	1.08	−3.00
Alexa 546	PubChem	25164103	1056.4	0.8920	0.86	2.63	1.53	−3.00
Alexa 594	ChEBI	51250	819.9	0.6980	0.80	1.84	1.15	−2.00
Antipyrine	PubChem	2206	188.2	0.1695	0.40	1.19	1.49	0.00
ATP	PubChem	5957	507.2	0.3792	0.62	1.22	0.98	−3.49
Atto 655	PubChem	16218785	527.6	0.4522	0.79	1.74	1.10	−1.00
BCECF	PubChem	4241719	520.4	0.4380	0.65	1.71	1.32	−4.48
Bleomycin A_2	ChEBI	MSDCHEM:BLM	1416.6	1.2470	0.89	2.76	1.55	+0.67
Bleomycin B_2	ChEBI	MSDCHEM:BLB	1426.5	1.2480	1.14	3.83	1.68	+0.84
Calcein	PubChem	65079	622.5	0.5204	0.58	1.89	1.63	−3.61
Congo Red	PubChem	11314	652.7	0.5259	0.49	2.81	2.87	−2.00
Cy5	ChEBI	38047	752.9	0.6555	0.92	2.49	1.35	−1.00
Eosin Bluish	PubChem	452704	580.1	0.4092	0.67	1.49	1.11	−2.00
Eosin Yellowish	PubChem	27020	647.9	0.4523	0.64	1.26	0.99	−1.85
Ethidium	PubChem	3624	314.4	0.2872	0.56	1.37	1.22	+1.00
Ethidium Homodimer	ChEBI	52843	650.9	0.6014	0.65	2.51	1.93	+3.11
Fast Scarlet	PubChem	13817	680.8	0.5610	0.53	2.80	2.64	−2.00
FITC	PubChem	18730	389.4	0.3103	0.60	1.51	1.27	−0.05
Fluorescein	PubChem	16850	332.3	0.2712	0.57	1.28	1.12	−0.05
Glucose	PubChem	24749	180.2	0.1503	0.32	1.09	1.70	0.00
Glutamic Acid	PubChem	104813	146.1	0.1215	0.32	0.96	1.50	−1.01
Lucifer Yellow	PubChem	93368	445.4	0.3172	0.61	1.46	1.20	−2.00
Meglumine	PubChem	4049	195.2	0.1738	0.33	1.30	1.97	+0.98
Methylene Blue	PubChem	4139	284.4	0.2514	0.38	1.65	2.17	+1.00
Oregon Green 488	PubChem	5289081	412.3	0.3124	0.63	1.43	1.13	−2.88
Propidium	PubChem	4939	414.6	0.4041	0.69	1.55	1.12	+2.00
Rhodamine 110	PubChem	65204	330.3	0.2852	0.61	1.23	1.01	−0.19
Rhodamine 123	PubChem	65218	344.4	0.3062	0.59	1.25	1.07	+0.66
Rhodamine 6G	PubChem	65211	443.6	0.4174	0.68	1.61	1.18	+0.05
Rhodamine B	PubChem	6695	443.6	0.4115	0.69	1.74	1.26	0.00
Serva Blue	PubChem	5856033	833.0	0.7804	0.72	2.52	1.75	−1.00
Sucrose	PubChem	5988	342.3	0.2827	0.45	1.21	1.33	0.00
Trehalose	PubChem	7427	342.3	0.2798	0.47	1.27	1.35	0.00
Trypan Blue	PubChem	5904246	868.8	0.6663	0.59	3.16	2.68	−4.00
Urea	PubChem	1176	60.1	0.0499	0.29	0.58	1.00	0.00
Yo-pro-1	PubChem	6913121	375.5	0.3531	0.53	1.71	1.63	+2.00
Cytochrome *c*	PDB	2B4Z	12212.0	12.4900	2.04	4.27	1.05	+9.00
HSA/BSA*	PDB	1N5U	68330.2	71.3500	4.32	9.26	1.07	−11.02
Lactalbumin	PDB	1A4V	14173.4	15.5100	1.76	4.30	1.22	−4.00
Calcium	PubChem	271	40.1	0.0335	0.20	0.40	1.00	+2.00
Chloride	PubChem	312	35.5	0.0225	0.18	0.35	1.00	−1.00
Potassium	PubChem	813	39.1	0.0871	0.28	0.55	1.00	+1.00
Sodium	PubChem	923	23.0	0.0490	0.23	0.45	1.00	+1.00

*HSA (human serum albumin) was used for all structural measurements and charge and diffusivity calculations. BSA (bovine serum albumin) was used for experimental diffusivity values. M_s: Molar mass (g/mol). V_s: van der Waals molecular volume (nm^3). r_s: Radius of cylindrical approximation to molecule (nm). l_s: Length of cylindrical approximation to molecule (nm). S_s: Ratio of length to diameter ($l_s/2r_s$). z_s: Net charge (valence) of molecule at pH 7.4.

The measurements were made using the Chimera *Axes* and *Plane* tools. The *Axes* tool aligns a semi-transparent cylindrical axis with the molecule using the orientation that minimizes the average distance from each atom to the axis. The radius of the cylindrical axis was adjusted until it was just large enough to encompass the VDW surface of the entire molecule. The radius r_s and length l_s of the cylindrical axis were then recorded. The cylindrical dimensions of the molecules are summarized in Table 2.1.

The Chimera *Plane* tool was used to double-check the length measurement. The *Plane* tool aligns a circular plane with the molecule using the orientation that minimizes the average distance from each atom to the plane. The diameter of the circular plane was adjusted until it was just large enough to encompass the VDW surface of the entire molecule. In general, the diameter measured by the *plane* tool agreed very well with the length measured with the *Axes* tool.

The ChemAxon *Calculator Plugins* were used to provide a final check on both the radius and length of each molecule. The *Calculator* features a tool that can determine the orientation of a molecule whose projection has minimum area and compute both the radius of the projection and the length of the molecule parallel to the projection (perpendicular to the surface onto which the projection is cast). Similarly, the *Calculator* can determine the orientation of a molecule whose projection has maximum area and compute both the radius of the projection and the length of the molecule parallel to the projection. Although the ChemAxon *Calculator Plugins* did not measure the molecules in exactly the same way as the Chimera manual measurements, they provided a check on the Chimera measurements, and the results were generally consistent.

Figure 2.1 shows two example molecules: trypan blue (Fig. 2.1A) and calcein (Fig. 2.1B). Trypan blue, with a length-to-diameter ratio of 2.68, was among the most elongated, non-spherical molecules studied. Calcein, with a length-to-diameter ratio of 1.63, was more typical. For both molecules, the cylindrical approximation effectively characterizes the general molecular shape.

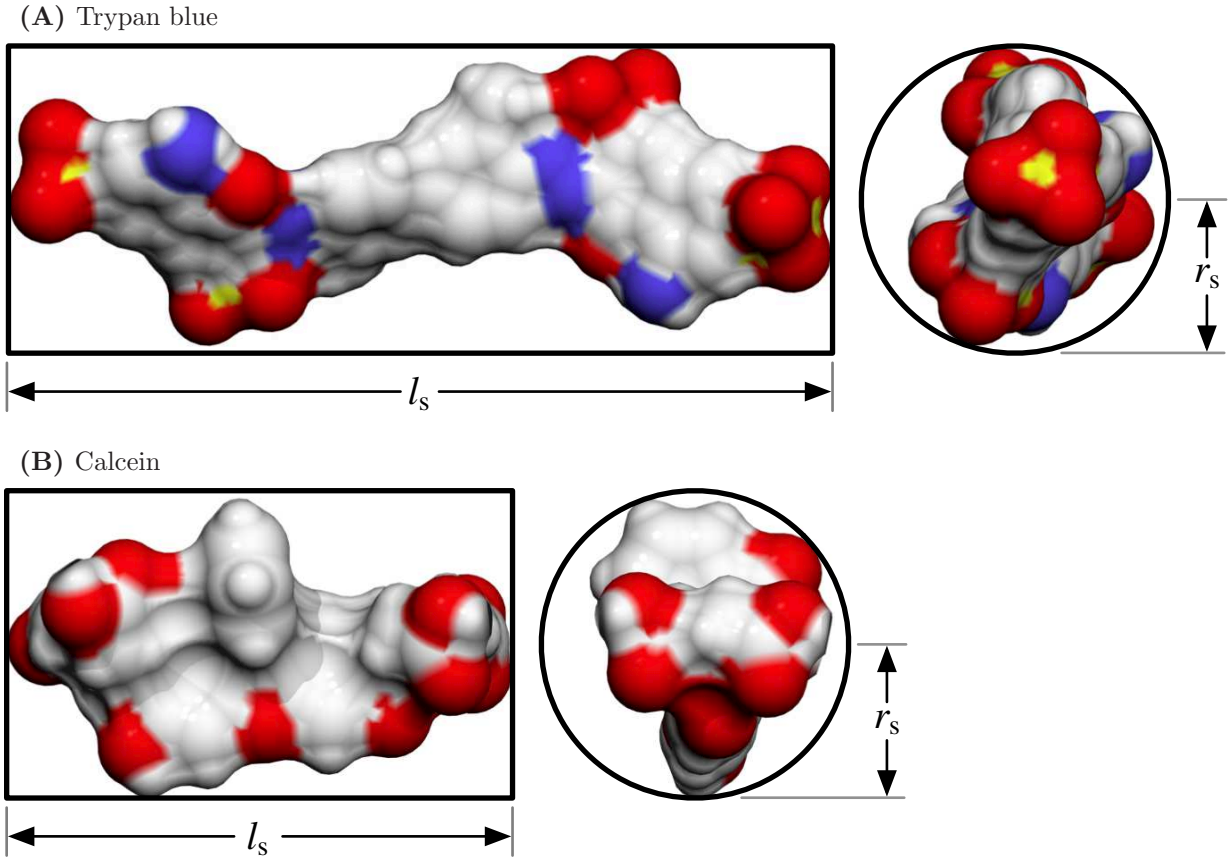

Figure 2.1: Cylindrical approximation to molecular shape. **(A)** Trypan blue (r_s = 0.59 nm, l_s = 3.16 nm). **(B)** Calcein (r_s = 0.58 nm, l_s = 1.89 nm). Note that the two molecules are not shown to the same scale. The cylindrical approximation to molecular shape gives a more precise description of molecular shape than a spherical approximation, while still being simple enough to facilitate in silico "measurement" of molecular dimensions.

2.2.3 Molecular Charge

The ChemAxon *Calculator Plugins* were used to determine the net charge z_s of each small (non-protein) molecule. This was done by using the *Calculator Plugins* to determine the distribution of microstates, or configurations, of each molecule at pH 7.4 and the charge of each microstate. The net charge of each molecule was then calculated as the weighted average of its microstate charges.

The online tool H++ [38, 39] (version 2.0, 2010, http://biophysics.cs.vt.edu/H++) was used to calculate net charge of each protein at pH 7.4. This computational tool is specifically designed for

macromolecules and evaluates their charge z_s in a manner similar to that described for the small molecules.

The molecular charge data are summarized in Table 2.1.

2.2.4 Molecular Diffusivity

The use of diffusivity correlations is one strategy for estimating the diffusivities of molecules for which accurate measurements are unavailable [40]. The basic idea behind a diffusivity correlation is to correlate experimentally measured diffusivities with some other quantity that is available for a wider range of molecules (e.g., molar mass). Then that quantity can be used with the correlation equation to estimate diffusivity for molecules for which diffusivity is unknown. The quality of the correlation can be tested by inputing the quantity into the correlation for molecules with known diffusivity and then comparing the predicted diffusivity with the experimentally measured diffusivity.

Experimental Diffusivity Data

We searched the research literature for diffusivity values for the molecules in our library, and were able to find values for all of the proteins and about half of the small molecules (Table 2.2). In a few cases, diffusivity values were found but excluded from this study. The reasons for exclusion included:

1. Clear from context that diffusivity value was only approximate (only one significant figure given, large error estimate, etc.).
2. No temperature information provided.
3. Referenced a primary source that could not be obtained.
4. Multiple more recent studies using more precise methods showed an older or less precise measurement to be inaccurate.

The range of experimental diffusivities found for each molecule is shown in Table 2.2 under the heading "D_{exp} range" along with citations of their sources.

For the purposes of developing the diffusivity correlation, if multiple diffusivity values were found, it was necessary to reduce the range of diffusivity values to a single value D_{exp} for each molecule. Generally, the average value was used. However, in some cases, one value was given more weight than others based on the data source. For example, a study whose sole focus was on using high-precision methods to measure diffusivity was given more weight than a study that mentioned measuring diffusivity in passing as a means to some other end.

Temperature Dependence of Diffusivity

Diffusivity is a temperature-dependent quantity. Therefore, in developing a diffusivity correlation, diffusivity values must be adjusted to a standard temperature, here 25 °C. The temperature dependence of diffusivity is clear from the Stokes-Einstein equation:

$$D_{\text{s}} = \frac{kT}{6\pi\eta r_{\text{st}}}. \tag{2.1}$$

Here, D_{s} is the solute diffusivity, k is the Boltzmann constant, T is the absolute temperature, η is the solvent viscosity, and r_{st} is the Stokes radius. The Stokes radius is that of the sphere that will have diffusivity D_{s} when diffusing in the solvent. It is often used as a rough estimate of the size of a molecule when its diffusivity is known.

The temperature dependence of diffusivity arises not just from the explicit T in Eq. 2.1, but also, and indeed mostly, from the implicit temperature dependence of the solvent viscosity η.

It follows from Eq. 2.1 that if a molecule has diffusivity $D_{\text{s},0}$ at absolute temperature T_0 with solvent viscosity η_0 and has diffusivity D_{s} at absolute temperature T with solvent viscosity η, then D_{s} is related to $D_{\text{s},0}$ by

$$D_{\text{s}} = D_{\text{s},0}\left(\frac{T}{T_0}\right)\left(\frac{\eta_0}{\eta}\right). \tag{2.2}$$

Equation 2.2 was used, when necessary, to adjust experimental diffusivity values to 25 °C (T = 298.15 K). The viscosity values were calculated using the tabulated viscosity values in Ref. [60].

Table 2.2: Diffusivity Values for Small Molecules, Proteins, and Ions

Molecule	D_{exp} range	D_{exp}	D_M	$\hat{D}_M$	D_V	$\hat{D}_V$	References
Alexa 350			46.92	59.79	48.78	62.22	
Alexa 488*†	46.5	46.5	41.99	40.02	43.91	42.06	[28]
Alexa 546*	36.5	36.5	32.46	36.58	33.08	37.30	[28]
Alexa 594			35.70	35.13	36.12	35.69	
Antipyrine*†	65	65	62.06	67.29	59.95	65.54	[41]
ATP*	40.1 – 47.5	43	42.76	39.41	44.94	41.65	[42, 43]
Atto 655*†	40.7 – 42.7	41.7	42.13	40.51	42.19	40.82	[30, 36]
BCECF			42.35	43.86	42.68	44.41	
Bleomycin A_2			29.07	33.14	29.34	33.44	
Bleomycin B_2			29.00	34.59	29.34	34.95	
Calcein			39.59	45.92	40.12	46.62	
Congo Red*	50 – 76.3	67	38.90	69.44	39.97	70.87	[44–46]
Cy5*†	37	37	36.87	38.90	36.94	39.12	[47]
Eosin Bluish			40.66	39.33	43.73	42.46	
Eosin Yellowish			39.01	36.16	42.19	39.28	
Ethidium			51.18	50.97	49.64	49.84	
Ethidium Homodimer			38.94	50.07	38.10	49.03	
Fast Scarlet*	68.2 – 72.2	70.2	38.29	63.21	39.06	64.15	[44, 45]
FITC			47.23	47.89	48.28	49.24	
Fluorescein*†	46.6 – 50.04	48	50.13	48.27	50.66	49.16	[28, 48]
Glucose*	67.28	67.28	63.09	73.51	62.58	73.38	[49]
Glutamic Acid*†	76.23 – 78.1	77	68.25	74.07	67.53	73.91	[49, 50]
Lucifer Yellow			44.90	44.51	47.90	47.70	
Meglumine			61.22	78.58	59.41	76.63	
Methylene Blue*	76	76	53.15	73.57	52.06	72.20	[51]
Oregon Green 488*†	41.1	41.1	46.22	44.81	48.16	46.96	[30]
Propidium			46.13	44.54	43.92	42.77	
Rhodamine 110*†	46	46	50.24	46.45	49.76	46.42	[29]
Rhodamine 123*†	47	47	49.46	46.72	48.51	46.22	[29]
Rhodamine 6G*†	41.4 – 45.5	43.2	44.97	44.39	43.42	43.17	[28–30]
Rhodamine B*†	44.9	44.9	44.97	45.60	43.64	44.55	[29]
Serva Blue			35.49	43.08	34.71	42.17	
Sucrose*†	52.09	52.09	49.57	51.27	49.92	51.95	[49]
Trehalose			49.57	51.68	50.10	52.54	
Trypan Blue			34.93	58.68	36.73	61.25	
Urea	137.3 – 145	138	95.32	85.77	92.88	84.86	[41, 52, 53]
Yo-pro-1			47.88	55.00	46.10	53.22	
Cytochrome *c*†*	13.51	13.51	12.94	12.75	12.86	12.62	[54]
HSA/BSA*†	6.53 – 7.83	6.9	6.78	6.90	6.89	6.94	[54–58]
Lactalbumin*†	10.5 – 13.0	11.8	12.24	12.84	11.90	12.43	[55, 57, 59]
Calcium	79.2	79.2	110.97	99.34	107.09	97.51	[60]
Chloride	203.2	203.2	116.20	103.85	123.61	112.09	[60]
Potassium	195.7	195.7	112.00	100.24	76.08	69.93	[60]
Sodium	133.4	133.4	136.74	121.47	93.48	85.43	[60]

All diffusivity values are for 25 °C and have units of $10^{-11}\,m^2/s$. *Used for development of initial and shape-corrected diffusivity correlations. †Used for development of basic (non-shape-corrected) diffusivity correlation ($S_s \leq 1.5$). D_{exp}: experimental diffusivity. D_M: mass-based diffusivity without shape-correction. $\hat{D}_M$: mass-based diffusivity with shape-correction. D_V: volume-based diffusivity without shape-correction. $\hat{D}_V$: volume-based diffusivity with shape-correction.

A cubic spline interpolation of the tabulated viscosity values was used to determine viscosity values at intermediate temperatures.

Diffusivity Correlations

The Stokes-Einstein equation (Eq. 2.1) shows that diffusivity is related to solute size: $D_s \propto r_{st}^{-1}$. The Stokes radius r_{st} is itself not a useful correlation quantity because it is generally not known. Moreover, even when the size of a molecule is known (e.g., using the method described above), it is unclear how the measured dimensions relate to the Stokes radius because most molecules are not perfectly spherical in shape.

In this study, we considered two other means of quantifying size: molar mass M_s and (VDW) molecular volume V_s. Importantly, these are ideal quantities for a correlation because they are widely available and easily obtained, much more so than diffusivity itself. Because $D_s \propto r_{st}^{-1}$ and $r_{st} \propto M_s^{1/3}$ and $r_{st} \propto V_s^{1/3}$, it follows that $D_s \propto M_s^{-1/3}$ and $D_s \propto V_s^{-1/3}$. Indeed, the assumption that $D_s \propto M_s^{-1/3}$ is the basis of several diffusivity correlations [55]. Here, rather than impose a particular exponent, we determined the exponent that best fit the data.

The molar mass-based diffusivity correlation proposed here is

$$D_M = a_M \left(\frac{T}{\eta}\right) M_s^{b_M}, \tag{2.3}$$

and the molecular volume-based diffusivity correlation proposed here is

$$D_V = a_V \left(\frac{T}{\eta}\right) V_s^{b_V}. \tag{2.4}$$

Here, D_M and D_V are the molar mass-based and molecular volume-based diffusivities, respectively. a_M, b_M, a_V, and b_V, are parameters to be fit by the experimental data. The temperature T and solvent viscosity η were not absorbed into a_M and a_V to allow easier calculation of D_M and D_V at non-standard temperatures.

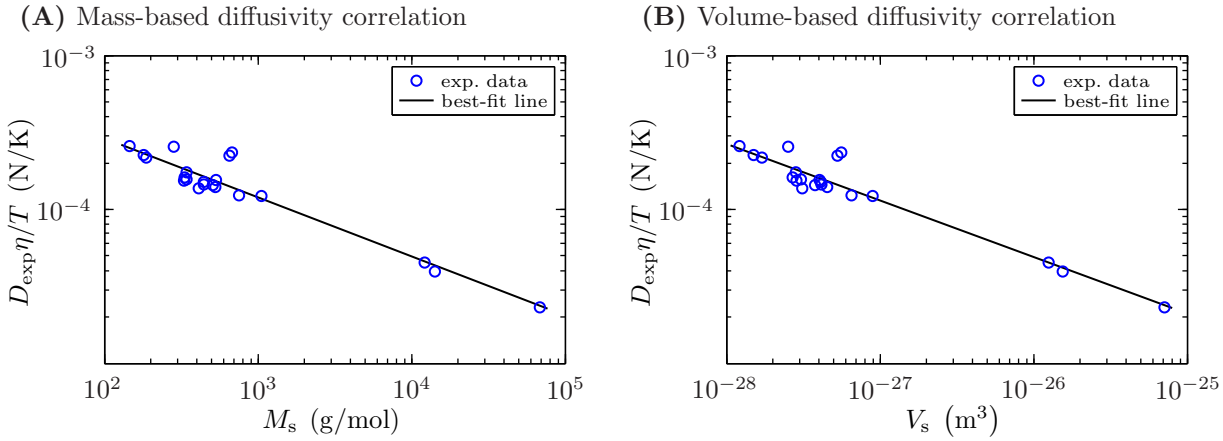

Figure 2.2: Correlations between diffusivity and **(A)** molar mass and **(B)** molecular volume. Diffusivity D_{exp} decreases as molar mass M_s and molecular volume V_s increase. The slope of the best-fit line is $\sim -1/3$ (in a log-log representation). The plots are similar in appearance because molar mass and molecular volume are strongly correlated. On each plot, there are three experimental data points located significantly farther from (above) the best-fit line than the other data points. These outlying points correspond to molecules that are particularly elongated in shape.

Figure 2.2 shows the results of plotting $D_{exp}\eta/T$ vs. M_s and V_s using the diffusivity, molar mass, and molecular volume data in Table 2.1. For a perfect correlation, the point plotted for each molecule would be located on the best-fit line. Indeed, most of the plotted points do lie on or near the best-fit line. However, there are three points that lie relatively far off (above) the best-fit line. For these points, the experimentally measured diffusivity is significantly larger than the diffusivity that would be predicted by either the mass-based or volume-based correlation.

Effect of Molecular Shape on Diffusivity

After creating the initial correlation, we compared the predicted diffusivity values with the experimentally measured diffusivity values to see whether there was a pattern to the error. Specifically, we hypothesized that molecular shape and charge, which were not factored into the correlations, might affect diffusivity and thereby affect the accuracy of the correlations.

We did not find a relationship between molecular charge and the error in the predicted diffusivities,

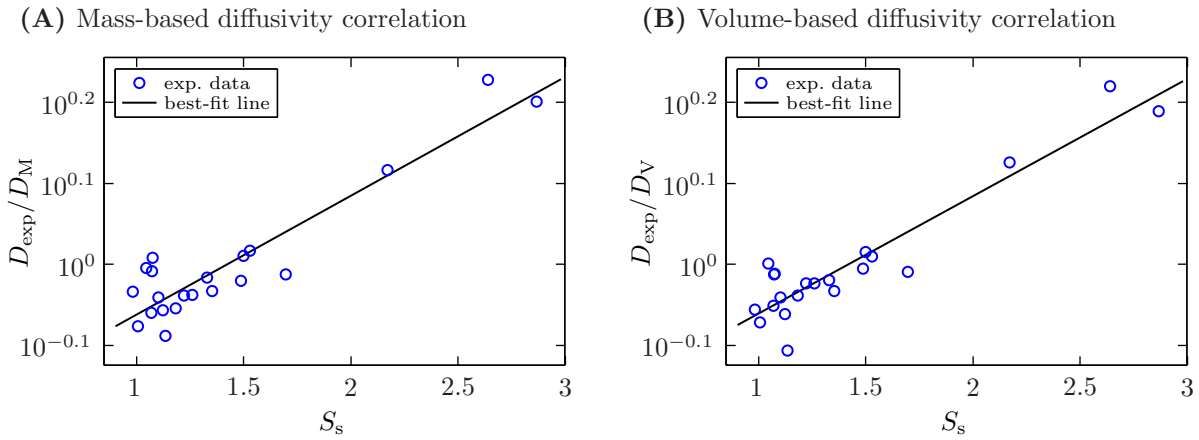

Figure 2.3: Effect of molecular shape on the **(A)** molar mass-based and **(B)** molecular volume-based diffusivity correlations. For each molecule, the ratio of the experimental diffusivity D_{exp} to predicted diffusivities D_M and D_V is plotted against the shape factor S_s, which is the ratio of the molecule's length to its diameter. When $S_s \lesssim 1.5$, the correlations slightly overestimate diffusivity (i.e., $D_M > D_{exp}$ and $D_V > D_{exp}$). When $S_s \gtrsim 1.5$, the correlations underestimate diffusivity (i.e., $D_M < D_{exp}$ and $D_V < D_{exp}$).

but we did find a relationship between the molecular shape and the error in the predicted diffusivity values. Figure 2.3 shows D_{exp}/D_M plotted against the shape factor S_s for the molar mass-based correlation (Fig. 2.3A) and D_{exp}/D_V plotted against the shape factor S_s for the molecular volume-based correlation (Fig. 2.3B). Here, the shape factor $S_s \equiv l_s/2r_s$ is the ratio of a molecule's length to its diameter. $S_s \approx 1$ for molecules that are approximately spherical and $S_s > 1$ for less spherical, more rod-like molecules, like trypan blue (Fig. 2.1A).

The relationship found between D_{exp}/D_M and S_s is, as shown in Fig. 2.3, a linear relationship between the logarithm of D_{exp}/D_M and S_s. (The same is true of the relationship between D_{exp}/D_V and S_s, but here we will focus on the molar mass-based correlation for brevity.) Thus, the best-fit line is described by an equation of the form

$$\frac{D_{exp}}{D_M} \approx \alpha_M \beta_M^{S_s}, \tag{2.5}$$

where α_M and β_M are parameters determined by the best-fit line. The right-hand side of Eq. 2.5 can be viewed as a shape-correction factor for the molar mass-based diffusivity correlation. Therefore,

given the initial estimate of diffusivity D_M from Eq. 2.3, an improved diffusivity estimate $\hat{D}_M$ that takes into account the effect of shape on diffusivity is

$$\hat{D}_M = D_M \alpha_M \beta_M^{S_s}. \tag{2.6}$$

Substituting for D_M, the molar mass-based diffusivity correlation with shape-correction is

$$\hat{D}_M = \hat{a}_M \left(\frac{T}{\eta}\right) M_s^{\hat{b}_M} \hat{c}_M^{S_s}, \tag{2.7}$$

where $\hat{a}_M$, $\hat{b}_M$, and $\hat{c}_M$ are parameters. The simplest set of values that could be used for these parameters is $\hat{a}_M = a_M \alpha_M$, $\hat{b}_M = b_M$, and $\hat{c}_M = \beta_M$, where a_M, α_M, b_M, and β_M are all calculated from best-fit lines to their respective plots, as described above. However, in using this set of values, the shape-corrected correlation is stuck with some of the deficiencies of the original correlation. For example, the points in Fig. 2.2 associated with the molecules with large S_s values cause the initial correlation to overestimate the diffusivity of small molecules and thereby increases the magnitude of the slope. This would only be partially corrected by this simple set of parameters because the $\hat{b}_M$, which describes the slope of the best-fit line in Fig. 2.2, would remain the same.

A better approach to setting $\hat{a}_M$, $\hat{b}_M$, and $\hat{c}_M$ is to simultaneously fit all three using a nonlinear fitting algorithm. To do this, we used the MATLAB (version R2009a, 2009, http://www.mathworks.com) *nlinfit* function using the simple set of parameters as initial guesses. In using *nlinfit*, the objective was to find the parameters $\hat{a}_M$, $\hat{b}_M$, and $\hat{c}_M$ that result in the best-fit

$$D_{exp} \approx \hat{a}_M \left(\frac{T}{\eta}\right) M_s^{\hat{b}_M} \hat{c}_M^{S_s}. \tag{2.8}$$

Taking the logarithm of both sides and rearranging,

$$\log_{10}(D_{exp}) \approx \log_{10}(\hat{a}_M) + \log_{10}\left(\frac{T}{\eta}\right) + \hat{b}_M \log_{10}(M_s) + S_s \log_{10}(\hat{c}_M). \tag{2.9}$$

As input into *nlinfit*, the independent variables were $\log_{10}(M)$ and S_s, and the dependent variable was $\log_{10}(D_{exp})$. The fit parameters returned by *nlinfit* were $\log_{10}(\hat{a}_M)$, $\hat{b}_M$, and $\log_{10}(\hat{c}_M)$, from which the desired $\hat{a}_M$, $\hat{b}_M$, and $\hat{c}_M$ were easily determined.

Through similar development, the molecular volume-based diffusivity correlation with shape-correction is

$$\hat{D}_V = \hat{a}_V \left(\frac{T}{\eta}\right) V_s^{\hat{b}_V} \hat{c}_V^{S_s}. \tag{2.10}$$

The best-fit parameters found for the correlations are shown in Table 2.3.

Table 2.3: Diffusivity Correlation Parameters

Parameter	Value
a_M	1.3255×10^{-14} N/K
b_M	−0.3757
$\hat{a}_M$	7.9520×10^{-15} N/K
$\hat{b}_M$	−0.3618
$\hat{c}_M$	1.4174
a_V	2.0512×10^{-25} N/K
b_V	−0.3580
$\hat{a}_V$	2.5534×10^{-25} N/K
$\hat{b}_V$	−0.3480
$\hat{c}_V$	1.4080

Basic Diffusivity Correlation

After examining the effect of shape on diffusivity, we reevaluated the parameters for the basic correlation (i.e., without shape-correction) using only the molecules with $S_s \leq 1.5$ to prevent the more elongated molecules from skewing the correlation. (Most molecules in this study meet the $S_s \leq 1.5$ criterion, as the median S_s across all of the small molecules and proteins is 1.29.) The resulting a_M and b_M for the molar mass-based diffusivity correlation (Eq. 2.3) and a_V and b_V for the molecular volume-based diffusivity correlation (Eq. 2.4) are shown in Table 2.3.

The basic correlations, though less accurate than the shape-corrected correlations, are appropriate when a molecule is known to be relatively spherical, its structure/dimensions are unavailable, or

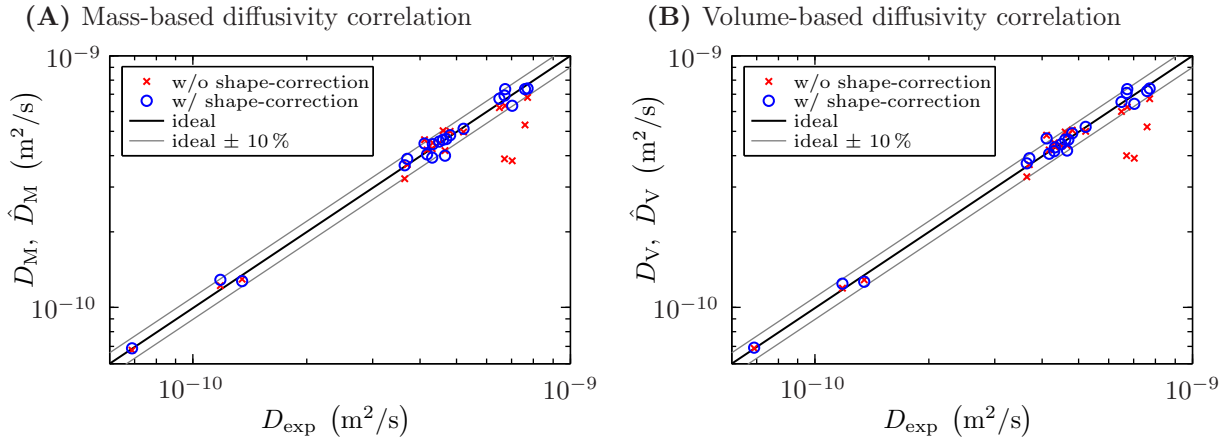

Figure 2.4: Quality of the **(A)** molar mass-based and **(B)** molecular volume-based diffusivity correlations both with (*blue circles*) and without (*red x-marks*) shape-correction. The diffusivity values D_{M} and D_{V} calculated with the basic correlations (i.e., without shape-correction) are generally in good agreement with the experimental values D_{exp}, except for elongated molecules, for which the predicted diffusivity values are significantly smaller than the measured values. The diffusivity values $\hat{D}_{\mathrm{M}}$ and $\hat{D}_{\mathrm{V}}$ calculated with the shape-corrected correlations are in excellent agreement with the experimental values D_{exp}, regardless of molecular shape, and are generally closer to the experimental values than the diffusivity values calculated using the basic correlations. The mean and median relative error are ∼10 % and ∼5 % for the basic correlations, and the mean and median relative error are ∼4 % and ∼4 % for the shape-corrected correlations.

when an approximate diffusivity value is adequate.

Quality of Diffusivity Correlations

Figure 2.4 shows the predicted diffusivity values plotted against the experimentally measured values for both correlations, with and without shape-correction. The diffusivity values calculated with the basic correlations are generally in good agreement with the experimental values, except for elongated molecules, for which the predicted diffusivity values are significantly smaller than the measured values. The mean and median relative error are 10.1 % and 4.1 % for the basic molar mass-based correlation, and the mean and median relative error are 10.1 % and 5.6 % for the basic molecular volume-based correlation.

The diffusivity values calculated with the shape-corrected correlations are in excellent agreement with the experimental values, regardless of molecular shape, and are generally closer to the ex-

perimental values than the diffusivity values calculated using the basic correlations. Almost every diffusivity value predicted by the shape-corrected correlations is within ±10 % of the experimentally measured value (Fig. 2.4). The mean and median relative error are 4.5 % and 3.5 % for the molar mass-based correlation with shape-correction, the mean and median relative error are 4.2 % and 3.2 % for the molecular volume-based correlation with shape-correction.

There is not a significant difference between the quality of the molar mass-based and molecular volume-based diffusivity predictions. From a practical standpoint, the molar mass-based correlation is better simply because molar mass is more easily obtained than molecular volume. The molar mass is available in the structural database entry for each molecule. The molecular volume, on the other hand, has to be calculated using software (e.g., Chimera).

2.2.5 Stokes Radii

While we have focused on characterizing molecular shape and size in terms of cylindrical dimensions, it is common in the research literature to characterize the size of molecules in terms of their Stokes radii. Thus, it is instructive to compare the dimensions measured using Chimera to the Stokes radii calculated from the experimental and correlation-based diffusivity values.

The Stokes-Einstein equation, as given in Eq. 2.1, relates the diffusivity to the size of sphere diffusing in a smooth medium. However, when the size of the solute molecule is on the same order as the size of the solvent molecule, continuum assumptions break down, and the Stokes-Einstein equation (Eq. 2.1) must be modified to account for microfriction [61]. Without this correction, the Stokes radius calculated from the Stokes-Einstein equation will underestimate the size of small solute molecules.

Rearranging the Stokes-Einstein equation (Eq. 2.1), an initial guess at the corrected Stokes radius is

$$r_{\mathrm{st},0} = \frac{kT}{6\pi\eta D_{\mathrm{s}}}. \tag{2.11}$$

Starting with $i = 0$ and $r_{st,i} = r_{st,0}$, the following iteration will converge on the corrected Stokes radius r_{st} as $i \to \infty$ [61]:

$$r_{st,i+1} = r_{st,i}\left(1 + 0.695\left(\frac{r_w}{r_{st,i}}\right)^{2.234}\right). \tag{2.12}$$

Here, r_w is the radius of the solvent molecule, which in this case is water ($r_w = 0.14\,\text{nm}$).

Table 2.4 shows the cylindrical dimensions of each molecule found using Chimera and the micro-friction-corrected Stokes radii of the molecules found using the experimental and correlation-based diffusivity values. In addition to the Stokes radii, the volume equivalent radius is shown for each molecule. This is the radius of a sphere with the same volume as the molecule.

In general, all of the calculated Stokes radii for each molecule are relatively similar, as expected, since the diffusivity values from which they are calculated are in good agreement. The Stokes radii tend to be larger than the volume equivalent radii because most molecules are much less tightly packed than spheres. It is interesting to note that the cylindrical radii are in relatively good agreement with the Stokes radii, even for elongated molecules, like fast scarlet and congo red.

2.3 Discussion

2.3.1 Molecular Size and Shape

In this study, molecular size and shape were shown to affect transport properties primarily through their effect on diffusivity. However, there are many biological systems in which transport occurs in confined spaces, such as in the cytoplasm of a cell [4, 5] or through a membrane pore [8, 9] or channel [6, 7]. In these cases, an understanding of the size and shape of a molecule can be critical in understanding its transport [9]. The ability of a molecule to fit through a tight pore is determined by the actual size of molecule, not the diameter of a sphere that has the same diffusivity as the molecule (Stokes sphere).

Here, small ions (e.g., calcium, chloride, sodium, and potassium) bear special mention because,

Table 2.4: Cylindrical and Spherical Approximations of Molecular Size

Molecule	r_s	l_s	r_{exp}	r_M	$\hat{r}_M$	r_V	$\hat{r}_V$	r_{Veq}
Alexa 350	0.43	1.65		0.54	0.43	0.52	0.42	0.42
Alexa 488	0.67	1.44	0.55	0.60	0.63	0.58	0.60	0.46
Alexa 546	0.86	2.63	0.69	0.77	0.68	0.75	0.67	0.60
Alexa 594	0.80	1.84		0.70	0.71	0.69	0.70	0.55
Antipyrine	0.40	1.19	0.40	0.42	0.39	0.43	0.40	0.34
ATP	0.62	1.22	0.59	0.59	0.64	0.56	0.60	0.45
Atto 655	0.79	1.74	0.60	0.60	0.62	0.60	0.62	0.48
BCECF	0.65	1.71		0.60	0.58	0.59	0.57	0.47
Bleomycin A_2	0.89	2.76		0.85	0.75	0.85	0.75	0.67
Bleomycin B_2	1.14	3.83		0.86	0.72	0.85	0.71	0.67
Calcein	0.58	1.89		0.63	0.55	0.63	0.54	0.50
Congo Red	0.49	2.81	0.39	0.65	0.38	0.63	0.37	0.50
Cy5	0.92	2.49	0.68	0.68	0.65	0.68	0.64	0.54
Eosin Bluish	0.67	1.49		0.62	0.64	0.58	0.59	0.46
Eosin Yellowish	0.64	1.26		0.64	0.69	0.60	0.64	0.48
Ethidium	0.56	1.37		0.50	0.50	0.51	0.51	0.41
Ethidium Homodimer	0.65	2.51		0.64	0.51	0.66	0.52	0.52
Fast Scarlet	0.53	2.80	0.38	0.66	0.41	0.64	0.41	0.51
FITC	0.60	1.51		0.54	0.53	0.53	0.52	0.42
Fluorescein	0.57	1.28	0.53	0.51	0.53	0.50	0.52	0.40
Glucose	0.32	1.09	0.39	0.41	0.36	0.42	0.36	0.33
Glutamic Acid	0.32	0.96	0.35	0.39	0.36	0.39	0.36	0.31
Lucifer Yellow	0.61	1.46		0.56	0.57	0.53	0.53	0.42
Meglumine	0.33	1.30		0.42	0.34	0.44	0.35	0.35
Methylene Blue	0.38	1.65	0.35	0.48	0.36	0.49	0.37	0.39
Oregon Green 488	0.63	1.43	0.61	0.55	0.56	0.53	0.54	0.42
Propidium	0.69	1.55		0.55	0.57	0.58	0.59	0.46
Rhodamine 110	0.61	1.23	0.55	0.51	0.55	0.51	0.55	0.41
Rhodamine 123	0.59	1.25	0.54	0.51	0.54	0.52	0.55	0.42
Rhodamine 6G	0.68	1.61	0.58	0.56	0.57	0.58	0.58	0.46
Rhodamine B	0.69	1.74	0.56	0.56	0.56	0.58	0.57	0.46
Serva Blue	0.72	2.52		0.70	0.59	0.72	0.60	0.57
Sucrose	0.45	1.21	0.49	0.51	0.50	0.51	0.49	0.41
Trehalose	0.47	1.27		0.51	0.49	0.51	0.49	0.41
Trypan Blue	0.59	3.16		0.72	0.44	0.68	0.42	0.54
Urea	0.29	0.58	0.22	0.29	0.32	0.30	0.32	0.23
Yo-pro-1	0.53	1.71		0.53	0.47	0.55	0.48	0.44
Cytochrome *c*	2.04	4.27	1.82	1.90	1.93	1.91	1.95	1.44
HSA/BSA	4.32	9.26	3.56	3.62	3.56	3.56	3.54	2.57
Lactalbumin	1.76	4.30	2.08	2.01	1.91	2.06	1.98	1.55
Calcium	0.20	0.40	0.34	0.26	0.28	0.27	0.29	0.20
Chloride	0.18	0.35	0.17	0.25	0.27	0.24	0.26	0.18
Potassium	0.28	0.55	0.18	0.26	0.28	0.35	0.38	0.28
Sodium	0.23	0.45	0.23	0.22	0.24	0.30	0.32	0.23

All lengths have units of nm. r_s: radius measured using Chimera software. l_s: length measured using Chimera software. r_{exp}: radius calculated from Stokes-Einstein equation using experimental diffusivity. r_M: radius calculated from Stokes-Einstein equation using diffusivity from mass-based correlation without shape-correction. $\hat{r}_M$: radius calculated from Stokes-Einstein equation using diffusivity from mass-based correlation with shape-correction. r_V: radius calculated from Stokes-Einstein equation using diffusivity from volume-based correlation without shape-correction. $\hat{r}_V$: radius calculated from Stokes-Einstein equation using diffusivity from volume-based correlation with shape-correction. r_{Veq}: radius of sphere with same volume as molecule.

in contrast to the larger species, they are truly spherical. Therefore, the corrected Stokes radius is a reasonable means of characterizing the size of small ions. Moreover, because of the strong interaction between the ions and surrounding water molecules [62], the corrected Stokes radius, relative to the VDW radius, will better capture the effective size of an ion insofar as it interacts with its surroundings and is transported through tight spaces, like pores [9].

2.3.2 Molecular Charge

Molecular charge is an important transport parameter because it determines how a molecule will move in response to gradients in electric potential, which are common in biological systems, especially at the interfaces like membranes. Molecular charge also affects the interactions among molecules in solution and between transported molecules and structures like pores through partitioning [9].

The net charge values calculated for the small molecules and proteins were in good agreement with analytically determined and experimentally measured values. The net charges of the small molecules were consistent with their formal charge values. The advantage of charge calculation method described here is that it considers the distribution of microstates to give a clearer picture of the net charge when there are multiple microstates with different charge.

The net charge values calculated for the proteins were also consistent with experimental measurements. BSA has a charge of about -10 at pH 7.4 [63], consistent with the value of -11 (for HSA) found here. Similarly, the reported charge of cytochrome *c* at pH 7.4 is in the range +6 to +9 [64–66]. The value determined here was +9.

2.3.3 Molecular Diffusivity

Numerous diffusivity correlations have been proposed in the past [40, 55, 67, 68]. The typical average error of correlations is in the range $8-16\,\%$ [40, 55, 67, 68]. The basic molar mass and molecular volume-based correlations developed here are comparable with an average error of $\sim 10\,\%$, and the shape-corrected correlations do significantly better with an average error of just

$\sim$4 %. It should be noted, however, that the library of molecules considered here was considerably smaller than some others. Tyn and Gusek, for example, considered 86 macromolecules in developing their correlation [55]. Additionally, the small error found here benefits from the inclusion of recent precisely measured experimental diffusivities. A diffusivity correlation, no matter how good, will exhibit large error if the measurements on which it is based exhibit large error.

To our knowledge, the explicit inclusion of shape in our diffusivity correlation is largely new, at least for small molecules. Hayduk and Buckley [69] found that "linear" (i.e., more elongated and rod-like) molecules had diffusivities $\sim$30 % higher than spherical molecules of the same volume, which is broadly consistent with our findings here. However, Hayduk and Buckley did not quantify shape in any way (i.e., molecules were either spherical or linear). Here, we found an explicit relationship between a measurable shape factor and diffusivity. The significant reduction in the error that resulted from the inclusion of a shape factor suggests that molecular shape may have been an overlooked, or at least unaccounted for, source of error in the development of other diffusivity correlations.

The shape-based correlations do come with a few caveats. First, the shape factors for the molecules considered ranged from about 1 to 3, and the data in this range supported the exponential form of the shape-correction factor developed. However, because the relationship between shape and diffusivity is empirical, rather than based on basic physical insights, it is not clear that the relationship will hold for shape factors greater than 3, and we would suggest further validation before using the shape-based correction factors for such elongated molecules. Second, all of the elongated molecules considered here were small molecules; the three proteins were all relatively spherical, with shape factors $\sim$1. Therefore, it is not clear from the data that the shape-correction factors will extend to larger molecules (proteins, nucleic acids, etc.). We would suggest further validation before using the shape-correction factors for larger molecules. Considerable work has been done relating diffusivity to shape for ellipsoidal [68] and rod-shaped macromolecules [68, 70], like nucleic acids, and these may be more appropriate for molecules that are especially large or long.

The diffusivity correlations should also not be used for exceptionally small solute molecules, as they tend to break down in this regime due to the granularity of the solvent. It is for this reason that the small ions (chloride, calcium, potassium, and sodium) and urea (60.1 g/mol) were not used in the development of the correlation, even though experimentally measured diffusivity values are available. We note that the diffusivity values predicted by the correlations for the next larger molecules in the library, glutamic acid (146.1 g/mol), glucose (180.2 g/mol), and antipyrine (188.2 g/mol), are all consistent with experimental values. This suggests that the lower limit for validity of the correlations is perhaps $\sim$100 g/mol.

References

[1] Bird, R.B., Stewart, W.E., and Lightfoot, E.N. *Transport Phenomena*. Wiley, New York, 1960.

[2] Deen, W.M. *Analysis of Transport Phenomena*. Oxford University Press, Oxford, 1998.

[3] Grodzinsky, A.J. *Fields, Forces, and Flows in Biological Systems*. Garland Science, London, 2011.

[4] Mastro, A.M., Babich, M.A., Taylor, W.D., and Keith, A.D. Diffusion of a small molecule in the cytoplasm of mammalian cells. *P Natl Acad Sci USA*, 81(11):3414–8, 1984.

[5] Verkman, A.S. Solute and macromolecule diffusion in cellular aqueous compartments. *Trends Biochem Sci*, 27(1):27–33, 2002.

[6] Hille, B. *Ionic Channels of Excitable Membranes, Third Edition*. Sinaur Associates, Sunderland, 2001.

[7] Rostovtseva, T. and Colombini, M. VDAC channels mediate and gate the flow of ATP: Implications for the regulation of mitochondrial function. *Biophys J*, 72(5):1954–62, 1997.

[8] Prausnitz, M.R., Lau, B.S., Milano, C.D., Conner, S., Langer, R., and Weaver, J.C. A quantitative study of electroporation showing a plateau in net molecular-transport. *Biophys J*, 65(1):414–422, 1993.

[9] Smith, K.C. and Weaver, J.C. Effects of hindrance and partitioning on ionic and molecular transport through small lipidic pores (in preparation).

[10] Kalia, Y.N., Naik, A., Garrison, J., and Guy, R.H. Iontophoretic drug delivery. *Adv Drug Deliv Rev*, 56(5):619–58, 2004.

[11] Nugroho, A.K., Della Pasqua, O., Danhof, M., and Bouwstra, J.A. Compartmental modeling of transdermal iontophoretic transport: I. In vitro model derivation and application. *Pharm Res*, 21(11):1974–84, 2004.

[12] Nugroho, A.K., Della-Pasqua, O., Danhof, M., and Bouwstra, J.A. Compartmental modeling of transdermal iontophoretic transport II: In vivo model derivation and application. *Pharm Res*, 22(3):335–46, 2005.

[13] Güngör, S., Delgado-Charro, M.B., Ruiz-Perez, B., Schubert, W., Isom, P., Moslemy, P., Patane, M.A., and Guy, R.H. Trans-scleral iontophoretic delivery of low molecular weight therapeutics. *J Control Release*, 147(2):225–31, 2010.

[14] Mehier-Humbert, S. and Guy, R.H. Physical methods for gene transfer: Improving the kinetics of gene delivery into cells. *Adv Drug Deliv Rev*, 57(5):733–53, 2005.

[15] Mir, L.M., Orlowski, S., Belehradek, J., and Paoletti, C. Electrochemotherapy potentiation of antitumor effect of bleomycin by local electric pulses. *Eur J Cancer*, 27(1):68–72, 1991.

[16] Sersa, G., Cemazar, M., and Miklavcic, D. Antitumor effectiveness of electrochemotherapy with cis-diamminedichloroplatinum(II) in mice. *Cancer Res*, 55(15):3450–3455, 1995.

[17] Heller, R., Jaroszeski, M.J., Glass, L.F., Messina, J.L., Rapaport, D.P., DeConti, R.C., Fenske, N.A., Gilbert, R.A., Mir, L.M., and Reintgen, D.S. Phase I/II trial for the treatment of cutaneous and subcutaneous tumors using electrochemotherapy. *Cancer*, 77(5):964–971, 1996.

[18] Hofmann, G.A., Dev, S.B., and Nanda, G.S. Electrochemotherapy: Transition from laboratory to the clinic. *IEEE Eng Med Biol*, 15:124–132, 1996.

[19] Conjeevaram, R., Banga, A.K., and Zhang, L. Electrically modulated transdermal delivery of fentanyl. *Pharm Res*, 19(4):440–4, 2002.

[20] Neumann, E., Schaefer-Ridder, M., Wang, Y., and Hofschneider, P.H. Gene transfer into mouse lyoma cells by electroporation in high electric fields. *EMBO J*, 1(7):841–5, 1982.

[21] Neumann, E., Kakorin, S., Tsoneva, I., Nikolova, B., and Tomov, T. Calcium-mediated DNA adsorption to yeast cells and kinetics of cell transformation by electroporation. *Biophys J*, 71(2):868–77, 1996.

[22] Heller, R., Jaroszeski, M., Atkin, A., Moradpour, D., Gilbert, R., Wands, J., and Nicolau, C. In vivo gene electroinjection and expression in rat liver. *FEBS Lett*, 389(3):225–8, 1996.

[23] Neumann, E., Kakorin, S., and Toensing, K. Fundamentals of electroporative delivery of drugs and genes. *Bioelectroch Bioener*, 48(1):3–16, 1999.

[24] Mir, L.M., Bureau, M.F., Gehl, J., Rangara, R., Rouy, D., Caillaud, J.M., Delaere, P., Branellec, D., Schwartz, B., and Scherman, D. High-efficiency gene transfer into skeletal muscle mediated by electric pulses. *P Natl Acad Sci USA*, 96(8):4262–4267, 1999.

[25] Jaroszeski, M.J., Gilbert, R., and Heller, R., editors. *Electrically Mediated Delivery of Molecules to Cells: Electrochemotherapy, Electrogenetherapy and Transdermal Delivery by Electroporation*. Humana Press, Totowa, 2000.

[26] Bodles-Brakhop, A.M., Heller, R., and Draghia-Akli, R. Electroporation for the delivery of DNA-based vaccines and immunotherapeutics: Current clinical developments. *Mol Ther*, 17(4):585–92, 2009.

[27] Magde, D., Elson, E.L., and Webb, W.W. Fluorescence correlation spectroscopy. II. An experimental realization. *Biopolymers*, 13(1):29–61, 1974.

[28] Petrásek, Z. and Schwille, P. Precise measurement of diffusion coefficients using scanning fluorescence correlation spectroscopy. *Biophys J*, 94(4):1437–48, 2008.

[29] Gendron, P.O., Avaltroni, F., and Wilkinson, K.J. Diffusion coefficients of several rhodamine derivatives as determined by pulsed field gradient-nuclear magnetic resonance and fluorescence correlation spectroscopy. *J Fluoresc*, 18(6):1093–101, 2008.

[30] Mueller, C.B., Loman, A., Pacheco, V., Koberling, F., Willbold, D., Richtering, W., and Enderlein, J. Precise measurement of diffusion by multi-color dual-focus fluorescence correlation spectroscopy. *EPL-Europhys Lett*, 83(4), 2008.

[31] Canatella, P.J., Karr, J.F., Petros, J.A., and Prausnitz, M.R. Quantitative study of electroporation-mediated molecular uptake and cell viability. *Biophys J*, 80(2):755–764, 2001.

[32] Puc, M., Kotnik, T., Mir, L.M., and Miklavcic, D. Quantitative model of small molecules uptake after in vitro cell electropermeabilization. *Bioelectrochemistry*, 60(1-2):1–10, 2003.

[33] Vernier, P.T., Sun, Y.H., and Gundersen, M.A. Nanoelectropulse-driven membrane perturbation and small molecule permeabilization. *BMC Cell Biol*, 7:37, 2006.

[34] Kennedy, S.M., Ji, Z., Hedstrom, J.C., Booske, J.H., and Hagness, S.C. Quantification of electroporative uptake kinetics and electric field heterogeneity effects in cells. *Biophys J*, 94(12):5018–5027, 2008.

[35] Pakhomov, A.G., Bowman, A.M., Ibey, B.L., Andre, F.M., Pakhomova, O.N., and Schoenbach, K.H. Lipid nanopores can form a stable, ion channel-like conduction pathway in cell membrane. *Biochem Bioph Res Co*, 385(2):181–6, 2009.

[36] Dertinger, T., Pacheco, V., von der Hocht, I., Hartmann, R., Gregor, I., and Enderlein, J. Two-focus fluorescence correlation spectroscopy: A new tool for accurate and absolute diffusion measurements. *Chemphyschem*, 8(3):433–43, 2007.

[37] Pettersen, E.F., Goddard, T.D., Huang, C.C., Couch, G.S., Greenblatt, D.M., Meng, E.C., and Ferrin, T.E. UCSF Chimera–A visualization system for exploratory research and analysis. *J Comput Chem*, 25(13):1605–12, 2004.

[38] Gordon, J.C., Myers, J.B., Folta, T., Shoja, V., Heath, L.S., and Onufriev, A. H++: A server for estimating pKas and adding missing hydrogens to macromolecules. *Nucleic Acids Res*, 33(Web Server issue):W368–71, 2005.

[39] Anandakrishnan, R. and Onufriev, A. Analysis of basic clustering algorithms for numerical estimation of statistical averages in biomolecules. *J Comput Biol*, 15(2):165–84, 2008.

[40] Wilke, C.R. and Chang, P. Correlation of diffusion coefficients in dilute solutions. *AIChe J*, 1(2):264–270, 1955.

[41] Renkin, E.M. Filtration, diffusion, and molecular sieving through porous cellulose membranes. *J Gen Physiol*, 38(2):225–43, 1954.

[42] de Graaf, R., van Kranenburg, A., and Nicolay, K. In vivo P-31-NMR diffusion spectroscopy of ATP and phosphocreatine in rat skeletal muscle. *Biophys J*, 78(4):1657–1664, 2000.

[43] Rostovtseva, T.K., Komarov, A., Bezrukov, S.M., and Colombini, M. Dynamics of nucleotides in VDAC channels: Structure-specific noise generation. *Biophys J*, 82(1 Pt 1):193–205, 2002.

[44] Valkó, E. Measurements of the diffusion of dyestuffs. *T Faraday Soc*, 31:230–245, 1935.

[45] Robinson, C. The diffusion coefficients of dye solutions and their interpretation. *P Roy Soc Lond A Mat*, 148(865):681–695, 1935.

[46] Trivedi, R. and Vasudeva, K. Axial dispersion in laminar flow in helical coils. *Chem Eng Sci*, 30(3):317–325, 1975.

[47] Dertinger, T., Loman, A., Ewers, B., Müller, C.B., Krämer, B., and Enderlein, J. The optics and performance of dual-focus fluorescence correlation spectroscopy. *Opt Express*, 16(19):14353–68, 2008.

[48] Paul, P., Garguilo, M., and Rakestraw, D. Imaging of pressure- and electrokinetically driven flows through open capillaries. *Anal Chem*, 70(13):2459–2467, 1998.

[49] Longsworth, L.G. Diffusion measurements, at 25-degrees, of aqueous solutions of amino acids, peptides and sugars. *J Am Chem Soc*, 75(22):5705–5709, 1953.

[50] Germann, M.W., Turner, T., and Allison, S.A. Translational diffusion constants of the amino acids: Measurement by NMR and their use in modeling the transport of peptides. *J Phys Chem A*, 111(8):1452–5, 2007.

[51] Wopschall, R.H. and Shain, I. Adsorption characteristics of methylene blue system using stationary electrode polarography. *Anal Chem*, 39(13):1527–1534, 1967.

[52] Beck, R.E. and Schultz, J.S. Hindrance of solute diffusion within membranes as measured with microporous membranes of known pore geometry. *Biochim Biophys Acta*, 255(1):273–303, 1972.

[53] Ma, Y., Zhu, C., Ma, P., and Yu, K. Studies on the diffusion coefficients of amino acids in aqueous solutions. *J Chem Eng Data*, 50(4):1192–1196, 2005.

[54] Bor Fuh, C., Levin, S., and Giddings, J.C. Rapid diffusion coefficient measurements using analytical SPLITT fractionation: Application to proteins. *Anal Biochem*, 208(1):80–7, 1993.

[55] Tyn, M.T. and Gusek, T.W. Prediction of diffusion coefficients of proteins. *Biotechnol Bioeng*, 35(4):327–38, 1990.

[56] Liu, M.K., Li, P., and Giddings, J.C. Rapid protein separation and diffusion coefficient measurement by frit inlet flow field-flow fractionation. *Protein Sci*, 2(9):1520–31, 1993.

[57] Johnson, E.M., Berk, D.A., Jain, R.K., and Deen, W.M. Diffusion and partitioning of proteins in charged agarose gels. *Biophys J*, 68(4):1561–8, 1995.

[58] Tong, J. and Anderson, J.L. Partitioning and diffusion of proteins and linear polymers in polyacrylamide gels. *Biophys J*, 70(3):1505–13, 1996.

[59] Saltzman, W.M., Radomsky, M.L., Whaley, K.J., and Cone, R.A. Antibody diffusion in human cervical mucus. *Biophys J*, 66(2 Pt 1):508–15, 1994.

[60] Lide, D.R., editor. *CRC Handbook of Chemistry and Physics*. CRC Press, Boca Raton, FL, 2005.

[61] Chen, H.C. and Chen, S.H. Diffusion of crown ethers in alcohols. *J Phys Chem-US*, 88(21):5118–5121, 1984.

[62] Nightingale, E.R. Phenomenological theory of ion solvation – Effective radii of hydrated ions. *J Phys Chem-US*, 63(9):1381–1387, 1959.

[63] Boehme, U. and Scheler, U. Effective charge of bovine serum albumin determined by electrophoresis NMR. *Chem Phys Lett*, 435(4-6):342–345, 2007.

[64] Matthew, J.B., Friend, S.H., Botelho, L.H., Lehman, L.D., Hanania, G.I., and Gurd, F.R. Discrete charge calculations of potentiometric titrations for globular proteins: sperm whale myoglobin, hemoglobin alpha chain, cytochrome c. *Biochem Bioph Res Co*, 81(2):416–21, 1978.

[65] Feinberg, B.A. and Ryan, M.D. Molecular interpretation of kinetic-ionic strength effects. *J Inorg Biochem*, 15(3):187–99, 1981.

[66] Laue, T.M., Hazard, A.L., Ridgeway, T.M., and Yphantis, D.A. Direct determination of macromolecular charge by equilibrium electrophoresis. *Anal Biochem*, 182(2):377–82, 1989.

[67] Hayduk, W. and Minhas, B.S. Correlations for prediction of molecular diffusivities in liquids. *Can J of Chem Eng*, 60(2):295–299, 1982.

[68] He, L. and Niemeyer, B. A novel correlation for protein diffusion coefficients based on molecular weight and radius of gyration. *Biotechnol Prog*, 19(2):544–8, 2003.

[69] Hayduk, W. and Buckley, W. Effect of molecular-size and shape on diffusivity in dilute liquid solutions. *Chem Eng Sci*, 27(11):1997–2003, 1972.

[70] Tirado, M., Martinez, C., and Delatorre, J. Comparison of theories for the translational and rotational diffusion-coefficients of rod-like macromolecules – Application to short DNA fragments. *J Chem Phys*, 81(4):2047–2052, 1984.

Chapter 3

Electrodiffusion of Molecules in Aqueous Media: A Robust, Discretized Description for Electroporation and Other Transport Phenomena

Abstract

Electrically driven transport of molecules and ions within aqueous electrolyte is of long-standing interest, with direct relevance to applications involving the delivery or release of exogenous and endogenous biologically active solutes. Motivating examples include iontophoretic and electroporation-mediated drug delivery. Here we describe a robust method for characterizing electrodiffusive transport in physiologic aqueous media. Specifically, we treat the case of solute present in sufficiently low concentration as to negligibly contribute to the total ionic current within the system. In this limiting case, which applies to many systems of interest, the predominant electrical behavior due small ions is decoupled from solute transport. Thus, electrical behavior may be characterized using existing methods and treated as known in characterizing electrodiffusive molecular transport. First, we present traditional continuum equations governing electrodiffusion of charged solutes within aqueous electrolytes and then adapt them to discretized systems. Second, we examine the time-dependent and steady state interfacial concentration gradients that result from the combination of diffusion and electrical drift. Third, we show how interfacial concentration gradients are related to electric field strength and duration. Finally, we examine how discretization size affects the accuracy of these methods. Overall these methods are motivated by and well-suited to addressing an outstanding goal: Estimation of the net ionic and molecular transport facilitated by electroporation in biological systems.

3.1 Introduction

Understanding electrically driven transport within biological systems is of general importance [1, 2]. Here we consider continuum descriptions of transport for spatial scales ranging from nanometers (cell membranes) to tens of micrometers (cells or multiple cells). Over this range, exogenous and endogenous electric fields may lead to large gradients in solute concentration and electric potential. Therefore, the combination of diffusion and electrical drift underlies resulting transport.

In this study, we limit our consideration to movement of solutes within physiologic aqueous electrolytes that have a relatively large electrical conductivity due to the presence of many small, monovalent ions. In bulk, these electrolytes contain $\sim 0.1 - 0.3\,\mathrm{M}$ total concentration of small ions (sodium, potassium, and chloride). Solutes used and studied in biological applications and research are typically present at much lower concentrations. As a result, the transport number (transference number), which accounts for the fraction of the total ionic current (drift) due to a charged solute [3], is small for typical solutes of interest (e.g., drugs and fluorescent probe molecules). Thus, electrical transport can be characterized independently of the contribution of the solute of interest and then treated as known in characterizing the electrodiffusive transport of the solute of interest.

Our primary motivation is the characterization of molecular transport that results from the highly nonlinear and hysteretic phenomenon of electroporation, which is generally believed to involve the creation of dynamic pores within the lipid regions of cell membranes [4–9]. Electroporation significantly increases solute transport though membranes, and thereby leads to delivery, release, or redistribution of biologically active ions and molecules within electroporated cellular systems. Because of the large electric fields required for electroporation, we expect that electrodiffusion is fundamentally involved in the biological response.

Indeed, electrodiffusion has been considered in a number of electroporation studies. For exam-

ple, Klenchin et al. [10] reported, based on their experiments, that electroporation-mediated DNA delivery into cells is a fast process involving electrophoresis. In contrast, Neumann et al. [11] reported that DNA uptake can involve calcium-mediated adsorption of DNA as an initial step at the membrane level, followed by a multi-step process involving electrodiffusion, which is noted to be an order of magnitude more effective than simple diffusion. Small molecule delivery into electroporated cells has also been analyzed quantitatively by considering electrodiffusion [12]. Additionally, the response of the more complex system of the skin's stratum corneum at low voltages (<1 V) has also been related to electrodiffusion [13].

Electrodiffusion is also relevant to biological responses to electric fields much smaller than those used for electroporation. For many decades iontophoresis has been used for transdermal drug delivery [14, 15]. In most cases iontophoresis involves a small current density, usually at essentially steady state. This is an example of transport by electrodiffusion in which drift is the major contributor, but iontophoresis can also involve electro-osmosis. Additionally, electrodiffusion has been used to describe morphogen concentration profiles in developmental biology [16].

The method described here for approaching electrodiffusive transport problems is explicitly appropriate for dealing with the large concentration solute gradients that arise in electroporation. Unlike many transport phenomena in biology, electroporation stands out as having large gradients in space, time, and pore size (radius) distribution.

Within biological systems, these gradients occur over distances from sub-membrane size (nanometer scale) to cell and organelle scale (micrometer scale) to tissue scale with both interstitial volumes and irregularly shaped cells participating. The corresponding electroporation time scales range from nanoseconds (slightly greater than the bulk charge relaxation time, ~ 0.5 ns, of bulk physiologic saline) to microseconds (the approximate plasma membrane charging time) to milliseconds and seconds (post-pulse behavior). This appears to hold for biological systems exposed to electric field pulses of greatly varying durations (~ 4 ns – 100 ms) and corresponding magnitudes

(10 MV/m – 10 kV/m).

The electrodiffusion of solutes within electroporated systems thus involves a wide range of electrical pulse stimuli. The resulting, diverse responses involve fields and small ion currents that redistribute throughout the cell. This redistribution takes place by rapidly changing small ion currents that respond to the evolving heterogeneous pore populations throughout cell membranes within the system. The co-transport of larger solutes by electrodiffusion also changes rapidly in space and time because of combination of current redistribution and the solute selectivity of dynamic populations of different size pores [7, 8]. The present, robust discretized description of electrodiffusion appears well-suited to this important, long standing, and challenging problem.

3.2 Methods

3.2.1 Basic Assumptions

As noted in the *Introduction*, we focus on solute electrodiffusion within aqueous electrolytes relevant to biological systems. In this case there is a large background total concentration (typically 0.1 – 0.3 M) of small ions, mainly sodium, potassium, and chloride. The solute concentration is much less than this, so that the transport number (transference number) can be used to describe fraction of the total ionic current that is due to charged solutes.

3.2.2 Electrodiffusion

Electrodiffusion is the transport of charged solute by the combination of electrical drift and diffusion. The electrodiffusive flux $\boldsymbol{J}_\mathrm{s}$ is described by [1, 2]

$$\boldsymbol{J}_\mathrm{s} = -D_\mathrm{s}\nabla\gamma - \frac{D_\mathrm{s}}{kT}q_\mathrm{e}z_\mathrm{s}\gamma\nabla\phi. \tag{3.1}$$

Here, γ is solute concentration, ϕ is electric potential, D_s is solute diffusivity, z_s is solute charge (valence), q_e is elementary charge, k is the Boltzmann constant, and T is absolute temperature. The first term in Eq. 3.1 describes the flux of solute resulting from a gradient in concentration

(diffusion), and the second term describes the flux of solute resulting from a gradient in electric potential (electrical drift).

In the absence of sources and sinks (e.g., chemical reactions), the amount of solute is conserved as the solute is transported. Thus, for transport alone, the time rate of change of solute concentration is related to the solute flux by the continuity equation

$$\frac{\partial \gamma}{\partial t} = -\nabla \cdot \boldsymbol{J}_\mathrm{s} = D_\mathrm{s}\nabla^2\gamma + \frac{D_\mathrm{s}}{kT}q_\mathrm{e}z_\mathrm{s}(\nabla\gamma)\cdot(\nabla\phi) + \frac{D_\mathrm{s}}{kT}q_\mathrm{e}z_\mathrm{s}\gamma\nabla^2\phi. \tag{3.2}$$

This is simply a statement that if the net flux into an infinitesimal region of space is non-zero, then the amount of solute, and therefore the concentration of solute, must be changing in time.

3.2.3 Electrodiffusion in 1-D

Our focus here will be on transport in 1-D. We note that higher order systems can be modeled using 1-D flux equations to describe transport between nodes distributed in higher-dimensional systems [17–19]. Specifically, 2-D cell models are already in use [20–22], and the extension to 3-D cell models should be relatively straightforward but more computationally demanding.

In 1-D, electrodiffusive flux J_s in the $+x$-direction (and dispensing with the vector notation) becomes

$$J_\mathrm{s} = -D_\mathrm{s}\frac{\partial \gamma}{\partial x} - \frac{D_\mathrm{s}}{kT}q_\mathrm{e}z_\mathrm{s}\gamma\frac{\partial \phi}{\partial x}, \tag{3.3}$$

and the continuity equation becomes

$$\frac{\partial \gamma}{\partial t} = -\frac{\partial J_\mathrm{s}}{\partial x} = D_\mathrm{s}\frac{\partial^2\gamma}{\partial x^2} + \frac{D_\mathrm{s}}{kT}q_\mathrm{e}z_\mathrm{s}\frac{\partial\gamma}{\partial x}\frac{\partial\phi}{\partial x} + \frac{D_\mathrm{s}}{kT}q_\mathrm{e}z_\mathrm{s}\frac{\partial^2\phi}{\partial x^2}. \tag{3.4}$$

For convenience, we define a dimensionless electric potential

$$\psi = \frac{q_\mathrm{e}z_\mathrm{s}}{kT}\phi. \tag{3.5}$$

Written in terms ψ, the electrodiffusive flux equation (Eq. 3.3) simplifies to

$$J_s = -D_s\left(\frac{\partial \gamma}{\partial x} + \gamma\frac{\partial \psi}{\partial x}\right), \tag{3.6}$$

and the continuity equation simplifies to

$$\frac{\partial \gamma}{\partial t} = D_s\left(\frac{\partial^2 \gamma}{\partial x^2} + \frac{\partial \gamma}{\partial x}\frac{\partial \psi}{\partial x} + \frac{\partial^2 \psi}{\partial x^2}\right). \tag{3.7}$$

3.2.4 Electrodiffusive Flux in a Discretized 1-D System

Here, we recast established continuum theory in a fashion that anticipates large transport networks with many discrete nodes [18, 19, 23]. Consider adjacent nodes i and j in a 1-D system with positions x_i and x_j. We seek to calculate the instantaneous electrodiffusive flux $J_s^{i,j}$ from x_i to x_j in terms of the solute concentrations γ_i and γ_j and electric potentials ϕ_i and ϕ_j, with associated dimensionless potentials ψ_i and ψ_j. No assumptions are made about how concentration γ varies from x_i to x_j. In contrast, the electric potential ϕ is assumed to vary linearly from x_i to x_j. Thus, between x_i and x_j

$$\left.\frac{\partial \phi}{\partial x}\right|_{i,j} \approx \frac{(\Delta\phi)_{i,j}}{(\Delta x)_{i,j}} \quad \text{and} \quad \left.\frac{\partial \psi}{\partial x}\right|_{i,j} \approx \frac{(\Delta\psi)_{i,j}}{(\Delta x)_{i,j}}, \tag{3.8}$$

where $(\Delta\phi)_{i,j} \equiv \phi_j - \phi_i$, $(\Delta\psi)_{i,j} \equiv \psi_j - \psi_i$, and $(\Delta x)_{i,j} \equiv x_j - x_i$. Similarly, for concentration $(\Delta\gamma)_{i,j} \equiv \gamma_j - \gamma_i$.

Substituting, Eq. 3.8 into Eq. 3.6, the electrodiffusive flux $J_s^{i,j}$ from x_i to x_j is

$$J_s^{i,j} = -D_s\frac{\partial \gamma}{\partial x} - D_s\gamma\frac{(\Delta\psi)_{i,j}}{(\Delta x)_{i,j}}. \tag{3.9}$$

Solving for $\partial\gamma/\partial x$,

$$\frac{\partial \gamma}{\partial x} = -\frac{J_s^{i,j}}{D_s} - \frac{(\Delta\psi)_{i,j}}{(\Delta x)_{i,j}}\gamma. \tag{3.10}$$

This differential equation can be solved using separation of variables:

$$-\int_{\gamma_i}^{\gamma_j} \frac{\partial \gamma}{\frac{J_s^{i,j}}{D_s} + \frac{(\Delta\psi)_{i,j}}{(\Delta x)_{i,j}}\gamma} = \int_{x_i}^{x_j} \partial x \tag{3.11}$$

$$-\left[\frac{(\Delta x)_{i,j}}{(\Delta\psi)_{i,j}} \ln\left(\frac{J_s^{i,j}}{D_s} + \frac{(\Delta\psi)_{i,j}}{(\Delta x)_{i,j}}\gamma\right)\right]_{\gamma_i}^{\gamma_j} = [x]_{x_i}^{x_j}. \tag{3.12}$$

Simplifying and solving for $J_s^{i,j}$,

$$J_s^{i,j} = -D_s \frac{(\Delta\psi)_{i,j}}{(\Delta x)_{i,j}} \left(\frac{\gamma_i}{1 - e^{(\Delta\psi)_{i,j}}} + \frac{\gamma_j}{1 - e^{-(\Delta\psi)_{i,j}}}\right). \tag{3.13}$$

Note that Eq. 3.13 is of indeterminate form when $(\Delta\psi)_{i,j} = 0$. However,

$$\lim_{(\Delta\psi)_{i,j}\to 0} J_s^{i,j} = -D_s \frac{(\Delta\gamma)_{i,j}}{(\Delta x)_{i,j}}. \tag{3.14}$$

In other words, when there is no gradient in the dimensionless electric potential, the flux $J_s^{i,j}$ reduces to that of simple diffusion. Thus, to be rigorous, $J_s^{i,j}$ is described by the piecewise continuous function

$$J_s^{i,j} = \begin{cases} -D_s \frac{(\Delta\gamma)_{i,j}}{(\Delta x)_{i,j}} & \text{if } (\Delta\psi)_{i,j} = 0, \\ -D_s \frac{(\Delta\psi)_{i,j}}{(\Delta x)_{i,j}} \left(\frac{\gamma_i}{1-e^{(\Delta\psi)_{i,j}}} + \frac{\gamma_j}{1-e^{-(\Delta\psi)_{i,j}}}\right) & \text{if } (\Delta\psi)_{i,j} \neq 0. \end{cases} \tag{3.15}$$

It is instructive to consider the behavior of the flux $J_s^{i,j}$ in limits of $(\Delta\psi)_{i,j}$:

$$J_s^{i,j} \approx \begin{cases} -D_s \frac{(\Delta\psi)_{i,j}}{(\Delta x)_{i,j}} \gamma_j & \text{if } (\Delta\psi)_{i,j} \gg 1, \\ -D_s \frac{(\Delta\gamma)_{i,j}}{(\Delta x)_{i,j}} & \text{if } (\Delta\psi)_{i,j} \approx 0, \\ -D_s \frac{(\Delta\psi)_{i,j}}{(\Delta x)_{i,j}} \gamma_i & \text{if } (\Delta\psi)_{i,j} \ll -1. \end{cases} \tag{3.16}$$

As expected, when diffusion dominates drift ($(\Delta\psi)_{i,j} \approx 0$), the equation for the flux $J_s^{i,j}$ reduces to that of simple diffusion. Likewise, when drift dominates diffusion ($|(\Delta\psi)_{i,j}| \gg 1$), the equation for

the flux $J_s^{i,j}$ reduces to that of electrical drift. Note that the concentration γ that determines the flux $J_s^{i,j}$ depends on the sign of $(\Delta\psi)_{i,j}$: when $(\Delta\psi)_{i,j} > 0$, $\gamma = \gamma_j$, and when $(\Delta\psi)_{i,j} < 0$, $\gamma = \gamma_i$.

That is, when drift dominates diffusion, the flux $J_s^{i,j}$ is proportional to the concentration of the *source* node and independent of the *destination* node. This makes intuitive sense. It also implies that when the concentration of the source node $\to 0$, the flux $J_s^{i,j} \to 0$. This is an important property because it ensures that solute cannot be "pulled out" of a node that does not have any, which would cause its concentration to become negative (when solute conservation is imposed).

It is tempting to make the simplifying assumption that the concentration γ varies linearly in space (e.g., in Eq. 3.9). Under this assumption, diffusion and drift would be decoupled and the total flux would be the sum of the independently determined fluxes:

$$J_s^{i,j} = -D_s \frac{(\Delta\gamma)_{i,j}}{(\Delta x)_{i,j}} - D_s \frac{(\Delta\psi)_{i,j}}{(\Delta x)_{i,j}} \left(\frac{\gamma_i + \gamma_j}{2}\right). \tag{3.17}$$

The corresponding behavior of the linear flux $J_s^{i,j}$ in limits of $(\Delta\psi)_{i,j}$ is

$$J_s^{i,j} \approx \begin{cases} -D_s \frac{(\Delta\psi)_{i,j}}{(\Delta x)_{i,j}} \left(\frac{\gamma_i+\gamma_j}{2}\right) & \text{if } (\Delta\psi)_{i,j} \gg 1, \\ -D_s \frac{(\Delta\gamma)_{i,j}}{(\Delta x)_{i,j}} & \text{if } (\Delta\psi)_{i,j} \approx 0, \\ -D_s \frac{(\Delta\psi)_{i,j}}{(\Delta x)_{i,j}} \left(\frac{\gamma_i+\gamma_j}{2}\right) & \text{if } (\Delta\psi)_{i,j} \ll -1. \end{cases} \tag{3.18}$$

Importantly, note that when drift dominates diffusion ($|(\Delta\psi)_{i,j}| \gg 1$), the flux is proportional to the *average* of the node concentrations. This is a marked contrast to the nonlinear case (Eq. 3.16), in which the drift flux depends only on the concentration of the source node. This behavior of the linear flux formulation can lead to nonphysical and unstable behavior, such as a nonzero flux of solute out of a node without any solute ($\gamma = 0$). Use of the nonlinear formulation avoids numerical pathologies and is therefore robust in the presence of steep gradients in γ.

Using Eqs. 3.16 and 3.18, the relative error in the linear formulation of the flux $J_s^{i,j}$ is found to be

$$\text{Linear } J_s^{i,j} \text{ Relative Error} \approx \begin{cases} \frac{(\Delta\gamma)_{i,j}}{2\gamma_j} & \text{if } (\Delta\psi)_{i,j} \gg 1, \\ 0 & \text{if } (\Delta\psi)_{i,j} \approx 0, \\ \frac{(\Delta\gamma)_{i,j}}{2\gamma_i} & \text{if } (\Delta\psi)_{i,j} \ll -1. \end{cases} \tag{3.19}$$

The error is small when the difference in dimensionless electric potential $(\Delta\psi)_{i,j}$ between the nodes is small and also when the difference in concentrations between the nodes $(\Delta\gamma)_{i,j}$ is small relative to the absolute concentration γ_i and γ_j. Otherwise, the error is large.

This is particularly true when the sign of the dimensionless potential is such that it contributes to drift from the node with lower concentration to the node with higher concentration. This is the case because, as discussed, in the linear flux formulation, the drift contribution to the flux depends on the average of the node concentrations, rather than on the source node concentration alone.

Figure 3.1 shows the nonlinear (Eq. 3.15) and linear (Eq. 3.17) electrodiffusive flux $J_s^{i,j}$ from node i to j (scaled by $(\Delta x)_{i,j}/D_s$, as the values of these parameters are not relevant to the results displayed) plotted against the dimensionless potential $(\Delta\psi)_{i,j}$ between nodes i and j for a few combinations of concentrations γ_i and γ_j, and Fig. 3.1B shows the error in the linear electrodiffusive flux.

When $\gamma_i = \gamma_j = 1$ (i.e., when $(\Delta\gamma)_{i,j} = 0$) (dimensionless), $J_s^{i,j}$ is linear in $(\Delta\psi)_{i,j}$ for both the nonlinear and linear formulations because solute transport results from drift alone. When $\psi_i = \psi_j$ (i.e., when $(\Delta\psi)_{i,j} = 0$), $J_s^{i,j}$ is linear in $(\Delta\gamma)_{i,j}$ for both the nonlinear and linear formulations because transport results from diffusion alone. It is only for these two limiting cases that the assumption of linearity is valid and the linear flux formulation is accurate.

In general, however, $\gamma_i \neq \gamma_j$ and $\psi_i \neq \psi_j$, and the flux $J_s^{i,j}$ is determined by the combination of drift and diffusion. It is for these realistic conditions that the assumption of linearity becomes numeri-

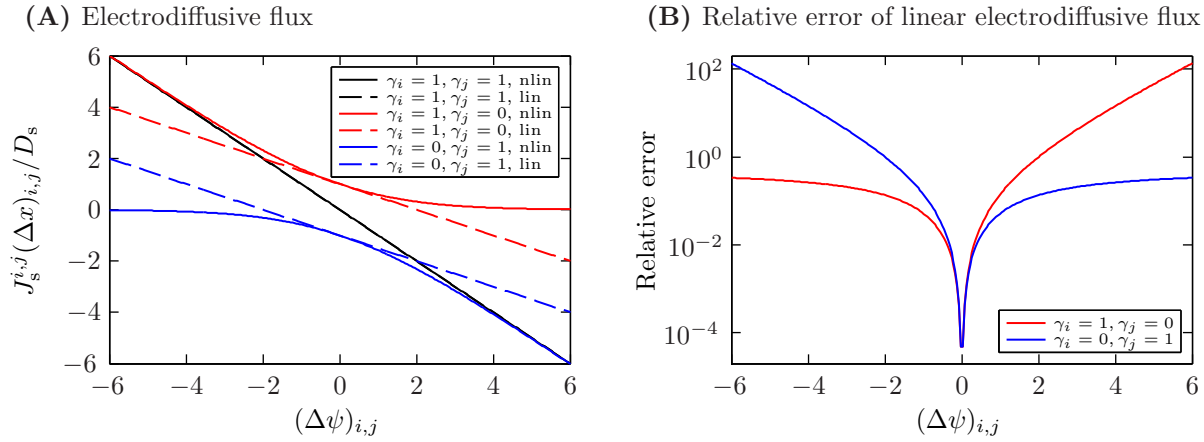

Figure 3.1: Electrodiffusive flux between adjacent nodes in a discretized system. **(A)** Electrodiffusive flux $J_s^{i,j}$ between nodes i and j for three sets of concentrations γ_i and γ_j calculated using the nonlinear ("nlin", *solid* lines) and linear ("lin", *dashed* lines) flux formulations. $(\Delta\psi)_{i,j}$ is the dimensionless electric potential between nodes i and j. Note that the flux $J_s^{i,j}$ is scaled by $(\Delta x)_{i,j}/D_s$, as the values of these parameters are not relevant to the results displayed. **(B)** Relative error of the linear flux formulation. The error is small when either $|(\Delta\gamma)_{i,j}|$ is small or $|(\Delta\psi)_{i,j}|$ is small; otherwise, the error is large.

cally pathological and leads to significant error. This is illustrated for the case $\gamma_i = 1$ and $\gamma_j = 0$ and the case $\gamma_i = 0$ and $\gamma_j = 1$ in Fig. 3.1.

In the case of the nonlinear flux formulation (Eq. 3.15) (Fig. 3.1), when the sign of $(\Delta\psi)_{i,j}$ is such that drift proceeds from the node with higher concentration ($\gamma = 1$) to the node with lower concentration ($\gamma = 0$), $J_s^{i,j}$ is increasingly dominated by drift as $|(\Delta\psi)_{i,j}|$ increases, and approaches the flux $J_s^{i,j}$ found in the case of pure drift (i.e., when $\gamma_i = \gamma_j = 1$). Similarly, when the sign of $(\Delta\psi)_{i,j}$ is such that drift proceeds from the node with lower concentration ($\gamma = 0$) to the node with higher concentration ($\gamma = 1$), $J_s^{i,j}$ is increasingly dominated by drift as $|(\Delta\psi)_{i,j}|$ increases, and approaches the flux $J_s^{i,j}$ found in the case of pure drift (i.e., when $\gamma_i = \gamma_j = 0$). The key finding is that when drift dominates over diffusion, the flux $J_s^{i,j}$ is proportional to the concentration of the drift source node.

The behavior of the linear flux formulation (Eq. 3.17) is very different from that of the nonlinear flux formulation (Fig. 3.1). The flux is linear in $(\Delta\psi)_{i,j}$ with a vertical offset equal to the diffusive

contribution to the flux, which is independent of $(\Delta\psi)_{i,j}$. Regardless of the sign of $(\Delta\psi)_{i,j}$, the flux is determined by the average node concentration $(\gamma_i + \gamma_j)/2$. Therefore, when the sign of $(\Delta\psi)_{i,j}$ is such that drift proceeds from the node with higher concentration ($\gamma = 1$) to the node with lower concentration ($\gamma = 0$), the linear formulation underestimates the magnitude of the flux $J_s^{i,j}$. And when the sign of $(\Delta\psi)_{i,j}$ is such that drift proceeds from the node with lower concentration ($\gamma = 0$) to the node with higher concentration ($\gamma = 1$), the linear formulation overestimates the magnitude of the flux $J_s^{i,j}$. The latter case is particularly problematic, as it predicts flux out of a node that contains zero solute. This is clearly impossible.

One could use the linear flux formulation and ensure that $(\Delta\psi)_{i,j} \approx 0$ by choosing a small $(\Delta x)_{i,j}$, but the $(\Delta x)_{i,j}$ required to keep the error in the flux under control is very small. Suppose one wanted to use the linear flux formulation and choose $(\Delta x)_{i,j}$ to keep $|(\Delta\psi)_{i,j}| < 0.1$. If $z_s = \pm 1$, this corresponds to a potential difference $|(\Delta\phi)_{i,j}| < 2.6\,\mathrm{mV}$ (at 25 °C). The node spacing $(\Delta x)_{i,j}$ required to meet this condition is $(\Delta x)_{i,j} < |(\Delta\phi)_{i,j}/E|$, where is E is the electric field magnitude. For a conventional electroporation pulse, $E \approx 1\,\mathrm{kV/cm}$, and thus, the node spacing $(\Delta x)_{i,j}$ must be $< 26\,\mathrm{nm}$ to meet the error criterion. Recently, pulses with magnitudes of up to $E \approx 10\,\mathrm{MV/m}$ have been used. Such conditions would require an incredibly small $(\Delta x)_{i,j} < 0.26\,\mathrm{nm}$. Moreover, the typical field in a cell membrane under rest conditions is also $\sim 10\,\mathrm{MV/m}$ ($=\sim 50\,\mathrm{mV}/5\,\mathrm{nm}$), and the membrane is precisely where one expects large relative changes in concentration γ. For these reasons, the use of the linear formulation is likely to be particularly problematic in examining the transmembrane flux of solute. The nonlinear flux formulation avoids this problem.

3.2.5 Electrodiffusive Continuity in a Discretized 1-D System

The electrodiffusive flux $J_s^{i,j}$ describes the instantaneous movement of solute from one node (position) to another, but it does not describe the resulting change in concentration γ at a node (position). It is the continuity equation (Eq. 3.4) that describes the change in γ that results from the net electrodiffusive flux into the node.

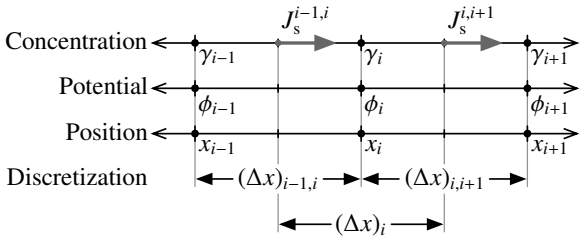

Figure 3.2: Discretized 1-D electrodiffusion system. Node i has adjacent nodes $i-1$ and $i+1$. The position x, electric potential ϕ, and concentration γ for each node is indicated by its subscript. Nodes $i-1$ and i are separated by distance $(\Delta x)_{i-1,i}$, nodes i and $i+1$ are separated by distance $(\Delta x)_{i,i+1}$. The region of space associated with node i has length $(\Delta x)_i$. $J_s^{i-1,i}$ is the electrodiffusive flux from node $i-1$ to node i, and $J_s^{i,i+1}$ is the electrodiffusive flux from node i to node $i+1$. The electrodiffusive flux between adjacent nodes is determined by the positions, electric potentials, and concentrations of the nodes, as well as solute (e.g., diffusivity) and system (e.g., temperature) properties. The rate at which the concentration γ_i changes is determined by the net flux $J_s^{i-1,i} - J_s^{i,i+1}$ into node i and the length $(\Delta x)_i$.

More specifically, consider the 1-D system shown in Fig. 3.2. Node i with position x_i has adjacent nodes $i-1$ and $i+1$ with positions x_{i-1} and x_{i+1} such that $x_{i-1} < x_i < x_{i+1}$. The nodes $i-1$, i, and $i+1$ have concentrations γ_{i-1}, γ_i, and γ_{i+1}, electric potentials ϕ_{i-1}, ϕ_i, and ϕ_{i+1}, and associated dimensionless electric potentials ψ_{i-1}, ψ_i, and ψ_{i+1}.

The distance between nodes $i-1$ and i is $(\Delta x)_{i-1,i} \equiv x_i - x_{i-1}$, and the distance between nodes i and $i+1$ is $(\Delta x)_{i,i+1} \equiv x_{i+1} - x_i$. There is a region of space associated with node i for which all points are close to x_i than to the position of any other node. More specifically, all x such that $x_{i-1} + (\Delta x)_{i-1,i}/2 < x < x_{i+1} - (\Delta x)_{i,i+1}/2$ are associated with node i. The length of this region associated with node i is $(\Delta x)_i \equiv (\Delta x)_{i-1,i}/2 + (\Delta x)_{i,i+1}/2$.

The flux $J_s^{i-1,i}$ from $i-1$ to i and flux $J_s^{i,i+1}$ from i to $i+1$ at any instant in time can be determined using Eq. 3.15, as described. The derivative of the flux with respect to x at x_i can be approximated by the following discretized relation:

$$\left.\frac{\partial J_s}{\partial x}\right|_i \approx \frac{J_s^{i,i+1} - J_s^{i-1,i}}{(\Delta x)_i}. \tag{3.20}$$

Substituting into Eq. 3.4, the continuity equation for node i is

$$\frac{\partial \gamma_i}{\partial t} = -\frac{J_s^{i,i+1} - J_s^{i-1,i}}{(\Delta x)_i} = \frac{J_s^{i-1,i} - J_s^{i,i+1}}{(\Delta x)_i}. \tag{3.21}$$

Thus, the concentration γ_i of node i increases when the influx of solute exceeds the efflux of solute and decreases when the efflux of solute exceeds the influx of solute.

Having now developed discretized versions of both Eqs. 3.3 and 3.4, a complete approach has been described. The combination of the flux and continuity equations fully characterizes the electrodiffusion in the 1-D system.

3.3 Results and Discussion

3.3.1 Electrodiffusion in 1-D: An Illustrative Example

In systems for which an electric field is applied transiently (e.g., in electroporating cells), the initial state of the system is such that concentration and electric potential are separately uniform over large regions of the system and only change significantly at boundaries (e.g., membranes) that impede molecular and electrical transport. As a result, upon initiation of an applied field in such systems, the electrodiffusive flux throughout most of the system is dominated by drift (as in the case $\gamma_i = \gamma_j = 1$ described above). The notable exception is at boundaries, where transport is impeded and large concentration gradients can form rapidly over time. It is here that an accurate description of transport becomes very important.

We illustrate the principles described above by considering electrodiffusion in a simple 1-D model system (Fig. 3.3). Specifically, consider a 1-D system with no-flux (reflecting) boundaries at $x = 0$ and $x = L = 10\,\mu\text{m}$. The system contains a solute with diffusivity $D_s = 40 \times 10^{-11}\,\text{m}^2/\text{s}$ and charge $z_s = +1$, which are typical of a small molecule [24]. Initially ($t < 0\,\text{s}$), the solute concentration is uniform and with $\gamma(x) = \gamma_b$, and the applied electric field is uniform with magnitude $E = 0\,\text{V/m}$.

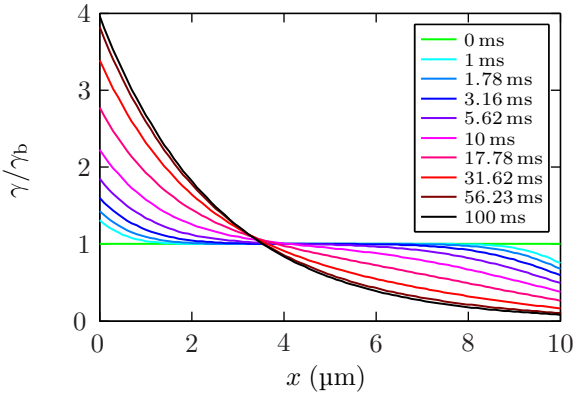

Figure 3.3: Electrodiffusion in a simple 1-D system. The concentration $\gamma(x)$ at selected time points is shown for a typical small molecule with diffusivity $D_s = 40 \times 10^{-11}\,\mathrm{m}^2/\mathrm{s}$ and charge $z_s = +1$ in a 1-D system with length $L = 10\,\mu\mathrm{m}$ and no-flux (reflecting) boundaries at $x = 0\,\mu\mathrm{m}$ and $x = 10\,\mu\mathrm{m}$. Initially ($t < 0\,\mathrm{s}$), the concentration is uniform with $\gamma(x) = \gamma_b$ and there is no applied electric field. At $t = 0\,\mathrm{s}$ a uniform electric field (in the $+x$-direction) $E = -10^4\,\mathrm{V/m}$ is applied, and the positively charged solute thus drifts toward $x = 0\,\mu\mathrm{m}$. The concentration $\gamma(x)$ approaches a steady state of exponential form for which the diffusion and electrical drift contributions to the electrodiffusive flux are equal and opposite, and the resulting net flux is zero.

Here, E is defined as

$$E = -\frac{\partial \phi}{\partial x} = \frac{\phi(0) - \phi(L)}{L}. \tag{3.22}$$

At $t = 0\,\mathrm{s}$, an electric field is applied with magnitude $E = -10^4\,\mathrm{V/m}$. The negative value of E indicates that $\phi(L) > \phi(0)$, and thus positively charged solute ($z_s > 0$) will drift toward $x = 0$. The voltage difference across the system is $\phi(L) - \phi(0) = -EL = 1\,\mathrm{V}$.

Figure 3.3, shows how $\gamma(x)$ changes in time. Immediately after the application of the electric field, solute begins to be drift toward $x = 0$ and $\gamma(0)$ increases while $\gamma(L)$ decreases, as required by the continuity equation. The flux in the central region of the system initially results entirely from electrical drift, as the concentration is uniform over the central region.

As the solute drifts toward $x = 0$, the concentration profile $\gamma(x)$ becomes increasingly nonuni-

form. Initially, the concentration gradients are largest near $x = 0$ and $x = L$. As electrodiffusion continues, both the concentration and concentration gradient near $x = 0$ increase while both the concentration and concentration gradient near $x = L$ decrease.

As the concentration gradient near $x = 0$ grows, the diffusive flux in the $+x$-direction increasingly counterbalances the drift flux in the $-x$-direction. Eventually, the net electrodiffusive flux throughout the system approaches zero and the concentration $\gamma(x)$ approaches a steady state profile of exponential form.

3.3.2 Electrodiffusion in 1-D: Steady State Solution

As demonstrated in Fig. 3.3, electrical drift causes solute to accumulate against (impermeable) system boundaries ($x = 0$ in this case), and this accumulation results in increased concentration gradients that, through diffusion, oppose the electrical drift. At steady state, diffusion and electrical drift counterbalance one another. That is, they are equal and opposite. Thus, at steady state, the net flux throughout the system approaches zero and Eq. 3.3 becomes

$$J_s = 0 = -D_s \frac{\partial \gamma}{\partial x} + \frac{D_s}{kT} q_e z_s \gamma E. \tag{3.23}$$

Rearranging,

$$\frac{\partial \gamma}{\partial x} = -\frac{\gamma}{\lambda}, \tag{3.24}$$

where λ is the length constant

$$\lambda \equiv -\frac{kT}{q_e z_s E}. \tag{3.25}$$

Note that for the example shown above, the value of λ is positive because the value of E is negative.

Equation 3.24 has solution

$$\gamma(x) = \gamma_0 e^{-x/\lambda}, \tag{3.26}$$

where γ_0 is an integration constant determined by the initial conditions. γ_0 can be found by apply-

ing conservation: the total amount of solute in the system remains constant. Thus,

$$\gamma_0 \int_0^L \mathrm{e}^{-x/\lambda}\, dx = \gamma_\mathrm{b} L. \tag{3.27}$$

Solving the integral and rearranging,

$$\gamma_0 = \left(\frac{L/\lambda}{1 - \mathrm{e}^{-L/\lambda}} \right) \gamma_\mathrm{b}. \tag{3.28}$$

Substituting for γ_0 in Eq. 3.26 yields the steady state concentration

$$\gamma(x) = \left(\frac{L/\lambda}{1 - \mathrm{e}^{-L/\lambda}} \right) \gamma_\mathrm{b} \mathrm{e}^{-x/\lambda}. \tag{3.29}$$

Figure 3.4 shows the steady state concentration profiles $\gamma(x)$ for a number of electric field magnitudes E for the example system described in the previous section. As E increases, the magnitude of the drift flux toward $x = 0$ also increases. Consequently, the steady state concentration gradient at $x = 0$ must also increase such that the diffusive flux counterbalances the increased drift flux. Additionally, as E increases, the steady state concentration at $x = 0$ increases and the steady state concentration at $x = L$ decreases.

3.3.3 Characteristic Length, Time, and Speed of Electrodiffusion

At steady state, diffusion and drift are in balance everywhere in system (i.e., for all x). Prior to reaching steady state, diffusion and drift are not in balance throughout most of the system, but they must be in balance at the boundaries because of the no-flux boundary condition. As a result, at all times there is a region very near the boundaries that exhibits an (approximately) exponential concentration profile of the same form as at steady state (Eq. 3.29). This boundary layer has

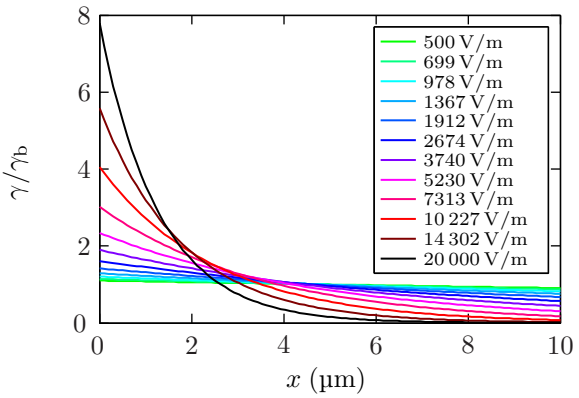

Figure 3.4: Steady state concentration profiles in a simple 1-D system. The steady state concentration $\gamma(x)$ (normalized by the initial, uniform concentration γ_b) is shown for selected electric field magnitudes for a typical small molecule with diffusivity $D_s = 40 \times 10^{-11}\,\mathrm{m}^2/\mathrm{s}$ and charge $z_s = +1$ in a 1-D system with length $L = 10\,\mu\mathrm{m}$. The uniform electric field is oriented such that the positively charged solute drifts toward $x = 0\,\mu\mathrm{m}$. At steady state, the diffusion and electrical drift contributions to the electrodiffusive flux are equal and opposite, resulting in a concentration profile $\gamma(x)$ of exponential form. As the electric field magnitude increases, the steady state concentration increases at $x = 0\,\mu\mathrm{m}$ and decreases at $x = 10\,\mu\mathrm{m}$.

characteristic length

$$\lambda = \frac{kT}{q_e|z_s E|}. \tag{3.30}$$

The length constant λ (Fig. 3.5) characterizes the length scale over which solute accumulates at boundaries (e.g., membranes). It is in this interfacial region that the concentration and concentration gradient change most dramatically in time as the result of the interplay between electrical drift and diffusion.

The Debye length, λ_D, screens charged solutes and also charged surfaces. For most applied electric fields of interest, the electrodiffusion length λ is larger than λ_D (Fig. 3.5). Benedek and Villars give values of $\lambda_D \approx 0.31\,\mathrm{nm}$ for bulk 1 M saline and $\lambda_D \approx 0.96\,\mathrm{nm}$ for 0.1 M saline [26]. More relevant to the cytoplasm, Ando and Skolnick 2010 [25] reported $\lambda_D \approx 0.8\,\mathrm{nm}$ inside the cell ($\sim 0.15\,\mathrm{M}$ salt). Thus, in most of the applications that motivated our approach, the effect of the Debye length can be neglected.

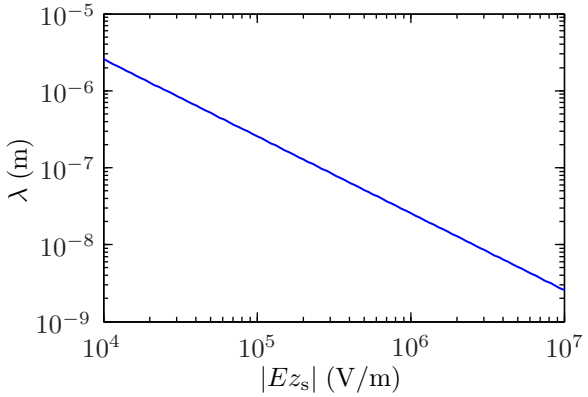

Figure 3.5: Dependence of electrodiffusion length constant on electric field magnitude. The electrodiffusion length constant λ is inversely proportional to the product of the electric field magnitude E and molecular charge (valence) z_s. Note that λ exceeds the Debye length $\lambda_D \approx 0.8\,\text{nm}$ [25] (inside cells), even at the largest electric magnitude ($10^7\,\text{V/m}$) and can therefore be neglected.

The bulk electrolyte is the source of the solute that accumulates in the boundary layer. Within the bulk electrolyte (i.e., outside the boundary layer), electrical drift is the dominant mode of transport, as gradients in concentration are small. Thus, the rate at which solute enters the boundary layer is determined by the bulk electrolyte concentration γ_b and the solute drift velocity ν, where

$$\nu = D_s \frac{q_e |z_s E|}{kT} = \frac{D_s}{\lambda}. \tag{3.31}$$

The characteristic time τ of electrodiffusion is related to the characteristic length λ and drift velocity ν by

$$\tau = \frac{\lambda}{\nu} = \frac{1}{D_s}\left(\frac{kT}{q_e z_s E}\right)^2 = \frac{\lambda^2}{D_s}. \tag{3.32}$$

τ is the time required for the solute to drift a distance λ at speed ν. τ is also the time required for the solute to diffuse a distance λ. This is consistent with the notion that drift and diffusion counterbalance one another in the boundary layer.

τ also describes the rate at which the concentration increases in the boundary layer. Assuming the

$x = L$ boundary is sufficiently far from the $x = 0$ boundary ($L \gg vt$), the concentration $\gamma(x)$ within the boundary layer is described by the exponential function

$$\gamma(x) \approx (\gamma(0) - \gamma_b)e^{-x/\lambda} + \gamma_b \quad \text{for } t > \tau \text{ and } 0 \leq x \leq \lambda \,, \tag{3.33}$$

and the flux of solute into the boundary layer is $v\gamma_b$. Continuity requires that this flux result in a corresponding increase in concentration within the boundary layer described by

$$\frac{\partial \gamma}{\partial t} \approx \frac{\gamma_b}{\tau} e^{-x/\lambda} \quad \text{for } t > \tau \text{ and } 0 \leq x \leq \lambda \,. \tag{3.34}$$

Thus, for every time constant τ, the concentration at the boundary $\gamma(0)$ increases by an amount γ_b.

3.3.4 Discretization Error

As a practical matter, it is important to examine the effect that discretization has on the accuracy of the model results. How fine a discretization is fine enough? If the discretization is too coarse, the results may be inaccurate, but if the discretization is too fine (i.e., finer than necessary to achieve results within some margin of error), obtaining a numerical solution will come at an unnecessarily large computational cost.

Here, we consider a 1-D system with no-flux (reflective) boundaries as $x = 0$ and $x = L$. Initially ($t < 0$), the uniform concentration $\gamma(x) = \gamma_b$, and the electric field magnitude $E = 0$. At $t = 0$, a uniform electric field is applied with magnitude E. The solute charge z_s and electric field magnitude are of opposite sign such that the solute drifts toward the $x = 0$ boundary. The system length L is sufficiently large that the $x = L$ boundary has no effect on the results near the $x = 0$ boundary on the time scales examined. (I.e., L is much greater than the electrical drift distance on the time scales considered.) This simplifies the analysis by removing any effect that the $x = L$ boundary might otherwise have. The system can be viewed as analogous to cells in system for which the boundaries far away (e.g., an electroporation cuvette).

Unfortunately, a time-dependent analytical solution for our system of interest is, to our knowledge, unavailable. As an alternative, for comparison we use as a reference modeling results obtained using an extremely fine discretization (so fine that it would be impractical to use for 2-D or 3-D systems). We then compare the model results found using more reasonably sized discretizations with the model results found using the extremely fine discretization. This approach is of course predicated on the assumption that as the discretization size shrinks, the model results converge on the true solution.

In the interest of generality, the results are presented in terms of a length constant λ (Eq. 3.30) and time constant τ (Eq. 3.32). All systems with the same λ and τ will exhibit exactly the same spatiotemporal dynamics.

Figure 3.6A shows the concentration γ relative to the bulk concentration γ_b near the $x = 0$ boundary for a few different discretization sizes Δx at time $t = \tau$. The $\Delta x/\lambda = 0.001$ discretization, which is much finer than the others, can be considered the exact solution. As the discretization size decreases, the discretized concentration profile $\gamma(x)$ approaches the true $\gamma(x)$. $\Delta x = 2\lambda$ is clearly too coarse to spatially resolve the large concentration gradient at $x = 0$, but $\Delta x = \lambda$ and $\Delta x = \lambda/2$ do reasonably well. Note that while the concentration tends to be underestimated at the discretized points, the total solute is not necessarily underestimated because the total solute at a node is proportional to Δx.

Figure 3.6B shows the error in the concentration profiles (relative to the $\Delta x = \lambda/1000$ results) for the discretizations shown in Fig. 3.6A, as well as a few others. As one would expect based on Fig. 3.6A, the error decreases as Δx decreases. For example, when $\Delta x = \lambda$, the error at $x = 0$ is 11 %. When Δx is decreased to $\lambda/16$, the error drops to just 0.05 %. For all of the discretizations, the error decreases with distance from the boundary. Over the 4λ shown, the error drops by 2–3 orders of magnitude. The reason is that the concentration gradient decreases with distance from the boundary and effectively become more linear, such that even the coarser discretizations can cap-

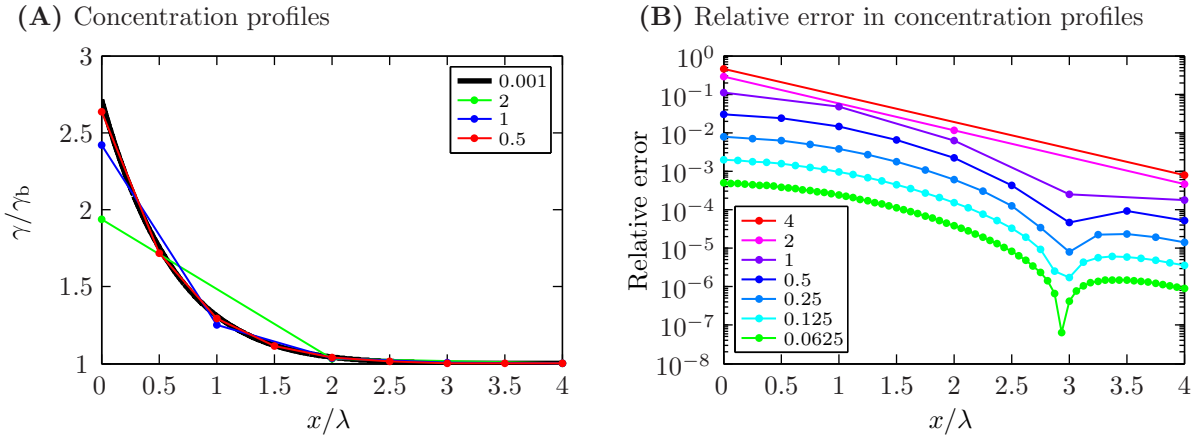

Figure 3.6: Concentration profiles and error near boundary. **(A)** Concentration $\gamma(x)$ (normalized by bulk concentration γ_b) near $x = 0$ boundary at $t = \tau$ for various discretization sizes Δx relative to the length constant λ. (The inset shows $\Delta x/\lambda$.) As $\Delta x/\lambda$ decreases, the associated concentration profile converges. **(B)** Relative error in concentration $\gamma(x)$ near $x = 0$ boundary at $t = \tau$ for various discretization sizes Δx relative to the length constant λ. (The inset shows $\Delta x/\lambda$.) The error is relative to concentration profile found with $\Delta x/\lambda = 0.001$. The error decreases as the size of the discretization decreases. The error also decreases with distance from the boundary. The dip in the error near $x/\lambda \approx 3$ is simply the result of a sign change in the error. Note that the $x = L$ boundary is sufficiently far away as to have no effect on the results at the $x = 0$ boundary.

ture the changing concentration. The fact that the Δx required to accurately model $\gamma(x)$ at a fixed error threshold decreases with distance from the boundary is significant. It suggests that variable nodes spacing would be an excellent approach to achieving high accuracy in model results near the boundary without the large computational cost of a fine node spacing throughout the system [17–19].

While Fig. 3.6 shows the discretization error at $t = \tau$, it should be recognized that the concentration and error change in time. Accordingly, Fig. 3.7 shows the error for a broad range of discretizations and times. The error is shown in two different ways. Figure 3.7A shows the error (relative to a much finer discretization) at $x = 0$. By contrast, Fig. 3.7B shows the error in the concentration of the boundary layer ($0 \leq x \leq \lambda$) taken as a whole. This estimation is equivalent to measuring the error in the total amount of solute contained in the boundary layer. As noted, the coarser discretizations tend to underestimate the concentration at nodes, but because they have larger Δx, they do

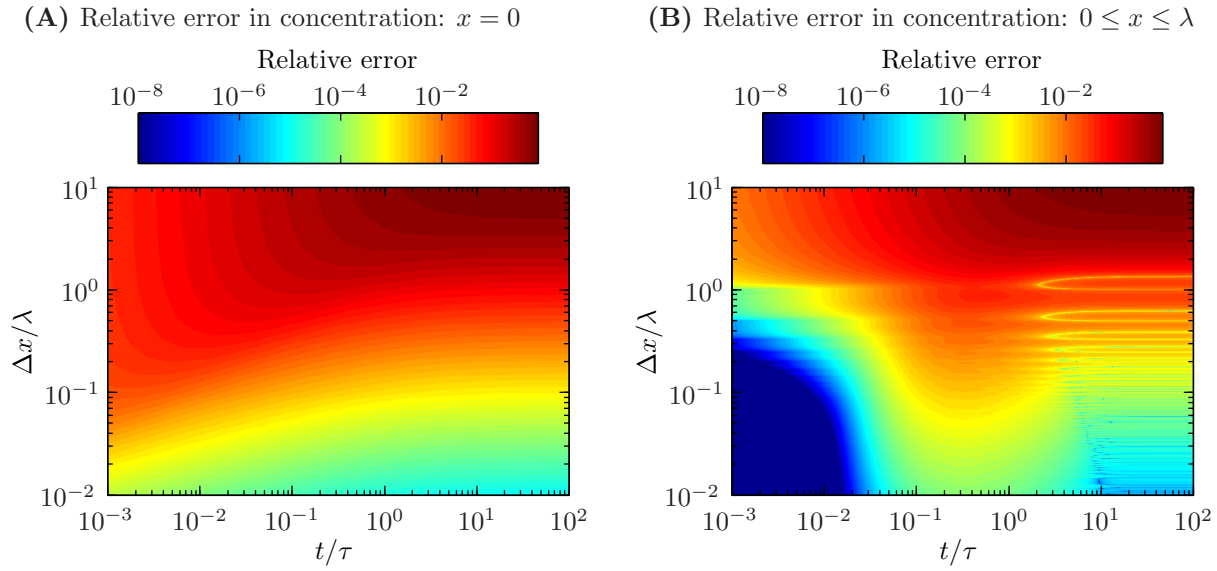

Figure 3.7: Temporal behavior of error in concentration near boundary. **(A)** Relative error in concentration at $x = 0$ is shown for a range of durations t (relative to electrodiffusion time constant τ) and discretization sizes Δx (relative to electrodiffusion length constant λ). The error is relative to the results of using an extremely fine discretization ($\Delta x/\lambda = 2 \times 10^{-4}$ near $x = 0$). **(B)** Relative error in concentration averaged over $0 \le x \le \lambda$ is shown for a range of durations t (relative to electrodiffusion time constant τ) and discretization sizes Δx (relative to electrodiffusion length constant λ). The error is relative to the results of using an extremely fine discretization ($\Delta x/\lambda = 2 \times 10^{-4}$ near $x = 0$). Both plots use the same pseudocolor error scale, thereby allowing direct comparison. The results demonstrate that the error decreases as the size of the discretization decreases relative to the electrodiffusion length constant λ. The error concentration at $x = 0$ is generally larger than the error in the concentration averaged over $0 \le x \le \lambda$. Note that the $x = L$ boundary is sufficiently far away as to have no effect on the results at the $x = 0$ boundary.

not necessarily underestimate the total solute within a region. This is clear in comparing Fig. 3.7A and B, as the error of the boundary layer concentration tends to be smaller than the error in the concentration at $x = 0$.

Figure 3.8 shows the maximum error for each discretization across $0 \le t \le 100\tau$, and can serve as a guide in determining the size of the discretization required to achieve a specified degree of accuracy. Note that the error in the concentration at $x = 0$ is much larger than the error of the concentration of the boundary layer ($0 \le x \le \lambda$) taken as a whole. Which measure of error is more meaningful depends on the particular application and its duration. In the case of electroporation,

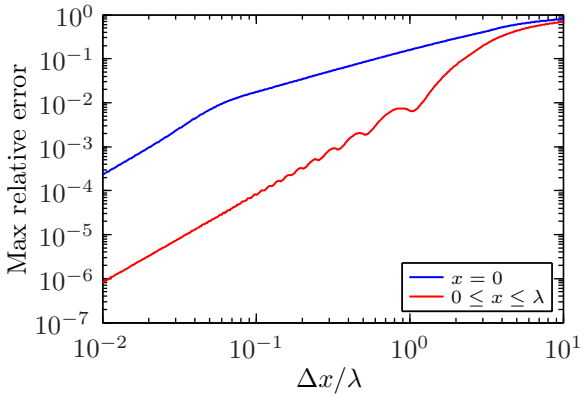

Figure 3.8: Maximum error in concentration near boundary. The maximum relative error in the concentration over all times $0 \leq t \leq 100\tau$ is shown for a range of discretization sizes Δx (relative to electrodiffusion length constant λ). The error is shown for the concentration at $x = 0$ and averaged over $0 \leq x \leq \lambda$. For all discretization sizes, the error at $x = 0$ significantly exceeds the error averaged over $0 \leq x \leq \lambda$. In both cases, error decreases as the size of the discretization decreases relative to the electrodiffusion length constant λ. The error over $0 \leq x \leq \lambda$ is proportional to $(\Delta x/\lambda)^2$.

in which transmembrane transport depends on the concentration the membrane, the error at $x = 0$ is more meaningful if $t \lesssim \tau$. For longer pulses ($t \gtrsim \tau$), the error for the boundary layer as whole is more meaningful because solute will drift a distance λ in time τ. Thus, for longer pulses ($t > \tau$), solute within the boundary layer can drift to the boundary on the time scale of the pulse.

These results provide guidance in determining the discretization size appropriate for a particular system. Specifically, one can use Fig. 3.8 to determine the discretization size Δx required to limit error in the interfacial concentration to a specified level. This Δx should be considered a starting point, as the particulars of a system may require a smaller Δx or permit a larger Δx while remaining within error limits. We suspect that for many systems of interest, Δx as given by Fig. 3.8 is conservative (i.e., smaller than necessary). For example, if a boundary is semi-permeable (allowing transport through it), this will limit the accumulation of solute at the boundary. Similarly, in 2-D in 3-D systems, transport around a boundary (e.g., around a cell in solution) may limit accumulation of solute at the boundary. Both cases are likely to permit a larger Δx than shown in Fig. 3.8.

3.4 Conclusions

We have described a robust method of characterizing electrodiffusive transport in a discretized system. This method is appropriate for modeling transport of solutes that do not contribute significantly to the total ionic current in a system. Many solutes of interest (e.g., drugs and fluorescent probes) meet this criterion, as they are typically present in much lower concentration than the primary charge carriers (sodium, potassium, and chloride ions) in physiologic electrolyte. Under these circumstance, the molecular transport problem may treated separately from the electrical transport problem.

As a result, the molecular transport model presented here may be coupled to existing models of electrical transport (e.g., spatially distributed electroporation models [6–9, 18, 19, 27, 28]) to yield a useful picture of transport in biological systems that experience exogenous or endogenous electric fields.

References

[1] Bockris, J.O. and Reddy, A.K.N. *Modern Electrochemistry, Vol. 1*. Plenum, New York, 1970.

[2] Grodzinsky, A.J. *Fields, Forces, and Flows in Biological Systems*. Garland Science, London, 2011.

[3] Mudry, B., Guy, R.H., and Delgado-Charro, M.B. Transport numbers in transdermal iontophoresis. *Biophys J*, 90(8):2822–30, 2006.

[4] Weaver, J.C. and Chizmadzhev, Y.A. Theory of electroporation: A review. *Bioelectroch Bioener*, 41(2):135–160, 1996.

[5] Weaver, J.C. Electroporation of biological membranes from multicellular to nano scales. *IEEE T Dielect El In*, 10(5):754–768, 2003.

[6] Krassowska, W. and Filev, P.D. Modeling electroporation in a single cell. *Biophys J*, 92(2):404–417, 2007.

[7] Esser, A.T., Smith, K.C., Gowrishankar, T.R., and Weaver, J.C. Towards solid tumor treatment by irreversible electroporation: Intrinsic redistribution of fields and currents in tissue. *Technol Cancer Res T*, 6(4):261–273, 2007.

[8] Esser, A.T., Smith, K.C., Gowrishankar, T.R., Vasilkoski, Z., and Weaver, J.C. Mechanisms for the intracellular manipulation of organelles by conventional electroporation. *Biophys J*, 98(11):2506–14, 2010.

[9] Talele, S., Gaynor, P., Cree, M.J., and van Ekeran, J. Modelling single cell electroporation with bipolar pulse parameters and dynamic pore radii. *J Electrostat*, 68(3):261–274, 2010.

[10] Klenchin, V.A., Sukharev, S.I., Serov, S.M., Chernomordik, L.V., and Chizmadzhev, Y.A. Electrically induced DNA uptake by cells is a fast process involving DNA electrophoresis. *Biophys J*, 60(4):804–811, 1991.

[11] Neumann, E., Kakorin, S., Tsoneva, I., Nikolova, B., and Tomov, T. Calcium-mediated DNA adsorption to yeast cells and kinetics of cell transformation by electroporation. *Biophys J*, 71(2):868–77, 1996.

[12] Neumann, E., Toensing, K., Kakorin, S., Budde, P., and Frey, J. Mechanism of electroporative dye uptake by mouse B cells. *Biophys J*, 74(1):98–108, 1998.

[13] Chizmadzhev, Y.A., Indenbom, A.V., Kuzmin, P.I., Galichenko, S.V., Weaver, J.C., and Potts, R.O. Electrical properties of skin at moderate voltages: Contribution of appendageal macropores. *Biophys J*, 74(2 Pt 1):843–56, 1998.

[14] Hall, D.A. A modified ionophoresis apparatus. *Nature*, 162(4107):105–106, 1948.

[15] Sage, B.H. and Riviere, J.E. Model systems in iontophoresis transport efficacy. *Adv Drug Deliv Rev*, 9(2-3):265–287, 1992.

[16] Esser, A.T., Smith, K.C., Weaver, J.C., and Levin, M. Mathematical model of morphogen electrophoresis through gap junctions. *Dev Dynam*, 235(8):2144–2159, 2006.

[17] Stewart, D.A., Gowrishankar, T.R., Smith, K.C., and Weaver, J.C. Cylindrical cell membranes in uniform applied electric fields: Validation of a transport lattice method. *IEEE T Bio-Med Eng*, 52:1643–1653, 2005.

[18] Smith, K.C., Gowrishankar, T.R., Esser, A.T., Stewart, D.A., and Weaver, J.C. The spatially distributed dynamic transmembrane voltage of cells and organelles due to 10-ns pulses: Meshed transport networks. *IEEE T Plasma Sci*, 34:1394–1404, 2006.

[19] Smith, K.C. and Weaver, J.C. Active mechanisms are needed to describe cell responses to submicrosecond, megavolt-per-meter pulses: Cell models for ultrashort pulses. *Biophys J*, 95(4):1547–1563, 2008.

[20] Smith, K.C. and Weaver, J.C. A unified model of electroporation and molecular transport I: Model design and validation (in preparation).

[21] Smith, K.C. and Weaver, J.C. A unified model of electroporation and molecular transport II: Dynamics of electrical, molecular, and pore transport (in preparation).

[22] Smith, K.C. and Weaver, J.C. An in silico study of potential mechanisms by which extremely large pulsed electric fields induce apoptosis in cells (in preparation).

[23] Smith, K.C. *Cell and Tissue Electroporation*. Master's thesis, Massachusetts Institute of Technology, Cambridge, Massachusetts, 2006.

[24] Smith, K.C. and Weaver, J.C. Compilation and computation of the size, charge, and diffusivity of fluorescent dyes and other small molecules (in preparation).

[25] Ando, T. and Skolnick, J. Crowding and hydrodynamic interactions likely dominate in vivo macromolecular motion. *P Natl Acad Sci USA*, 107(43):18457–62, 2010.

[26] Benedek, G.B. and Villars, F.M.H. *Physics with Illstrative Examples from Medicine and Biology: Volume 3, Electricity and Magnetism*. Addison-Wesley, Reading, 1979. (see Chapter 3).

[27] Gowrishankar, T.R., Esser, A.T., Vasilkoski, Z., Smith, K.C., and Weaver, J.C. Microdosimetry for conventional and supra-electroporation in cells with organelles. *Biochem Bioph Res Co*, 341:1266–1276, 2006.

[28] Esser, A.T., Smith, K.C., Gowrishankar, T.R., and Weaver, J.C. Towards solid tumor treatment by nanosecond pulsed electric fields. *Technol Cancer Res T*, 8(4):289–306, 2009.

Chapter 4

Effects of Hindrance and Partitioning on Ionic and Molecular Transport Through Small Lipidic Pores

Abstract

Quantitative, mechanistic description and understanding of electroporation is important to diverse applications in biology, biotechnology, and clinical medicine. Two broad application categories can be distinguished: (1) delivery of exogenous ions and molecules into cells, and (2) redistribution or release of endogenous molecules within or from cells. In both cases, transport through membrane pores are critical events that influence downstream biological outcomes. Here we consider two fundamental effects that partially govern solute transport through lipidic pores: steric hindrance and partitioning. These effects account approximately for the impact of solute size (hindrance) and charge (partitioning) on transport. We first show how classic descriptions of hindrance and partitioning for spherical solute in infinitely long pores can be approximately adapted to electropores and to non-spherical solutes. As partial validation, we then use our methods to interpret the important lipid bilayer membrane pore conductance measurements of Melikov et al. (Biophys. J., 80:1829–1836, 2001). The Melikov et al. experiments report the average pore conductance values for two very different electrolyte solutions, KCl and NMDG-glutamate, for which we find that both are consistent with an average pore radius value 1.03 nm at 180 mV transmembrane voltage. More broadly, our analysis suggests that the minimum-size pore radius for bilayer lipid membrane, an important quantity in electroporation models, lies in the approximate range $0.9 - 1.0$ nm. Finally, we describe how steric hindrance affects the solute size selectivity of small pores. In future experiments our results could be exploited to estimate the minimum-size pore radius in cell plasma membranes using established experimental techniques. Overall these approximate descriptions and estimates comprise basic ingredients for local electroporation models embedded in either single planar membranes or curved cell membranes.

4.1 Introduction

Two broadly distinguishable applications of electroporation continue to grow: (1) delivery of molecules into cells (and less often, release of molecules from cells), and (2) non-thermal cell removal by necrosis or apoptosis, with the type of cell death suspected to result from differing lethal redistribution of one or more types of biologically active ions or molecules. In both broad cases, lasting biological effects are hypothesized to depend on the net (cumulative) molecular transport through electroporated cell membranes.

Significantly, increasingly realistic quantitative descriptions of cell-level electroporation are therefore important. For this reason, our goal is improved, useful descriptions of net (cumulative) molecular and ionic transport. Here, we consider two fundamental effects that partially govern pore-mediated transport: steric hindrance and partitioning. Specifically, we consider short cylindrical aqueous pathways, which provide an approximation to the internal (central) region of a toroidal lipidic pore. Further, while a cell membrane toroidal pore is envisioned, our results are also relevant to iontophoresis pathways that can be approximated as cylindrical within low dielectric constant (relative permittivity) media.

Movement of solutes (ions and molecules) through electrically created transient aqueous pores is complicated, involving both "insertion" (partitioning) and "frictional drag" (hindrance). In comparison to electrodiffusion within bulk media such as aqueous electrolytes, most solutes are energetically reluctant to enter the small volume of a pore interior region. This is the conceptual basis of the partition factor, K. Moreover, after a solute enters a pore its movement is sterically restricted, which is often described by a hindrance factor, H. In short, "getting in" involves partitioning, and "moving through" involves hindrance. Both hindrance and partitioning are significant if the solute size is close to that of the pore interior region.

Much of what is known about electroporation and pores has been determined through the analysis

of transport, whether electrical [1–7] or molecular [8–18], because the very short characteristic time and length scales limit the ways in which pores, and the effects of pores, can be observed. It is for this reason that characterizing the interaction between pores and solutes is important: Analysis of electroporation-mediated transport can tell us much about pores, but only in the context of a useful, quantitative characterization of the how pores affect transport. Here, as a first step, we describe the pore hindrance and partitioning, the primary means by which pores restrict transport.

Much of the basic work on hindrance and partitioning has been carried out by chemical engineers, motivated by topics such as molecular transport through artificial porous membranes and narrow diameter cylindrical tubes [19–24], and by electrical engineers motivated by problems posed by biological systems and clinical applications [25]. We build on this substantial work in adapting hindrance and partitioning for approximate, but realistic, pore geometries and non-spherical solutes.

In addition to our interest in electroporation, we recognize that pharmaceutical science has a persistent, strong interest in drug delivery, and therefore provides many examples of experiments and modeling for ionic and molecular transport [22, 23]. Electrical drug delivery by iontophoresis is a major example [26–29]. However, electroporation applications provide the primary motivation for the present paper.

4.2 Methods

For clarity of presentation we begin with implications of pore shape, including molecular properties [30]. We then consider the relatively simple case of electrodiffusion in bulk electrolyte [31], and progress to the electrical resistance of pores, and the distinction between transmembrane voltage and transpore voltage. The next topic of hindrance is closely related to electrical resistance, so we treat that before partitioning.

4.2.1 Pore Shape and Size

Hydrophilic lipid pores have long been assumed to be toroidal in shape [1–3, 32, 33], with the heads of the lipid molecules rotated into the interior of the pore wall to minimize exposure of the hydrophobic lipid tails to water molecules. Molecular dynamics simulations [34–39] over the past decade have provided further evidence of the toroidal shape of pores.

In the analysis here, we will generally assume that pores are indeed toroidal in shape, as shown in Fig. 4.1A. However, we find it convenient to sometimes approximate this shape as trapezoidal, as shown in Fig. 4.1B. That is, as a trapezoid rotated about an axis, rather than a circle rotated around an axis (as for a toroid). While some relevant analyses have been based on toroidal pores, such as the electrical force that drives pore expansion [40], others have been based, out of convenience, on trapezoidal pores. An example of toroidal pore use is the estimation of the energy of charge in a pore [2, 3]. As is apparent from Fig. 4.1, the differences between the toroidal and trapezoidal pores are minor. The fluctuating pores created in molecular dynamics simulations variously resemble both pore conformation.

For both toroidal and trapezoidal pores, the pore radius r_p refers to that of the centermost position along the axis of the pore (Fig. 4.1). We will refer to this central region as the "internal" region of the pore, and the entrance and exit regions (on either side of the internal region of the pore) as the "vestibules" or "vestibular" regions of the pore. The membrane has thickness $d_m = 5\,\text{nm}$ and internal region of the pore has a thickness $d_p = d_m/2 = 2.5\,\text{nm}$. The value of d_p was chosen such that the geometry of the trapezoidal pore closely approximated the geometry of the toroidal pore.

4.2.2 Molecular Properties

Several molecular species (solutes), ranging from ions to proteins, were selected for their relevance to electroporation research (Table 4.1). Their widely ranging size and charge also illustrate how these molecular properties can affect the interaction between transported species and membrane pores. These considerations are particularly relevant when a solute is similar in size to a pore.

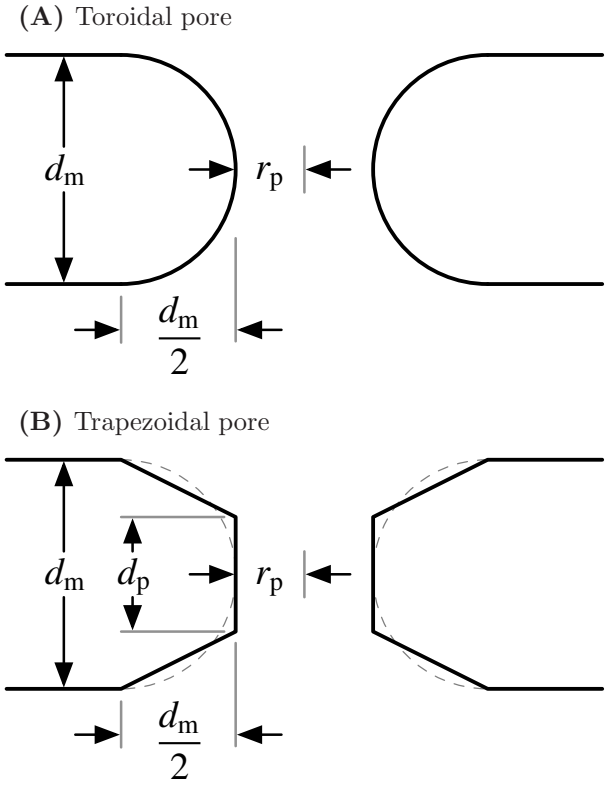

Figure 4.1: Pore shape and size. **(A)** Toroidal pore. **(B)** Trapezoidal pore. Both pore conformations have radius r_p and lie within a membrane of thickness $d_m = 5\,\text{nm}$. The "internal" region of the trapezoidal pore has thickness $d_p = d_m/2 = 2.5\,\text{nm}$, and each broad "vestibule" on either side of the "internal region" has thickness $d_p/4 = 1.25\,\text{nm}$. The wide vestibule contributes relatively little to pore electrical resistance, partitioning and hindrance. The value of d_p was chosen such that the geometry of the trapezoidal pore closely approximates the geometry of the toroidal pore. In this model, pore expansion and contraction are assumed to change only r_p.

The structures of the small (non-protein) molecules were obtained from the PubChem (http://pubchem.ncbi.nlm.nih.gov) and Chemical Entities of Biological Interest (ChEBI) (http://www.ebi.ac.uk/chebi) databases. The structures of the proteins were obtained from the Protein Data Bank (PDB) (http://www.pdb.org). The source of each structure is shown in Table 4.1.

The size and shape of the molecules were examined with UCSF Chimera [41] (version 1.4.1, 2010, http://www.cgl.ucsf.edu/chimera). For the purposes of assessing the molecular sizes and

Table 4.1: Sources of Molecular Structures and Basic Molecular Properties

Molecule	Database	ID	r_s (nm)	l_s (nm)	z_s
Calcium	PubChem	271	0.34	0.68	+2.00
Chloride	PubChem	312	0.17	0.34	−1.00
Potassium	PubChem	813	0.18	0.36	+1.00
Sodium	PubChem	923	0.23	0.46	+1.00
Bleomycin A_2	ChEBI	MSDCHEM:BLM	0.89	2.76	+0.67
Glutamic Acid	PubChem	104813	0.32	0.96	−1.01
Meglumine	PubChem	4049	0.33	1.30	+0.98
Propidium	PubChem	4939	0.69	1.55	+2.00
Yo-pro-1	PubChem	6913121	0.53	1.71	+2.00
Cytochrome *c*	PDB	2B4Z	2.04	4.27	+9.00
HSA	PDB	1N5U	4.32	9.26	−11.02

r_s: Radius of cylindrical approximation to molecule (nm). l_s: Length of cylindrical approximation to molecule (nm). z_s: Net charge (valence) of molecule at pH 7.4.

dimensions, the molecules were assumed to be cylindrical in shape with radius r_s and length l_s. The detailed computational methods used to "measure" the species based on their van der Waals surface are described in Ref. [30]. For the small ions (calcium, chloride, potassium, and sodium), the corrected Stokes radius [30] was used for r_s, and because they are spherical, we assume $l_s = 2r_s$.

Figure 4.2 illustrates the approximation of yo-pro-1, propidium, and bleomycin A_2 as cylinders. While the molecules are clearly far from perfect cylinders, their shape and size are much better represented by cylinders than by spheres.

The ChemAxon *Calculator Plugins* (version 5.3.8, 2010, http://www.chemaxon.com) were used to determine the net charge z_s of each small molecule (non-protein) [30]. This was done by using the *Calculator Plugins* to determine the distribution of microstates of each molecule at pH 7.4 and the charge of each microstate. The net charge of each molecule was then calculated as the weighted average of its microstate charges.

The online tool H++ [42, 43] (version 2.0, 2010, http://biophysics.cs.vt.edu/H++) was used to calculate net charge of each protein at pH 7.4 [30]. This computational tool is specifically designed for macromolecules and evaluates their charge in a manner similar to that described for the small molecules.

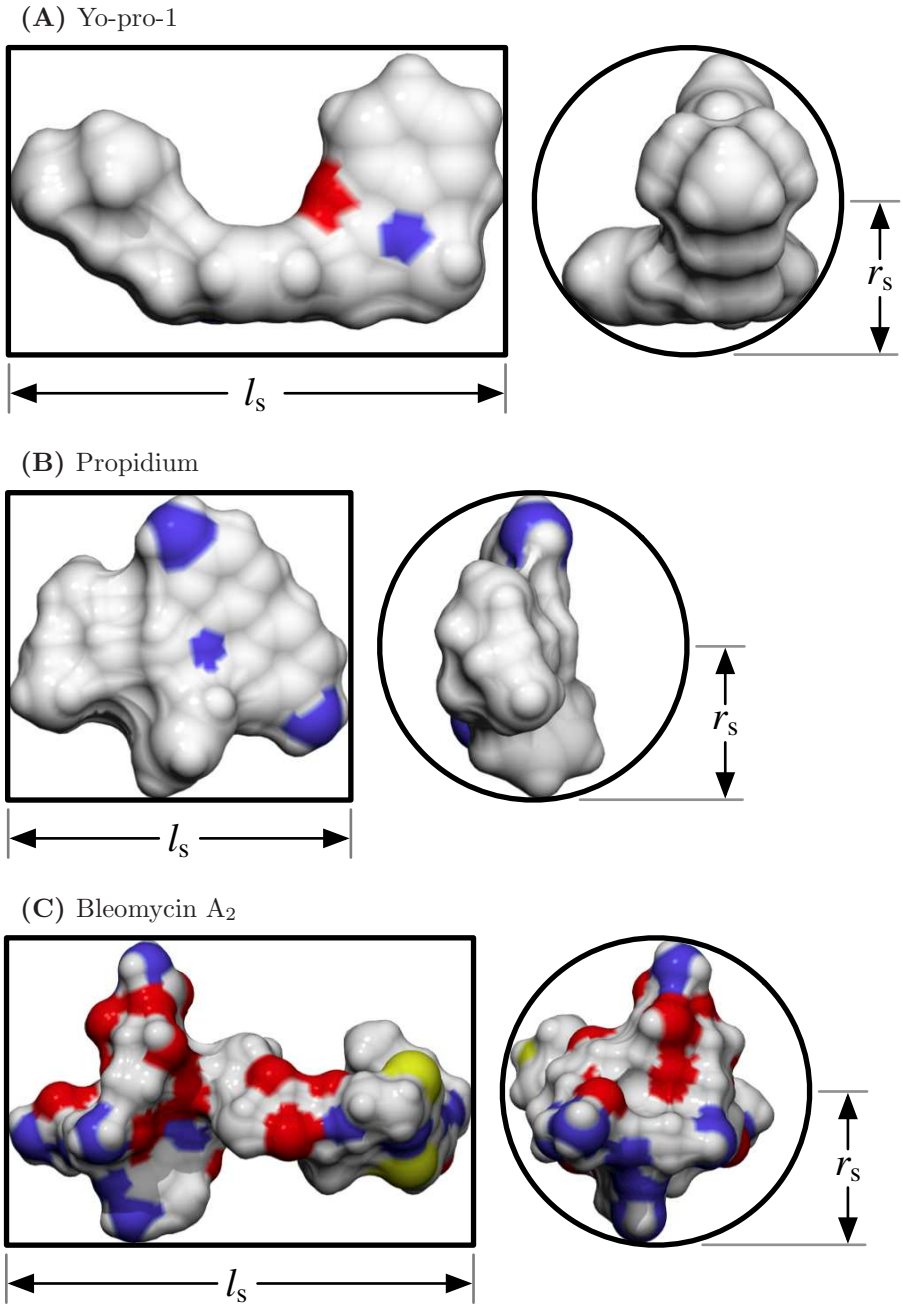

Figure 4.2: Cylindrical approximation to molecular shape. **(A)** Yo-pro-1 (r_s = 0.53 nm, l_s = 1.71 nm). **(B)** Propidium (r_s = 0.69 nm, l_s = 1.55 nm). **(C)** Bleomycin A_2 (r_s = 0.89 nm, l_s = 2.76 nm). Note that the three molecules are not shown to the same scale. The cylindrical approximation to molecular shape gives a more precise description of molecular shape than a spherical approximation, while still being simple enough to facilitate in silico "measurement" of molecular dimensions.

The molecular charge data are summarized in Table 4.1.

4.2.3 Transport in Bulk Electrolyte

Electrodiffusion is the transport of charged solute by the combination of electrical drift and diffusion. The electrodiffusive flux $\boldsymbol{J}_\mathrm{s}$ in bulk electrolyte is described by [25, 31, 44]

$$\boldsymbol{J}_\mathrm{s} = -D_\mathrm{s}\nabla\gamma - \frac{D_\mathrm{s}}{kT}q_\mathrm{e}z_\mathrm{s}\gamma\nabla\phi. \tag{4.1}$$

Here, γ is solute concentration, ϕ is electric potential, D_s is solute diffusivity, z_s is solute charge (valence), q_e is elementary charge, k is the Boltzmann constant, and T is absolute temperature. The first term in Eq. 4.1 describes the flux of solute resulting from a gradient in concentration (diffusion), and the second term describes the flux of solute resulting from a gradient in electric potential (electrical drift).

In electrolytic systems, the primary charge carriers (generally small ions, e.g., chloride, potassium, and sodium) can be treated collectively for simplicity. The properties that characterize the ions and influence their transport (i.e., diffusivity and charge) are subsumed into the single macroscopic quantity conductivity σ. The electrical flux $\boldsymbol{J}_\mathrm{s}$ in bulk electrolyte is described by [44]

$$\boldsymbol{J}_\mathrm{s} = -\sigma\nabla\phi. \tag{4.2}$$

That is, the flux of charge results from the gradient in electric potential.

The equations describing transport in bulk electrolyte, whether electrodiffusive (Eq. 4.1) or electrical (Eq. 4.2), implicitly regard the transported solute as consisting of point charges. This continuum assumption is reasonable in the bulk electrolyte, but not in the limited confines of a pore, where the finite size of the solute, as well as the specific electrical interactions between the charge and the nearby lipids of a low dielectric constant pore, become significant.

The objective of this study is to relate electrical and molecular transport through pores to electrical and molecular transport in bulk electrolyte. Therefore, the electric potential and solute concentration will be treated as known quantities. It follows that the flux through a pore based on bulk electrolyte assumptions is also known (through Eqs. 4.1 and 4.2). Specifically, we show that the flux $J_{s,p}$ through a pore is simply related to the flux J_s calculated using bulk electrolyte assumptions (Eqs. 4.1 and 4.2) by

$$J_{s,p} = HKJ_s, \tag{4.3}$$

where H is the hindrance factor and K is the partition factor.

4.2.4 Electrical Resistance of Pores

When an ion subject to an electric field approaches a pore (Fig. 4.1), its surroundings may no longer be considered homogenous (as in bulk electrolyte) and its size and charge become important determinants of its interaction with its environment and resulting transport. Chief among these interactions are hindrance and partitioning.

Consider the internal region of the trapezoidal pore in Fig. 4.1. It has radius r_p, depth d_p, cross-sectional area $A_p = \pi r_p^2$ and conductivity σ_p. Ignoring any interaction between the ions that comprise the medium (and give rise to the conductivity σ_p) and assuming that the ions are point charges (i.e., using bulk electrolyte assumptions), the conductance $g_{p,p}$ of the internal pore region is

$$g_{p,p} = \sigma_p \frac{A_p}{d_p}. \tag{4.4}$$

In general, the conductivities σ_1 and σ_2 on the two sides of the membrane (e.g., extracellular and intracellular) are not the same. If half of the pore (i.e., a cylindrical region with radius r_p and length $d_p/2$) is assumed to contain medium of conductivity σ_1 and half is assumed to contain medium of conductivity σ_2, then the average conductivity σ_p in the pore is

$$\sigma_p = \frac{2\sigma_1\sigma_2}{\sigma_1 + \sigma_2}. \tag{4.5}$$

As will be described in the following sections, interaction between solute ions (or molecules) in a pore and the pore gives rise to a pore hindrance factor H and partition factor K that scale the pore conductance as it is given in Eq. 4.4. That is, accounting for hindrance and partitioning, the pore conductance becomes

$$g_{\mathrm{p,p}} = \sigma_{\mathrm{p}} \frac{A_{\mathrm{p}}}{d_{\mathrm{p}}} HK. \tag{4.6}$$

The resistance $R_{\mathrm{p,p}}$ of the internal pore region is thus

$$R_{\mathrm{p,p}} = \frac{1}{g_{\mathrm{p,p}}} = \frac{d_{\mathrm{p}}}{\sigma_{\mathrm{p}} A_{\mathrm{p}} HK}. \tag{4.7}$$

In addition to the resistance $R_{\mathrm{p,p}}$ of the internal pore region, there is an access resistance $R_{\mathrm{p,a}}$ [45, 46] associated with each side of the membrane/pore. It is clear from Eq. 4.7, that pore resistance is determined by both material properties (e.g., σ_{p}) and geometric properties (e.g., A_{p} and d_{p}) of a system. Access resistance (which is also known as spreading resistance [47]) arises from the fact, in order to pass through a pore, ions follow local, inhomogeneous electric fields in the electrolyte before entering and after exiting a pore. That is, because the ions can only traverse the membrane by passing through pores, their paths are “focused” through pores, and this results in the access resistance.

The pore access resistance $R_{\mathrm{p,a}}$ is the sum of the access resistance for each side of the pore, which are not, in general, the same:

$$R_{\mathrm{p,a}} = \frac{1}{4\sigma_1 r_{\mathrm{p}}} + \frac{1}{4\sigma_2 r_{\mathrm{p}}} = \frac{\sigma_1 + \sigma_2}{4\sigma_1 \sigma_2 r_{\mathrm{p}}}. \tag{4.8}$$

Nonetheless, $R_{\mathrm{p,a}}$ can be written in terms of σ_{p} as

$$R_{\mathrm{p,a}} = \frac{1}{2\sigma_{\mathrm{p}} r_{\mathrm{p}}}. \tag{4.9}$$

The total resistance R_p associated with a pore is therefore the sum of the resistance of the internal pore region $R_{p,p}$ and the access resistance $R_{p,a}$:

$$R_p = R_{p,p} + R_{p,a} = \frac{d_p}{\sigma_p A_p HK} + \frac{1}{2\sigma_p r_p}. \tag{4.10}$$

4.2.5 Transmembrane and Transpore Voltage

A transmembrane voltage $\Delta\phi_m$ can arise due to either endogenous (e.g., metabolically established ion concentration differences or ion pumps) or exogenous (e.g., electric pulse generator) sources. Far from a pore, the transmembrane voltage is simply, as the name implies, the voltage drop across the membrane. In the vicinity of a pore, the transmembrane voltage is the voltage drop across the pore and the electrolyte regions near the pore entrance/exit that give rise to the pore access resistance.

The definitions of transmembrane voltage in the absence and presence of a pore may appear contradictory, since the former includes only the voltage drop across the membrane whereas the latter includes the voltage drop across the membrane and a region of electrolyte. The apparent discrepancy is resolved by realizing that the voltage drop across a system comprising electrolyte and an intact membrane occurs almost entirely across the membrane because the membrane resistivity is orders of magnitude larger than the electrolyte resistivity. Therefore, the voltage drop across an intact membrane alone is the same as the voltage drop across the membrane and some amount of electrolyte.

In the vicinity of a pore, a transpore voltage $\Delta\phi_p$ can also be defined. This is the voltage drop across the internal pore region (i.e., not across the pore access region). The transpore voltage $\Delta\phi_p$ is related to transmembrane voltage $\Delta\phi_m$ through voltage division:

$$\Delta\phi_p = \frac{R_{p,p}}{R_{p,p} + R_{p,a}} \Delta\phi_m = \frac{R_{p,p}}{R_p} \Delta\phi_m. \tag{4.11}$$

The circuit diagram in Fig. 4.3 shows the relationship between $\Delta\phi_m$, $\Delta\phi_p$, and the resistances $R_{p,a}$ and $R_{p,p}$ that comprise the total resistance R_p associated with a pore.

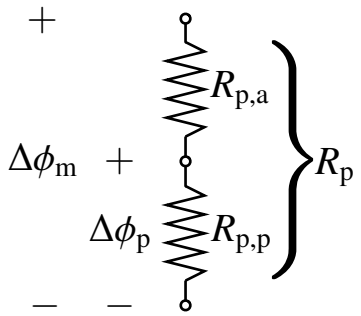

Figure 4.3: Pore voltages and resistances. The total resistance R_p associated with a pore is the sum of the pore access resistance $R_{p,a}$ and the resistance of the pore itself $R_{p,p}$. The total voltage drop across the pore and pore access regions is the transmembrane voltage $\Delta\phi_m$, while the voltage drop across the pore alone is the transpore voltage $\Delta\phi_p$. The magnitude of $\Delta\phi_p$ relative to $\Delta\phi_m$ is determined by the voltage division between the $R_{p,a}$ and $R_{p,p}$. Generally, the ratio $\Delta\phi_p/\Delta\phi_m$ decreases as r_p increases.

4.2.6 Hindrance for Spherical Ions and Molecules

Continuum models of the bulk medium implicitly assume that transported molecular species exist as infinitesimal points. However, real molecules are not, of course, infinitesimal. They have finite size, and this affects the transport of molecules through pores, especially when the size of the molecule is on the same order as the size of the pore. Continuum models are smoothed representations of molecular systems. They are useful and justified when the spatial scale of the system region is large enough that statistical fluctuations within the region are small and thus enable a spatiotemporal average to approximate the state of that system region [24].

The general problem motivating our analysis is transport of a solute that is present at a relatively small concentration compared with the background ubiquitous small ions (sodium, potassium, and chloride) of physiologic aqueous media. Small ions should be distinguished, as they are essentially ionized, hydrated atoms, which can be regarded as spherical. Physiologic media usually exist outside or within a cell in vivo, and are often (but not always) provided experimentally in vitro.

The effect that a molecule's finite size has on its transport through a pore can be accounted for through a hindrance factor [48] that diminishes the transport that one would calculate in the absence of hindrance. In other words, if one calculated a current i through a pore in the absence of hindrance, then accounting for hindrance, the current would be iH, where H is the hindrance factor. The hindrance factor is dimensionless and lies in the range $0 \leq H \leq 1$.

Hindrance arises from two effects that impede transport through pores: (1) the decreased effective (accessible) area of a pore when solute size is accounted for and (2) the drag (kinetic dissipation) exerted on the solute by the pore walls [49]. Thus, the hindrance factor, which is a function of the solute radius r_s and the pore radius r_p, is itself the product of an effective area factor f_A and a drag factor f_D:

$$H = f_A f_D. \tag{4.12}$$

Accounting for hindrance is difficult. Accordingly, a number of different approximate equations for hindrance have been developed [50, 51]. Here, we use the equation developed by Bungay and Brenner [52] because, in contrast to most other hindrance equations, it is valid over the entire range $0 \leq r_s \leq r_p$. While the hindrance equation developed by Renkin [48] is perhaps better known, it only holds for $0 \leq r_s < 0.4 r_p$ [50].

It should also be noted that these hindrance equations were derived for systems in which the pore length is much greater than the pore radius ($d_p \gg r_p$) and solute molecules are spherical in shape. Here, the initial development and description of hindrance will be consistent with these traditional assumptions. However, we will then show how the hindrance estimate can be modified for more realistic geometries (i.e., less elongated pores with cylindrical solute molecules).

Effective Pore Area Factor

In contrast to an idealized infinitesimal solute, which can access the entire interior of a pore, a realistic solute of finite size can access (occupy) only the central region of a pore. This means that the distance from the center of the solute to the pore wall must exceed r_s. As the radius of the solute approaches the radius of the pore ($r_s \to r_p$), the solute becomes increasingly restricted, and when size of the solute exceeds the size of the pore ($r_s \geq r_p$), the solute cannot even enter the pore. This basic concept is well-established. It is mainly a question of which approximate, numerical description to employ.

More specifically, a cylindrical pore of radius r_p has cross-sectional area $A_p = \pi r_p^2$. However, a solute of radius r_s can only access the central region with radius $r_p - r_s$, which has the effective pore area $A_{eff} = \pi(r_p - r_s)^2$. The (dimensionless) effective area factor f_A is simply the ratio [48]:

$$f_A = \frac{A_{eff}}{A_p} = \frac{\pi(r_p - r_s)^2}{\pi r_p^2} = \left(1 - \frac{r_s}{r_p}\right)^2 . \tag{4.13}$$

Drag Factor

The second source of hindrance for a solute traversing a pore is the drag exerted on the solute molecule by the walls of the pore. The (dimensionless) drag factor developed by Bungay and Brenner [52] is

$$f_D = \frac{6\pi}{f_t}, \tag{4.14}$$

where

$$f_t(\lambda) = \frac{9}{4}\pi^2 \sqrt{2}\,(1-\lambda)^{-\frac{5}{2}} \left(1 + a_1(1-\lambda) + a_2(1-\lambda)^2\right) + a_3 + a_4\lambda + a_5\lambda^2 + a_6\lambda^3 + a_7\lambda^4 \tag{4.15}$$

and $\lambda \equiv r_s/r_p$. The constants a_i ($i = 1, 2, \ldots, 7$) are shown in Table 4.2.

Figure 4.4 shows how the pore hindrance factor H and its component factors f_A and f_D vary with λ.

Table 4.2: Values of Coefficients in the Bungay-Brenner Hindrance Equation

Parameter	Value
a_1	−1.2167
a_2	1.5336
a_3	−22.5083
a_4	−5.6117
a_5	−0.3363
a_6	−1.216
a_7	1.647

For all λ, the drag factor contributes more significantly than the effective area factor in hindering transport of a solute through a pore. To our knowledge, there is not intuitive explanation for Eq. 4.15 and the parameters in Table 4.2. Instead, it is an example of the complexity of solute transport within even a simple pore geometry. This forces the use of numerical methods.

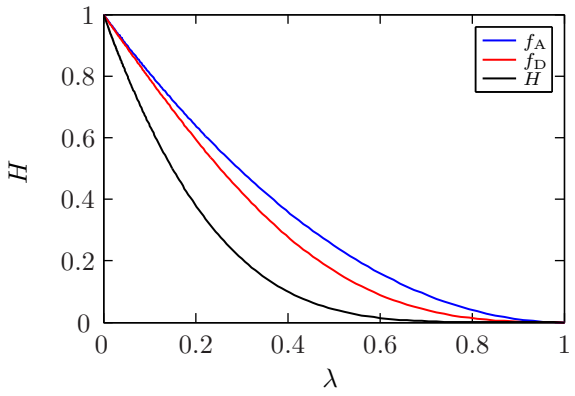

Figure 4.4: Hindrance factor for spherical solutes. The pore hindrance factor H is shown with the effective pore area factor f_A and drag factor f_D that comprise it ($H = f_A f_D$). λ is the radius of the solute relative to the radius of the pore ($\lambda \equiv r_s/r_p$). The hindrance factor H ($0 \leq H \leq 1$) scales the transport through a pore. Thus, when $H \to 0$, transport is maximally hindered (transport goes to zero), and when $H \to 1$, transport is minimally hindered or unhindered (transport is as in bulk electrolyte). For all λ, the drag factor f_D contributes more significantly than the effective area factor f_A in hindering transport.

4.2.7 Hindrance for Cylindrical Molecules

We emphasize the fact that Eq. 4.12 was developed for spherical solute molecules ($l_s \approx 2r_s$) in long, slender cylindrical pores ($d_p \gg r_p$). It follows from these two conditions that the solute molecules are much smaller than the pore length ($l_s \ll d_p$). These three conditions generally do not apply to electroporation-mediated transport because solute molecules may be large (relative

to the pore length), solute molecules may be non-spherical, and pores are not long and slender. Even for minimum-size pores ($r_p \approx 0.8\,\text{nm}$) [3]), $d_m/2r_p$ is only ~ 3. In response to conventional electroporation pulses, pores expand to significantly larger size [53–55], and then $d_m/2r_p$ becomes even smaller.

Due to these limitations of the hindrance equation (Eq. 4.12), we developed simple modifications to generalize it for systems with any or all of the following three characteristics: (1) large solute relative to the pore length ($l_s \not\ll d_p$), (2) cylindrical (non-spherical) solute molecules ($l_s \not\approx 2r_s$), and (3) short, wide pores ($d_p \not\gg r_p$). To avoid confusion, hats are placed over symbols specific to the modified hindrance factor $\hat{H}$ and differentiate them from the original pore hindrance factor H.

As in the case of the original pore hindrance factor H (Eq. 4.12), the modified pore hindrance factor $\hat{H}$ is the product of an effective pore area factor $\hat{f}_A$ and a drag factor $\hat{f}_D$:

$$\hat{H} = \hat{f}_A \hat{f}_D. \tag{4.16}$$

We assume that differential torques due to both heterogeneous flow and fields near the pore entrance (and exit) on a cylindrical molecule align the molecule such that it enters a pore with its long dimension parallel to the axis of the pore (Fig. 4.5). With this orientation, the effective pore area factor $\hat{f}_A$ is that of the original formulation (Eq. 4.13):

$$\hat{f}_A = f_A = \left(1 - \frac{r_s}{r_p}\right)^2. \tag{4.17}$$

The relationship between the modified hindrance drag factor f_D and the original hindrance drag factor f_D is more complicated. First we must relate the drag factor f_D to the drag resistance itself.

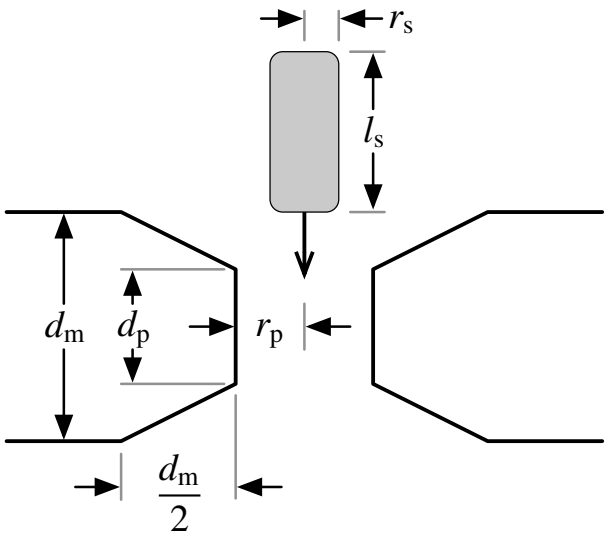

Figure 4.5: Movement of a cylindrical molecule through a pore. The cylindrical molecule has radius r_s and length l_s, and the pore has radius r_p and thickness d_p in a membrane of thickness d_m. As shown, the molecule is assumed to traverse the pore with its long axis parallel to the axis of the pore.

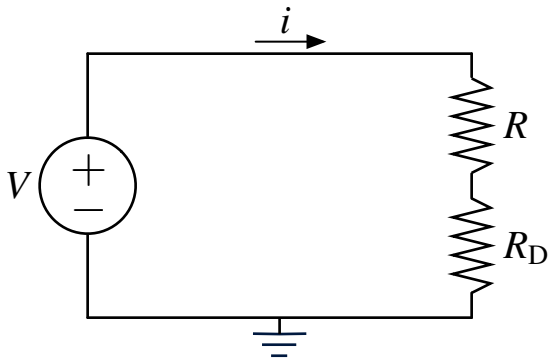

Figure 4.6: Circuit analog for molecular transport through a pore. V is the driving force for molecular transport, which is determined by the gradients in solute concentration and electric potential across a membrane pore. R is the resistance to molecular transport, excluding hindrance due to drag. R is determined by factors such as the solute diffusivity and the cross-sectional area and length of a pore. In other words, R relates the rate of transport i to the driving force V, ignoring hindrance due to drag. R_D is the resistance to molecular transport that arises specifically due to the drag on a molecule as it traverses a pore. Like R, R_D influences the rate of transport i for a given driving force V.

Figure 4.6 shows a simple circuit representation of molecular transport through a pore. In this mathematically analogous circuit abstraction, V is the driving force for molecular transport, which is determined by the gradients in solute concentration and electric potential across a membrane pore (Eq. 4.1).

In this analogy, R is the resistance to molecular transport, excluding hindrance due to drag. R is determined by factors such as the solute diffusivity and the cross-sectional area and length of a pore. In other words, R relates the rate of transport i to the driving force V, ignoring hindrance due to drag. R_D is the resistance to molecular transport that arises specifically due to the drag on a molecule as it traverses a pore. Like R, R_D influences the rate of transport i for a given driving force V.

The hindrance drag factor f_D is, by definition, the ratio of the diminished transport that occurs with drag to the transport that would occur without drag. Therefore, in terms of the resistances R and R_D in Fig. 4.6,

$$f_D = \frac{R}{R + R_D}. \tag{4.18}$$

Rearranging Eq. 4.18, the drag resistance R_D is related to the drag factor f_D by

$$R_D = R\left(\frac{1}{f_D} - 1\right). \tag{4.19}$$

Note that when $f_D \to 0$ (maximal hindrance), $R_D \gg R$, and when $f_D \to 1$ (minimal hindrance), $R_D \ll R$.

We assume that the resistance due to drag on a molecule traversing a pore is proportional to the length of the interface $l_{s,p}$ between the molecule and internal pore region:

$$l_{s,p} \equiv \min\left(l_s, d_p\right). \tag{4.20}$$

In other words, $l_{s,p}$ is the lesser of l_s and d_p. Additionally, we assume $\hat{f}_D = f_D$ when $l_s = 2r_s$. That is, a cylindrical molecule with length $l_s = 2r_s$ is considered equivalent to a spherical molecule with length r_s. Thus, the drag resistance $\hat{R}_D$ on a cylindrical molecule with radius r_s and molecule-pore interface length $l_{s,p}$ is approximately related to the drag resistance R_D on a spherical molecule with the same radius r_s by

$$\hat{R}_D = R_D\left(\frac{l_{s,p}}{2r_s}\right). \tag{4.21}$$

Substituting for $\hat{R}_D$ and R_D based on Eq. 4.19,

$$R\left(\frac{1}{\hat{f}_D} - 1\right) = R\left(\frac{1}{f_D} - 1\right)\left(\frac{l_{s,p}}{2r_s}\right). \tag{4.22}$$

Solving for $\hat{f}_D$ yields

$$\hat{f}_D = \frac{f_D}{f_D + (1 - f_D)\left(\frac{l_{s,p}}{2r_s}\right)}. \tag{4.23}$$

A spherical molecule of radius r_s is regarded as a cylindrical molecule of radius r_s and length $l_s = 2r_s$ so that $\hat{H} = H$. Accordingly, there is no need to use one hindrance equation for spherical molecules (Eq. 4.12) and another for cylindrical molecules (Eq. 4.16) because the $\hat{H}$ is equivalent to H for small, spherical molecules.

Figure 4.7 shows the dependence of the hindrance $\hat{H}$ on pore radius r_p for the ions and molecules in Table 4.1. The hindrance factor $\hat{H}$ ($0 \leq \hat{H} \leq 1$) is determined by the size of a solute relative to the size of a pore and scales the transport through a pore. Thus, when $\hat{H} \to 0$, transport is maximally hindered (transport goes to zero), and when $\hat{H} \to 1$, transport is minimally hindered or unhindered (transport is the same as in bulk electrolyte). As the pore radius r_p increases the hindrance factor $\hat{H}$ also increases, and solute can more easily pass through a pore.

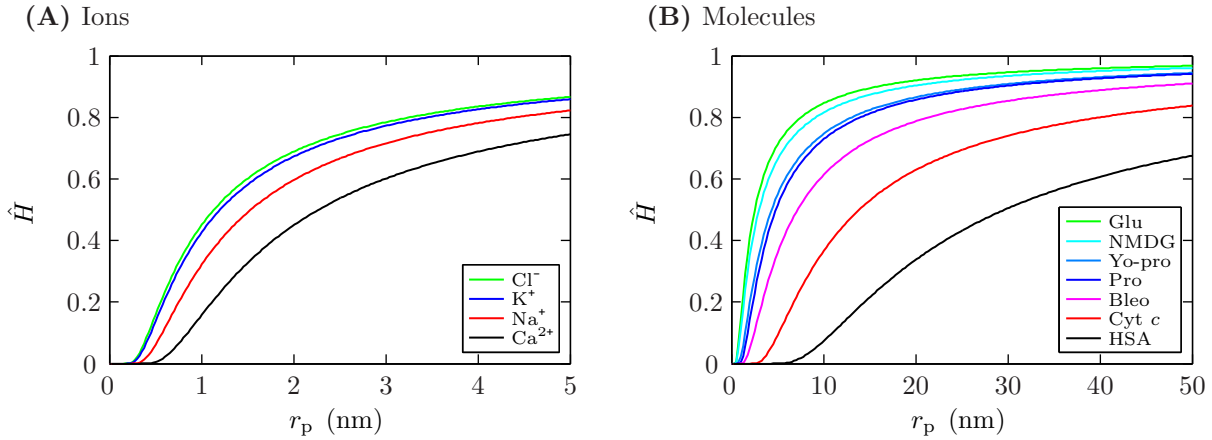

Figure 4.7: Hindrance factor for cylindrical solutes. The hindrance factor $\hat{H}$ is shown for **(A)** ions and **(B)** molecules. Note that the distinction between ions and charged molecules is somewhat arbitrary, and the same hindrance equation treats both. The hindrance factor $\hat{H}$ ($0 \leq \hat{H} \leq 1$) is determined by the size of a solute relative to the size of a pore and scales the transport through a pore. Thus, when $\hat{H} \to 0$, transport is maximally hindered (transport goes to zero), and when $\hat{H} \to 1$, transport is minimally hindered or unhindered (transport is the same as in bulk electrolyte). As the pore radius r_p increases, the hindrance factor $\hat{H}$ also increases, and solute can more easily pass through a pore.

4.2.8 Partitioning

The partition factor is an equilibrium-based quantity that describes the decreased concentration of a charged solute found inside a pore relative to in the bulk solution. The lowered concentration results from the energy cost of moving a charge in a medium with a high dielectric constant (e.g., water) into membrane pore with a low dielectric constant (e.g., pore in lipid bilayer) [56, 57]. More generally, the partition factor is the ratio of concentrations (activities, strictly) between two contacting media in equilibrium [22].

The partition factor, like the pore hindrance factor, plays a fundamental role in determining the transport of charged solute through membrane pores. The original development of the partition factor for an ion within a membrane by Parsegian [56, 57] makes many of the same assumptions as those made by Bungay and Brenner [52] for hindrance, for example that the solute is an ion in the center of a long, cylindrical pore. Chernomordik et al. [2] were the first to develop a partition factor equation for ionic transport through lipid membrane pores by assuming a trapezoidal energy

profile for an ion passing through pore, which reflects the approximately trapezoidal shape of the pore itself. As in the development of hindrance, we will make some simple modifications to generalize the partition factor equation developed by Chernomordik et al. [2] for use with larger solutes, which we will also treat as cylindrical.

Effective Charge of Molecule in Pore

In developing a partition factor equation relevant for solute molecules with size of the same order as or larger than a pore, we must address the fact that the solute (and its charge) may not fully fit within a pore. As in the development of the hindrance equation, we assume that molecules can be characterized as cylindrical in shape and that the most energetically favorable orientation in a pore is with the long dimension of the molecule parallel to the pore axis (Fig. 4.5). Given this orientation, we further assume that the charge on the solute molecule molecule, z_s, is evenly distributed along its length, l_s. This is a useful simplifying assumption that cannot be completely correct. With this assumption, when a molecule is centered within a pore of thickness d_p, the charge within the pore is

$$z_{s,p} \equiv z_s \min\left(1, \frac{d_p}{l_s}\right). \tag{4.24}$$

For small molecules ($l_s \leq d_p$), $z_{s,p} = z_s$. For larger molecules ($l_s > d_p$), $z_{s,p} < z_s$ (in magnitude).

Born Energy

Placing a charge at the center of a pore in a low dielectric membrane results in an energy cost (relative to being in the bulk medium) termed the Born energy w_0. Parsegian calculated the Born energy for an ion in an infinitely long pore [56, 57], which is of theoretical interest but not directly applicable to pores of finite length, like those considered here. Indeed, Vasilkoski et al. [47] used numerical techniques to show that Born energy for a cylindrical pore with $d_p = 5\,\text{nm}$ is significantly smaller than for an infinitely long pore.

Using notation previously established by others, we use the following equation for Born energy w_0:

$$w_0(r_p) = 5.3643 \frac{(z_{s,p} q_e)^2}{kT} r_p^{-1.803}. \tag{4.25}$$

This is the energy (in units of kT) required to place (insert) a charge $z_{s,p}$ into the center of a toroidal pore of radius r_p for zero transpore voltage. We note that Eq. 4.25 is an unpublished result developed by Axel Esser (M.I.T.) and Zhen Ji (U. Wisconsin, Madison) using a numerical approach along the lines of those in Kuyucak et al. [58].

Partitioning Equation

Chernomordik et al. [2] developed the following equation (with one small difference: they used transmembrane rather than transpore voltage, as noted below) for the partition factor K, assuming that the energy profile (vs. position along axis of pore) of a charged solute in a pore is trapezoidal in shape:

$$K(r_p, \Delta\psi_p) = \frac{e^{\Delta\psi_p} - 1}{\frac{w_0 e^{w0 - n\Delta\psi_p} - n\Delta\psi_p}{w_0 - n\Delta\psi_p} e^{\Delta\psi_p} - \frac{w_0 e^{w0 + n\Delta\psi_p} + n\Delta\psi_p}{w_0 + n\Delta\psi_p}}. \tag{4.26}$$

Here, q_e is the electronic charge, n is the relative entrance length of a pore, and

$$\Delta\psi_p \equiv \frac{q_e z_{s,p}}{kT} \Delta\phi_p. \tag{4.27}$$

$\Delta\psi_p$ is the dimensionless transpore voltage. In their formulation, Chernomordik et al. [2] used the dimensionless transmembrane voltage $\Delta\psi_m$, rather than $\Delta\psi_p$, where

$$\Delta\psi_m \equiv \frac{q_e z_{s,p}}{kT} \Delta\phi_m. \tag{4.28}$$

We assume that this is because they did not account for voltage division due to the pore access resistance, in which case the transmembrane voltage $\Delta\phi_m$ and transpore voltage $\Delta\phi_p$ would be equivalent. We argue that the transpore voltage seems more appropriate for partitioning, as it is the transpore voltage that relates to the magnitude of the electric field within the pore ($E_p \approx \Delta\phi_p / d_p$).

In Eq. 4.26, n is the relative entrance length of a pore, or the fraction of the membrane thickness d_m over which the trapezoidal energy profile is increasing or decreasing. Chernomordik et al. [2] use $n = 0.31$, and Glaser et al. [3] use $n = 0.15$. These values were chosen to fit their experimental data, rather than based on considerations of pore geometry. Here, we use a geometry-based value

$n = 0.25$ for two reasons. First, this value is intermediate between those of Chernomordik et al. and Glaser et al., the only experimental determinations we are aware of. Second, it is reasonable to assume that the trapezoidal energy profile should be at least in part related to the trapezoidal pore geometry (Fig. 4.1) [3]. In other words, we assume $n \equiv d_p/2d_m$. Neither the early nor the present values of n are based on detailed calculations but appear to be reasonable estimates.

In using Eq. 4.26, one should note that K is indeterminate when $\Delta\psi_p = 0$. This problem can be resolved by evaluating Eq. 4.26 in the limit $\Delta\psi_p \to 0$, using L'Hôpital's rule twice to obtain

$$\lim_{\Delta\psi_p \to 0} K(r_p, \Delta\psi_p) = \frac{w_0}{(w_0(1-2n)+2n)e^{w_0} - 2n}. \tag{4.29}$$

Figure 4.8 shows the partition factor as a function of pore radius r_p and solute charge (in pore) $z_{s,p}$ for a few transmembrane voltages $\Delta\phi_m$. As r_p increases, $z_{s,p}$ decreases, and/or $\Delta\phi_m$ increases, K increases (approaches 1), as all of these decrease the energy barrier for a charged solute entering a pore.

4.3 Results and Discussion

4.3.1 Estimation of Radius of Minimum-size Pores in Bilayer Lipid Membrane

Transport through pores is both size-dependent and charge-dependent due to hindrance (Eq. 4.16) and partitioning (Eq. 4.26). As a result, quantitative determinations of pore conductance for solutes that differ in size and/or charge can enable estimation of pore size.

Melikov et al. [6] examined pore conductance in voltage-clamped bilayer lipid membranes (BLM). Using highly sensitive methods, they measured noisy but quantized steps up and down in membrane conductance, which they attributed to the creation and destruction of discrete pores. Given

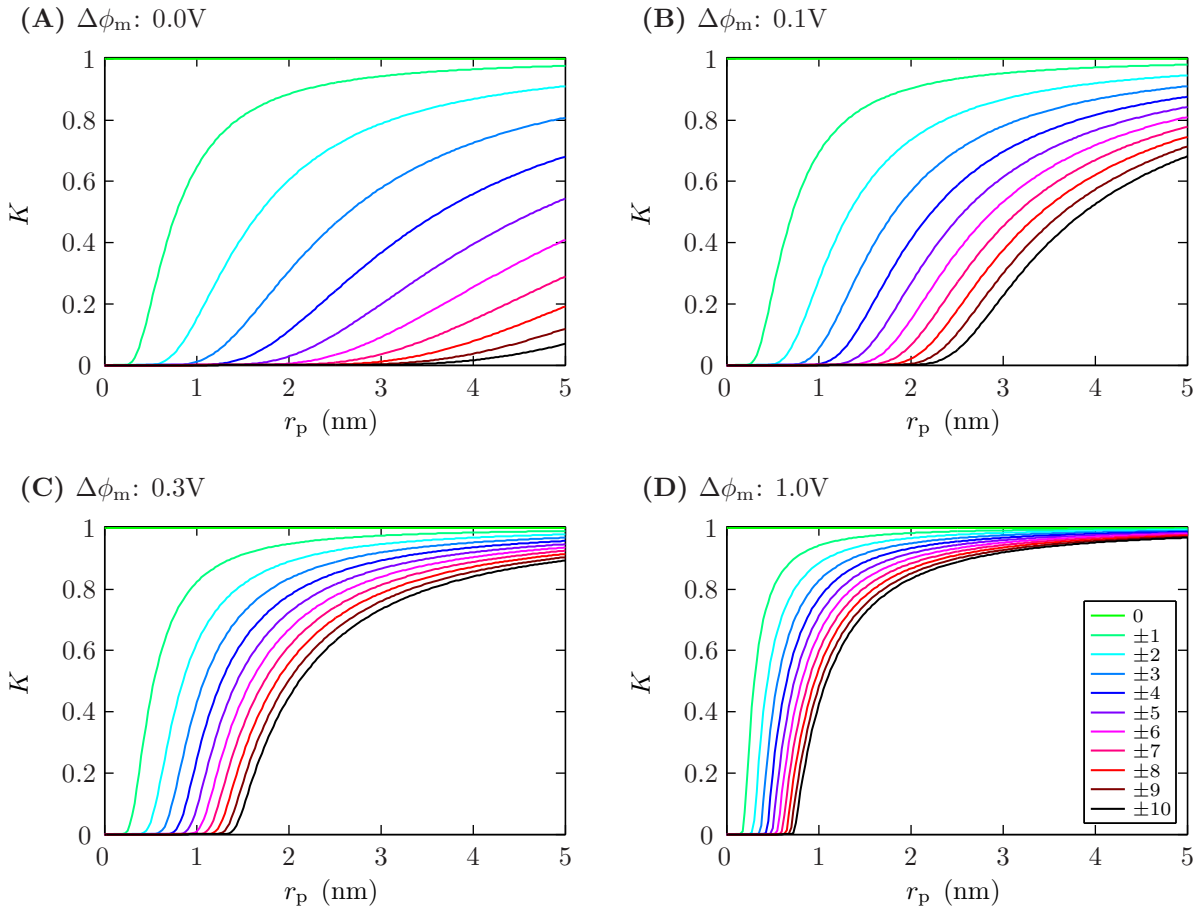

Figure 4.8: Partition factor for transmembrane voltage $\Delta\phi_m$ values **(A)** 0.0 V, **(B)** 0.1 V, **(C)** 0.3 V, and **(D)** 1.0 V. For each, the partition factor K is plotted against the pore radius r_p for a range of solute charges (in the pore) $z_{s,p}$, as indicated by the inset. The partition factor K ($0 \leq K \leq 1$) arises because of the Born energy cost (relative to being in the bulk medium) required to place a charge in pore. K scales transport through a pore. Thus, when $K \to 0$, transport is maximally affected (transport goes to zero), and when $K \to 1$, transport is minimally affected (transport is as if bulk electrolyte filled the pore). Increases in the pore radius r_p and transmembrane voltage $\Delta\phi_m$ increase the partition factor K, resulting in greater transport, and increases in the solute charge (in the pore) $z_{s,p}$ decreases the partition factor K, resulting in less transport.

the relatively small magnitude of the transmembrane voltages applied ($\lesssim 500\,\mathrm{mV}$), we expect that the pores were at or near $r_{\mathrm{p,min}}$, the radius at which there is a local minimum in pore energy when the transmembrane voltage is $\lesssim 500\,\mathrm{mV}$ [55, 59, 60].

To probe pore size, Melikov et al. [6] insightfully performed their experiments using two different electrolyte solutions: KCl and NMDG-glutamate. (Note that NMDG and glutamate are also known as meglumine and glutamic acid, respectively.) Because the latter solution resulted in a decrease in average pore conductance relative to the former, Melikov et al. reasoned that pores should be roughly the same size as NMDG^{+} and $\mathrm{glutamate}^{-1}$ ions and that the results were consistent with a pore radius of $\sim 1\,\mathrm{nm}$ reported in the literature at that time. Here, we use the methods developed above to take a closer look at the Melikov et al. experiment and the implications for pore size. Furthermore, we use the results to test our methods, as the pore size predicted by KCl and NMDG-glutamate should be the same.

Melikov et al. [6] did not specify the temperature at which their experiments were performed, so we assumed a typical room temperature of 22 °C. The conductivity of 100 mM KCl is $1.298\,\mathrm{S/m}$ at 25 °C [61], which we adjusted to $1.20\,\mathrm{S/m}$ at 22 °C, as described by Smith et al. [30]. Melikov et al. reported that the conductivity of their NMDG-glutamate solution was smaller than their KCl solution by a factor of 1.5 [6], or $0.80\,\mathrm{S/m}$ at the assumed 22 °C.

We examined the relationship between pore radius r_{p} and pore conductance g_{p} ($= 1/R_{\mathrm{p}}$) using the methods described above for calculating pore conductance and the solute properties of potassium, chloride, NMDG, and glutamate listed in Table 4.1. For the transmembrane voltage, we used $\Delta\phi_{\mathrm{m}} = 180\,\mathrm{mV}$. It is unclear from Melikov et al. [6] exactly what transmembrane voltage was used for the KCl and NMDG-glutamate comparison, but we took $\Delta\phi_{\mathrm{m}} = 180\,\mathrm{mV}$ to be most likely, as it was this transmembrane voltage that was used to present their histogram of conductance measurements for KCl (Fig. 5 of Ref. [6]). Additionally, the mean pore conductance in their histogram was consistent with the mean pore conductance reported for KCl in the main text.

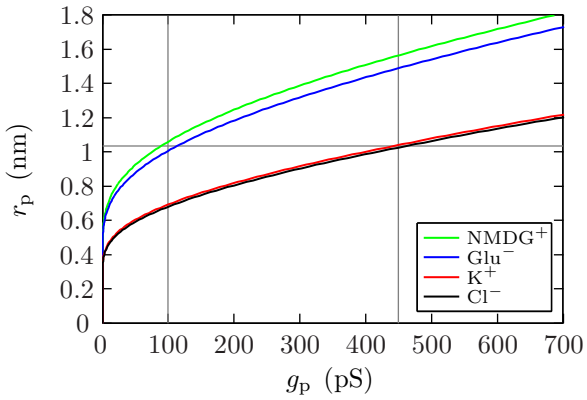

Figure 4.9: Relationship between pore conductance and pore radius for ions used in Melikov et al. [6]. That study investigated the average conductance of pores in BLM using solutions of KCl and NMDG-glutamate at transmembrane voltage $\Delta\phi_m$ we take to be 180 mV. This figure shows, for each species, the pore radius r_p corresponding to pore conductance g_p. In their important experiments, Melikov et al. [6] found that the mean pore conductance was 450 pS for the KCl solution and 100 pS for the NMDG-glutamate solution. As shown, the pore radius r_p corresponding to 450 pS for KCl is 1.03 nm, and the pore radius r_p corresponding to 100 pS for NMDG-glutamate is also 1.03 nm. That both electrolyte solutions, which comprise solute of very different shape and size, are consistent with the same average pore size $\overline{r}_p$ provides partial validation of the methods presented in this study and suggests that the average pore size $\overline{r}_p$ in BLM is indeed $\sim$1.03 nm.

Figure 4.9 shows the relationship between pore conductance g_p and pore radius r_p for all four solutes. In their experiments, Melikov et al. [6] found that the mean pore conductance was 450 pS for the KCl solution and 100 pS for the NMDG-glutamate solution. In our analysis, 450 pS was consistent with a mean pore radius of 1.041 nm for potassium and 1.026 nm for chloride, for an average of 1.03 nm for KCl. 100 pS was consistent with a mean pore radius of 1.060 nm for NMDG and 1.007 nm for glutamate, for the same average of 1.03 nm for NMDG-glutamate. Both solutions were therefore in fortuitous agreement, and the overall mean pore size we found was $\overline{r}_p = 1.03$ nm.

The analysis of Melikov et al. [6] provides important validation because the transport associated with two different solutions comprising solutes of very different shape and size are in excellent agreement (Fig. 4.9). And this would still be the case if some of our assumptions, such as temperature, were inaccurate because changes in the assumptions (e.g., temperature) will shift the pore

radius calculated for the two electrolyte solutions by a similar amount. However, these assumptions do have some effect on the mean pore radius that we calculated. A lower temperature would result in a slightly larger mean pore radius and a higher temperature would result in a slightly smaller mean pore radius because of the impact that temperature has on electrolyte conductivity. Similarly, if our assumptions about conductivity itself, which was not reported for either solution by Melikov et al., were inaccurate, this would also affect our calculations.

The value we determined for the pore radius of average conductance $\overline{r}_p$ (1.03 nm) based on our analysis of the Melikov et al. conductance measurements [6] provides insight into the approximate value of $r_{p,min}$, the pore radius at which the pore energy has a minimum when $\Delta\phi_m \approx 0\,V$ [60]. Accurate estimation of $r_{p,min}$ is important for both the interpretation of electroporation experiments and as an input into electroporation models, as it strongly influences the size selectivity (through hindrance) and charge selectivity (through partitioning) of minimum-size pores, which predominate both during short pulses [62] and following all pulses (post-pulse), when pores shrink to radius $r_{p,min}$. As a result, an accurate value of $r_{p,min}$ is critical for accurate modeling of molecular transport.

The value of $r_{p,min}$ is likely slightly smaller than the value of $\overline{r}_p$ for two reasons. First, the radius of the energy minimum increases slightly in going from the idealized value of $\Delta\phi_m = 0\,V$ (fully depolarized membrane) to the Melikov et al. experimental value of 180 mV [60]. Second, the pore density distribution is approximately centered at $r_{p,min}$, but because of the nonlinear relationship between pore radius r_p and pore conductance g_p (Fig. 4.9), the pores with $r_{p,min}+\Delta r_p$ will contribute slightly more significantly to the total conductance than pores with $r_{p,min} - \Delta r_p$, thereby slightly skewing the average toward $r_{p,min} + \Delta r_p$. (Here, Δr_p is a small distance with $\Delta r_p \ll r_{p,min}$.) Given these considerations, we estimate that $r_{p,min}$ is in the approximate range $0.9 - 1.0$ nm.

4.3.2 Estimation of Radius of Minimum-size Pores in Plasma Membrane

Much of the interest in electroporation centers on its ability to facilitate transmembrane transport of various solutes of interest, such as drugs and nucleic acids. One of the primary determinants

of the magnitude of transmembrane transport mediated by electroporation is the size of the pores through which solute passes. While experiments on BLM, such as those performed by Melikov et al. [6], provide fundamental insights into the basic mechanisms of electroporation, we must bear in mind that the properties of BLM differ from those of the plasma membrane (PM) of cells, which contain a wide variety of lipids and proteins [63, 64].

Given the importance of pore size in mediating transport through the PM, we sought a robust method of determining the size of pores in the PM, specifically the minimum-size pores present post-pulse. Note that the analysis of pore size above relied on the fact that Melikov et al. [6] performed their experiment with two different electrolyte solutions. This aspect of their experiment could not be repeated in a patch-clamped cell because, while the extracellular electrolyte can be set by the experimentalists, the intracellular electrolyte cannot. Nonetheless, the essence of our approach to estimating pore size relied on the fact that pores discriminate based on solute size. That is true of electrical drift-dominated transport, as in the Melikov et al. experiments [6], and it is also true of diffusion-dominated transport. We can exploit this size-discrimination to estimate the size of pores in the PM.

Here, we propose an approach for estimating the radius of minimum-size pores in the PM of cells by using established experimental techniques to measure differences in molecular transport between different types of fluorescent probe molecules. The set of experiments we propose is similar to those in Vernier et al. [65] in which they subjected cells to one or more very short pulses (4 ns, 8 MV/m) in pulsing medium with either propidium or yo-pro-1 and measured the relative change in intracellular fluorescence for each. They reported larger increases in relative intracellular fluorescence for yo-pro-1 than for propidium for the same number of pulses [65]. However, their measurement system was not calibrated (i.e., the measurement detection limits were not determined), and thus one cannot determine how much yo-pro-1 was transported into cells relative to propidium. Suzuki et al. [66], for example, stained DNA (in gel) with yo-pro-1, propidium, and similar dyes and found significant variation in the fluorescence of the DNA-bound dyes. The ap-

proach we propose requires a calibrated measurement system to allow determination of the number of fluorescent probe molecules taken up by cells. A number of previous studies have made these measurements using flow cytometry [8, 10, 16]. Temporal uptake information is not required.

As will become apparent in the analysis that follows, one can minimize the number of assumptions required through careful selection of the electroporating pulse and fluorescent probe molecules used.

It turns out that the 4 ns, 8 MV/m electrical pulse used by Vernier et al. [65] is ideal. The large magnitude ensures the creation of many pores ("supra-electroporation") [47, 67, 68], and the short duration ensures that essentially all transport occurs as a result of post-pulse diffusion, rather than electrical drift during the pulse [62]. This greatly simplifies the transport analysis. Additionally, post-pulse, pores can be assumed to be tightly distributed around the minimum pore size $r_{p,min}$ [60], and this too simplifies the analysis.

The choice of fluorescent probes is also important. By choosing probes that have some common features (e.g., charge), fewer assumptions are required in analyzing the relative transport of the probes. The use of the propidium and yo-pro-1 solute pair, as in Vernier et al. [65], is ideal for several reasons. First, both have a charge of +2, so the partition factors will be essentially the same. Second, propidium and yo-pro-1 are both intercalating dyes [69], which means that they bind tightly to intracellular DNA (and indeed, it is the bound dye that fluoresces strongly). As a result, the intracellular concentration γ_i of free (unbound) dye can reasonably be assumed $\gamma_i \approx 0\,\text{molecules/m}^3$, which simplifies the analysis. Third, while propidium and yo-pro-1 are otherwise similar (e.g., in charge), they differ in size, and thus differences in the transport of propidium and yo-pro-1 can attributed primarily to differences in hindrance. (The difference in their diffusivities is also a factor, but a much more minor one.) Moreover, though differing, both propidium and yo-pro-1 have sizes approaching that expected for a minimum-size pores (e.g., 0.6 – 1.0 nm reported by Glaser et al. [3]). For these reasons, the hindrance factors for the two molecules should

be highly nonlinear and different over the plausible size range of minimum-size pores, thereby resulting in high sensitivity.

Post-pulse, the transmembrane voltage $\Delta\phi_m \approx 0\,\mathrm{V}$, and the electrodiffusion equation (Eq. 4.1) reduces to simple diffusion. Thus, given the considerations above, the instantaneous post-pulse flux $J_s(t)$ of solute into a cell is

$$J_s(t) = D_s\left(\frac{\gamma_e}{d_m}\right)\pi r_{p,min}^2\,\hat{H}(r_s, l_s, r_{p,min})\,K(z_{s,p}, r_{p,min}, 0)\,N(t), \tag{4.30}$$

where D_s is the solute diffusivity, γ_e is the extracellular concentration of solute, d_m is the membrane thickness, $r_{p,min}$ is the minimum-size pore radius, $\hat{H}(r_s, l_s, r_{p,min})$ is the hindrance factor for the solute (of radius r_s and length l_s) at radius $r_{p,min}$, $K(z_{s,p}, r_{p,min}, 0)$ is the partition factor for the solute (of charge $z_{s,p}$ with $\Delta\phi_p \approx 0\,\mathrm{V}$ at radius $r_{p,min}$), and $N(t)$ is the pore density (pores/m^2) at time t. Equation 4.30 will hold for both propidium and yo-pro-1.

Denoting variables specific to yo-pro-1 with "yo" and variables specific to propidium with "pro" and noting that $K(z_{yo,p}, r_{p,min}, 0) = K(z_{pro,p}, r_{p,min}, 0)$, the instantaneous flux of yo-pro-1 $J_{yo}(t)$ relative to the instantaneous flux of propidium $J_{pro}(t)$ is

$$\frac{J_{yo}(t)}{J_{pro}(t)} = \frac{D_{yo}\left(\frac{\gamma_{e,yo}}{d_m}\right)\pi r_{p,min}^2\,\hat{H}_{yo}(r_{p,min})\,K(z_{yo,p}, r_{p,min}, 0)\,N(t)}{D_{pro}\left(\frac{\gamma_{e,pro}}{d_m}\right)\pi r_{p,min}^2\,\hat{H}_{pro}(r_{p,min})\,K(z_{pro,p}, r_{p,min}, 0)\,N(t)} = \frac{\gamma_{e,yo}\,D_{yo}\,\hat{H}_{yo}(r_{p,min})}{\gamma_{e,pro}\,D_{pro}\,\hat{H}_{pro}(r_{p,min})}. \tag{4.31}$$

Here, $\hat{H}_{yo}(r_{p,min}) \equiv \hat{H}(r_{yo}, l_{yo}, r_{p,min})$ and $\hat{H}_{pro}(r_{p,min}) \equiv \hat{H}(r_{pro}, l_{pro}, r_{p,min})$.

Note that the ratio of the fluxes in Eq. 4.31 is independent of time. Therefore, the ratio of the total transport of yo-pro-1 to the total transport of propidium is the same as the ratio of their instantaneous fluxes. Similarly, the ratio of the final intracellular concentration of bound yo-pro-1 $\hat{\gamma}_{i,yo}$ to the final intracellular concentration of bound propidium $\hat{\gamma}_{i,pro}$ is also the same as the ratio of

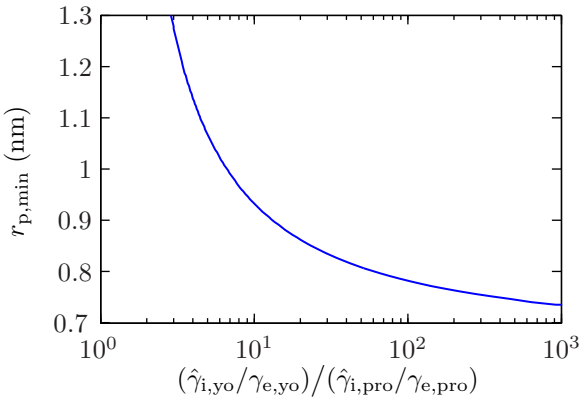

Figure 4.10: Relationship between pore radius and relative transport of yo-pro-1 and propidium. The plot shows the ratio of (bound) intracellular yo-pro-1 concentration $\hat{\gamma}_{i,yo}$ (normalized by extracellular yo-pro-1 concentration $\gamma_{e,yo}$) to (bound) intracellular propidium concentration $\hat{\gamma}_{i,pro}$ (normalized by extracellular propidium concentration $\gamma_{e,pro}$) plotted against $r_{p,min}$. For very short (nanosecond time scale) pulses, essentially all transport through pores occurs post-pulse through minimum-size pores of radius $r_{p,min}$. The value of $r_{p,min}$ can be determined by measuring the transport ratio of yo-pro-1 to propidium because the relative transport of these species is related by the relative values of their hindrance factors $\hat{H}(r_{p,min})$, which are functions of $r_{p,min}$.

the instantaneous fluxes:

$$\frac{\hat{\gamma}_{i,yo}}{\hat{\gamma}_{i,pro}} = \frac{\gamma_{e,yo}\, D_{yo}\, \hat{H}_{yo}(r_{p,min})}{\gamma_{e,pro}\, D_{pro}\, \hat{H}_{pro}(r_{p,min})}. \tag{4.32}$$

If the final intracellular concentrations of bound yo-pro-1 and propidium are normalized by their extracellular concentrations, then the ratio of their normalized transported is purely a function of their diffusivity and hindrance factors:

$$\frac{\hat{\gamma}_{i,yo}/\gamma_{e,yo}}{\hat{\gamma}_{i,pro}/\gamma_{e,pro}} = \frac{D_{yo}\, \hat{H}_{yo}(r_{p,min})}{D_{pro}\, \hat{H}_{pro}(r_{p,min})}. \tag{4.33}$$

Using the diffusivities of yo-pro-1 and propidium (Table 4.1) and the hindrance equation for cylindrical solute (Eq. 4.16) and its dependence on pore radius, the ratio of yo-pro-1 to propidium transport can be related to the minimum-size pore radius, as shown in Fig. 4.10.

Note that we would arrive at the same transport ratio (Eq. 4.33) even if we did not assume that post-pulse transport occurs purely by diffusion. The reason is that the drift flux (Eq. 4.1) through

pores, like the diffusive flux, is proportional to $D_s\gamma_e\hat{H}KN(t)\pi r_{p,min}^2/d_m$, and thus the same factors would drop out of the transport ratio. (Drift is also proportional to z_s, but yo-pro-1 and propidium have the z_s, and thus z_s would also drop out of the transport ratio.) Thus, even if junction potentials or a slowly recovering resting potential are non-zero, our analysis still holds.

While it is interesting that the transport ratio (Eq. 4.33) can be expressed so simply in terms of diffusivity and hindrance, in some sense it is not surprising. In the model presented here, the transport properties of a solute are fully characterized by its diffusivity, size, and charge, with the size determining the hindrance factor and the charge determining the partition factor. Because yo-pro-1 and propidium have the same charge (and therefore partition factor), the only characteristics that differentiate yo-pro-1 and propidium are their diffusivity and size (and therefore hindrance factor). Thus, it is these quantities that determine the relative transport of the two solutes.

Importantly, the relationship between the transport and ratio and the minimum-size pore radius $r_{p,min}$ is very nonlinear (Fig. 4.10). Thus, the proposed experiment allows estimation of $r_{p,min}$ with excellent sensitivity. For example, a yo-pro-1 to propidium transport ratio of 5 would correspond to $r_{p,min} = 1.07\,\text{nm}$, and a ratio of 10 would correspond to $r_{p,min} = 0.93\,\text{nm}$. If $r_{p,min}$ were 1.03 nm, as we estimated based on Melikov et al., then we would expect the yo-pro-1 to propidium transport ratio to be 5.8.

Here, we considered the fluorescent probe pair yo-pro-1 and propidium. However, there are other such sets that one could use and, indeed, repeating the proposed experiment with multiple sets would enable calculation of $r_{p,min}$ with greater confidence. Some specific sets, chosen such that the probes have the same charge (and therefore partition factor), include Lucifer Yellow and Alexa 594 (-2); Alexa 488 and Alexa 546 (-3); and Alexa 350, Atto 666, Cy5, and ethidium ($+1$). Probes with different charges from one another could also be used, but their differing partition factors would have to be accounted for in because they would not drop out in simplifying Eq. 4.31.

4.4 Conclusions

We have motivated and described methods for estimating quantities needed in models of membrane and cell electroporation. Although we presented several topics, we emphasized the effect that the hindrance factor H and partition factor K have on ionic and molecular transport through lipidic pores. The impact of these factors is particularly significant when the size of the solute and pore are similar and, in the case of the partition factor, when the solute charge is large.

Together, hindrance and partitioning constrain the size and charge of significantly participating solutes, both small and large. This has clear implications for electroporation-mediated transport. Longer duration pulses that have conventionally been used for electroporation provide sufficient time for some pores to expand to well beyond the minimum-size pore radius $r_{\mathrm{p,min}} \approx 0.8\,\mathrm{nm}$, and thus these pulses result in transport of large and highly charged solutes. In contrast, nanosecond duration pulses do not provide sufficient time for pores to expand much beyond $r_{\mathrm{p,min}}$, and thus these pulses result in significant transport small and minimally charged solute (e.g., monovalent ions) only.

Thus, hindrance and partitioning are both important to quantitative understanding of solute transport during and after pulsing.

References

[1] Abidor, I.G., Arakelyan, V.B., Chernomordik, L.V., Chizmadzhev, Y.A., Pastushenko, V.F., and Tarasevich, M.R. Electric breakdown of bilayer lipid-membranes I. Main experimental facts and their qualitative discussion. *Bioelectroch Bioener*, 6(1):37–52, 1979.

[2] Chernomordik, L.V., Sukharev, S.I., Popov, S.V., Pastushenko, V.F., Sokirko, A.V., Abidor, I.G., and Chizmadzhev, Y.A. The electrical breakdown of cell and lipid membranes: The similarity of phenomenologies. *Biochim Biophys Acta*, 902(3):360–73, 1987.

[3] Glaser, R.W., Leikin, S.L., Chernomordik, L.V., Pastushenko, V.F., and Sokirko, A.I. Reversible electrical breakdown of lipid bilayers: Formation and evolution of pores. *Biochim Biophys Acta*, 940(2):275–287, 1988.

[4] Hibino, M., Shigemori, M., Itoh, H., Nagayama, K., and Kinosita, K.J. Membrane conductance of

an electroporated cell analyzed by submicrosecond imaging of transmembrane potential. *Biophys J*, 59(1):209–220, 1991.

[5] Hibino, M., Itoh, H., and Kinosita, K. Time courses of cell electroporation as revealed by submicrosecond imaging of transmembrane potential. *Biophys J*, 64(6):1789–1800, 1993.

[6] Melikov, K.C., Frolov, V.A., Shcherbakov, A., Samsonov, A.V., Chizmadzhev, Y.A., and Chernomordik, L.V. Voltage-induced nonconductive pre-pores and metastable single pores in unmodified planar lipid bilayer. *Biophys J*, 80(4):1829–1836, 2001.

[7] Frey, W., White, J.A., Price, R.O., Blackmore, P.F., Joshi, R.P., Nuccitelli, R., Beebe, S.J., Schoenbach, K.H., and Kolb, J.F. Plasma membrane voltage changes during nanosecond pulsed electric field exposure. *Biophys J*, 90:3608–3615, 2006.

[8] Bartoletti, D.C., Harrison, G.I., and Weaver, J.C. The number of molecules taken up by electroporated cells: Quantitative determination. *FEBS Lett*, 256(1-2):4–10, 1989.

[9] Tekle, E., Astumian, R.D., and Chock, P.B. Electro-permeabilization of cell membranes: Effect of the resting membrane potential. *Biochem Bioph Res Co*, 172(1):282–7, 1990.

[10] Prausnitz, M.R., Lau, B.S., Milano, C.D., Conner, S., Langer, R., and Weaver, J.C. A quantitative study of electroporation showing a plateau in net molecular-transport. *Biophys J*, 65(1):414–422, 1993.

[11] Prausnitz, M.R., Milano, C.D., Gimm, J.A., Langer, R., and Weaver, J.C. Quantitative study of molecular-transport due to electroporation – Uptake of bovine serum-albumin by erythrocyte-ghosts. *Biophys J*, 66(5):1522–1530, 1994.

[12] Djuzenova, C.S., Zimmermann, U., Frank, H., Sukhorukov, V.L., Richter, E., and Fuhr, G. Effect of medium conductivity and composition on the uptake of propidium iodide into electropermeabilized myeloma cells. *Biochim Biophys Acta*, 1284(2):143–52, 1996.

[13] Neumann, E., Kakorin, S., Tsoneva, I., Nikolova, B., and Tomov, T. Calcium-mediated DNA adsorption to yeast cells and kinetics of cell transformation by electroporation. *Biophys J*, 71(2):868–77, 1996.

[14] Neumann, E., Toensing, K., Kakorin, S., Budde, P., and Frey, J. Mechanism of electroporative dye uptake by mouse B cells. *Biophys J*, 74(1):98–108, 1998.

[15] Neumann, E., Kakorin, S., and Toensing, K. Fundamentals of electroporative delivery of drugs and genes. *Bioelectroch Bioener*, 48(1):3–16, 1999.

[16] Canatella, P.J., Karr, J.F., Petros, J.A., and Prausnitz, M.R. Quantitative study of electroporation-mediated molecular uptake and cell viability. *Biophys J*, 80(2):755–764, 2001.

[17] Puc, M., Kotnik, T., Mir, L.M., and Miklavcic, D. Quantitative model of small molecules uptake after in vitro cell electropermeabilization. *Bioelectrochemistry*, 60(1-2):1–10, 2003.

[18] Zaharoff, D.A., Henshaw, J.W., Mossop, B., and Yuan, F. Mechanistic analysis of electroporation-induced cellular uptake of macromolecules. *Exp Biol Med*, 233(1):94–105, 2008.

[19] Bird, R.B., Stewart, W.E., and Lightfoot, E.N. *Transport Phenomena*. Wiley, New York, 1960.

[20] Katchalsky, A. and Curran, P.F. *Nonequilibrium Thermodynamics in Biophysics*. Harvard University Press, Cambridge, 1965.

[21] Crank, J. *The Mathematics Of Diffusion*. Oxford University Press, Oxford, 1975.

[22] Dunn III, W.J., Block, J.H., and Pearlman, R.S. *Partition coefficient: Determination and estimation*. Pergamon Press, New York, 1986.

[23] Bronaugh, R.L. and Maibach, H.I., editors. *Percutaneous absorption: Mechanisms-methodology-drug delivery*. Marcel Dekker, New York, 1989.

[24] Deen, W.M. *Analysis of Transport Phenomena*. Oxford University Press, Oxford, 1998.

[25] Grodzinsky, A.J. *Fields, Forces, and Flows in Biological Systems*. Garland Science, London, 2011.

[26] Kalia, Y.N., Naik, A., Garrison, J., and Guy, R.H. Iontophoretic drug delivery. *Adv Drug Deliv Rev*, 56(5):619–58, 2004.

[27] Nugroho, A.K., Della Pasqua, O., Danhof, M., and Bouwstra, J.A. Compartmental modeling of transdermal iontophoretic transport: I. In vitro model derivation and application. *Pharm Res*, 21(11):1974–84, 2004.

[28] Nugroho, A.K., Della-Pasqua, O., Danhof, M., and Bouwstra, J.A. Compartmental modeling of transdermal iontophoretic transport II: In vivo model derivation and application. *Pharm Res*, 22(3):335–46, 2005.

[29] Güngör, S., Delgado-Charro, M.B., Ruiz-Perez, B., Schubert, W., Isom, P., Moslemy, P., Patane, M.A., and Guy, R.H. Trans-scleral iontophoretic delivery of low molecular weight therapeutics. *J Control Release*, 147(2):225–31, 2010.

[30] Smith, K.C. and Weaver, J.C. Compilation and computation of the size, charge, and diffusivity of fluorescent dyes and other small molecules (in preparation).

[31] Smith, K.C. and Weaver, J.C. Electrodiffusion of molecules in aqueous media: A robust, discretized description for electroporation and other transport phenomena (in preparation).

[32] Litster, J.D. Stability of lipid bilayers and red blood-cell membranes. *Phys Lett A*, A 53(3):193–194, 1975.

[33] Neumann, E., Schaefer-Ridder, M., Wang, Y., and Hofschneider, P.H. Gene transfer into mouse lyoma cells by electroporation in high electric fields. *EMBO J*, 1(7):841–5, 1982.

[34] Tieleman, D.P., Leontiadou, H., Mark, A.E., and Marrink, S.J. Simulation of pore formation in lipid bilayers by mechanical stress and electric fields. *J Am Chem Soc*, 125(21):6382–6383, 2003.

[35] Tieleman, D.P. The molecular basis of electroporation. *BMC Biochem*, 5(10), 2004.

[36] Vernier, P.T., Ziegler, M.J., Sun, Y.H., Chang, W.V., Gundersen, M.A., and Tieleman, D.P. Nanopore formation and phosphatidylserine externalization in a phospholipid bilayer at high transmembrane potential. *J Am Chem Soc*, 128:6288–6289, 2006.

[37] Wohlert, J., den Otter, W.K., Edholm, O., and Briels, W.J. Free energy of a trans-membrane pore calculated from atomistic molecular dynamics simulations. *J Chem Phys*, 124, 2006.

[38] Leontiadou, H., Mark, A.E., and Marrink, S.J. Ion transport across transmembrane pores. *Biophys J*, 92(12):4209–4215, 2007.

[39] Bockmann, R.A., de Groot, B.L., Kakorin, S., Neumann, E., and Grubmuller, H. Kinetics, statistics, and energetics of lipid membrane electroporation studied by molecular dynamics simulations. *Biophys J*, 95(4):1837–1850, 2008.

[40] Neu, J.C., Smith, K.C., and Krassowska, W. Electrical energy required to form large conducting pores. *Bioelectrochemistry*, 60(1–2):107–114, 2003.

[41] Pettersen, E.F., Goddard, T.D., Huang, C.C., Couch, G.S., Greenblatt, D.M., Meng, E.C., and Ferrin, T.E. UCSF Chimera–A visualization system for exploratory research and analysis. *J Comput Chem*, 25(13):1605–12, 2004.

[42] Gordon, J.C., Myers, J.B., Folta, T., Shoja, V., Heath, L.S., and Onufriev, A. H++: A server for estimating pKas and adding missing hydrogens to macromolecules. *Nucleic Acids Res*, 33(Web Server issue):W368–71, 2005.

[43] Anandakrishnan, R. and Onufriev, A. Analysis of basic clustering algorithms for numerical estimation of statistical averages in biomolecules. *J Comput Biol*, 15(2):165–84, 2008.

[44] Bockris, J.O. and Reddy, A.K.N. *Modern Electrochemistry, Vol. 1*. Plenum, New York, 1970.

[45] Newman, J. Resistance for flow of current to a disk. *J Electrochem Soc*, 113(5):501–502, 1966.

[46] Hall, J.E. Access resistance of a small circular pore. *J Gen Physiol*, 66(4):531–2, 1975.

[47] Vasilkoski, Z., Esser, A.T., Gowrishankar, T.R., and Weaver, J.C. Membrane electroporation: The absolute rate equation and nanosecond time scale pore creation. *Phys Rev E*, 74(2), 2006.

[48] Renkin, E.M. Filtration, diffusion, and molecular sieving through porous cellulose membranes. *J Gen Physiol*, 38(2):225–43, 1954.

[49] Beck, R.E. and Schultz, J.S. Hindrance of solute diffusion within membranes as measured with microporous membranes of known pore geometry. *Biochim Biophys Acta*, 255(1):273–303, 1972.

[50] Deen, W.M. Hindered transport of large molecules in liquid-filled pores. *AIChE J*, 33(9):1409–1425, 1987.

[51] Silva, V., Pradanos, P., Palacio, L., and Hernandez, A. Alternative pore hindrance factors: What one should be used for nanofiltration modelization? *Desalination*, 245(1-3):606–613, 2009.

[52] Bungay, P.M. and Brenner, H. The motion of a closely-fitting sphere in a fluid-filled tube. *Int J of Multiphas Flow*, 1(1):25–56, 1973.

[53] Smith, K.C., Neu, J.C., and Krassowska, W. Model of creation and evolution of stable electropores for DNA delivery. *Biophys J*, 86(5):2813–2826, 2004.

[54] Krassowska, W. and Filev, P.D. Modeling electroporation in a single cell. *Biophys J*, 92(2):404–417, 2007.

[55] Esser, A.T., Smith, K.C., Gowrishankar, T.R., Vasilkoski, Z., and Weaver, J.C. Mechanisms for the intracellular manipulation of organelles by conventional electroporation. *Biophys J*, 98(11):2506–14, 2010.

[56] Parsegian, A. Energy of an ion crossing a low dielectric membrane: Solutions to four relevant electrostatic problems. *Nature*, 221(5183):844–6, 1969.

[57] Parsegian, V.A. Ion-membrane interactions as structural forces. *Ann N Y Acad Sci*, 264:161–71, 1975.

[58] Kuyucak, S., Hoyles, M., and Chung, S.H. Analytical solutions of Poisson's equation for realistic geometrical shapes of membrane ion channels. *Biophys J*, 74(1):22–36, 1998.

[59] Barnett, A. and Weaver, J.C. Electroporation – A unified, quantitative theory of reversible electrical breakdown and mechanical rupture in artificial planar bilayer-membranes. *Bioelectroch Bioener*, 25(2):163–182, 1991.

[60] Neu, J.C. and Krassowska, W. Asymptotic model of electroporation. *Phys Rev E*, 59(3):3471–3482, 1999.

[61] Lide, D.R., editor. *CRC Handbook of Chemistry and Physics*. CRC Press, Boca Raton, FL, 2005.

[62] Smith, K.C. and Weaver, J.C. Transmembrane molecular transport during versus after nanosecond electric pulses (in preparation).

[63] Engelman, D.M. Membranes are more mosaic than fluid. *Nature*, 438(7068):578–580, 2005.

[64] Jacobson, K., Mouritsen, O.G., and Anderson, R.G.W. Lipid rafts: At a crossroad between cell biology and physics. *Nat Cell Biol*, 9(1):7–14, 2007.

[65] Vernier, P.T., Sun, Y.H., and Gundersen, M.A. Nanoelectropulse-driven membrane perturbation and small molecule permeabilization. *BMC Cell Biol*, 7:37, 2006.

[66] Suzuki, T., Fujikura, K., Higashiyama, T., and Takata, K. DNA staining for fluorescence and laser confocal microscopy. *J Histochem Cytochem*, 45(1):49–53, 1997.

[67] Gowrishankar, T.R., Esser, A.T., Vasilkoski, Z., Smith, K.C., and Weaver, J.C. Microdosimetry for conventional and supra-electroporation in cells with organelles. *Biochem Bioph Res Co*, 341:1266–1276, 2006.

[68] Smith, K.C. and Weaver, J.C. Active mechanisms are needed to describe cell responses to submicrosecond, megavolt-per-meter pulses: Cell models for ultrashort pulses. *Biophys J*, 95(4):1547–1563, 2008.

[69] Wilson, W.D., Krishnamoorthy, C.R., Wang, Y.H., and Smith, J.C. Mechanism of intercalation: Ion effects on the equilibrium and kinetic constants for the interaction of propidium and ethidium with DNA. *Biopolymers*, 24(10):1941–61, 1985.

Chapter 5

The Energy Landscape and Dynamics of Electropores

Abstract

Electroporation is a valuable tool for diverse applications of biological and clinical significance. The appeal of electroporation is that it provides an essentially universal method of facilitating transmembrane transport of a variety of solutes, particularly bioactive molecules (e.g., nucleic acids and drugs). The amount of electroporation-mediated transport (molecular dose) that results from a particular pulsed electric field depends strongly on the number and size of the pores that develop in the membrane. Thus, to understand and interpret electroporation experiments and to optimize electroporation-based applications, it is necessary to first understand the creation and subsequent evolution of pores that result from a particular pulsed electric field. Accordingly, here we describe the pore energy landscape and a discretized model of dynamic pores. First, we provide quantitative descriptions of the total pore energy and its four interaction energies: steric repulsion of lipid head groups, edge energy, membrane tension, and electrical energy. Second, we show that the evolution of pores in radius space is analogous to electrodiffusive transport in physical space. We utilize this analogy to adapt a description of electrodiffusion to the characterization of pore evolution in response to the gradients in pore density and pore energy. Third, we use the resulting model to generate a description of pore dynamics. This in turn provides a straightforward means of understanding the apparently complex results generated by models of electroporation with dynamic pores. Finally, as partial validation, we relate the pore conductance measurements of Melikov et al. (Biophys. J., 80:1829–1836, 2001) to pore radius. This yields insights into the pore energy landscape and approximate values of the important electroporation model parameters r_*, the radius of hydrophilic pore creation and destruction, and r_m, the radius of minimum energy at zero transmembrane voltage.

5.1 Introduction

Electroporation is widely used to deliver bioactive molecules, such as nucleic acids [1–19] and drugs [20–29], into cells. It is an attractive approach to delivery because it provides an operationally simple means of delivering a variety of solutes. Yet, despite the widespread use of electroporation, there is little fundamental understanding of how to optimally deliver a particular solute in particular cell system. This is evidenced by the sheer number of studies that have sought optimized electroporation protocols for specific applications [12, 13, 15, 19, 30–42].

Transport through pores is expected to be strongly dependent on the size and number of pores and the size and charge of the transported solute [43]. Thus, to understand, interpret, and optimize electroporation experiments and applications on a fundamental level, we must first understand the creation, evolution, and destruction of pores. To that end, our objective in this study is to develop a quantitative, mechanistic description of pore dynamics.

In a series of previous papers [43–45], we investigated fundamental biophysical topics that may be considered "ingredients" for increasingly comprehensive, mechanistic models of electroporation with concomitant molecular transport. First, we described [44] how important transport parameters of ionic and molecular solutes, specifically size, charge, and diffusivity, may be estimated in silico. Second, we reported a general method [45] of describing electrodiffusive transport in discretized 1-D systems, noting that that higher dimension models can be constructed through the assignment of 1-D elemental models in a discretized 2-D or 3-D system [46, 47]. Third, we showed [43] how ionic and molecular properties affect transport through small (minimum-size and somewhat expanded), lipidic pores. In particular, we showed how steric hindrance and partitioning strongly influence transport through pores relative to bulk electrolyte. This influence is especially significant when the solute is approximately the same size as the pore or when the solute is highly charged.

In this study, the final in this series of basic methods-oriented papers, we consider the energetics and dynamics of pores. Our previous work on electrodiffusion [45] and pore conductance [43] have direct relevance here. We show that electrodiffusion is directly related (mathematically equivalent) to transport of pores in pore radius space. This is equivalent to a quantitative description of the evolution of heterogeneous pore populations. We use our description of pore conductance to relate the pore conductance measurements of Melikov et al. [48] to pore radius and then use this data to provide partial validation of our description of the pore energy landscape. At the outset, we emphasize that this description builds on the work of many others [49–56].

5.2 Methods

5.2.1 Pore Geometry

Hydrophilic lipidic pores have long been assumed to be toroidal in shape [49, 51, 52, 57], with the head groups of the lipid molecules rotated into the interior of the pore wall to minimize exposure of the hydrophobic lipid tails to water molecules. Molecular dynamics simulations over the past decade have provided further evidence of the toroidal shape of pores [58–63].

In the analysis here, we generally assume that pores are indeed toroidal in shape (Fig. 5.1A). However, we find it convenient to sometimes approximate pore shape as trapezoidal (Fig. 5.1B). While some analyses have been based on toroidal pores, such as the electrical force that drives pore expansion [54], others have been based on trapezoidal pores, such as the Born energy (energy to place a charge within a pore) [51, 52]. The trapezoidal pore approximation provides relative simplicity, clarity, and ease of computation while deviating only slightly from a toroidal pore. Further, molecular dynamics simulations show that pore geometry fluctuates and is variable. As is apparent in Fig. 5.1, the differences between the toroidal and trapezoidal pores are minor.

For both toroidal and trapezoidal pores, the pore radius r_p refers to that of the centermost position along the axis of the pore (Fig. 5.1). We will refer to this central region as the “internal” region of the pore, and the entrance and exit regions (on either side of the internal region of the pore) as

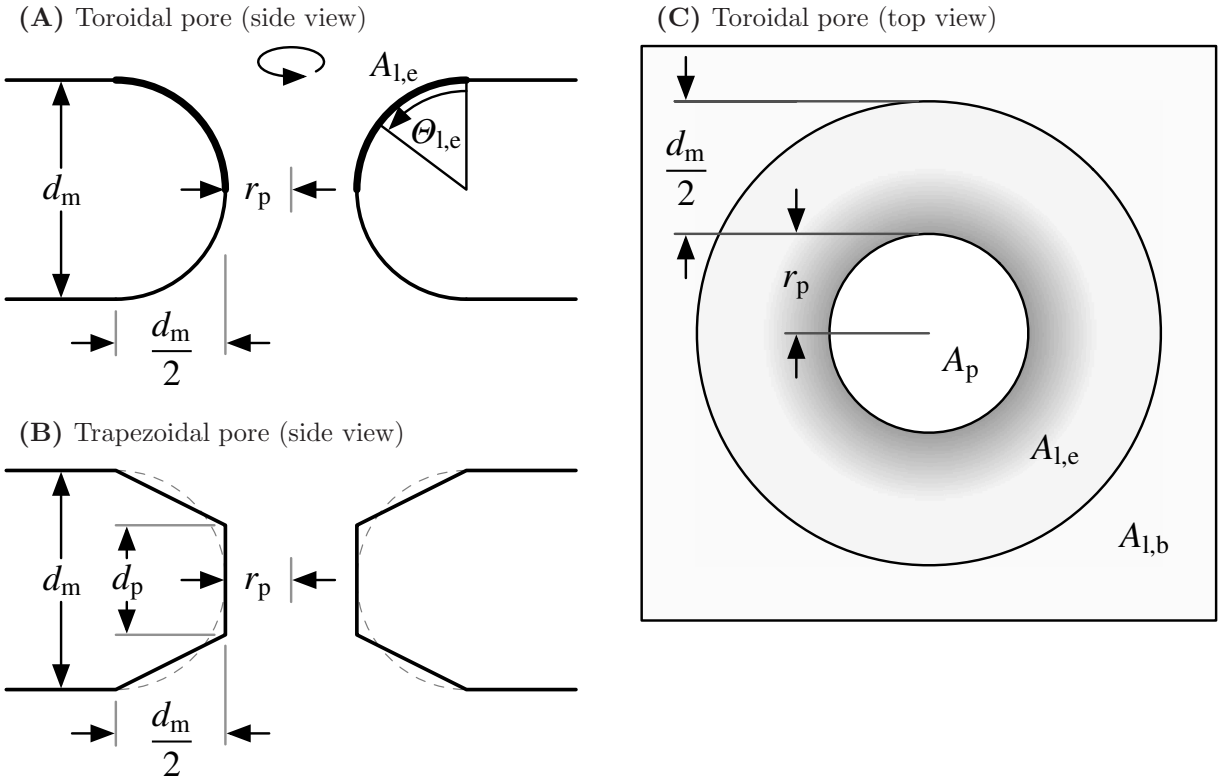

Figure 5.1: Pore shape and size. **(A)** and **(C)** Toroidal approximations to pore shape. **(B)** Trapezoidal approximation to pore shape. Both pore conformations have radius r_p and lie within a membrane of thickness $d_m = 5\,\text{nm}$. The "internal" region of the trapezoidal pore has thickness $d_p = d_m/2 = 2.5\,\text{nm}$, and each "vestibule" on either side of the "internal region" has thickness $d_p/4 = 1.25\,\text{nm}$. The value of d_p was chosen such that the geometry of the trapezoidal pore closely approximated the geometry of the toroidal pore. The *thin dashed line* shows the toroidal shape, as in **(A)**. **(C)** The total area of lipid A_l (associated with each side) of the membrane is the sum of the area of the bilayer region $A_{l,b}$ and the pore edge region $A_{l,e}$. The aqueous area of the pore is $A_p = \pi r_p^2$.

the "vestibules" or "vestibular" regions of the pore. The membrane has thickness $d_m = 5\,\text{nm}$ and internal region of the pore has a thickness $d_p = d_m/2 = 2.5\,\text{nm}$. The value of d_p was chosen such that the geometry of the trapezoidal pore closely approximates the geometry of the toroidal pore.

We refer to the relatively large region of the pore-membrane system for which lipid molecules are rotated into the pore as the "edge" of a pore (Fig. 5.1). The pore edge includes all lipid within a distance $r_p + d_m/2$ of the axis of a pore. We refer to the lipid outside the edge as "bilayer". The bilayer includes all lipid that is a distance greater than $r_p + d_m/2$ from the axis of a pore.

5.2.2 Pore and Lipid Area

To our knowledge, in previous publications, a pore of radius r_p is assumed to reduce the area of lipid A_l (associated with each side of the membrane) by an amount $A_p = \pi r_p^2$, with A_p regarded as the aqueous area of a pore (Fig. 5.1C). However, it is clear from Fig. 5.1 that this does not properly account for the area $A_{l,e}$ of lipid in the edge of the pore. Assuming that a pore reduces the lipid area by an amount A_p is equivalent to assuming that a pore is cylindrical in shape. If so, there would be no lipid head groups lining the pore interior, and this is inconsistent with the view that pores are approximately toroidal in shape, or at least lined by lipid head groups so as to reduce the exposure of the lipid tails to water.

Effect of a Single Pore on Lipid Area

Consider the effect that adding a single pore to a membrane has on the total lipid area A_l in a system with fixed area A. As shown in Fig. 5.1C, all lipid contributes to either the area $A_{l,b}$ of the bilayer region or area $A_{l,e}$ of the pore edge region. Thus, the total lipid area A_l is simply the sum of the two:

$$A_l = A_{l,b} + A_{l,e}. \tag{5.1}$$

Initially, the membrane is intact (no pores). Therefore $A_l = A$, $A_{l,b} = A$, and $A_{l,e} = 0$. (Note, that A_l, $A_{l,b}$, and $A_{l,e}$ all refer to the area associated with one side (leaflet) of the bilayer membrane.)

Introducing a pore with radius r_p has two effects: it decreases $A_{l,b}$ and it increases $A_{l,e}$. The combination of these effects determines the net change A_l (Eq. 5.1). Let us consider each effect in turn.

First, the introduction of the pore reduces the area of the bilayer to

$$A_{l,b} = A - \pi\left(r_p + \frac{d_m}{2}\right)^2. \tag{5.2}$$

This is clear upon inspection of Fig. 5.1C.

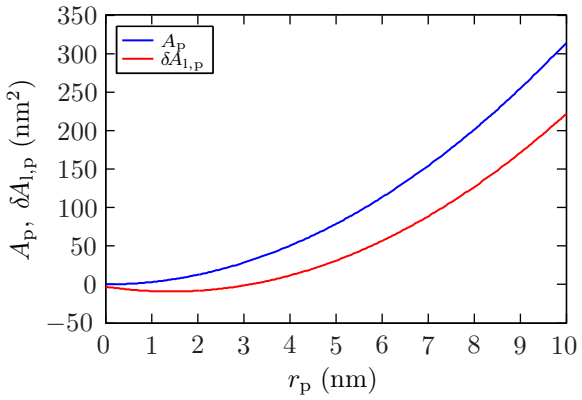

Figure 5.2: Aqueous vs. lipid reduction area of pores. The pore aqueous area A_p and lipid reduction area $\delta A_{l,p}$ are plotted against pore radius r_p. A_p describes the area of the fluid-filled region in the center of a pore, while $\delta A_{l,p}$ describes the net change in lipid area A_l that results from the introduction of a toroidal pore of radius r_p. Though not apparent in the plot, in the limit $r_p \to \infty$, $A_p \approx \delta A_{l,p}$. However, for smaller pores, like those plotted here, A_p is significantly larger than $\delta A_{l,p}$. Indeed, for $r_p < 3.14\,\text{nm}$, $\delta A_{l,p} < 0$, which implies that small pores actually increase the total lipid area A_l.

Second, the introduction of the pore increases the area of the pore edge to

$$A_{l,e} = \pi^2 \left(\frac{d_m}{2}\right)\left(r_p + \frac{d_m}{2}\right) - 2\pi\left(\frac{d_m}{2}\right)^2. \tag{5.3}$$

This formula can be found through integration, as described in the *Appendix*.

Thus, the net reduction $\delta A_{l,p}$ in total lipid area A_l that results from the introduction of a single pore of radius r_p is

$$\delta A_{l,p}(r_p) = \pi\left(r_p + \frac{d_m}{2}\right)^2 - \pi^2\left(\frac{d_m}{2}\right)\left(r_p + \frac{d_m}{2}\right) + 2\pi\left(\frac{d_m}{2}\right)^2. \tag{5.4}$$

Figure 5.2 shows a comparison of the aqueous area $A_p(r_p)$ and lipid reduction area $\delta A_{l,p}(r_p)$ of pores. A_p exceeds $\delta A_{l,p}$ for all r_p, and the relative difference between the two is quite large for small pores.

Note that $A_p > 0$ for all $r_p > 0$, but $\delta A_{l,p} < 0$ for $r_p < 3.14\,\text{nm}$ and $\delta A_{l,p} > 0$ for $r_p > 3.14\,\text{nm}$ (for $d_m = 5\,\text{nm}$). In other words, small pores ($r_p < 3.14\,\text{nm}$) actually increase the total area of lipid A_l.

Table 5.1: Model Parameters

Symbol	Value	Description and Source
d_m	5 nm	Membrane thickness [52]
d_p	2.5 nm	Pore thickness (internal region) [43]
r_*	0.65 nm	Pore radius at local energy maximum*
r_m	0.98 nm	Pore radius at local energy minimum*
W_*	45 kT	Energy at local maximum [52]
W_m	28.341 kT	Energy at local minimum*
W_d	16.659 kT	Energy barrier to pore destruction*
B	1.47×10^{-19} J	Steric repulsion constant*
b	3.3965	Steric repulsion constant*
C	-5.2456×10^{-20} J	Steric repulsion constant*
γ	2.0×10^{-11} J/m	Pore line tension [64]
Γ	1×10^{-3} J/m^2	Membrane tension (BLM) [64]
Γ'	20×10^{-3} J/m^2	Hydrocarbon-water interface tension [55]
F_{max}	6.9×10^{-10} N/V^2	Maximum electric force for $\Delta\phi_m$ = 1 V [54]
r_h	0.95 nm	Electric force constant [54]
r_t	0.23 nm	Electric force constant [54]
D_p	5×10^{-14} m^2/s	Pore diffusion coefficient [64]
a	1×10^9 /(m^2 s)	Pore creation rate density [56]
β	20 kT/V^2	Pore creation constant [56]
f_{prot}	0	Membrane protein fraction (BLM)
τ_p	0.5 s	Pore resealing time constant*
T	295.15 K	Absolute temperature*
σ	1.20 S/m	Conductivity of electrolyte* (100 mM KCl at 22 °C)
r_s	0.175 nm	Radius of charge carrier* (KCl) [44]
n	0.25	Pore relative entrance length [43]

*Value selected or calculated as described in main text.

The slope of $A_{l,p}(r_p) < 0$ for $r_p < 1.43$ nm, and the slope of $A_{l,p}(r_p) > 0$ for $r_p > 1.43$ nm. This implies that the membrane tension will contribute to the contraction of small pores and expansion of larger pores.

Effect of a Distribution of Pores on Lipid Area

The effect that a distribution of pores has on the total lipid area A_l is the sum of the effect that each pore has on A_l. (We assume that pore edges cannot overlap.) Again, consider a membrane system with fixed area A. The membrane has a distribution of pores given by the pore density distribution $n(r_p)$ that describes the number of pores per unit area with radii between r_p and $r_p + dr_p$ [53]. Thus, the total number of pores in the system with radii between r_p and $r_p + dr_p$ is $An(r_p)dr_p$, and each of these pores contributes an amount $\delta A_{l,p}(r_p)$ (Eq. 5.4) to the reduction in lipid area. The net reduction $A_{l,p}$ in lipid area that results from the distribution of pores may be found by integrating over all r_p:

$$A_{l,p} = A \int_0^\infty \delta A_{l,p}(r_p)\, n(r_p)\, dr_p. \tag{5.5}$$

5.2.3 Pore Energy

The dynamic behavior of pores is determined by the transmembrane voltage-dependent pore energy landscape, as pores tend to expand or contract so as to minimize their free energy W. Figure 5.3 shows the energy landscape $W(r_p)$ of a pore with zero transmembrane voltage ($\Delta\phi_m$= 0 V) (Fig. 5.3A) and the equilibrium pore density $n(r_p)$ associated with this energy landscape (Fig. 5.3B). Pores created with radius $r_p < r_*$ are assumed to be short-lived, hydrophobic pores (full "water chains" in molecular dynamics studies) that are rapidly destroyed through thermal fluctuations in the membrane [49]. Pores created with radius $r_p > r_*$ are assumed to spontaneously transform from hydrophobic pores to metastable hydrophilic pores, with lipid head groups lining the pore edge (Fig. 5.1) [49]. This view of pore evolution is supported by recent molecular dynamics studies.

The critical radius r_*, at which $W(r_*) = W_*$ (Fig. 5.3A), is determined by the relative energy of hydrophobic pores $W_{phobic}(r_p)$ and hydrophilic pores $W_{philic}(r_p)$. Hydrophobic pores created with radius $r_p < r_*$ remain hydrophobic because $W_{phobic}(r_p) < W_{philic}(r_p)$. Hydrophobic pores created with radius $r_p > r_*$, spontaneously transform into hydrophilic pores because $W_{philic}(r_p) < W_{phobic}(r_p)$. Thus, (hydrophilic) pore creation requires that a pore overcome W_*, the energy barrier to pore creation.

The energy of hydrophilic pores has a minimum at $r_p = r_m$, at which $W(r_m) = W_m$ (Fig. 5.3A). (Note that the symbol $r_{p,min}$ is often used in place of r_m. Here, we use r_m for succinctness.) As a result, pores accumulate near r_m, thereby leading to a pore density distribution $n(r_p)$, as shown in Fig. 5.3B. Just as W_* is the energy barrier to pore creation, $W_d = W_* - W_m$ is the barrier to pore destruction.

The model presented here only explicitly describes the dynamics of hydrophilic pores ($r_p > r_*$) because hydrophobic pores are assumed to be very short-lived and nonconductive [49]. Nonetheless,

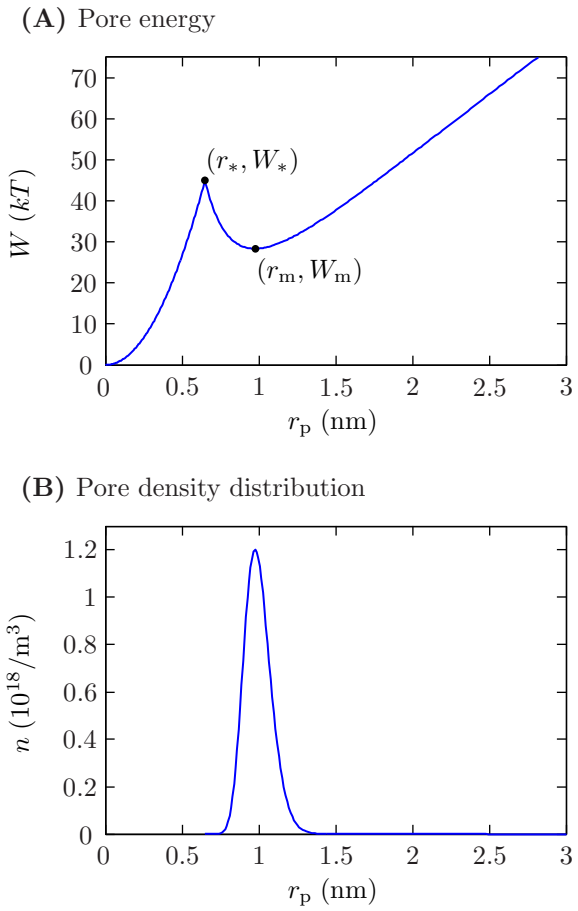

Figure 5.3: Pore energy landscape and pore density distribution. **(A)** The pore energy $W(r_\mathrm{p})$ at transmembrane voltage $\Delta\phi_\mathrm{m} = 0\,\mathrm{V}$ is plotted against pore radius r_p. Pores created with radius $r_\mathrm{p} < r_*$ are assumed to be short-lived, hydrophobic pores that are rapidly destroyed through thermal fluctuations in the membrane, while those created with $r_\mathrm{p} > r_*$ are assumed to spontaneously transform from hydrophobic pores to metastable hydrophilic pores. Thus, the critical radius r_*, which has energy W_*, is the minimum radius of hydrophilic pores. Pores tend to expand or contract so as to minimize their energy W. Therefore, newly created hydrophilic pores slide down the energy gradient and accumulate near the radius of minimum energy r_m, which has energy W_m. **(B)** The pore density distribution $n(r_\mathrm{p})$, which describes the number of pores per area per dr_p, associated with the pore energy in **(A)** is plotted against pore radius r_p. The distribution is centered at r_m, where the pore energy has its minimum $W = W_\mathrm{m}$. W_* is the energy barrier to pore creation, and $W_\mathrm{d} = W_* - W_\mathrm{m}$ is the barrier to pore destruction. In this study, $r_* = 0.65\,\mathrm{nm}$ and $r_\mathrm{m} = 0.98\,\mathrm{nm}$.

we include the approximate energy of hydrophobic pores [53] for completeness:

$$W_{\text{phobic}}(r_p) \approx W_* \left(\frac{r_p}{r_*}\right)^2 . \tag{5.6}$$

The energy of hydrophilic pores is the sum of several contributions (Fig. 5.4):

$$W(r_p, \Delta\phi_m) = W_{\text{steric}}(r_p) + W_{\text{edge}}(r_p) + W_{\text{surf}}(r_p) + W_{\text{elec}}(r_p, \Delta\phi_m). \tag{5.7}$$

Here, $W_{\text{steric}}(r_p)$ is the energy that results from the steric repulsion of lipid head groups, $W_{\text{edge}}(r_p)$ is the energy that results from the bending of lipid around the interior edge of a pore, $W_{\text{surf}}(r_p)$ is the interfacial energy of water contacting lipid molecules, and $W_{\text{elec}}(r_p, \Delta\phi_m)$ accounts for the energy that results from the force exerted on the pore edge by the electric field. In the following sections, we describe each of these energy contributions in depth.

Steric Repulsion Energy

The first contribution to the pore energy is the steric repulsion energy [52]:

$$W_{\text{steric}} = B\left(\frac{r_*}{r_p}\right)^b + C. \tag{5.8}$$

The mathematical form of this version of the steric repulsion energy term is not based on any basic physical insight, other than that the derivative of the term with respect to pore radius r_p should rapidly decrease to zero with increasing pore radius. It is primarily the decrease of the steric repulsion energy with pore radius and the increase of the edge energy with pore radius that determine the radius r_m of the energy minimum.

Neu and Krassowska [53] first introduced a similar term, $(C/r_p)^4$, in which C and the exponent were chosen such that the resulting pore energy would give would give values of r_*, W_*, and r_m, close to those reported by Glaser et al. [52]. We have altered the form of this term slightly and

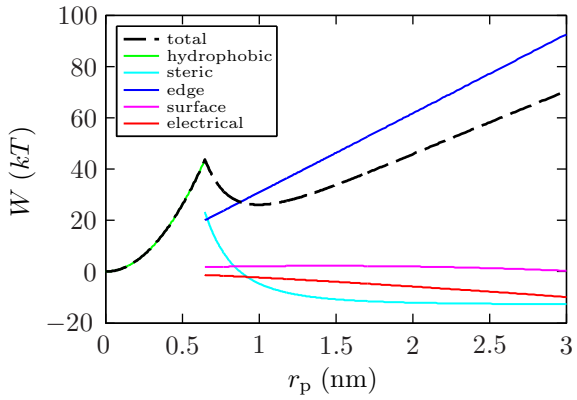

Figure 5.4: Pore energy components. The total pore energy $W(r_p)$ and its components (*inset*) are plotted against pore radius r_p at transmembrane voltage $\Delta\phi_m = 180\,\text{mV}$. The total pore energy $W(r_p)$ (of hydrophilic pores) is the sum of several contributions: (1) $W_{steric}(r_p)$ is the energy that results from the steric repulsion of lipid head groups, (2) $W_{edge}(r_p)$ is the energy that results from the bending of lipid around the interior edge of a pore, (3) $W_{surf}(r_p)$ is the interfacial energy of lipid molecules, and (4) $W_{elec}(r_p, \Delta\phi_m)$ accounts for the energy that results from the force exerted on the pore edge by the electric field. Also shown is the energy $W_{phobic}(r_p)$ of hydrophobic pores ($r_p < r_*$). The edge energy W_{edge} contributes to pore contraction, while all other energy components contribute to pore expansion. For $r_p < 1.43\,\text{nm}$, the interfacial energy W_{surf} also contributes to pore contraction, though its contribution is much smaller than that of the edge energy W_{edge}.

introduced another parameter, which enables us to ensure that three conditions are met (when $\Delta\phi_m = 0\,\text{V}$): (1) The energy curve passes through (r_*, W_*), (2) the energy curve passes through (r_m, W_m), and (3) the energy curve has a local minimum at (r_m, W_m) (i.e., the derivative of energy with respect to r_p is zero at (r_m, W_m)). (Here, r_*, W_*, r_m, and W_m should be regarded as established, or known, parameters.)

The advantage of this description of the steric repulsion energy term lies in its flexibility. The values of r_* and r_m have not been well-established. Additionally, reported values of the pore resealing time constant τ_p, which is directly related to the size of the pore resealing energy barrier $W_d = W_* - W_m$, vary widely [48, 52, 65–67]. Thus, the form described here (Eq. 5.8) allows one to specify r_*, r_m, and τ_p, and the constants B, b, and C can then be calculated, as described in the *Appendix*.

Edge Energy

The second contribution to the pore energy is the edge energy. This term accounts for the energy associated with the bending of the lipid about the interior of a pore. The edge energy is described by [49]

$$W_{\text{edge}}(r_{\text{p}}) = 2\pi\gamma r_{\text{p}}, \tag{5.9}$$

where γ is line tension.

Note that one could consider the steric repulsion energy (Eq. 5.8) and the edge energy (Eq. 5.9) to be a single entity, as in Wohlert et al. [61], because both result from bending the lipid bilayer, though in different (orthogonal) directions. As defined here, the steric repulsion energy is associated with bending the lipid about the central axis of a pore, and the edge energy is associated with bending the lipid around a circle defining a pore (i.e., wrapping around the toroidal interior of the pore).

Interfacial Energy

The third contribution to the pore energy is the interfacial energy of lipid in the membrane. A reduction in lipid area reduces the interfacial energy. This contribution to the energy has generally been given as

$$W_{\text{surf}}(r_{\text{p}}) = -\Gamma A_{\text{p}}, \tag{5.10}$$

where Γ is the membrane tension and $A_{\text{p}} = \pi r_{\text{p}}^2$ is the aqueous area of a pore. The problem with this expression is that, as discussed, the creation of a pore of radius r_{p} does not reduce the lipid area by an amount A_{p}. Rather, it decreases the lipid area by an amount $\delta A_{\text{l,p}}$ (Eq. 5.4), and the difference between the two is quite significant, especially for small pores (Fig. 5.2). Making the appropriate substitution, the effect that a pore has on the interfacial energy is given by

$$W_{\text{surf}}(r_{\text{p}}) = -\Gamma \delta A_{\text{l,p}}(r_{\text{p}}). \tag{5.11}$$

Note that the membrane tension Γ is treated as a constant. However, as Neu and Krassowska [55] noted, the creation and expansion of pores generally decreases the membrane tension and this affects the interfacial energy. This relaxation of the membrane can be accounted for through the use of an effective membrane tension that is a function of pore density [55].

In their treatment, Neu and Krassowska [55] assumed that a pore reduces the lipid area by an amount A_p. Here, we replace A_p width $\delta A_\mathrm{l,p}$. Given that consideration, the effective membrane tension in a system with fixed area A and pore distribution $n(r_\mathrm{p})$ is [55]

$$\Gamma_\mathrm{eff}(A_\mathrm{l,p}) = -\frac{\partial W}{\partial A_\mathrm{l,p}} = 2\Gamma' - \frac{2\Gamma' - \Gamma}{\left(1 - \frac{A_\mathrm{l,p}}{A}\right)^2}. \tag{5.12}$$

Here, Γ' is the interfacial energy per area of the hydrocarbon-water interface, Γ is the surface tension of the intact membrane, and $A_\mathrm{l,p}$ is the total reduction in lipid area that results from the pore distribution (Eq. 5.5). Thus, with effective membrane tension, the energy of a pore is given by

$$W_\mathrm{surf}(r_\mathrm{p}) = -\Gamma_\mathrm{eff}(A_\mathrm{l,p})\, \delta A_\mathrm{l,p}(r_\mathrm{p}). \tag{5.13}$$

Electrical Energy

The final contribution to the pore energy results from the force exerted on a pore by an electric field. Neu et al. [54] developed an expression, based on a fit to numerical simulations of the electric field in the vicinity of a toroidal pore, for the electrical force $F(r_\mathrm{p}, \Delta\phi_\mathrm{m})$ expanding pores:

$$F(r_\mathrm{p}, \Delta\phi_\mathrm{m}) = \frac{F_\mathrm{max}}{1 + \frac{r_\mathrm{h}}{r_\mathrm{p} + r_\mathrm{t}}} \left(\Delta\phi_\mathrm{m}\right)^2. \tag{5.14}$$

Here, F_max is the maximum force expanding a pore with $\Delta\phi_\mathrm{m} = 1\,\mathrm{V}$ and r_h and r_t are constants.

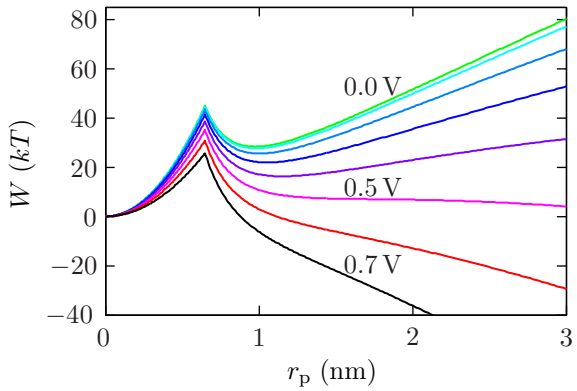

Figure 5.5: Dependence of pore energy on transmembrane voltage. The total pore energy $W(r_p, \Delta\phi_m)$ is shown for several (evenly spaced) transmembrane voltages $|\Delta\phi_m|$ in the range $0.0-0.7$ V. For $|\Delta\phi_m| \lesssim 0.5$ V, a local energy minimum exists near r_m. However, for $|\Delta\phi_m| \gtrsim 0.5$ V, this energy minimum disappears. Thus, pores tend to expand when $|\Delta\phi_m| \gtrsim 0.5$ V and remain at or contract to $\sim r_m$ when $|\Delta\phi_m| \lesssim 0.5$ V. In this study, $r_m = 0.98$ nm.

The electrical energy of a pore $W_{elec}(r_p, \Delta\phi_m)$ can be found by integrating the force (Eq. 5.14):

$$W_{elec}(r_p, \Delta\phi_m) = -\int_0^{r_p} F(r)\, dr \tag{5.15}$$

$$= -F_{max}\left(r_p + r_h \ln\left(\frac{r_t + r_h}{r_p + r_t + r_h}\right)\right)(\Delta\phi_m)^2 . \tag{5.16}$$

Note that W_{elec} goes as $(\Delta\phi_m)^2$. Therefore, (1) W_{elec} does not depend on the sign of $\Delta\phi_m$ and (2) the influence of W_{elec} on the total energy W increases rapidly with $|\Delta\phi_m|$.

Figure 5.5 shows the how the pore energy $W(r_p, \Delta\phi_m)$ changes with transmembrane voltage $|\Delta\phi_m|$. For $|\Delta\phi_m| \lesssim 0.5$ V, a local energy minimum exists near r_m. However, for $|\Delta\phi_m| \gtrsim 0.5$ V, this energy minimum disappears. Importantly, all pores in a local membrane region experience the same transmembrane voltage $\Delta\phi_m$, regardless of their radii r_p. Therefore, all pores in a local membrane region are located on the same energy curve (Fig. 5.5). While the energy curve shifts with $\Delta\phi_m$, all pores will necessarily remain on that changing curve.

5.2.4 Pore Flux and Continuity

In a recent study [45], we developed a description of electrodiffusion, the transport of charged solute resulting from the combination of electrical drift and diffusion, in a discretized 1-D system. Interestingly, our mathematical description and analysis of electrodiffusion is directly relevant to the dynamics of pores. Indeed, the same equations that govern electrodiffusion in 1-D also govern the dynamics of electropores in pore radius space. Put simply, pore radius space involves pores being transported from one size to another as the result of gradients in pore density and pore energy in a manner analogous to charged solutes being transported from one position to another as the result of gradients in concentration and electric potential. This mathematical analogy is presented in more detail below.

In 1-D, electrodiffusive flux J_s of solute in the $+x$-direction is [45]

$$J_s = -D_s \frac{\partial \gamma}{\partial x} - \frac{D_s}{kT} q_e z_s \gamma \frac{\partial \phi}{\partial x}, \tag{5.17}$$

where γ is solute concentration, ϕ is electric potential, D_s is solute diffusivity, z_s is solute charge (valence), q_e is elementary charge, k is the Boltzmann constant, and T is absolute temperature. The first term in Eq. 5.17 describes the flux of solute resulting from a gradient in concentration (diffusion), and the second term describes the flux of solute resulting from a gradient in electric potential (electrical drift).

In Eq. 5.17, the electrical drift flux term is written in terms of electric potential ϕ. However, it can also be written in terms of the electrical energy of solute molecules W. The gradient in electrical energy W is related to the gradient in the electric potential ϕ by

$$\frac{\partial W}{\partial x} = q_e z_s \frac{\partial \phi}{\partial x} \tag{5.18}$$

This is essentially a statement of the Lorentz force on a molecule with charge $q_e z_s$ (in the absence

of a magnetic field). Thus, the electrodiffusive flux (Eq. 5.17) may be written in terms of the electrical energy W as

$$J_s = -D_s \frac{\partial \gamma}{\partial x} - \frac{D_s}{kT} \gamma \frac{\partial W}{\partial x}. \tag{5.19}$$

This is mathematically equivalent to the form used to describe the flux J_p of pores in radius space [50]:

$$J_p = -D_p \frac{\partial n}{\partial r_p} - \frac{D_p}{kT} n \frac{\partial W}{\partial r_p}, \tag{5.20}$$

where J_p is flux of pores (per unit area), n is the pore density (per unit area per dr_p), W is the pore energy, D_p is the pore diffusion coefficient, k is the Boltzmann constant, and T is the absolute temperature. This description of pore transport was introduced by Pastushenko et al. [50] and has been used in a number of subsequent studies and models [53, 55, 56, 64, 68–70]. Just as the electrodiffusive flux is determined by gradients in solute concentration and electrical energy, pore flux in radius space is determined by gradients in pore density and energy (the energy landscape). This mathematical analogy is important because it allows improved analytic methods for electrodiffusion [45] to be carried over directly to pore dynamics.

5.2.5 Discretized Pore Flux and Continuity

Because the continuum-based pore flux has the same mathematical form as the electrodiffusive flux, the discretized pore flux has the same mathematical form as the discretized electrodiffusive flux [45]. Thus, it follows that the flux of pores $J_p^{i,j}$ between adjacent nodes i and j in a discretized pore radius space is

$$J_p^{i,j} = \begin{cases} -\frac{D_p}{kT} \frac{(\Delta n)_{i,j}}{(\Delta r_p)_{i,j}} & \text{if } (\Delta W)_{i,j} = 0, \\ -\frac{D_p}{kT} \frac{(\Delta W)_{i,j}}{(\Delta r_p)_{i,j}} \left(\frac{n_i}{1 - e^{(\Delta W)_{i,j}/kT}} + \frac{n_j}{1 - e^{-(\Delta W)_{i,j}/kT}} \right) & \text{if } (\Delta W)_{i,j} \neq 0. \end{cases} \tag{5.21}$$

Here, nodes i and j have pore radii r_p^i and r_p^j, pore densities n_i and n_j, and pore energies W_i and W_j. $(\Delta n)_{i,j} \equiv n_j - n_i$, $(\Delta r_p)_{i,j} \equiv r_j - r_i$, and $(\Delta W)_{i,j} \equiv W_j - W_i$.

The number of pores is conserved during transport, except at the boundary $r_p = r_*$, where pores

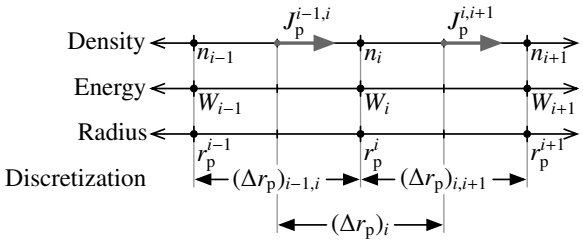

Figure 5.6: Discretized 1-D pore transport system. Node i has adjacent nodes $i-1$ and $i+1$. The pore radius r_p, energy W, and density n for each node is indicated by its subscript or superscript. Nodes $i-1$ and i are separated by distance (in radius space) $(\Delta r_p)_{i-1,i}$, nodes i and $i+1$ are separated by distance (in radius space) $(\Delta r_p)_{i,i+1}$. The region of radius space associated with node i has length $(\Delta r_p)_i$. $J_p^{i-1,i}$ is the pore flux from node $i-1$ to node i, and $J_p^{i,i+1}$ is the pore flux from node i to node $i+1$. The pore flux between adjacent nodes is determined by the pore radii, energies, and densities of the nodes, as well as pore (e.g., diffusivity) and system (e.g., temperature) properties. The rate at which the pore density n_i changes is determined by the net flux $J_p^{i-1,i} - J_p^{i,i+1}$ into node i and the length $(\Delta r_p)_i$.

are created and destroyed. Thus, the time rate of change of pore density is related to the pore flux by the continuity equation

$$\frac{\partial n}{\partial t} = -\frac{\partial J_p}{\partial r_p} = D_p \frac{\partial^2 n}{\partial r_p^2} + \frac{D_p}{kT}\frac{\partial n}{\partial r_p}\frac{\partial W}{\partial r_p} + \frac{D_p}{kT}\frac{\partial^2 W}{\partial r_p^2}. \tag{5.22}$$

Figure 5.6 shows a discretized 1-D pore transport system. Node i with radius r_p^i has adjacent nodes $i-1$ and $i+1$ with radii r_p^{i-1} and r_p^{i+1} such that $r_p^{i-1} < r_p^i < r_p^{i+1}$. The nodes $i-1$, i, and $i+1$ have pore densities n_{i-1}, n_i, and n_{i+1}, pore energies W_{i-1}, W_i, and W_{i+1}. The distance between nodes $i-1$ and i is $(\Delta r_p)_{i-1,i} \equiv r_p^i - r_p^{i-1}$, and the distance between nodes i and $i+1$ is $(\Delta r_p)_{i,i+1} \equiv r_p^{i+1} - r_p^i$. There is a region of radius space associated with node i for which all points are close to r_i than to the radius of any other node. More specifically, all r_p such that $r_p^{i-1} + (\Delta r_p)_{i-1,i}/2 < r_p < r_p^{i+1} - (\Delta r_p)_{i,i+1}/2$ are associated with node i. The length of this region associated with node i is $(\Delta r_p)_i \equiv (\Delta r_p)_{i-1,i}/2 + (\Delta r_p)_{i,i+1}/2$.

In this discretized system, the continuity equation (Eq. 5.22) becomes

$$\frac{\partial n_i}{\partial t} = -\frac{J_\mathrm{p}^{i,i+1} - J_\mathrm{p}^{i-1,i}}{(\Delta r_\mathrm{p})_i} = \frac{J_\mathrm{p}^{i-1,i} - J_\mathrm{p}^{i,i+1}}{(\Delta r_\mathrm{p})_i}. \tag{5.23}$$

The flux $J_\mathrm{p}^{i-1,i}$ from $i-1$ to i and flux $J_\mathrm{p}^{i,i+1}$ from i to $i+1$ at any instant in time can be determined using Eq. 5.21, as described.

5.2.6 Pore Creation and Destruction

r_* is the smallest pore radius explicitly represented in the model and is the smaller radius boundary of pore radius space. Therefore, in contrast to other nodes, whose pore densities change purely as a result of pore flux to and from adjacent nodes (Eq. 5.23), the r_* node's pore density also changes as a result of pore creation and destruction. (The larger radius boundary of pore radius space at $r_{\mathrm{p,max}}$ is simply a no-flux (reflecting) boundary.)

Pore creation and destruction can be cast as additional flux terms at the r_* node. Applying continuity (as in Eq. 5.23) then determines the time rate of change of $n_* \equiv n(r_*)$:

$$\frac{\partial n_*}{\partial t} = \frac{J_\mathrm{p}^{*,\mathrm{c}} - J_\mathrm{p}^{*,\mathrm{d}} - J_\mathrm{p}^{*,*+1}}{(\Delta r_\mathrm{p})_*}. \tag{5.24}$$

Here, $J_\mathrm{p}^{*,\mathrm{c}}$ is the creation flux, $J_\mathrm{p}^{*,\mathrm{d}}$ is the destruction flux, $J_\mathrm{p}^{*,*+1}$ is the flux from the r_* node to the adjacent (larger radius) node (as described by Eq. 5.21), and $(\Delta r_\mathrm{p})_*$ is the discretization size at r_*. By construction, $J_\mathrm{p}^{*,\mathrm{c}} > 0$ and $J_\mathrm{p}^{*,\mathrm{d}} > 0$. That is, $J_\mathrm{p}^{*,\mathrm{c}}$ can only increase n_* and $J_\mathrm{p}^{*,\mathrm{d}}$ can only decrease n_*.

The pore creation flux is described by [52]

$$J_\mathrm{p}^{*,\mathrm{c}}(\Delta\phi_\mathrm{m}) = a f_\mathrm{c} \mathrm{e}^{\beta(\Delta\phi_\mathrm{m})^2/kT}. \tag{5.25}$$

Here, a is the pore creation rate density, β is a pore creation constant, and f_c is the fraction of the

membrane available for pore creation, as discussed below. Note that the pore creation flux $J_p^{*,c}$ is highly nonlinear in $\Delta\phi_m$ and thus a small relative increase in $|\Delta\phi_m|$ will result in a much large relative increase in $J_p^{*,c}$.

The pore destruction flux $J_p^{*,d}$ results from applying an absorbing boundary condition at r_* [53]. Specifically, $J_p^{*,d}$ is equal to the flux from r_* to a slightly smaller radius $r_* - \Delta r_p$ node with pore density $n(r_* - \Delta r_p) = 0$.

In Eq. 5.25, f_c is the fraction of the membrane available for pore creation. This factor arises because we assume that pores cannot be created in the edges of existing pores, as this would result in overlapping pores. Additionally, for biological membranes, a major fraction f_{prot} of the membrane is occupied by protein and therefore presumed unavailable for pore creation. The f_c factor accounts for the reduced participation. In a region of membrane with area A, protein fraction f_{prot}, and pore density distribution $n(r_p)$, the fraction of the membrane available for pore creation is

$$f_c = 1 - f_{prot} - \int_0^\infty \pi \left(r_p + \frac{d_m}{2} \right)^2 n(r_p)\, dr_p. \tag{5.26}$$

As the membrane becomes saturated with pores, $f_c \to 0$, and therefore $J_p^{*,c} \to 0$. Thus, f_c prevents the generation of nonphysical pore density in response to very large magnitude pulses.

5.2.7 Pore Resealing

The application of a sufficiently large pulsed electric field will charge the membrane and lead to a burst of pore creation (Eq. 5.25). Because of the large energy gradient between r_* and r_m (Fig. 5.3), newly created pores rapidly expand to $\sim r_m$ or larger, depending on the energy landscape (Fig. 5.5). This large energy gradient is smallest at $\Delta\phi_m = 0$ and grows significantly larger for increased $|\Delta\phi_m|$.

Post-pulse, $\Delta\phi_m \approx 0$ V until most pores reseal [47]. Therefore, pore creation is minimal (Eq. 5.25), but pore destruction is significant. While some previous models (e.g., [70]) have implemented resealing using explicit resealing expressions that remove pores from radius space, in the model pre-

sented here, resealing occurs as pores diffuse over the pore destruction energy barrier $W_d = W_* - W_m$ at r_* (Fig. 5.3). Resealing continues until the pore density distribution reaches its equilibrium. At equilibrium, $\partial n/\partial t = 0$ (including $\partial n_*/\partial t$) and $J_p^{*,*+1} = 0$. Thus, the continuity equation (Eq. 5.24) requires that that $J_p^{*,c} = J_p^{*,d}$. In other words, pore creation is non-zero (Eq. 5.25) but is exactly offset by pore destruction, on average. (Pore creation and destruction events are stochastic.)

We have found that resealing time constant τ_p is approximately related to the energy barrier to pore destruction W_d by

$$\tau_p \approx \frac{(r_m - r_*)^2}{D_p} \left(\frac{W_d}{kT}\right)^{-\frac{3}{2}} e^{W_d/kT}. \tag{5.27}$$

This expression is adapted from a nondimensionalized expression for the resealing rate in Neu and Krassowska [53].

Equation 5.27 can be numerically solved to find the value of the pore destruction barrier W_d that will result in approximately the desired resealing time constant τ_p. We have found that estimating W_d using Eq. 5.27 generally results in a τ_p value within ~10 % of the desired value. In practice, we use simply use Eq. 5.27 to estimate the value of W_d and then use an algorithm to adjust the value until the resulting τ_p is equal to the desired value.

Note that, in this model, W_* is a fixed constant and W_d is chosen to given the specified τ_p. W_m is then calculated as $W_m = W_* - W_d$.

5.2.8 Pore Electrical Conductance

In a previous study [43], we developed a detailed description of the conductance of pores, including the effects of hindrance and partitioning. Here, for the convenience of the reader, we give a brief description and note that greater detail may be found in Ref. [43].

Consider the internal region of the trapezoidal pore in Fig. 5.1B. It has radius r_p, depth d_p, aqueous area $A_p = \pi r_p^2$, and conductivity σ. The interaction between solute ions in a pore and the pore

gives rise to a pore hindrance factor H and partition coefficient K that scale the pore conductance relative to a region of the same dimensions in bulk electrolyte. (These factors are described in the *Appendix* and Ref. [43].) Thus, accounting for hindrance and partitioning, the conductance of the internal pore region is given by

$$g_{p,p} = \sigma \frac{A_p}{d_p} HK, \tag{5.28}$$

and the resistance $R_{p,p}$ of the internal pore region is thus

$$R_{p,p} = \frac{1}{g_{p,p}} = \frac{d_p}{\sigma A_p HK}. \tag{5.29}$$

In addition to the resistance $R_{p,p}$ of the internal pore region, there is an access resistance [71, 72] $R_{p,a}$ associated with each side of the membrane/pore that accounts for the fact that ions are focused by heterogeneous fields into and out of a pore. This access resistance is described by [71, 72]

$$R_{p,a} = \frac{1}{2\sigma r_p}. \tag{5.30}$$

The total resistance R_p associated with a pore is therefore the sum of the resistance of the internal pore region $R_{p,p}$ and the access resistance $R_{p,a}$:

$$R_p = R_{p,p} + R_{p,a} = \frac{d_p}{\sigma A_p HK} + \frac{1}{2\sigma r_p}. \tag{5.31}$$

The total pore conductance is simply the reciprocal of R_p:

$$g_p = \frac{1}{R_p}. \tag{5.32}$$

5.3 Results and Discussion

5.3.1 Relative Significance of Pore Energy Components

Pores expand and contract in response to the time-dependent gradient in the pore energy (Eq. 5.20). Thus, in a particular region of radius space, the relative significance of each energy term in Eq. 5.7 can be determined by considering its gradient relative to the gradients of the other terms.

It is clear from Fig. 5.4 that the steric repulsion energy term (Eq. 5.8) is the dominant mechanical energy term when $r_p < r_m$ and that the edge energy term (Eq. 5.9) is the dominant mechanical energy term when $r_p > r_m$. Indeed, it is primarily the combination of these opposing terms that determines the radius r_m of the energy minimum (Fig. 5.3).

The significance of the electrical energy term (Eq. 5.16) depends strongly on the transmembrane voltage $\Delta\phi_m$, as demonstrated in Fig. 5.5. When $\Delta\phi_m$ is small, the electrical energy term contributes negligibly to pore dynamics. However, when $\Delta\phi_m$ is large, it significantly affects pore behavior. Indeed for pores with $r_p > r_m$, pore expansion and contraction are determined by the relative sizes of the gradients in edge energy and electrical energy.

For the range of radii ($r_p < 3\,\text{nm}$) shown in Fig. 5.3, the gradient in the interfacial energy term (Eq. 5.11) is quite small. However, the gradient in interfacial energy, and thus its significance, grows linearly with r_p. Therefore, the relative significance of the interfacial energy term depends on the membrane tension Γ and pore radius r_p.

The significance of the interfacial energy term can be assessed by comparing its gradient with the gradient of the edge energy:

$$\frac{\left|\frac{dW_{surf}}{dr_p}\right|}{\left|\frac{dW_{edge}}{dr_p}\right|} = \left(\frac{\Gamma}{\gamma}\right)\left|r_p + \left(\frac{d_m}{2}\right)\left(1 - \frac{\pi}{2}\right)\right|. \tag{5.33}$$

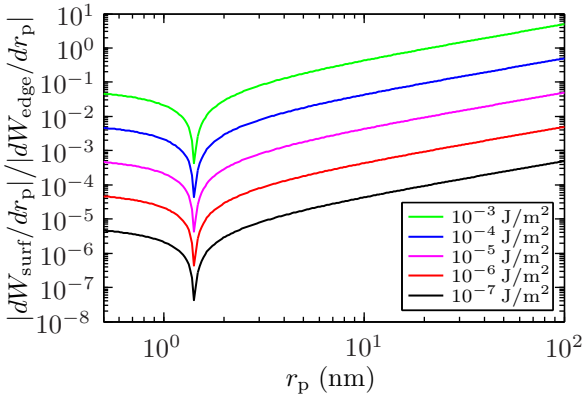

Figure 5.7: Ratio of the interfacial energy gradient to the edge energy gradient. The relative importance of a pore energy component is determined by the magnitude of its energy gradient relative to the energy gradients of the other components. This is because pores expand and contract in response to the gradient in total energy. Here, the ratio of the interfacial energy gradient $|dW_{\mathrm{surf}}/dr_{\mathrm{p}}|$ to the edge energy gradient $|dW_{\mathrm{edge}}/dr_{\mathrm{p}}|$ is plotted against pore radius r_{p} for a selection of membrane tension values, as shown in the *inset*. When $\Gamma = 10^{-3}\,\mathrm{J/m^2}$, the ratio is >1 for $r_{\mathrm{p}} \gtrsim 20\,\mathrm{nm}$ and the interfacial energy gradient is larger than the edge energy gradient. However, for the rest of plotted Γ ($10^{-7}-10^{-4}\,\mathrm{J/m^2}$), the ratio is $\ll 1$ for all radii plotted ($r_{\mathrm{p}} < 100\,\mathrm{nm}$) and the interfacial energy gradient is much smaller than the edge energy gradient. Note that the typical membrane tension for BLM is $\Gamma \approx 1\times10^{-3}\,\mathrm{J/m^2}$ [64], while the typical membrane tension for cell plasma membranes is a much smaller $\Gamma \approx 2\times10^{-6}-20\times10^{-6}\,\mathrm{J/m^2}$ [73]. Thus, these results suggest that the impact of membrane tension on pore dynamics is small or negligible for cells.

Figure 5.7 shows the ratio of the interfacial energy gradient to the edge energy gradient for surface tension Γ in the range $10^{-7}-10^{-3}\,\mathrm{J/m^2}$ and pore radii r_{p} up to 100 nm. The ratio increases in proportion to r_{p} and Γ. When $\Gamma = 10^{-3}\,\mathrm{J/m^2}$, the ratio is >1 for $r_{\mathrm{p}} \gtrsim 20\,\mathrm{nm}$ and the interfacial energy gradient is larger than the edge energy gradient. However, for the rest of plotted Γ ($10^{-7}-10^{-4}\,\mathrm{J/m^2}$), the ratio is $\ll 1$ for all radii plotted ($r_{\mathrm{p}} < 100\,\mathrm{nm}$) and the interfacial energy gradient is much smaller than the edge energy gradient.

The tension of the cell plasma membrane is typically in the range $2\times10^{-6}-20\times10^{-6}\,\mathrm{J/m^2}$ [73]. This is $2-3$ orders of magnitude smaller than typical bilayer lipid membrane (BLM) tension of $\sim 1\times10^{-3}\,\mathrm{J/m^2}$ [64]. At the upper end of this membrane tension range ($20\times10^{-6}\,\mathrm{J/m^2}$) and at pore radius 100 nm, the ratio of the interfacial energy gradient to the edge energy gradient is just ~ 0.1, which is considerably smaller than the range of reported line tension values ($0.5\times10^{-11}-$

3×10^{-11} J/m) relative to the intermediate value used here (2×10^{-11} J/m).

In other words, for a typical plasma membrane, the uncertainty in the value of the line tension γ is a more significant determinant of pore behavior than the membrane tension. Moreover, as Neu and Krassowska [55] noted, the creation and expansion of pore will further decrease the membrane tension. The implication is that, if the tension of the membrane is insignificant when intact, then it will become even more insignificant upon the creation and expansion of pores.

The interfacial energy is significant in systems with large membrane tension (e.g., BLM and osmotically swollen cells) or large pores. However, in a typical plasma membrane, the contribution of interfacial energy to the behavior of pores is negligible unless very large pores are considered.

5.3.2 Description of Pore Dynamics

The dynamic behavior of pores is complicated. The transmembrane voltage determines the rates of pore creation, expansion, and contraction, and in response, pore creation, expansion, and contraction determine, in part, the transmembrane voltage. Additionally, in spatially distributed systems, the behavior of one system region may affect another communicating system region through its impact on system-level electrical response.

Despite this complexity, the results of mechanistic models of electroporation (featuring pore expansion) [64, 69, 70, 74, 75] exhibit some common features. Specifically: (1) During an applied electric pulse, the transmembrane voltage $\Delta\phi_{\mathrm{m}}$ tends to a plateau value of ~ 0.5 V. Notably, this is true for both trapezoidal (or square) pulses [69, 70, 74, 75] and exponential pulses [69, 70]. (2) During an applied electric pulse, some pores tend to shrink to (or remain at) the minimum-size pore radius r_{m}, while other pores expand significantly beyond r_{m}. These specific features and, indeed, the general behavior of pores can be understood through the pore dynamics phase space shown in Fig. 5.8.

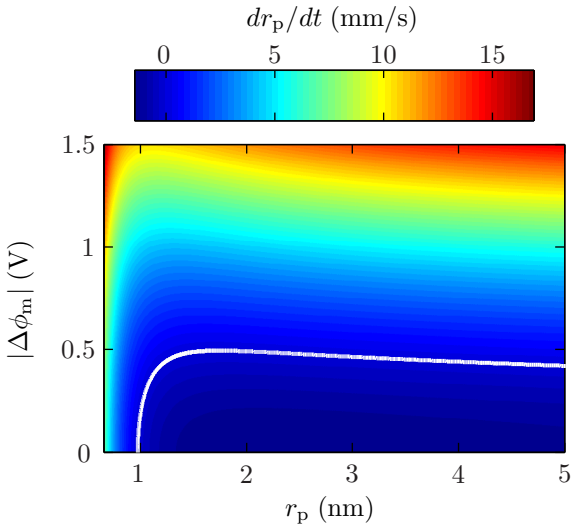

Figure 5.8: Pore dynamics phase space. The rate of pore expansion dr_p/dt is shown as a function of pore radius r_p and transmembrane voltage magnitude $|\Delta\phi_m|$. The *white curve* indicates $dr_p/dt = 0$. Note that the unit of drift speed, mm/s, is equivalent to μm/ms, nm/μs, and pm/ns. Most pores are "born" in the upper-left corner where dr_p/dt is positive and large, and therefore the pores initially expand rapidly. As they expand, their conductance increases and this leads to a decrease in $|\Delta\phi_m|$. The combination of increasing r_p and decreasing $|\Delta\phi_m|$ sets the ensemble of pores on a trajectory pointed *right* and *down*. As described in the main text, the exact trajectory depends largely on the magnitude of the applied electric pulse, with small pulses leading to a trajectory pointed more to the *right* and large pulses leading to trajectory pointed more *downward*. Regardless of the specific pulse applied, pores tend to accumulate along the *white curve*. This is an important result: pores evolve to join this curve. It is also the basis for the tendency to form two pore populations, one large and one small.

The drift speed of pores in radius space (from Eq. 5.20) is given by

$$\frac{dr_p}{dt} = -\frac{D_p}{kT}\frac{\partial W}{\partial r_p}. \tag{5.34}$$

Thus, pores expand ($dr_p/dt > 0$) when $\partial W/\partial r_p < 0$ and pores contract ($dr_p/dt < 0$) when $\partial W/\partial r_p > 0$. Because the pore energy W (Eq. 5.7) is a function of transmembrane voltage $\Delta\phi_m$ and pore radius r_p, the drift speed dr_p/dt is also fully determined by $\Delta\phi_m$ and r_p. Accordingly, Fig. 5.8 shows the drift speed dr_p/dt plotted against r_p and $\Delta\phi_m$.

Using Fig, 5.8 we can understand the "life cycle" of an ensemble of pores, as well as the cause of

the specific features of electroporation model results noted above.

The rate of pore creation is strongly dependent on transmembrane voltage magnitude $|\Delta\phi_m|$ (Eq. 5.25). (Pore creation and evolution, as described here, are independent of the sign of $\Delta\phi_m$. For simplicity, we use $\Delta\phi_m$, though $|\Delta\phi_m|$ is implied.) Upon application of an electric pulse, the membrane charges and then reaches a transient peak during which there is a burst of pore creation, which leads to a subsequent decrease in transmembrane voltage $\Delta\phi_m$. Thus, essentially all pores are created at a large transmembrane voltage, typically, $\Delta\phi_m \approx 1.0-1.5\,\mathrm{V}$, depending on the applied electric pulse. Recalling that in the present model pores are created at radius $r_* \approx 0.65\,\mathrm{nm}$, pores are "born" in the *upper-left corner* of Fig. 5.8. In this region, dr_p/dt is positive and large, and thus pores expand rapidly.

As the newly created pores expand, their conductances increase (Eq. 5.32). This leads to a decrease in $\Delta\phi_m$, by shifting some of the total system voltage drop from the membrane to the bulk electrolyte. The combination of increasing r_p and decreasing $\Delta\phi_m$ sets the ensemble of pores on a trajectory pointed *right* and *down* in Fig. 5.8.

Eventually, the ensemble of pores reaches the *white curve* defining $dr_p/dt = 0$. In other words, the *white curve*, which primarily lies along $\Delta\phi_m \approx 0.5\,\mathrm{V}$, defines the boundary between pore expansion and contraction. We refer to this transmembrane voltage with $dr_p/dt = 0$ as $\Delta\phi_{m,0}$, while noting that the exact value is dependent on r_p.

After reaching the *white curve*, the ensemble as a whole is not driven to expand or contract, and if the pores are not expanding or contracting, then the transmembrane voltage should remain constant. However, while in our model all pores in a local region have the same transmembrane voltage $\Delta\phi_m$, the population of pores contains a distribution of pore radii r_p as a result of (1) pores not being created at exactly the same time and position in phase space and (2) thermal fluctuations that lead to "diffusion" in radius space. Note also that the *white curve* has a slight *downward*

slope. Therefore, if the ensemble of pores is centered on the white curve at some radius $r_p = \bar{r}_p$ and transmembrane voltage $\Delta\phi_m$, then pores with radii $r_p < \bar{r}_p$ lie below the curve ($dr_p/dt < 0$) and pores with radii $r_p > \bar{r}_p$ lie above the curve ($dr_p/dt > 0$). As a result, the ensemble of pores splits, with some pores contracting and some pores expanding. The net effect is necessarily such that the $\Delta\phi_m$ remains relatively constant at the plateau voltage $\Delta\phi_m = \Delta\phi_{m,0} \approx 0.5\,\text{V}$.

The contraction of smaller pores enables the expansion of larger pores: the decreasing conductance of the contracting pores compensates for the increasing conductance of the expanding pores. However, this process cannot proceed indefinitely. Eventually, the smaller pores reach $r_p \approx r_m$ and cannot contract further. At this point, the smaller pores of the larger ensemble begin to contract, enabling the continued expansion of the largest pores. However, this too, cannot continue indefinitely. Eventually, essentially all pores contract. If the pulse is long enough, this outcome is inevitable. While pore creation (Eq. 5.25) proceeds at a much slower rate at $\Delta\phi_m \approx 0.5\,\text{V}$ than at higher $\Delta\phi_m$, over the course of a long pulse it may lead to a non-negligible increase in membrane conductance that then contributes to the decrease in $\Delta\phi_m$ and resulting contraction of large pores.

Following the end of the applied pulse, $\Delta\phi_m \approx 0\,\text{V}$. Thus, all pores will shrink to $r_p \approx r_m$, and the pores will assume a distribution like that shown in Fig 5.3. As pores diffuse into in the tail of the distribution at $r_p = r_*$ they are destroyed ("die"), thus completing the pore life cycle.

It is important to understand why the system tends to maintain the plateau transmembrane voltage $\Delta\phi_m = \Delta\phi_{m,0} \approx 0.5\,\text{V}$ (in the short term). Consider what would happen if $\Delta\phi_m$ decreased below $\Delta\phi_{m,0}$. As shown in Fig. 5.8, $dr_p/dt < 0$ when $\Delta\phi_m < \Delta\phi_{m,0}$, and therefore pores contract. However, as pores contract their conductance decreases, and this leads to an increase in $\Delta\phi_m$ that counteracts the hypothetical decrease. Now, consider what would happen if $\Delta\phi_m$ increased above $\Delta\phi_{m,0}$. $dr_p/dt < 0$ when $\Delta\phi_m < \Delta\phi_{m,0}$ (Fig. 5.8), and therefore pores expand. However, as pores expand their conductance increases, and this leads to an increase in $\Delta\phi_m$ that counteracts the hypothetical increase. Put simply, any shift in $\Delta\phi_m$ away from $\Delta\phi_{m,0}$ results in a shift in the distribution

of pore radii that restores $\Delta\phi_m \approx \Delta\phi_{m,0}$. This negative feedback response by dynamic pores even results in the temporary maintenance of $\Delta\phi_m = \Delta\phi_{m,0}$ during an exponential pulse [69, 70] as the applied electric field decreases.

The behavior described is typical for conventional electroporation pulses. However, other responses are possible, and they can be readily interpreted using Fig. 5.8. The rates of pore creation and expansion are both transmembrane voltage-dependent. Additionally, pore creation and expansion both increase membrane conductance and thereby lead to a decrease in transmembrane voltage that, in turn, causes a decrease in the rates of pore creation and expansion. That is, electroporation is self-limiting. Whether pore creation or expansion is dominant in increasing the membrane conductance depends on the peak transmembrane voltage, which, in turn, depends on the magnitude of the applied electric pulse. In terms of the phase plot (Fig. 5.8), this implies that the initial trajectory of the pores depends on the magnitude of the applied electric pulse.

In response to a very large magnitude pulse (e.g., 10 MV/m), pore creation increases the membrane conductance and decreases $\Delta\phi_m$ much faster than possible by pore expansion [56]. As a result, the pores are "born" in the *upper-left* corner of Fig. 5.8, as in the typical case described, but follow a trajectory pointed nearly straight *down.* Thus, the pores reach the *white curve* at a radius $r_p \approx r_m$, for which there is no possibility of any significant pore expansion.

In response to a relatively small magnitude pulse (i.e., a pulse too small to charge the membrane beyond $\sim$1 V), pore creation proceeds slowly, and thus pore expansion is the primary mechanism by which the membrane conductance increases and $\Delta\phi_m$ decreases. As a result, the pores are "born" in the *almost upper-left corner* of Fig. 5.8, as in the typical case described, but follow a trajectory pointed *right* and *slightly down.* Thus, the pores reach the *white curve* at a large radius r_p. If the max radius $r_{p,max}$ that a pore can attain is limited (e.g., by a boundary condition), then pores may accumulate at $r_{p,max}$ with $\Delta\phi_m > \Delta\phi_{m,0}$ until a large enough number of pores are created and expand to force $\Delta\phi_m$ to decrease and some pores to contract.

Note that, in spatially distributed cell models, this scenario is almost inescapable, occurring somewhere in the membrane. Because the peak transmembrane voltage depends on the membrane location (and orientation) in addition to the magnitude of the applied pulse. Thus, somewhere between the "pole" of the PM (where the membrane is normal to the applied field), where the peak $\Delta\phi_m$ is largest, and the "equator" of the PM (where the membrane is parallel to the applied field), where $\Delta\phi_m \approx 0\,\mathrm{V}$, there is a region where the peak $\Delta\phi_m$ is $\sim 1\,\mathrm{V}$ and the above scenario plays out. Krassowska et al. [75], for example, reported a region about halfway between the PM pole and equator with slightly elevated $\Delta\phi_m$ (relative to other regions of the PM) and very large pores.

The final possible deviation from the typical behavior described is the response to a pulse that is too small in magnitude to charge the membrane beyond $\Delta\phi_{m,0} \approx 0.5\,\mathrm{V}$. In this case, pores are "born" in the *lower-left corner* of Fig. 5.8 and follow a trajectory pointed *right* until reaching the *white curve*. In this case pores remain distributed about $r_p \approx r_m$.

The phase plot (Fig. 5.8) can also be applied to patch-clamp experiments. In these experiments, the transmembrane voltage $\Delta\phi_m$ is fixed over the entire plasma membrane, regardless of the resultant behavior of pores. Thus, if $\Delta\phi_m < \Delta\phi_{m,0}$, pores are "born" in the *lower-left corner* of Fig. 5.8 and follow a trajectory pointed *right* until reaching the *white curve*. In this case pores remain distributed about $r_p \approx r_m$. However, if $\Delta\phi_m > \Delta\phi_{m,0}$, pores will expand without bound ($dr_p/dt > 0$ for all $\Delta\phi_m > \Delta\phi_{m,0}$), thereby leading to irreversible membrane rupture.

5.3.3 Partial Validation of the Pore Energy Landscape

Melikov et al. [48] examined pore conductance in voltage-clamped BLM over the range 150 – 400 mV. Using highly sensitive methods, they measured noisy but quantized steps up and down in membrane conductance, which they attributed to the creation and destruction of discrete pores. Intriguingly, Melikov et al. [48] presented a histogram comprising thousands of individual pore conductance measurements with a distribution that appears strikingly similar to the distribution of

pores in radius space at low transmembrane voltage (Fig. 5.3B).

In a previous study [43], we analyzed the average pore conductance values $\overline{g}_p$ that Melikov et al. [48] reported for two different electrolyte solutions, KCl and NMDG-glutamate, that comprise ions of very different size and shape [43, 44]. Using our description of pore conductance, including hindrance and partitioning, we showed that the $\overline{g}_p$ reported for KCl is consistent with an average pore radius value $\overline{r}_p = 1.03\,\text{nm}$ and that the $\overline{g}_p$ reported for NMDG-glutamate is also consistent with $\overline{r}_p = 1.03\,\text{nm}$. That both electrolyte solutions were consistent with the same average pore radius $\overline{r}_p$ provides partial validation of our description of pore conductance [43].

In this study, we take our analysis of the Melikov et al. [48] experiments one step further by analyzing the full set of pore conductance measurements for BLM clamped at $\Delta\phi_m = 180\,\text{mV}$ (presented in Fig. 5 of Ref. [48]). We digitized this conductance data using the open-source Engauge Digitizer software (version 4.1, 2008, http://digitizer.sourceforge.net).

Melikov et al. [48] did not specify the temperature at which their experiments were performed, so we assumed a typical room temperature of 22 °C. The conductivity of 100 mM KCl is 1.298 S/m at 25 °C [76], which we adjusted to 1.20 S/m at 22 °C, as described by Smith et al. [44].

For the size of the KCl electrical charge carrier, we used $r_s = 0.175\,\text{nm}$, the average of the corrected Stokes radii for potassium and chloride ions [44]. (Note that the r_s values for potassium and chloride ions are nearly identical.)

Using Eq. 5.32, we calculated the pore conductance g_p for a range of r_p at $\Delta\phi_m = 180\,\text{mV}$, the transmembrane voltage at which Melikov et al. [48] made their conductance measurements (for the pore conductance histogram that they presented in their Fig. 5). Figure 5.9 shows the resulting relationship between pore conductance g_p and pore radius r_p.

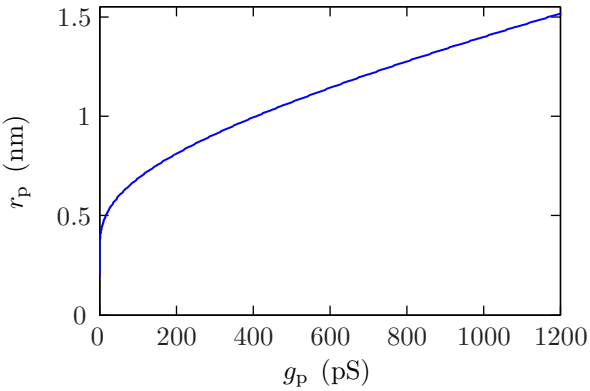

Figure 5.9: Relationship between pore conductance and pore radius for the Melikov et al. [48] experiments. The plot shows the pore radius r_p corresponding to pore conductance g_p for BLM clamped at $\Delta\phi_m = 180\,\text{mV}$ in KCl solution, as in the Melikov et al. [48] single-pore conductance measurements. The relationship between r_p and g_p was determined using Eq. 5.32 and enables the Melikov et al. pore conductance measurements to be mapped to pore radius.

We then used the relationship between g_p and r_p to map the Melikov et al. [48] data from pore conductance to pore radius. The resulting distribution of measurements is shown in Fig. 5.10A and B. The number of measurements M is normalized by the number of measurements of the local maximum M_{max} at $r_p \approx 1\,\text{nm}$, for reasons that will become clear. Note that the distribution of measurements has two peaks: one at $r_p \approx 0.65\,\text{nm}$ and another, smaller peak at $r_p \approx 1\,\text{nm}$.

Our interpretation of the bimodal distribution of the Melikov et al. measurements is that the sub-distribution of measurements at larger radius ($\sim 1\,\text{nm}$) corresponds to metastable pores. The interpretation of the distribution at smaller radius ($\sim 0.65\,\text{nm}$) is less clear. We note that a similar histogram for a cell membrane patch (though with far fewer measurements) in Fig. 3 of Melikov et al. [48], does not feature a sub-distribution at smaller conductance (radius) but does feature an approximately Gaussian distribution at larger conductance (radius). We reason that the sub-distribution at smaller r_p may approximately correspond to the radius r_* at which pores are created and destroyed. The number of conductance measurements falls off rapidly with radius below the assumed r_* (Fig. 5.10A). This is consistent with the view that r_* is the minimum radius of hydrophilic (i.e., conducting) pores.

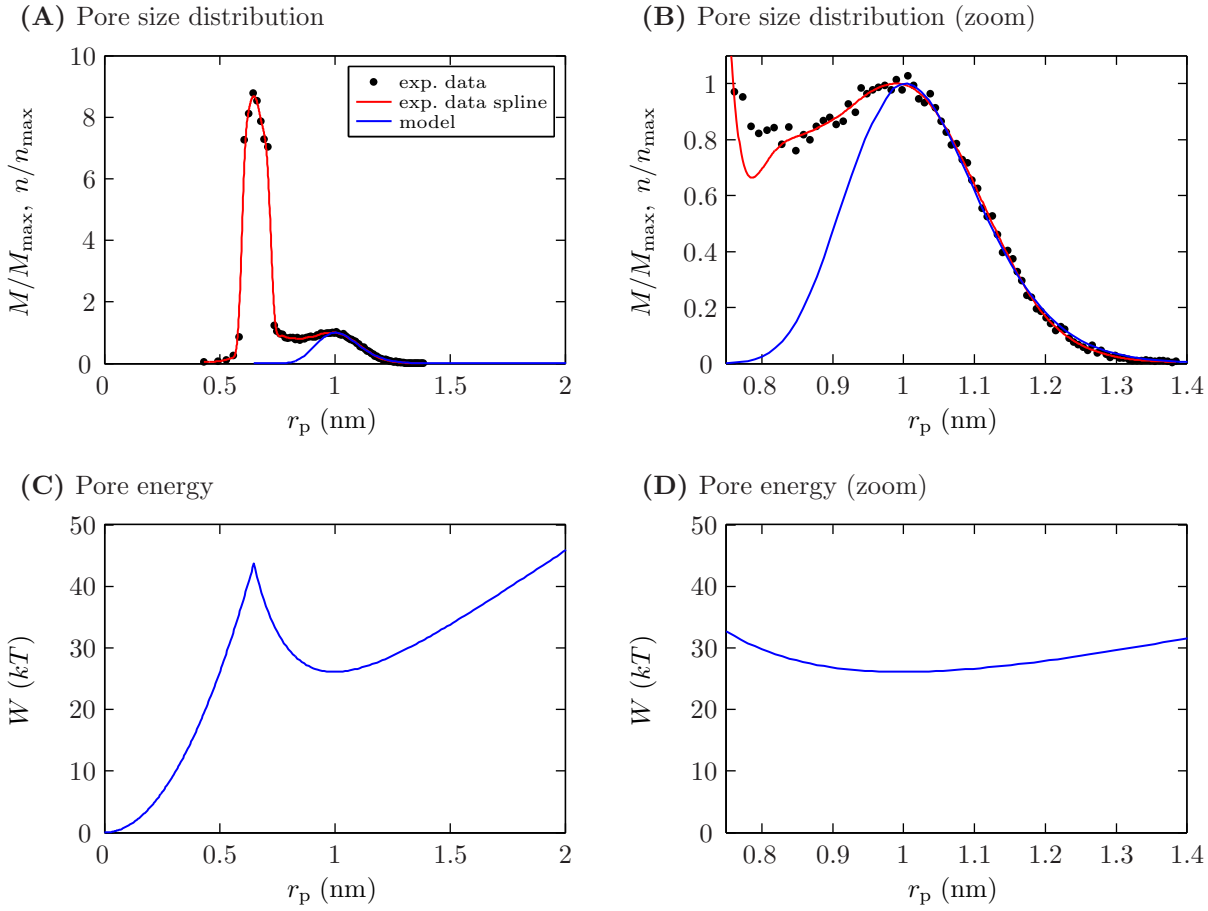

Figure 5.10: Comparison of the Melikov et al. [48] conductance measurement distribution with the model-generated pore density distribution. **(A)** and **(B)** The Melikov et al. [48] distribution is plotted as the number of measurements M at each pore radius (as determined through pore conductance) normalized by the number of measurements of the local maximum $M_{\max}$ at $r_p \approx 1\,\text{nm}$. Similarly, the normalized pore density $n/n_{\max}$ is plotted for comparison. The value of the minimum-energy radius r_m was selected such that the leading edges of the distributions were horizontally aligned. (The distributions were best aligned using $r_m = 0.975\,\text{nm}$.) The shape of the leading edges of the distributions are in very close agreement. **(C)** and **(D)** The pore energy landscape associated with the pore density distributions shown **(A)** and **(B)**. Note that the pore density distributions and pore energy profiles are shown such that their r_p align. At equilibrium for an enforced $\Delta\phi_m$ value, the shape of the pore density distribution is fundamentally determined by the shape of the underlying pore energy landscape. Thus, the fact that the pore density distribution generated by our model agrees well with the experimental data provides partial validation of the underlying description of the pore energy landscape, at least for $r_p \gtrsim r_m$.

Given this interpretation, we used our model to determine the equilibrium pore density distribution $n(r_p)$ for a membrane with transmembrane voltage $\Delta\phi_m = 180\,\text{mV}$ and $r_* = 0.65\,\text{nm}$. Because Melikov et al. reported that some pores persisted for up to $\sim$1s, we used the resealing time constant value $\tau_p = 0.5\,\text{s}$ to determine W_m and W_d. (The results were not sensitive to the value used for τ_p.) We adjusted the value of r_m used in the model until the leading edges of the normalized distributions of measurements, M/M_{max}, and pore density, n/n_{max}, were horizontally aligned, as shown in Fig. 5.10A and B. The distributions were best aligned using $r_m = 0.975\,\text{nm}$. As is clear in Fig. 5.10A and B, the agreement between the leading edges of the distributions is excellent.

Figure 5.10C and D show the pore energy (on two scales) associated with the pore density distributions shown in Fig. 5.10A and B. Note that the pore density distributions and pore energy profiles are displayed such that their *x*-axes align. The shape of the equilibrium pore density distribution is fundamentally determined by the shape of the underlying pore energy landscape. Thus, the finding that the pore density distribution generated by our model agrees well with the experimental data provides partial validation of the underlying description of the pore energy landscape, at least for $r_p \gtrsim r_m$. Note that this region of the energy landscape is dominated by the pore edge energy and, to a lesser extent, the steric repulsion energy (Fig. 5.4).

It is important to bear mind the differences between the Melikov et al. [48] distribution of measurements, or events, and the time-averaged pore distribution generated by our model. The former treats all pores equally, regardless of the duration of their existence, while the latter is fundamentally time-averaged (i.e., normalized by duration of existence). Melikov et al. [48] distinguish between conduction "spikes" with durations of a few milliseconds and conduction "steps" with durations of up to several hundred milliseconds. Thus, for example, if the sub-distribution of measurements at low conductance (radius) corresponded to pores that exist for milliseconds and the sub-distribution of measurements at high conductance (radius) corresponded to pores that exist for hundreds of milliseconds, then the resulting time-averaged distribution of measurements would

still look much like the model-generated pore distribution.

The estimation of r_m (~ 0.98 nm) in this analysis is significant, as r_m is an important parameter for electroporation models and in the interpretation of electroporation experiments. Small pores with $r_p \approx r_m$ predominate during short pulses ($\lesssim 100$ ns) [56, 77] and post-pulse, when pores shrink to $\sim r_m$. Thus, an accurate value of r_m is important in determining transport during pulses of short duration and following pulses of any duration. Note that our assumption that the temperature was ~ 22 °C does slightly affect the value determined for r_m through the effect of temperature on KCl conductivity, but this does not alter our conclusions.

5.4 Conclusions

We have described the energy landscape of electropores and a continuum approach to characterizing pore dynamics in radius space. Our description includes refinements to the steric repulsion and interfacial energy terms commonly used in electroporation models. Additionally, we have employed a phase space description of pore dynamics that provides a straightforward means of understanding the apparently complex, though related, results generated by models of electroporation. Finally, we related the pore conductance measurements of Melikov et al. [48] to pore radius, and used the results to provide partial validation of the description of the pore energy landscape and to determine approximate values of the important electroporation model parameters r_* and r_m.

As noted in the *Introduction*, this paper is the last in a series [43–45] of basic methods-oriented papers. In the previous papers, we characterized the transport properties of ionic and molecular solute [44], developed methods of modeling electrodiffusive transport in discretized systems [45], and described the factors that affect transport through pores [43]. The methods described here for modeling the dynamics of pores in discretized systems provide the final "ingredient" necessary for building spatially distributed cell models of electroporation with concomitant molecular transport. Such models will aid the interpretation of electroporation experiments, which often assess electrical or molecular transport, and be useful for investigating and optimizing applications of

electroporation.

5.5 Appendix

5.5.1 Pore Edge Area

Hydrophilic pores are assumed to have toroidal shape (Fig. 5.1), with lipid head groups lining the edge of the pore. Let $2A_{\mathrm{l,e}}$ be the total area of lipid lining the edge of a pore. Then the edge area associated with each side of the membrane is $A_{\mathrm{l,e}}$.

$A_{\mathrm{l,e}}$ can be found through integration. Consider a toroidal pore with radius r_{p} in a membrane with thickness d_{m} (Fig. 5.1). The area of a small region of the edge is $2\pi\left(r_{\mathrm{p}} + \frac{d_{\mathrm{m}}}{2} - \frac{d_{\mathrm{m}}}{2}\sin\Theta_{\mathrm{l,e}}\right)\left(\frac{d_{\mathrm{m}}}{2}\right)d\Theta_{\mathrm{l,e}}$, where $\Theta_{\mathrm{l,e}}$ is the angle of lipid molecules in the pore edge with respect to vertical. $A_{\mathrm{l,e}}$ is found by integrating this expression from $\Theta_{\mathrm{l,e}} = 0$ to $\Theta_{\mathrm{l,e}} = \frac{\pi}{2}$:

$$A_{\mathrm{l,e}}(r_{\mathrm{p}}) = 2\pi\left(\frac{d_{\mathrm{m}}}{2}\right)\int_0^{\frac{\pi}{2}}\left(r_{\mathrm{p}} + \frac{d_{\mathrm{m}}}{2} - \frac{d_{\mathrm{m}}}{2}\sin\Theta_{\mathrm{l,e}}\right)\mathrm{d}\Theta_{\mathrm{l,e}} \tag{5.35}$$

$$= 2\pi\left(\frac{d_{\mathrm{m}}}{2}\right)\left[\left(r_{\mathrm{p}} + \frac{d_{\mathrm{m}}}{2}\right)\Theta_{\mathrm{l,e}} + \frac{d_{\mathrm{m}}}{2}\cos\Theta_{\mathrm{l,e}}\right]_0^{\frac{\pi}{2}} \tag{5.36}$$

$$= \pi^2\left(\frac{d_{\mathrm{m}}}{2}\right)\left(r_{\mathrm{p}} + \frac{d_{\mathrm{m}}}{2}\right) - 2\pi\left(\frac{d_{\mathrm{m}}}{2}\right)^2. \tag{5.37}$$

5.5.2 Calculation of Steric Repulsion Energy Constants

At zero transmembrane voltage ($\Delta\phi_{\mathrm{m}} = 0\,\mathrm{V}$), the pore energy (Eq. 5.7) is described by

$$W(r_{\mathrm{p}}) = B\left(\frac{r_*}{r_{\mathrm{p}}}\right)^b + C + 2\pi r_{\mathrm{p}}\gamma - \delta A_{\mathrm{l,p}}(r_{\mathrm{p}})\Gamma. \tag{5.38}$$

Here, $\delta A_{\mathrm{l,p}}(r_{\mathrm{p}})$ is the pore lipid area reduction given by Eq. 5.4.

As noted in the main text, we impose three conditions on the energy curve, and this enables determination of the values of the three steric repulsion constants B, b, and C. The first condition is that

the pore energy $W(r_\mathrm{p})$ has a local minimum at $(r_\mathrm{m}, W_\mathrm{m})$. This implies that the derivative of energy with respect to pore radius be zero at this point:

$$\left.\frac{\partial W}{\partial r_\mathrm{p}}\right|_{r_\mathrm{m}} = 0 = -Bb\left(\frac{r_*^b}{r_\mathrm{m}^{b+1}}\right) + 2\pi\gamma - \left(2\pi r_\mathrm{m} + \left(\frac{d_\mathrm{m}}{2}\right)\left(2\pi - \pi^2\right)\right)\Gamma. \tag{5.39}$$

The last term arises as the result of taking the derivative of $\delta A_{\mathrm{l,p}}(r_\mathrm{p})$ with respect to r_p:

$$\frac{\partial(\delta A_{\mathrm{l,p}})}{\partial r_\mathrm{p}} = 2\pi r_\mathrm{p} + \left(\frac{d_\mathrm{m}}{2}\right)\left(2\pi - \pi^2\right). \tag{5.40}$$

Equation 5.39, can be solved for B and simplified to give

$$B = \left(\frac{2\pi r_\mathrm{m}\gamma - \left(2\pi r_\mathrm{m} + \left(\frac{d_\mathrm{m}}{2}\right)\left(2\pi - \pi^2\right)\right) r_\mathrm{m}\Gamma}{b}\right)\left(\frac{r_\mathrm{m}}{r_*}\right)^b. \tag{5.41}$$

B is given in terms of b. Thus, one must determine the value of b before using Eq. 5.41 to determine the value of B.

The second condition is that the energy barrier to destruction $W(r_*) - W(r_\mathrm{m})$ equal the specified value of the energy barrier to pore destruction W_d. Imposing this condition,

$$W_\mathrm{d} = W(r_*) - W(r_\mathrm{m}) \tag{5.42}$$

$$= B\left(1 - \left(\frac{r_*}{r_\mathrm{m}}\right)^b\right) + 2\pi\left(r_* - r_\mathrm{m}\right)\gamma - \left(\delta A_{\mathrm{l,p}}(r_*) - \delta A_{\mathrm{l,p}}(r_\mathrm{m})\right)\Gamma. \tag{5.43}$$

Note that in the last term

$$\delta A_{\mathrm{l,p}}(r_*) - \delta A_{\mathrm{l,p}}(r_\mathrm{m}) = \pi\left(r_*^2 - r_\mathrm{m}^2\right) + \left(\frac{d_\mathrm{m}}{2}\right)\left(2\pi - \pi^2\right)\left(r_* - r_\mathrm{m}\right). \tag{5.44}$$

Substituting for B (Eq. 5.41) and the $\delta A_{\mathrm{l,p}}(r_{\mathrm{p}})$ terms in Eq. 5.43 and simplifying,

$$\left(\frac{2\pi r_{\mathrm{m}}\gamma - \left(2\pi r_{\mathrm{m}} + \left(\frac{d_{\mathrm{m}}}{2}\right)\left(2\pi - \pi^2\right)\right) r_{\mathrm{m}}\Gamma}{b}\right)\left(\left(\frac{r_{\mathrm{m}}}{r_*}\right)^b - 1\right) + 2\pi\left(r_* - r_{\mathrm{m}}\right)\gamma$$
$$- \left(\pi\left(r_*^2 - r_{\mathrm{m}}^2\right) + \left(\frac{d_{\mathrm{m}}}{2}\right)\left(2\pi - \pi^2\right)\left(r_* - r_{\mathrm{m}}\right)\right)\Gamma - W_{\mathrm{d}} = 0. \quad (5.45)$$

b is the only unknown in Eq. 5.45, and its value can be determined by using a graphical method or root finding algorithm. After determining the value of b, the value of B can be found by substituting for b in Eq. 5.41.

The third condition is that the energy $W(r_*)$ equal the specified value W_*. Thus,

$$W(r_*) = W_* = B + C + 2\pi r_*\gamma - \delta A_{\mathrm{l,p}}(r_*)\Gamma. \quad (5.46)$$

Substituting for $\delta A_{\mathrm{l,p}}(r_*)$ and simplifying,

$$C = W_* - B - 2\pi r_*\gamma + \left(\pi\left(r_* + \frac{d_{\mathrm{m}}}{2}\right)^2 - \pi^2\left(\frac{d_{\mathrm{m}}}{2}\right)\left(r_* + \frac{d_{\mathrm{m}}}{2}\right) + 2\pi\left(\frac{d_{\mathrm{m}}}{2}\right)^2\right)\Gamma. \quad (5.47)$$

After substituting for the value determined for B (Eq. 5.41), Eq. 5.47 can be evaluated to give the value of the final steric repulsion constant C.

5.5.3 Hindrance Factor

We described the hindrance factor in detail in a previous publication [43]. Here, for the convenience of the reader, we provide an abbreviated description. For more details, please see Ref. [43].

The hindrance factor accounts for the effect that a solute's size has on its transport through a pore. The hindrance factor H is the product of an effective area factor f_{A} and a drag factor f_{D} [43]:

$$H = f_{\mathrm{A}} f_{\mathrm{D}}. \quad (5.48)$$

The effective area factor f_A accounts for the fact that a solute of finite size can only access the central region of a pore [43, 78]:

$$f_A = \left(1 - \frac{r_s}{r_p}\right)^2. \tag{5.49}$$

The drag factor f_D accounts for the drag exerted on a solute ion by the walls of a pore [43, 79]:

$$f_D = \frac{6\pi}{f_t}, \tag{5.50}$$

where

$$f_t(\lambda) = \frac{9}{4}\pi^2\sqrt{2}(1-\lambda)^{-\frac{5}{2}}\left(1 + a_1(1-\lambda) + a_2(1-\lambda)^2\right) + a_3 + a_4\lambda + a_5\lambda^2 + a_6\lambda^3 + a_7\lambda^4 \tag{5.51}$$

and $\lambda \equiv r_s/r_p$. Here, r_s is the solute radius and r_p is the pore radius. The constants a_i ($i = 1, 2, \ldots, 7$) are shown in Table 5.2.

Parameter	Value
a_1	−1.2167
a_2	1.5336
a_3	−22.5083
a_4	−5.6117
a_5	−0.3363
a_6	−1.216
a_7	1.647

Table 5.2: Values of Constants in the Bungay-Brenner Hindrance Equation

5.5.4 Partition Factor

We described the partition factor in detail in a previous publication [43]. Here, for the convenience of the reader, we provide an abbreviated description. For more details, please see Ref. [43].

The Born energy w_0 is the energy required to place a charge z_s in the center of a pore [43]:

$$w_0(r_p) = 5.3643\frac{(z_s q_e)^2}{kT} r_p^{-1.803}. \tag{5.52}$$

Here, w_0 is in units of kT.

The partition factor $K(r_p, \Delta\psi_p)$ is [43, 51]

$$K(r_p, \Delta\psi_p) = \frac{e^{\Delta\psi_p} - 1}{\frac{w_0 e^{w0 - n\Delta\psi_p} - n\Delta\psi_p}{w_0 - n\Delta\psi_p} e^{\Delta\psi_p} - \frac{w_0 e^{w0 + n\Delta\psi_p} + n\Delta\psi_p}{w_0 + n\Delta\psi_p}}. \tag{5.53}$$

Here, q_e is the electronic charge, n is the relative entrance length of a pore, and

$$\Delta\psi_p \equiv \frac{q_e z_s}{kT} \Delta\phi_p, \tag{5.54}$$

where $\Delta\phi_p$ is the transpore voltage, the voltage drop across the internal pore region. $\Delta\phi_p$ is related to transmembrane voltage $\Delta\phi_m$ by voltage division [43] :

$$\Delta\phi_p = \frac{R_{p,p}}{R_p} \Delta\phi_m. \tag{5.55}$$

Here, $R_{p,p}$ is the resistance of the internal pore region and R_p is the total resistance associated with the pore (i.e., the sum of $R_{p,p}$ and the access resistance $R_{p,a}$).

References

[1] Neumann, E., Schaefer-Ridder, M., Wang, Y., and Hofschneider, P.H. Gene transfer into mouse lyoma cells by electroporation in high electric fields. *EMBO J*, 1(7):841–5, 1982.

[2] Wong, T.K. and Neumann, E. Electric field mediated gene transfer. *Biochem Bioph Res Co*, 107(2):584–7, 1982.

[3] Klenchin, V.A., Sukharev, S.I., Serov, S.M., Chernomordik, L.V., and Chizmadzhev, Y.A. Electrically induced DNA uptake by cells is a fast process involving DNA electrophoresis. *Biophys J*, 60(4):804–811, 1991.

[4] Sukharev, S.I., Klenchin, V.A., Serov, S.M., Chernomordik, L.V., and Chizmadzhev, Y.A. Electroporation and electrophoretic DNA transfer into cells – The effect of DNA interaction with electropores. *Biophys J*, 63(5):1320–1327, 1992.

[5] Heller, R., Jaroszeski, M., Atkin, A., Moradpour, D., Gilbert, R., Wands, J., and Nicolau, C. In vivo gene electroinjection and expression in rat liver. *FEBS Lett*, 389(3):225–8, 1996.

[6] Aihara, H. and Miyazaki, J. Gene transfer into muscle by electroporation in vivo. *Nat Biotechnol*, 16(9):867–870, 1998.

[7] Rols, M.P., Delteil, C., Golzio, M., Dumond, P., Cros, S., and Teissie, J. In vivo electrically mediated protein and gene transfer in murine melanoma. *Nat Biotechnol*, 16(2):168–171, 1998.

[8] Rols, M.P. and Teissie, J. Electropermeabilization of mammalian cells to macromolecules: Control by pulse duration. *Biophys J*, 75(3):1415–1423, 1998.

[9] Mir, L.M., Bureau, M.F., Gehl, J., Rangara, R., Rouy, D., Caillaud, J.M., Delaere, P., Branellec, D., Schwartz, B., and Scherman, D. High-efficiency gene transfer into skeletal muscle mediated by electric pulses. *P Natl Acad Sci USA*, 96(8):4262–4267, 1999.

[10] Rizzuto, G., Cappelletti, M., Maione, D., Savino, R., Lazzaro, D., Costa, P., Mathiesen, I., Cortese, R., Ciliberto, G., Laufer, R., La Monica, N., and Fattori, E. Efficient and regulated erythropoietin production by naked DNA injection and muscle electroporation. *P Natl Acad Sci USA*, 96(11):6417–6422, 1999.

[11] Widera, G., Austin, M., Rabussay, D., Goldbeck, C., Barnett, S.W., Chen, M.C., Leung, L., Otten, G.R., Thudium, K., Selby, M.J., and Ulmer, J.B. Increased DNA vaccine delivery and immunogenicity by electroporation in vivo. *J Immunol*, 164:4635–4640, 2000.

[12] Goto, T., Nishi, T., Tamura, T., Dev, S.B., Takeshima, H., Kochi, M., Yoshizato, K., Kuratsu, J., Sakata, T., Hofmann, G.A., and Ushio, Y. Highly efficient electro-gene therapy of solid tumor by using an expression plasmid for the herpes simplex virus thymidine kinase gene. *P Natl Acad Sci USA*, 97(1):354–359, 2000.

[13] Canatella, P.J. and Prausnitz, M.R. Prediction and optimization of gene transfection and drug delivery by electroporation. *Gene Ther*, 8(19):1464–1469, 2001.

[14] Andre, F. and Mir, L.M. DNA electrotransfer: Its principles and an updated review of its therapeutic applications. *Gene Ther*, 11:S33–S42, 2004.

[15] Heller, L.C., Jaroszeski, M.J., Coppola, D., McCray, A.N., Hickey, J., and Heller, R. Optimization of cutaneous electrically mediated plasmid DNA delivery using novel electrode. *Gene Ther*, 14(3):275–280, 2007.

[16] Guignet, E.G. and Meyer, T. Suspended-drop electroporation for high-throughput delivery of biomolecules into cells. *Nat Methods*, 5(5):393–395, 2008.

[17] Hojman, P., Gissel, H., Andre, F., Cournil-Henrionnet, C., Eriksen, J., Gehl, J., and Mir, L. Physiological effects of high and low voltage pulse combinations for gene electrotransfer in muscle. *Hum Gene Ther*, 2008.

[18] André, F.M., Gehl, J., Sersa, G., Préat, V., Hojman, P., Eriksen, J., Golzio, M., Cemazar, M., Pavselj, N., Rols, M.P., Miklavcic, D., Neumann, E., Teissié, J., and Mir, L.M. Efficiency of high- and low-voltage pulse combinations for gene electrotransfer in muscle, liver, tumor, and skin. *Hum Gene Ther*, 19(11):1261–71, 2008.

[19] Cemazar, M., Golzio, M., Sersa, G., Hojman, P., Kranjc, S., Mesojednik, S., Rols, M., and Teissie, J. Control by pulse parameters of DNA electrotransfer into solid tumors in mice. *Gene Ther*, 2009.

[20] Okino, M. and Mohri, H. Effects of a high-voltage electrical impulse and an anticancer drug on in vivo growing tumors. *Jpn J Cancer Res*, 78:1319–1321, 1987.

[21] Mir, L.M., Orlowski, S., Belehradek, J., and Paoletti, C. Electrochemotherapy potentiation of antitumor effect of bleomycin by local electric pulses. *Eur J Cancer*, 27(1):68–72, 1991.

[22] Belehradek, J., Orlowski, S., Poddevin, B., Paoletti, C., and Mir, L.M. Electrochemotherapy of spontaneous mammary-tumors in mice. *Eur J Cancer*, 27(1):73–76, 1991.

[23] Belehradek, M., Domenge, C., Luboinski, B., Orlowski, S., Belehradek, J., and Mir, L.M. Electrochemotherapy, a new antitumor treatment - 1st clinical phase-I-II trial. *Cancer*, 72(12):3694–3700, 1993.

[24] Sersa, G., Cemazar, M., and Miklavcic, D. Antitumor effectiveness of electrochemotherapy with cis-diamminedichloroplatinum(II) in mice. *Cancer Res*, 55(15):3450–3455, 1995.

[25] Heller, R., Jaroszeski, M.J., Glass, L.F., Messina, J.L., Rapaport, D.P., DeConti, R.C., Fenske, N.A., Gilbert, R.A., Mir, L.M., and Reintgen, D.S. Phase I/II trial for the treatment of cutaneous and subcutaneous tumors using electrochemotherapy. *Cancer*, 77(5):964–971, 1996.

[26] Hofmann, G.A., Dev, S.B., and Nanda, G.S. Electrochemotherapy: Transition from laboratory to the clinic. *IEEE Eng Med Biol*, 15:124–132, 1996.

[27] Mir, L.M. and Orlowski, S. Mechanisms of electrochemotherapy. *Adv Drug Deliv Rev*, 35(1):107–118, 1999.

[28] Gothelf, A., Mir, L.M., and Gehl, J. Electrochemotherapy: Results of cancer treatment using enhanced delivery of bleomycin by electroporation. *Cancer Treat Rev*, 29(5):371–387, 2003.

[29] Soden, D.M., Larkin, J.O., Collins, C.G., Tangney, M., Aarons, S., Piggott, J., Morrissey, A., Dunne, C., and O'Sullivan, G.C. Successful application of targeted electrochemotherapy using novel flexible electrodes and low dose bleomycin to solid tumours. *Cancer Lett*, 232:300–310, 2006.

[30] Tekle, E., Astumian, R.D., and Chock, P.B. Electroporation by using bipolar oscillating electric field: An improved method for DNA transfection of NIH 3T3 cells. *P Natl Acad Sci USA*, 88(10):4230–4, 1991.

[31] Glogauer, M. and McCulloch, C.A. Introduction of large molecules into viable fibroblasts by electroporation: Optimization of loading and identification of labeled cellular compartments. *Exp Cell Res*, 200(2):227–34, 1992.

[32] Neumann, E., Toensing, K., Kakorin, S., Budde, P., and Frey, J. Mechanism of electroporative dye uptake by mouse B cells. *Biophys J*, 74(1):98–108, 1998.

[33] Gehl, J. and Mir, L.M. Determination of optimal parameters for in vivo gene transfer by electroporation, using a rapid in vivo test for cell permeabilization. *Biochem Bioph Res Co*, 261(2):377–380, 1999.

[34] Bettan, M., Ivanov, M.A., Mir, L.M., Boissiere, F., Delaere, P., and Scherman, D. Efficient DNA electrotransfer into tumors. *Bioelectrochemistry*, 52(1):83–90, 2000.

[35] Wells, J.M., Li, L.H., Sen, A., Jahreis, G.P., and Hui, S.W. Electroporation-enhanced gene delivery in mammary tumors. *Gene Ther*, 7(7):541–547, 2000.

[36] Shirakashi, R., Kostner, C.M., Muller, K.J., Kurschner, M., Zimmermann, U., and Sukhorukov, V.L. Intracellular delivery of trehalose into mammalian cells by electropermeabilization. *J Membrane Biol*, 189(1):45–54, 2002.

[37] Puc, M., Kotnik, T., Mir, L.M., and Miklavcic, D. Quantitative model of small molecules uptake after in vitro cell electropermeabilization. *Bioelectrochemistry*, 60(1-2):1–10, 2003.

[38] Bestman, J.E., Ewald, R.C., Chiu, S.L., and Cline, H.T. In vivo single-cell electroporation for transfer of DNA and macromolecules. *Nat Protoc*, 1(3):1267–1272, 2006.

[39] Sel, D., Lebar, A.M., and Miklavcic, D. Feasibility of employing model-based optimization of pulse amplitude and electrode distance for effective tumor electropermeabilization. *IEEE T Bio-Med Eng*, 54(5):773–781, 2007.

[40] Agarwal, A., Zudans, I., Orwar, O., and Weber, S.G. Simultaneous maximization of cell permeabilization and viability in single-cell electroporation using an electrolyte-filled capillary. *Anal Chem*, 79(1):161–167, 2007.

[41] Chen, C., Evans, J.A., Robinson, M.P., Smye, S.W., and O'Toole, P. Measurement of the efficiency of cell membrane electroporation using pulsed ac fields. *Phys Med Biol*, 53(17):4747–4757, 2008.

[42] Tanaka, M., Yanagawa, Y., and Hirashima, N. Transfer of small interfering RNA by single-cell electroporation in cerebellar cell cultures. *J Neurosci Meth*, 178(1):80–6, 2009.

[43] Smith, K.C. and Weaver, J.C. Effects of hindrance and partitioning on ionic and molecular transport through small lipidic pores (in preparation).

[44] Smith, K.C. and Weaver, J.C. Compilation and computation of the size, charge, and diffusivity of fluorescent dyes and other small molecules (in preparation).

[45] Smith, K.C. and Weaver, J.C. Electrodiffusion of molecules in aqueous media: A robust, discretized description for electroporation and other transport phenomena (in preparation).

[46] Smith, K.C., Gowrishankar, T.R., Esser, A.T., Stewart, D.A., and Weaver, J.C. The spatially distributed dynamic transmembrane voltage of cells and organelles due to 10-ns pulses: Meshed transport networks. *IEEE T Plasma Sci*, 34:1394–1404, 2006.

[47] Smith, K.C. and Weaver, J.C. Active mechanisms are needed to describe cell responses to submicrosecond, megavolt-per-meter pulses: Cell models for ultrashort pulses. *Biophys J*, 95(4):1547–1563, 2008.

[48] Melikov, K.C., Frolov, V.A., Shcherbakov, A., Samsonov, A.V., Chizmadzhev, Y.A., and Chernomordik, L.V. Voltage-induced nonconductive pre-pores and metastable single pores in unmodified planar lipid bilayer. *Biophys J*, 80(4):1829–1836, 2001.

[49] Abidor, I.G., Arakelyan, V.B., Chernomordik, L.V., Chizmadzhev, Y.A., Pastushenko, V.F., and Tarasevich, M.R. Electric breakdown of bilayer lipid-membranes I. Main experimental facts and their qualitative discussion. *Bioelectroch Bioener*, 6(1):37–52, 1979.

[50] Pastushenko, V.F., Chizmadzhev, Y.A., and Arakelyan, V.B. Electric breakdown of bilayer lipid-membranes .II. Calculation of the membrane lifetime in the steady-state diffusion approximation. *Bioelectroch Bioener*, 6(1):53–62, 1979.

[51] Chernomordik, L.V., Sukharev, S.I., Popov, S.V., Pastushenko, V.F., Sokirko, A.V., Abidor, I.G., and Chizmadzhev, Y.A. The electrical breakdown of cell and lipid membranes: The similarity of phenomenologies. *Biochim Biophys Acta*, 902(3):360–73, 1987.

[52] Glaser, R.W., Leikin, S.L., Chernomordik, L.V., Pastushenko, V.F., and Sokirko, A.I. Reversible electrical breakdown of lipid bilayers: Formation and evolution of pores. *Biochim Biophys Acta*, 940(2):275–287, 1988.

[53] Neu, J.C. and Krassowska, W. Asymptotic model of electroporation. *Phys Rev E*, 59(3):3471–3482, 1999.

[54] Neu, J.C., Smith, K.C., and Krassowska, W. Electrical energy required to form large conducting pores. *Bioelectrochemistry*, 60(1–2):107–114, 2003.

[55] Neu, J.C. and Krassowska, W. Modeling postshock evolution of large electropores. *Phys Rev E*, 67(2), 2003.

[56] Vasilkoski, Z., Esser, A.T., Gowrishankar, T.R., and Weaver, J.C. Membrane electroporation: The absolute rate equation and nanosecond time scale pore creation. *Phys Rev E*, 74(2), 2006.

[57] Litster, J.D. Stability of lipid bilayers and red blood-cell membranes. *Phys Lett A*, A 53(3):193–194, 1975.

[58] Tieleman, D.P., Leontiadou, H., Mark, A.E., and Marrink, S.J. Simulation of pore formation in lipid bilayers by mechanical stress and electric fields. *J Am Chem Soc*, 125(21):6382–6383, 2003.

[59] Tieleman, D.P. The molecular basis of electroporation. *BMC Biochem*, 5(10), 2004.

[60] Vernier, P.T., Ziegler, M.J., Sun, Y.H., Chang, W.V., Gundersen, M.A., and Tieleman, D.P. Nanopore formation and phosphatidylserine externalization in a phospholipid bilayer at high transmembrane potential. *J Am Chem Soc*, 128:6288–6289, 2006.

[61] Wohlert, J., den Otter, W.K., Edholm, O., and Briels, W.J. Free energy of a trans-membrane pore calculated from atomistic molecular dynamics simulations. *J Chem Phys*, 124, 2006.

[62] Leontiadou, H., Mark, A.E., and Marrink, S.J. Ion transport across transmembrane pores. *Biophys J*, 92(12):4209–4215, 2007.

[63] Bockmann, R.A., de Groot, B.L., Kakorin, S., Neumann, E., and Grubmuller, H. Kinetics, statistics, and energetics of lipid membrane electroporation studied by molecular dynamics simulations. *Biophys J*, 95(4):1837–1850, 2008.

[64] Barnett, A. and Weaver, J.C. Electroporation – A unified, quantitative theory of reversible electrical breakdown and mechanical rupture in artificial planar bilayer-membranes. *Bioelectroch Bioener*, 25(2):163–182, 1991.

[65] Djuzenova, C.S., Zimmermann, U., Frank, H., Sukhorukov, V.L., Richter, E., and Fuhr, G. Effect of medium conductivity and composition on the uptake of propidium iodide into electropermeabilized myeloma cells. *Biochim Biophys Acta*, 1284(2):143–52, 1996.

[66] Tekle, E., Astumian, R.D., Friauf, W.A., and Chock, P.B. Asymmetric pore distribution and loss of membrane lipid in electroporated DOPC vesicles. *Biophys J*, 81(2):960–8, 2001.

[67] He, H., Chang, D.C., and Lee, Y.K. Nonlinear current response of micro electroporation and resealing dynamics for human cancer cells. *Bioelectrochemistry*, 72(2):161–168, 2008.

[68] Powell, K.T. and Weaver, J.C. Transient aqueous pores in bilayer-membranes – A statistical-theory. *Bioelectroch Bioener*, 15(2):211–227, 1986.

[69] Freeman, S.A., Wang, M.A., and Weaver, J.C. Theory of electroporation of planar bilayer membranes: Predictions of the aqueous area, change in capacitance, and pore-pore separation. *Biophys J*, 67(1):42–56, 1994.

[70] Esser, A.T., Smith, K.C., Gowrishankar, T.R., Vasilkoski, Z., and Weaver, J.C. Mechanisms for the intracellular manipulation of organelles by conventional electroporation. *Biophys J*, 98(11):2506–14, 2010.

[71] Newman, J. Resistance for flow of current to a disk. *J Electrochem Soc*, 113(5):501–502, 1966.

[72] Hall, J.E. Access resistance of a small circular pore. *J Gen Physiol*, 66(4):531–2, 1975.

[73] Dai, J. and Sheetz, M.P. Regulation of endocytosis, exocytosis, and shape by membrane tension. *Cold Spring Harb Sym*, 60:567–71, 1995.

[74] Smith, K.C., Neu, J.C., and Krassowska, W. Model of creation and evolution of stable electropores for DNA delivery. *Biophys J*, 86(5):2813–2826, 2004.

[75] Krassowska, W. and Filev, P.D. Modeling electroporation in a single cell. *Biophys J*, 92(2):404–417, 2007.

[76] Lide, D.R., editor. *CRC Handbook of Chemistry and Physics*. CRC Press, Boca Raton, FL, 2005.

[77] Smith, K.C. and Weaver, J.C. Transmembrane molecular transport during versus after nanosecond electric pulses (in preparation).

[78] Renkin, E.M. Filtration, diffusion, and molecular sieving through porous cellulose membranes. *J Gen Physiol*, 38(2):225–43, 1954.

[79] Bungay, P.M. and Brenner, H. The motion of a closely-fitting sphere in a fluid-filled tube. *Int J of Multiphas Flow*, 1(1):25–56, 1973.

Chapter 6

Transmembrane Molecular Transport During Versus After Nanosecond Electric Pulses

Abstract

Recently there has been great and growing interest in the biological effects of nanosecond electric pulses, particularly apoptosis induction. These effects have been hypothesized to result from the widespread creation of small, lipidic pores in the plasma and organelle membranes of cells (supra-electroporation), and more specifically, ionic and molecular transport through these pores. Here we address the basic question of whether such transport occurs predominantly during or after pulsing. First, we demonstrate that the electrical drift distance for typical charged solutes during nanosecond pulses (up to 100 ns), even those with very large magnitudes (up to 10 MV/m), ranges from only a fraction of the membrane thickness (5 nm) to several membrane thicknesses. This is much smaller than the diameter of a typical cell ($\sim 16\,\mu$m). This implies that molecular drift transport during nanosecond pulses is necessarily minimal. This implication is not dependent on assumptions about pore density or the flux through pores. Furthermore, considerations of pore density, hindrance, and partitioning suggest that transport during nanosecond pulses is several orders of magnitudes smaller. Second, we show that molecular transport resulting from post-pulse diffusion through minimum-size pores is orders of magnitude larger than electrical drift-driven transport during nanosecond pulses. While field-assisted charge entry and the magnitude of flux favor transport during nanosecond pulses, these effects are too small to overcome the orders of orders of magnitude more time available for post-pulse transport. Accordingly, our basic conclusion holds across the plausible range of relevant parameters.

6.1 Introduction

In the past decade there has been intense and growing interest in the effects that extremely short duration ($< 1\,\mu s$), large magnitude ($10-100\,kV/cm$) pulsed electric fields have on cells [1–30]. A number of studies [6, 8, 11, 16, 18] have reported that such pulses result in significantly less transport than the longer duration ($10\,\mu s-10\,ms$), smaller magnitude ($1\,kV/cm$–$10\,kV/cm$) pulsed electric fields widely used for electroporation ("conventional electroporation"). In fact, some of these early studies [1–7, 9, 10, 13] even concluded that short pulses do not result in plasma membrane (PM) electroporation.

In a previous study [27], we showed that for short duration, large magnitude pulses to escape electroporation of the PM, the PM would have to endure extremely large transmembrane voltages, e.g., approaching $\sim 30\,V$. These extremely large values have not been observed and lead to implications that are not convincing. Moreover, such large transmembrane voltages are in marked contrast to experimental evidence [24] that suggests the transmembrane voltage has a maximum value closer to $\sim 1.5\,V$, consistent with the results of mechanistic models of electroporation [19–22, 27, 28].

We have argued that the primary mechanism by which short duration, large magnitude pulsed electric fields affect biological systems is through the widespread perturbation of cell membranes (both the PM and organelle membranes) by supra-electroporation [19–22, 27, 28]. The effects reported in response to these pulses, such as apoptosis [1–4, 8, 14, 23, 25, 26, 29, 30], are not seen in response to conventional electroporation pulses, and are thought to occur due to electroporation of the PM and organelle membranes and resultant transport of ions and molecules through these membranes.

To understand and potentially optimize and exploit these effects for therapeutic purposes, we must therefore gain a better understanding of the molecular and ionic transport that results from short pulses. To that end, here we address a basic question: When does transmembrane transport pre-

dominantly occur for these pulses? During or after pulsing?

We have previously argued [20–22, 27, 28] that short pulses should result in minimal molecular transport because small pores discriminate strongly based on solute size and charge. Here, we support and expand this assertion using simple, quantitative arguments. Specifically, we demonstrate that very little molecular transport occurs during short pulses ($\lesssim 100$ ns). Instead, essentially all molecular transport takes place post-pulse. This may be a surprise. However, it is consistent with the experimental findings that these pulses result in less transport per pulse than conventional pulses [6, 8, 16, 18] and that a large number of pulses (of order $10-1000$) is required to achieve significant effects [14, 16, 23, 25, 29, 30].

6.2 Methods

Here we consider approximate descriptions, first based on bulk electrolyte and then on additional estimates that involve pore properties. Out analysis is intentionally simplified, seeking general insight that is essentially independent of cell details. Throughout we consider electrodiffusion. Post-pulse inflow of water may also occur, particularly for in vitro conditions, but such hydrodynamic effects should only strengthen our conclusion that post-pulse molecular transport dominates.

6.2.1 Pore Creation, Expansion, and Destruction

Electroporation is a phenomenon in which pores are hypothesized to form in lipid bilayers in response to large transmembrane voltages $\Delta\phi_m$ [31]. The process is self-limiting because the creation and subsequent expansion of pores is driven by elevated transmembrane voltage $\Delta\phi_m$, but the creation and expansion of pores tends to decrease $\Delta\phi_m$ by increasing the conductance of the membrane and thereby decreasing the rate of creation and expansion of pores. That is, the dynamics of electroporation are such that they diminish its own driving force.

Whether pore creation or expansion is dominant in increasing the membrane conductance during a pulse, and thereby limiting further creation and expansion, is determined by the time scale and

magnitude of the pulse. For nanosecond time scale pulses with magnitudes on the order of several megavolts-per-meter, creation dominates and rapidly drives $\Delta\phi_m$ down to a level ($\sim$0.5 V) at which further pore creation and expansion effectively cease [22]. As a result, there is very little pore expansion for these pulses [22, 28], and pores accumulate near $r_p = r_{p,min} \approx 0.8$ nm [32], the radius at which there is an energy minimum when $\Delta\phi_m \lesssim 0.5$ V [33–35].

Rapid pore creation results in the establishment of a large pore density N in the PM (and other membranes) of the cell. For a nanosecond time scale pulse with a megavolt-per-meter magnitude, the pore density N may reach values up to $\sim 5 \times 10^{16}$ pores/m^2 [20, 27]. Nonetheless, the actual value of N is not important to the central point of this paper: Transport in response to short pulses occurs predominantly post-pulse. While there is a short transient (e.g., $\sim 1-3$ ns [19, 27], depending in part on the pulse rise-time) between the application of a pulse and the burst of pore creation, for clarity of presentation we assume that the initial pore density $N = N_0$ is established immediately and remains constant for the duration of the pulse. This simplifies our description, but it is a useful approximation.

Post-pulse, the pore density $N(t)$ is assumed to decay with an exponential resealing time-constant (pore lifetime) τ_p:

$$N(t) = N_0 e^{-t/\tau_p}. \tag{6.1}$$

Estimates of the resealing time-constant τ_p reported for various membrane systems (bilayer lipid membranes, vesicles, and cells) vary widely, from fractions of a second [36, 37] to minutes [38]. Here, we use an intermediate value $\tau_p = 1$ s.

Figure 6.1 shows a pore with toroidal conformation. As a hydrophilic pore forms, the lipid molecules wrap around the interior edge of a pore, giving it a toroidal shape [32, 39–41]. This general picture is supported by recent molecular dynamics simulation results [42–47].

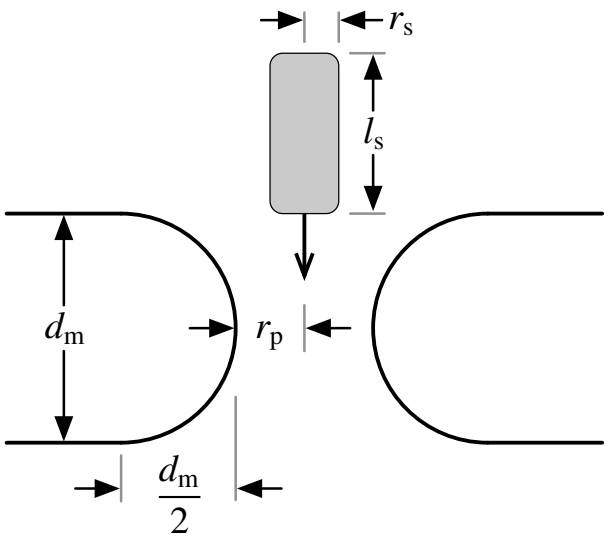

Figure 6.1: Movement of a cylindrical molecule through a toroidal pore. The cylindrical molecule has radius r_s and length l_s, and the pore has radius r_p in a membrane of thickness d_m. As shown, the molecule is assumed to traverse the pore with its long axis parallel to the axis of the pore [48, 49].

6.2.2 Molecular Transport in Bulk Electrolyte

Molecular transport in bulk electrolyte occurs by unhindered electrodiffusion, the combination of electrical drift and diffusion. The electrodiffusive flux $\boldsymbol{J}_s$ is described by [50, 51]

$$\boldsymbol{J}_s = -D_s \nabla\gamma - \frac{D_s}{kT} q_e z_s \gamma \nabla\phi. \tag{6.2}$$

Here, γ is solute concentration, ϕ is electric potential, D_s is solute diffusivity, z_s is solute charge (valence), q_e is elementary charge, k is the Boltzmann constant, and T is absolute temperature. The first term in Eq. 6.2 describes the flux of solute resulting from a gradient in concentration (diffusion), and the second term describes the flux of solute resulting from a gradient in electric potential (electrical drift).

During the application of a large electric field, molecular transport (for charged species) is dominated by electrical drift. The terminal velocity (steady state) v_{drift} at which charged solute drifts in

the presence of an applied electric field with magnitude E is

$$v_{\text{drift}} = \left(\frac{D_s q_e |z_s|}{kT}\right) E. \tag{6.3}$$

In time t, the solute will drift distance d_{drift}:

$$d_{\text{drift}} = v_{\text{drift}} t = \left(\frac{D_s q_e |z_s|}{kT}\right) Et. \tag{6.4}$$

In the absence of an applied electric field (e.g., following the application of an electric pulse), molecular transport is dominated by diffusion. In electroporation systems (e.g., cuvettes), the solute concentration γ tends to be uniform over large regions of the system. The important exception is at interfaces (e.g., membranes and electrodes), where concentration may change significantly over short distances, and it is in these regions that diffusion becomes important [52].

6.2.3 Molecular Transport Through Pores

The electrodiffusive flux equation (Eq. 6.2) for bulk electrolyte can be adapted to describe electrodiffusion through pores by scaling the flux J_s by the hindrance factor H and the partition coefficient K, as described in detail in Smith and Weaver [49]. That is, the flux $J_{s,p}$ through a pore is simply related to the flux J_s calculated using bulk electrolyte assumptions (Eq. 6.2) by

$$J_{s,p} = HKJ_s. \tag{6.5}$$

The hindrance factor H ($0 \leq H \leq 1$), is a function of solute size and pore radius [49, 53, 54] and accounts for the effect of finite size on a solute as it interacts with and moves through a pore. $H \to 0$ (and transport is significantly impeded) when the solute size approaches the pore size, and $H \to 1$

(and transport is not significantly impeded) when the solute size is much smaller than the pore size. We are aware of our invoking a "rigid sieving" approximation, appreciating that lipid pores experience both fluctuations and the possibility of some pore size change as solute approaches [55].

As examples, consider the hindrance factors for yo-pro-1 and propidium for the approximate radius of a minimum-size pore, $r_{p,min} = 0.8\,nm$. Yo-pro-1, which can be approximated as a cylinder with radius $r_s = 0.53\,nm$ and length $l_s = 1.71\,nm$ [48], has hindrance factor $H(r_{p,min}) = 4.0 \times 10^{-3}$. The larger propidium, which can be approximated as a cylinder with radius $r_s = 0.69\,nm$ and length $l_s = 1.55\,nm$ [48], has smaller hindrance factor $H(r_{p,min}) = 8.3 \times 10^{-5}$. It is important to note that for a minimum-size pore $H \ll 1$ for both molecules (and indeed all molecules of similar size), and thus, hindrance greatly diminishes transport through minimum-size pores.

The partition coefficient K ($0 \leq K \leq 1$) is a function of the solute charge, pore radius, and transmembrane voltage [32, 41, 49] and accounts for the effect that the solute charge has on its interaction with and transport through a pore in a low dielectric constant material (e.g., lipid) [56, 57]. To first order, partitioning only affects charged molecules, and thus $K = 1$ (and transport is to a reasonable approximation unimpeded by partitioning) if the solute charge $z_s = 0$. For charged solute ($z_s \neq 0$), $K \to 1$ (and transport is less impeded) as the pore radius r_p increases or the transmembrane voltage $\Delta\phi_m$ increases, and $K \to 0$ (and transport is more impeded) as the pore radius r_p decreases or the transmembrane voltage $\Delta\phi_m$ decreases. For any given r_p and $\Delta\phi_m$, K is smaller for solutes with larger charge $|z_s|$ [49].

Again, consider a minimum-size pore with radius $r_{p,min} = 0.8\,nm$. At $\Delta\phi_m = 0\,V$, the partition coefficients $K(z_s)$ for several solute charges z_s are $K(0) = 0$, $K(\pm1) = 0.51$, $K(\pm2) = 0.053$, $K(\pm3) = 8.9 \times 10^{-4}$, and $K(\pm4) = 2.6 \times 10^{-6}$. For a much larger (supra-physiological) $\Delta\phi_m = 1\,V$, the partition coefficients $K(z_s)$ for these same solute charges z_s are $K(0) = 0$, $K(\pm1) = 0.91$, $K(\pm2) = 0.83$, $K(\pm3) = 0.74$, and $K(\pm4) = 0.65$. (Note that yo-pro-1 and propidium both have charge $z_s = +2$ [49]). Thus, partitioning impedes transport through pores much more significantly

when $\Delta\phi_m = 0\,V$ (e.g., post-pulse) than when $\Delta\phi_m = 1\,V$ (e.g., during a pulse).

In the results and analysis that follow, we characterize transport during a pulse by partition coefficient K_{during} and characterize transport after a pulse by K_{after}. Here, K_{during} is the partition coefficient for a minimum-size pore $r_{p,min} = 0.8\,nm$ and transmembrane voltage $\Delta\phi_m = 1.5\,V$, approximately the maximum $\Delta\phi_m$ reported by Frey et al. [24]. This maximum transmembrane voltage value is also seen in mechanistic models of electroporation [20, 22, 27, 28]. K_{after} is the partition coefficient for a minimum-size pore $r_{p,min} = 0.8\,nm$ and transmembrane voltage $\Delta\phi_m \approx 0\,V$, the transmembrane voltage that persists for many multiples of τ_p following a large electric pulse, as the large number of pores shunts the resting potential sources, thereby preventing the recovery of the resting potential until nearly all pores have resealed [27].

6.3 Results and Discussion

6.3.1 Electrical Drift Distance During Short Pulses

The electrical drift distance d_{drift} (Eq. 6.4) provides an explicit but approximate and intuitive means for understanding why molecular uptake during short pulses must be extremely small: If molecules drift only a short distance during a pulse, then it is not possible for many of the molecules to pass through membrane pores and into a cell. In other words, the molecular dose (mass or molecules per cell) delivered during a pulse will be small. This is clear in Fig. 6.2.

Consider a circular plane with area $A_{cell}/2$ (area of one side of a cell with total area A_{cell}) in a standard pulsing medium containing a fluorescent probe (e.g., propidium or yo-pro-1). An electric field of magnitude E_{pulse} is applied normal to the plane for a duration t_{pulse}. The distance d_{drift} through which solute molecules with diffusivity D_s and valence z_s drift during the pulse is (from Eq. 6.4)

$$d_{drift} = \left(\frac{D_s q_e |z_s|}{kT}\right) E_{pulse}\, t_{pulse}, \tag{6.6}$$

where q_e is elementary charge, k is the Boltzmann constant, and T is absolute temperature. (The

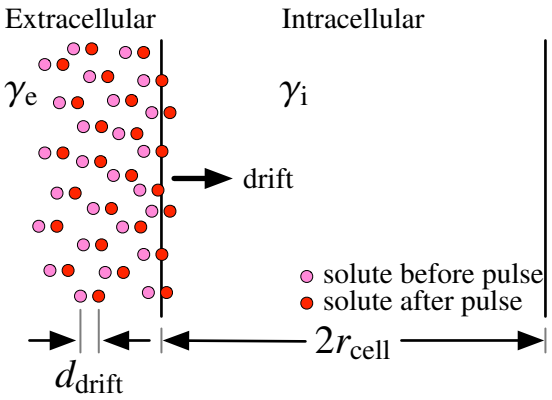

Figure 6.2: Electrical drift during short pulses. The position of a charged solute is shown before (*pink*) and immediately after (*red*) application of an electric pulse. During the pulse, the solute drifts a distance d_{drift}. Because the pulse is short ($\lesssim 100$ ns), d_{drift} is necessarily much smaller than the cell diameter $2r_{cell}$ ($d_{drift} \ll 2r_{cell}$). Consequently, only a small number of solute molecules enter the cell during the pulse, and the intercellular concentration of solute γ_i immediately following the pulse is much smaller than the extracellular concentration of solute γ_e ($\gamma_i \ll \gamma_e$).

grouped factor is electrical mobility.) For short pulses, d_{drift} is incredibly small. As an example, consider propidium ($D_s = 42.8 \times 10^{-11}\,m^2/s$, $z_s = +2$ [48]). With an applied electric field pulse with duration $t_{pulse} = 4$ ns and magnitude $E_{pulse} = 8$ MV/m [16] at 25 °C, d_{drift} is only 1.1 nm, a fraction (~0.2) of the membrane thickness ($d_m = 5$ nm). Even for a significantly longer pulse, with duration $t_{pulse} = 60$ ns and magnitude $E_{pulse} = 9.5$ MV/m [24], d_{drift} is just 19 nm, or ~4 times the membrane thickness d_m. Thus, very little solute will enter the cell.

Note that in both of these examples d_{drift} is much smaller than the diameter of a typical cell ($2r_{cell} \approx 16\,\mu m$). This implies that the amount of transport that takes place during a short pulse must be exceedingly small compared to what is needed to cause a substantial change in intracellular concentration. The number of molecules that can be delivered to the membrane on the time scale of a pulse is just $A_{cell} d_{drift} \gamma_e / 2$, where γ_e is the extracellular solute concentration (in molecules/m^3). Thus, even if the membrane posed no barrier to transport whatsoever (bulk electrolyte approximation), the relative intracellular concentration γ_i/γ_e immediately following a short pulse would be

limited to

$$\frac{\gamma_i}{\gamma_e} \approx \frac{A_{cell} d_{drift}}{2V_{cell}} = \frac{3d_{drift}}{2r_{cell}}. \tag{6.7}$$

Here, r_{cell} is the radius of a cell with area A_{cell}. Again taking propidium ($D_s = 42.8 \times 10^{-11}\,m^2/s$, $z_s = +2$ [48]) as an example and using a typical $r_{cell} = 8\,\mu m$, in the limit of the membrane posing no barrier to transport, $\gamma_i/\gamma_e \approx 2.0 \times 10^{-4}$ immediately following a 4 ns, 8 MV/m pulse [16] and $\gamma_i/\gamma_e \approx 3.6 \times 10^{-3}$ immediately following a 60 ns, 9.5 MV/m pulse [24]. This is orders of magnitude less transport than can be achieved by conventional electroporation pulses (e.g., [58]).

Moreover, the bound is very conservative because it does not consider the limited aqueous pore area ($\lesssim 0.1$ [27]), hindrance ($\sim 8 \times 10^{-5}$), or partitioning (~ 0.9), and accounting for these factors the actual transport would be ~ 5 orders of magnitude smaller.

Figure 6.3 shows the drift distance d_{drift} for a wide range of pulse durations and magnitudes. For illustrative purposes, d_{drift} was calculated using $D_s = 40 \times 10^{-11}\,m^2/s$ and charge $|z_s| = 1$, which are typical of small fluorescent probes [48]. The results can easily be scaled for other z_s by considering that $d_{drift} \propto |z_s|$ (Eq. 6.6).

6.3.2 Molecular Uptake During Short Pulses

Here, we extend the bulk electrolyte estimates by explicitly using basic properties of small pores. The number of molecules M_{during} entering a cell during a short pulse can be approximated by

$$M_{during} = \frac{1}{2}(d_{drift}\gamma_e)(A_{cell}A_p N_0)(HK_{during}), \tag{6.8}$$

where d_{drift} is the drift distance during the pulse (Eq. 6.6), γ_e is the extracellular concentration of solute, H is the hindrance factor, K_{during} is the partition coefficient during the pulse ($\Delta\phi_m = 1.5\,V$), N_0 is the pore density in the plasma membrane, and A_p ($= \pi r_p^2$) is the aqueous area of a single pore. The first grouped factor, $d_{drift}\gamma_e$, is the number of solute molecules that drift through a region of unit area during the pulse. The second grouped factor, $A_{cell}A_pN_0$, is the total area of pores in

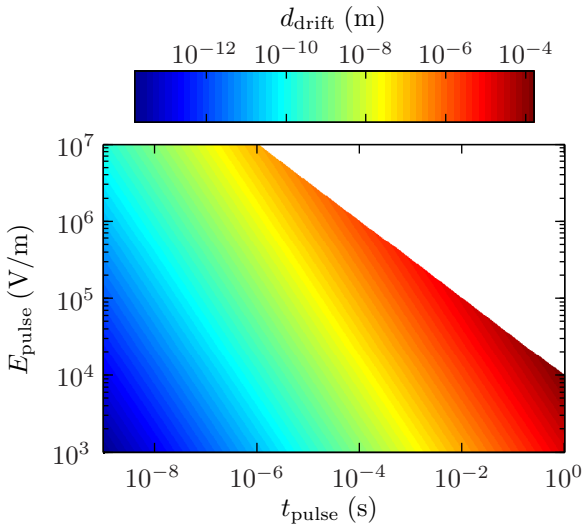

Figure 6.3: Electrical drift distance in bulk electrolyte resulting from rectangular electric pulses. The electrical drift distance d_{drift} is shown for a range of pulse durations t_{pulse} and magnitudes E_{pulse} for a molecule with diffusivity $D_s = 40 \times 10^{-11}\,\text{m}^2/\text{s}$ and charge $|z_s| = 1$. d_{drift} is shown only for pulses resulting in a temperature rise $\Delta T \leq 25\,^{\circ}\text{C}$ (assuming electrolyte conductivity $\sigma = 1\,\text{S/m}$ and volumetric heat capacity $s = 4.18 \times 10^6\,\text{J/(m K)}$). For pulses resulting in $\Delta T > 25\,^{\circ}\text{C}$, d_{drift} is shown as *white*. For a fixed temperature rise ΔT (e.g., 25 °C), d_{drift} is greater for smaller E_{pulse} because $d_{\text{drift}} \propto E_{\text{pulse}}$ but $\Delta T \propto E_{\text{pulse}}^2$.

the plasma membrane due to pulsing. The third grouped factor, HK_{during}, is the factor by which hindrance and partitioning diminish transport (relative to transport in bulk electrolyte). The $1/2$ prefactor accounts for the fact that electrical drift is only directed into the cell for one of its sides. Put simply, half of the cell accommodates entry, and the other half departure, because of field direction. Bipolar pulses can be treated by our approach, but are beyond the scope of this paper.

There are two important assumptions implicit in Eq. 6.8, both of which stem from the primary assumption that the pulse is short. The first is that pore expansion is negligible during the pulse, and therefore, the pores can be assumed to be distributed around the minimum-energy pore radius $r_{\text{p,min}}$ [22, 27, 28]. Thus, the hindrance factor H and partition coefficient K_{during} can be calculated based on $r_{\text{p,min}}$. The second assumption is that γ_e at the membrane interface is constant. This is reasonable for short pulses because d_{drift} is so small. However, for a longer pulse, the solute not immediately passing through membrane pores would accumulate at the membrane interface [52],

thereby raising γ_e (adjacent to the extracellular side of the membrane) and increasing the rate of transport through pores.

6.3.3 Molecular Uptake After Short Pulses

The number of molecules M_{after} entering a cell after a short pulse (post-pulse) can be approximated by

$$M_{after} = \int_0^{\infty} \left(D_s \frac{\gamma_e - \gamma_i}{d_m} \right) (A_p A_{cell} N(t))(HK_{after})\, dt, \tag{6.9}$$

where $N(t) = N_0 e^{-t/\tau_p}$ (Eq. 6.1), γ_i is the intracellular concentration of solute, τ_p is the pore resealing time constant, K_{after} is the partition coefficient after the pulse ($\Delta\phi_m = 0\,V$), and all other variables are as previously defined. The pore density $N(t)$ is the only time-dependent quantity.

We can assume $\gamma_i \approx 0\,\text{molecules}/\text{m}^3$ because very little molecular transport has been observed following short pulses [16], and even for longer pulses that result in more transport $\gamma_i \ll \gamma_e$ [59]. Additionally, for propidium and yo-pro-1, $\gamma_i \approx 0\,\text{molecules}/\text{m}^3$ because they are intercalating dyes that tightly bind to nucleic acids in the cytoplasm [60], thereby resulting in low levels of free (unbound) intracellular solute.

Taking these considerations into account, Eq. 6.9 can be simplified to

$$M_{after} = \left(\frac{D_s \tau_p}{d_m} \gamma_e \right) (A_{cell} A_p N_0)(HK_{after}). \tag{6.10}$$

The form of Eq. 6.10 is very similar to the form of Eq. 6.8. The first grouped factor, $D_s \tau_p \gamma_e / d_m$ is the number of solute molecules that would diffuse through a region of unit area during one resealing time constant τ_p for a concentration gradient γ_e / d_m. The second grouped factor, $A_{cell} A_p N_0$, is the total area of pores in plasma membrane immediately following the pulse (i.e., before resealing). The third grouped factor, HK_{after}, is the factor by which hindrance and partitioning diminish transport (relative to transport in bulk electrolyte).

Implicit in Eq. 6.10 is the assumption that post-pulse transport proceeds by diffusion alone. This is reasonable because $\Delta\phi_m \approx 0\,V$ for many multiples of τ_p following a pulse [27]. Nonetheless, we note that even a small $\Delta\phi_m$ could contribute to a drift component that would increase M_{after} (for positively charged species), and further support the primary conclusion of this study: $M_{after} \gg M_{during}$.

6.3.4 Ratio of Molecular Uptake During to After Short Pulses

Assuming drift dominates during a pulse and diffusion dominates after a pulse, the ratio of transport during the pulse to after the pulse can be determined from Eq. 6.8 and Eq. 6.10:

$$\frac{M_{during}}{M_{after}} = \frac{1}{2}\left(\frac{d_{drift} d_m}{D_s \tau_p}\right)\left(\frac{K_{during}}{K_{after}}\right). \tag{6.11}$$

Substituting for d_{drift} (Eq. 6.6) and simplifying,

$$\frac{M_{during}}{M_{after}} = \frac{1}{2}\left(\frac{q_e |z_s| E_{pulse} d_m}{kT}\right)\left(\frac{K_{during}}{K_{after}}\right)\left(\frac{t_{pulse}}{\tau_p}\right). \tag{6.12}$$

Note that the hindrance factors drop out of the ratio M_{during}/M_{after} (Eq. 6.12), thus reducing the number of assumptions implicit in the analysis. A key assumption is that the pores have the same radius ($r_{p,min}$) both during and after the pulse and therefore the same hindrance during and after the pulse. N_0 also drops out.

Figure 6.4 shows the ratio of molecular uptake during a pulse M_{during} to molecular uptake after a pulse M_{after} for a range of pulse durations and magnitudes. The transport ratio is shown for $|z_s|$ values of 1, 2, 3, and 4 because the partition coefficients K_{during} and K_{after} are functions of solute charge z_s (based on the Born energy) [49]. For all of the conditions considered, $M_{during}/M_{after} \ll 1$. M_{during}/M_{after} is particularly small for the smaller z_s values. For any given z_s, M_{during}/M_{after} is largest for the pulse with $t_{pulse} = 100\,ns$ and $E_{pulse} = 10\,MV/m$ (Fig. 6.4). For this pulse, M_{during}/M_{after} is 1.8×10^{-7} for $|z_s| = 1$, 3.2×10^{-6} for $|z_s| = 2$, 2.7×10^{-4} for $|z_s| = 3$, and 0.12 for $|z_s| = 4$.

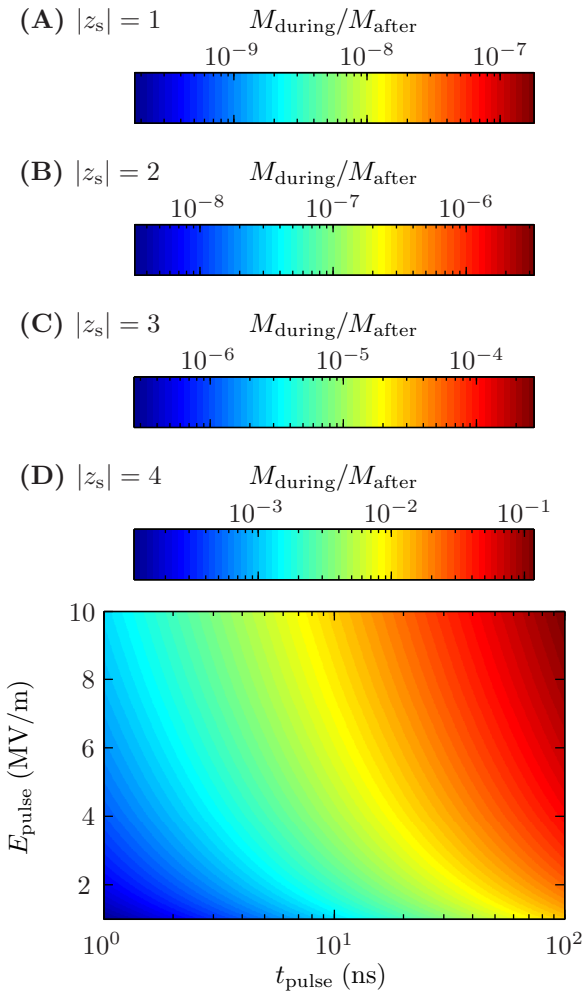

Figure 6.4: Molecular uptake during vs. after short pulses. The ratio of molecular uptake during a pulse M_{during} to molecular uptake after a pulse M_{after} is shown for a range of pulse durations t_{pulse} and magnitudes E_{pulse}. The transport ratio is shown for $|z_s|$ values of **(A)** 1, **(B)** 2, **(C)** 3, and **(D)** 4. Note that only the z-axis (colormap) changes with z_s, and thus the same pseudocolor plot applies for all z_s. The ratio M_{during}/M_{after} is proportional to t_{pulse} and E_{pulse}, and it is smaller for smaller values of solute charge $|z_s|$. For all of the conditions considered, $M_{during} \ll M_{after}$.

Consideration of the grouped factors in Eq. 6.12 provides insight into why $M_{\text{during}}/M_{\text{after}}$ is so small. The first, $q_e|z_s|E_{\text{pulse}}d_m/kT$, is the ratio of drift flux to diffusive flux over a distance d_m. This factor depends on $|z_s|$ and E_{pulse} and is somewhat larger than 1 for typical (relevant) values of these parameters. For example, with $|z_s| = 1$ and $E_{\text{pulse}} = 10\,\text{MV/m}$, the factor is ~ 19. Thus, this factor favors transport during the pulse.

The second grouped factor in Eq. 6.12, $K_{\text{during}}/K_{\text{after}}$, is the ratio of the partition coefficient during the pulse to the partition coefficient after the pulse. This factor depends strongly on $|z_s|$ and is always larger than 1 (field-assisted charge entry) [49]. The factor is 1.8 for $|z_s| = 1$, 17 for $|z_s| = 2$, 930 for $|z_s| = 3$, and 3.0×10^5 for $|z_s| = 4$. This factor also favors transport during the pulse, particularly for larger $|z_s|$.

The third grouped factor in Eq. 6.12, t_{pulse}/τ_p, is the ratio of the pulse duration to the pore resealing time-constant. This factor is much smaller than 1. Here, we consider pulses with durations $t_{\text{pulse}} \lesssim 100\,\text{ns}$, but $\tau_p = 1\,\text{s}$. Therefore, the ratio $t_{\text{pulse}}/\tau_p < 10^{-7}$, and it dominates.

Thus, while the drift flux (during a pulse) exceeds the diffusive flux (after a pulse) over distance d_m and the partition coefficient during a pulse exceeds, sometimes dramatically (i.e., for large $|z_s|$), the partition coefficient after a pulse, these factors simply are too small to compensate for the ratio t_{pulse}/τ_p. In other words, the flux of solute into a cell during a pulse exceeds the flux of solute into a cell after a pulse, but because the time available during a short pulse is so much smaller than after a pulse, the vast majority of transport takes place after a pulse.

To this point, we developed the results presented here using minimum-size pore radius $r_{p,\text{min}} = 0.8\,\text{nm}$ and pore resealing time constant $\tau_p = 1\,\text{s}$. However, the values reported for these parameters vary, and it is therefore important to consider how other values would affect our estimates.

6.3.5 Effects of the Minimum-size Pore Radius and Resealing Time Constant Values

The value used for the minimum-size pore radius $r_{p,min}$ is important because it affects M_{during}/M_{after} (Eq. 6.12) through the partition coefficients K_{during} and K_{after} [49]. Glaser et al. [32] reported that $r_{p,min}$ is in the range $0.6-1.0$ nm, and the average of $r_{p,min} = 0.8$ nm has been widely used in mathematical models of electroporation (e.g., [28, 35, 61]). According to Barnett et al. [33], packing constraints require that $r_{p,min}$ be somewhat larger than 0.7 nm, and they used $r_{p,min} = 1.0$ nm in their model. In a recent study [49] in which we analyzed the bilayer lipid membrane conductance measurements by Melikov et al. [36], we found $r_{p,min} \approx 1.0$ nm. Nonetheless, in the interest of taking a conservative approach, in this study we used the widely used $r_{p,min} = 0.8$ nm.

The extent to which changing $r_{p,min}$ affects K_{during}/K_{after} (and therefore M_{during}/M_{after}) depends on the solute charge z_s. For $|z_s| = 4$, decreasing $r_{p,min}$ to 0.7 nm increases K_{during}/K_{after} by a factor of 36, and increasing $r_{p,min}$ to 0.9 nm decreases K_{during}/K_{after} by a factor of 12. The effect of changing $r_{p,min}$ on K_{during}/K_{after} for smaller $|z_s|$ is much less significant. Thus, using other larger or smaller values of $r_{p,min}$ would not affect our general conclusion that $M_{during} \ll M_{after}$.

The value used for the pore resealing time constant τ_p is important because it directly affects M_{during}/M_{after} (Eq. 6.12). Values reported for the pore resealing time constant τ_p vary widely. While Glaser et al. [32] reported $\tau_p \approx 3$ s and He et al. [62] reported $\tau_p \approx 0.8-2.2$ s, Tekle et al. [37] reported a shorter $\tau_p \approx 0.16$ s and Djuzenova et al. [38] reported a much longer $\tau_p \approx 60-120$ s. Here, we used a resealing time constant $\tau_p = 1$ s, which is on the lower end of the range of experimentally determined values. Decreasing τ_p would decrease M_{during}/M_{after}, and increasing τ_p would increase M_{during}/M_{after}. While reported values of τ_p vary widely, they do not vary widely enough to change our general conclusion that $M_{during} \ll M_{after}$.

6.4 Conclusions

This analysis strongly suggests that the vast majority of electrodiffusive molecular transport that results from nanosecond electric pulses ($\lesssim 100$ ns) occurs post-pulse. Indeed, the transport during these pulses appears to be negligible. While simplifying assumptions were made in this analysis and some uncertainty exists in a few of the parameters (e.g., τ_p), the overall estimates appear conservative.

References

[1] Schoenbach, K.H., Beebe, S.J., and Buescher, E.S. Intracellular effect of ultrashort electrical pulses. *Bioelectromagnetics*, 22(6):440–448, 2001.

[2] Beebe, S.J., Fox, P.M., Rec, L.J., Somers, K., Stark, R.H., and Schoenbach, K.H. Nanosecond pulsed electric field (nsPEF) effects on cells and tissues: Apoptosis induction and tumor growth inhibition. *IEEE T Plasma Sci*, 30(1):286–292, 2002.

[3] Beebe, S.J., White, J., Blackmore, P.F., Deng, Y.P., Somers, K., and Schoenbach, K.H. Diverse effects of nanosecond pulsed electric fields on cells and tissues. *DNA Cell Biol*, 22(12):785–796, 2003.

[4] Beebe, S.J., Fox, P.M., Rec, L.J., Willis, L.K., and Schoenbach, K.H. Nanosecond, high-intensity pulsed electric fields induce apoptosis in human cells. *FASEB J*, 17(9), 2003.

[5] Buescher, E.S. and Schoenbach, K.H. Effects of submicrosecond, high intensity pulsed electric fields on living cells–Intracellular electromanipulation. *IEEE T Dielect El In*, 10(5):788–794, 2003.

[6] Deng, J.D., Schoenbach, K.H., Buescher, E.S., Hair, P.S., Fox, P.M., and Beebe, S.J. The effects of intense submicrosecond electrical pulses on cells. *Biophys J*, 84(4):2709–2714, 2003.

[7] Vernier, P.T., Sun, Y.H., Marcu, L., Salemi, S., Craft, C.M., and Gundersen, M.A. Calcium bursts induced by nanosecond electric pulses. *Biochem Bioph Res Co*, 310:286–295, 2003.

[8] Schoenbach, K.H., Joshi, R.P., Kolb, J.F., Chen, N.Y., Stacey, M., Blackmore, P.F., Buescher, E.S., and Beebe, S.J. Ultrashort electrical pulses open a new gateway into biological cells. *P IEEE*, 92(7):1122–1137, 2004.

[9] Chen, N.Y., Schoenbach, K.H., Kolb, J.F., Swanson, R.J., Garner, A.L., Yang, J., Joshi, R.P., and Beebe, S.J. Leukemic cell intracellular responses to nanosecond electric fields. *Biochem Bioph Res Co*, 317(2):421–427, 2004.

[10] White, J.A., Blackmore, P.F., Schoenbach, K.H., and Beebe, S.J. Stimulation of capacitative calcium entry in HL-60 cells by nanosecond pulsed electric fields. *J Biol Chem*, 279(22):22964–22972, 2004.

[11] Beebe, S.J., Blackmore, P.F., White, J., Joshi, R.P., and Schoenbach, K.H. Nanosecond pulsed electric fields modulate cell function through intracellular signal transduction mechanisms. *Physiol Meas*, 25(4):1077–93, 2004.

[12] Vernier, P.T., Sun, Y.H., Marcu, L., Craft, C.M., and Gundersen, M.A. Nanoelectropulse-induced phosphatidylserine translocation. *Biophys J*, 86:4040–4048, 2004.

[13] Vernier, P.T., Sun, Y.H., Marcu, L., Craft, C.M., and Gundersen, M.A. Nanosecond pulsed electric fields perturb membrane phospholipids in T lymphoblasts. *FEBS Lett*, 572:103–108, 2004.

[14] Pakhomov, A.G., Phinney, A., Ashmore, J., Walker, K., Kolb, J.F., Kono, S., Schoenbach, K.H., and Murphy, M.R. Characterization of the cytotoxic effect of high-intensity, 10-ns duration electrical pulses. *IEEE T Plasma Sci*, 32(4):1579–1586, 2004.

[15] Hu, Q., Joshi, R.P., and Schoenbach, K.H. Simulations of nanopore formation and phosphatidylserine externalization in lipid membranes subjected to a high-intensity, ultrashort electric pulse. *Phys Rev E*, 72, 2005.

[16] Vernier, P.T., Sun, Y.H., and Gundersen, M.A. Nanoelectropulse-driven membrane perturbation and small molecule permeabilization. *BMC Cell Biol*, 7:37, 2006.

[17] Vernier, P.T., Ziegler, M.J., Sun, Y., Gundersen, M.A., and Tieleman, D.P. Nanopore-facilitated, voltage-driven phosphatidylserine translocation in lipid bilayers–In cells and in silico. *Phys Biol*, 3(4):233–247, 2006.

[18] Sun, Y., Vernier, P., Behrend, M., Wang, J., Thu, M., Gundersen, M., and Marcu, L. Fluorescence microscopy imaging of electroperturbation in mammalian cells. *J Biomed Opt*, 11(2), 2006.

[19] Smith, K.C., Gowrishankar, T.R., Esser, A.T., Stewart, D.A., and Weaver, J.C. The spatially distributed dynamic transmembrane voltage of cells and organelles due to 10-ns pulses: Meshed transport networks. *IEEE T Plasma Sci*, 34:1394–1404, 2006.

[20] Gowrishankar, T.R., Esser, A.T., Vasilkoski, Z., Smith, K.C., and Weaver, J.C. Microdosimetry for conventional and supra-electroporation in cells with organelles. *Biochem Bioph Res Co*, 341:1266–1276, 2006.

[21] Gowrishankar, T.R. and Weaver, J.C. Electrical behavior and pore accumulation in a multicellular model for conventional and supra-electroporation. *Biochem Bioph Res Co*, 349:643–653, 2006.

[22] Vasilkoski, Z., Esser, A.T., Gowrishankar, T.R., and Weaver, J.C. Membrane electroporation: The absolute rate equation and nanosecond time scale pore creation. *Phys Rev E*, 74(2), 2006.

[23] Nuccitelli, R., Pliquett, U., Chen, X.H., Ford, W., Swanson, R.J., Beebe, S.J., Kolb, J.F., and Schoenbach, K.H. Nanosecond pulsed electric fields cause melanomas to self-destruct. *Biochem Bioph Res Co*, 343:351–360, 2006.

[24] Frey, W., White, J.A., Price, R.O., Blackmore, P.F., Joshi, R.P., Nuccitelli, R., Beebe, S.J., Schoenbach, K.H., and Kolb, J.F. Plasma membrane voltage changes during nanosecond pulsed electric field exposure. *Biophys J*, 90:3608–3615, 2006.

[25] Hall, E.H., Schoenbach, K.H., and Beebe, S.J. Nanosecond pulsed electric fields induce apoptosis in p53-wildtype and p53-null HCT116 colon carcinoma cells. *Apoptosis*, 12(9):1721–1731, 2007.

[26] Garon, E.B., Sawcer, D., Vernier, P.T., Tang, T., Sun, Y., Marcu, L., Gundersen, M.A., and Koeffler, H.P. In vitro and in vivo evaluation and a case report of intense nanosecond pulsed electric field as a local therapy for human malignancies. *Int J Cancer*, 121(3):675–682, 2007.

[27] Smith, K.C. and Weaver, J.C. Active mechanisms are needed to describe cell responses to submicrosecond, megavolt-per-meter pulses: Cell models for ultrashort pulses. *Biophys J*, 95(4):1547–1563, 2008.

[28] Esser, A.T., Smith, K.C., Gowrishankar, T.R., and Weaver, J.C. Towards solid tumor treatment by nanosecond pulsed electric fields. *Technol Cancer Res T*, 8(4):289–306, 2009.

[29] Nuccitelli, R., Chen, X., Pakhomov, A.G., Baldwin, W.H., Sheikh, S., Pomicter, J.L., Ren, W., Osgood, C., Swanson, R.J., Kolb, J.F., Beebe, S.J., and Schoenbach, K.H. A new pulsed electric field therapy for melanoma disrupts the tumor's blood supply and causes complete remission without recurrence. *Int J Cancer*, 125(2):438–45, 2009.

[30] Nuccitelli, R., Tran, K., Sheikh, S., Athos, B., Kreis, M., and Nuccitelli, P. Optimized nanosecond pulsed electric field therapy can cause murine malignant melanomas to self-destruct with a single treatment. *Int J Cancer*, 127(7):1727–36, 2010.

[31] Weaver, J.C. and Chizmadzhev, Y.A. Theory of electroporation: A review. *Bioelectroch Bioener*, 41(2):135–160, 1996.

[32] Glaser, R.W., Leikin, S.L., Chernomordik, L.V., Pastushenko, V.F., and Sokirko, A.I. Reversible electrical breakdown of lipid bilayers: Formation and evolution of pores. *Biochim Biophys Acta*, 940(2):275–287, 1988.

[33] Barnett, A. and Weaver, J.C. Electroporation – A unified, quantitative theory of reversible electrical breakdown and mechanical rupture in artificial planar bilayer-membranes. *Bioelectroch Bioener*, 25(2):163–182, 1991.

[34] Neu, J.C. and Krassowska, W. Asymptotic model of electroporation. *Phys Rev E*, 59(3):3471–3482, 1999.

[35] Esser, A.T., Smith, K.C., Gowrishankar, T.R., Vasilkoski, Z., and Weaver, J.C. Mechanisms for the intracellular manipulation of organelles by conventional electroporation. *Biophys J*, 98(11):2506–14, 2010.

[36] Melikov, K.C., Frolov, V.A., Shcherbakov, A., Samsonov, A.V., Chizmadzhev, Y.A., and Chernomordik, L.V. Voltage-induced nonconductive pre-pores and metastable single pores in unmodified planar lipid bilayer. *Biophys J*, 80(4):1829–1836, 2001.

[37] Tekle, E., Astumian, R.D., Friauf, W.A., and Chock, P.B. Asymmetric pore distribution and loss of membrane lipid in electroporated DOPC vesicles. *Biophys J*, 81(2):960–8, 2001.

[38] Djuzenova, C.S., Zimmermann, U., Frank, H., Sukhorukov, V.L., Richter, E., and Fuhr, G. Effect of medium conductivity and composition on the uptake of propidium iodide into electropermeabilized myeloma cells. *Biochim Biophys Acta*, 1284(2):143–52, 1996.

[39] Litster, J.D. Stability of lipid bilayers and red blood-cell membranes. *Phys Lett A*, A 53(3):193–194, 1975.

[40] Abidor, I.G., Arakelyan, V.B., Chernomordik, L.V., Chizmadzhev, Y.A., Pastushenko, V.F., and Tarasevich, M.R. Electric breakdown of bilayer lipid-membranes I. Main experimental facts and their qualitative discussion. *Bioelectroch Bioener*, 6(1):37–52, 1979.

[41] Chernomordik, L.V., Sukharev, S.I., Popov, S.V., Pastushenko, V.F., Sokirko, A.V., Abidor, I.G., and Chizmadzhev, Y.A. The electrical breakdown of cell and lipid membranes: The similarity of phenomenologies. *Biochim Biophys Acta*, 902(3):360–73, 1987.

[42] Tieleman, D.P., Leontiadou, H., Mark, A.E., and Marrink, S.J. Simulation of pore formation in lipid bilayers by mechanical stress and electric fields. *J Am Chem Soc*, 125(21):6382–6383, 2003.

[43] Tieleman, D.P. The molecular basis of electroporation. *BMC Biochem*, 5(10), 2004.

[44] Vernier, P.T., Ziegler, M.J., Sun, Y.H., Chang, W.V., Gundersen, M.A., and Tieleman, D.P. Nanopore formation and phosphatidylserine externalization in a phospholipid bilayer at high transmembrane potential. *J Am Chem Soc*, 128:6288–6289, 2006.

[45] Wohlert, J., den Otter, W.K., Edholm, O., and Briels, W.J. Free energy of a trans-membrane pore calculated from atomistic molecular dynamics simulations. *J Chem Phys*, 124, 2006.

[46] Leontiadou, H., Mark, A.E., and Marrink, S.J. Ion transport across transmembrane pores. *Biophys J*, 92(12):4209–4215, 2007.

[47] Bockmann, R.A., de Groot, B.L., Kakorin, S., Neumann, E., and Grubmuller, H. Kinetics, statistics, and energetics of lipid membrane electroporation studied by molecular dynamics simulations. *Biophys J*, 95(4):1837–1850, 2008.

[48] Smith, K.C. and Weaver, J.C. Compilation and computation of the size, charge, and diffusivity of fluorescent dyes and other small molecules (in preparation).

[49] Smith, K.C. and Weaver, J.C. Effects of hindrance and partitioning on ionic and molecular transport through small lipidic pores (in preparation).

[50] Bockris, J.O. and Reddy, A.K.N. *Modern Electrochemistry, Vol. 1*. Plenum, New York, 1970.

[51] Grodzinsky, A.J. *Fields, Forces, and Flows in Biological Systems*. Garland Science, London, 2011.

[52] Smith, K.C. and Weaver, J.C. Electrodiffusion of molecules in aqueous media: A robust, discretized description for electroporation and other transport phenomena (in preparation).

[53] Renkin, E.M. Filtration, diffusion, and molecular sieving through porous cellulose membranes. *J Gen Physiol*, 38(2):225–43, 1954.

[54] Bungay, P.M. and Brenner, H. The motion of a closely-fitting sphere in a fluid-filled tube. *Int J of Multiphas Flow*, 1(1):25–56, 1973.

[55] Gurtovenko, A.A., Anwar, J., and Vattulainen, I. Defect-mediated trafficking across cell membranes: Insights from in silico modeling. *Chem Rev*, 110(10):6077–103, 2010.

[56] Parsegian, A. Energy of an ion crossing a low dielectric membrane: Solutions to four relevant electrostatic problems. *Nature*, 221(5183):844–6, 1969.

[57] Parsegian, V.A. Ion-membrane interactions as structural forces. *Ann N Y Acad Sci*, 264:161–71, 1975.

[58] Canatella, P.J., Karr, J.F., Petros, J.A., and Prausnitz, M.R. Quantitative study of electroporation-mediated molecular uptake and cell viability. *Biophys J*, 80(2):755–764, 2001.

[59] Prausnitz, M.R., Lau, B.S., Milano, C.D., Conner, S., Langer, R., and Weaver, J.C. A quantitative study of electroporation showing a plateau in net molecular-transport. *Biophys J*, 65(1):414–422, 1993.

[60] Wilson, W.D., Krishnamoorthy, C.R., Wang, Y.H., and Smith, J.C. Mechanism of intercalation: Ion effects on the equilibrium and kinetic constants for the interaction of propidium and ethidium with DNA. *Biopolymers*, 24(10):1941–61, 1985.

[61] Krassowska, W. and Filev, P.D. Modeling electroporation in a single cell. *Biophys J*, 92(2):404–417, 2007.

[62] He, H., Chang, D.C., and Lee, Y.K. Nonlinear current response of micro electroporation and resealing dynamics for human cancer cells. *Bioelectrochemistry*, 72(2):161–168, 2008.

Chapter 7

A Unified Model of Electroporation and Molecular Transport I: Model Design and Validation

Abstract

Electroporation is well-established in biological research and is increasingly pursued for applications in clinical medicine. While the use of electroporation is compelling, the absence of a quantitative, mechanistic, and predictive understanding prevents utilization of engineering principles. Even though electroporation is driven by electrical interactions, its applications rest mainly on cumulative (net) ionic and molecular transport through transient, heterogeneous pore populations in cell membranes. Here we present a quantitative, mechanistic model of electroporation with concomitant molecular transport. The model comprises components that have been described and validated in a series of previous studies. Specifically, these components include the characterization of solute properties (size, charge, and diffusivity), electrical and molecular transport in bulk electrolyte (electrodiffusion), electrical and molecular transport through pores (conductance, hindrance, and partitioning), and pore energy and dynamics. We integrate these components into a comprehensive 2-D cell model that can describe the electrical potential, molecular solute concentration, and pore density on time scales ranging from nanoseconds to hundreds of seconds and length scales ranging from nanometers to millimeters. We validate the cell model by replicating in silico two extensive sets of experiments in the literature that measured total molecular uptake of fluorescent probes. The model predictions of molecular uptake are in excellent agreement with these experimental measurements, for which the applied electric pulses collectively span nearly three orders of magnitude in pulse duration ($50\,\mu s - 20\,ms$) and a corresponding order of magnitude in pulse magnitude ($3 - 0.3\,kV/cm$). We use the model and the experimental data to determine optimal values of several important electroporation parameters, including the first estimate of the asymmetric pore creation constant α and perhaps the most accurate estimate to date of the pore diffusion coefficient D_p. The advantages of the present model include the ability to (1) simulate electroporation dynamics that are difficult to assess experimentally, (2) analyze in silico the same quantities that are measured by experimental studies in vitro, and (3) quickly screen a wide array of electric pulse waveforms for particular applications. This is a step toward in silico screening of electroporation conditions for optimal outcomes.

7.1 Introduction

Electroporation is a widely used tool for delivering exogenous molecules (nucleic acids, drugs, and fluorescent probes) into cells in biological research laboratories and is increasingly pursued for medical applications [1, 2]. It is most often used to transfect cultured cells in vitro, though it has also found usage for a number of other more specialized experimental applications, such as transfecting retinal cells [3] and single neurons [4] in vivo and chick embryos in ovo [5]. Electroporation is fundamentally attractive because, by transiently disrupting the plasma membrane, it provides an operationally simple, effective means of facilitating the transport of a wide range of different molecules into cells. Additionally, for in vivo applications, by appropriately localizing the applied electric field, the region of tissue affected by electroporation can be controlled and limited [6–14], which is advantageous for many applications.

Following the success of in vitro electroporation in experimental applications, researchers began investigating potential electroporation-based medical therapies, most involving drug delivery, gene delivery, or electroporation alone to treat or ablate tissue. A number of in vivo studies have shown that electroporation can be used to treat solid tumors by greatly enhancing the delivery of non-permeant anticancer drugs [15–17] or suicide genes [18], with both approaches leading to the destruction of the treated tissue.

Perhaps even more intriguing, recent studies have shown that electric pulses alone with very short duration and large magnitude can induce apoptosis in cells in vitro [19–22] and in vivo [23–26], thereby leading to the destruction of treated cells or tissue without the need to introduce any drugs or genes. Rather large conventional electroporation pulses can be used to ablate tissue in a similar manner. However, this leads to necrosis rather than apoptosis [27, 28]. There is also ongoing interest in using electroporation to transfect skeletal muscle cells in vivo [29] for applications such as DNA vaccines [30] and increasing production of proteins like erythropoietin [31].

The common characteristic among all of these applications of electroporation is that they involve transmembrane transport though temporary pores. Indeed, transmembrane transport underlies not only electroporation-based applications but also the basic mechanisms of electroporation and therefore our fundamental understanding of electroporation. Much of what we know about electroporation has been determined though the analysis of measurements of electroporation-mediated electrical and molecular transport. More direct methods of observing pores appear infeasible because of the very short length scales (nanometers to micrometers) and time scales (nanoseconds to milliseconds) characteristic of electroporation and the absence of a significant contrast mechanism for imaging. With a few exceptions [32, 33], these measurements involve the collective effects of large ensembles of pores rather than single pores.

Specifically, most experimental studies of electroporation have examined the transmembrane voltage of pulsed cells during or after electroporation using voltage sensitive dyes [34–37] or patch clamp techniques [38, 39] or examined the changes in fluorescence of cells electroporated in the presence of fluorescent dyes [40–54]. The most insightful and useful of these molecular transport studies used quantitatively calibrated measurement systems [40, 43–45, 48–50, 52, 54], enabling them to report the number of transported molecules (with some quantified error), rather than just relative fluorescence [47, 51, 53], which cannot be interpreted with a useful degree of confidence.

The important implication is that to truly understand the basic mechanisms of electroporation, we must first come to understand electroporation-mediated transport and the implications of experimental quantitative measurements of transport. Additionally, because applications of electroporation rely on its ability to facilitate transmembrane transport, an improved quantitative understanding of transport will enable optimization of both existing and emerging applications of electroporation. Importantly, this will also set the stage for engineering, the application of science, and an increasingly used tool in basic research.

With these primary and pragmatic objectives as motivation, in this theory-based modeling study

we present a spatially distributed model of electroporation with mechanistic descriptions of electrical transport, electrodiffusive molecular transport, and dynamic pores. The comprehensive model presented includes independent, mechanistic components that we developed and described in a series of basic methods papers [55–58].

Specifically: First, we developed methods of estimating the size, charge, and diffusivity of solutes [55]. Second, we developed a robust method of describing electrodiffusive transport in discretized, spatially distributed systems [56]. Third, we characterized the interaction between ionic and molecular solutes and lipid pores and described the factors that affect electrical and molecular transport through pores [57]. Finally, we characterized the pore energy landscape and the role it plays in pore dynamics [58]. Where possible, we validated each of these basic mechanisms. For example, we used the single pore conductance measurements of Melikov et al. [32] to validate our descriptions of pore conductance [57] and pore energy [58].

Although a number of theoretical models have been used to describe and investigate electroporation [10, 14, 59–70], each has been limited in its scope or its assumptions. Some of these models have provided insights into particular aspects of electroporation, such as pore creation, but none has characterized the process of electroporation and its effects comprehensively. The model presented here enables the investigation of electroporation from the onset of the applied electric pulse to the resealing of pores, including the transport of molecules of interest. Thus, direct comparisons can be made with experimental measurements of electrical and molecular transport. Additionally, because electroporation affects biological systems by facilitating transport between cell compartments, the model can be used to investigate and optimize applications of electroporation.

To demonstrate the ability of the model to make accurate molecular transport predictions, we use it to test in silico the extensive experimental molecular transport measurements of Canatella et al. [49] and Puc et al. [50]. The Canatella et al. data set was specifically developed to be “used to optimize electroporation protocols, test theoretical models, and guide mechanistic interpretations”

[49]. The Canatella et al. [49] and Puc et al. [50] studies measured the cellular uptake of calcein and lucifer yellow [55], respectively, in response to electrical pulses that collectively span nearly three orders of magnitude in pulse duration ($50\,\mu s - 20\,ms$) and an order of magnitude in pulse magnitude ($0.3 - 3\,kV/cm$). As we demonstrate, the model is in excellent agreement with these results.

Additionally, we use the model and the Canatella et al. [49] and Puc et al. [50] measurements to determine optimal values of several important electroporation parameters, including the asymmetric pore creation constant α, which has not been previously estimated, and the pore diffusion coefficient D_p, which has previously only been estimated to within perhaps $1-2$ orders of magnitude of its actual value. The optimal values determined for the other parameters, including the symmetric pore creation constant β, the maximum size of pores $r_{p,max}$, and the pore resealing time constant τ_p, are all consistent with previous estimates.

The scope of this paper is such that it covers the response of the Canatella et al. and Puc et al. model cell system responses to a large number of different applied electric pulses but does not describe the detailed responses of the systems to particular pulses. However, in a companion paper [71], we comprehensively examine the responses of the Canatella et al. and Puc et al. systems, as described here, to two illustrative electric pulses. Additionally, we present a general theoretical framework for understanding the factors that dictate electroporation-mediated molecular transport.

7.2 Methods

7.2.1 Model Cell Systems

We represent the Canatella et al. [49] DU-145 cells and Puc et al. [50] DC-3F cells as simple, circular cells (plasma membranes) (Fig. 7.1). Though our basic approach is compatible with the inclusion of organelles [10, 66, 68, 72], we elected not to include them as they should have negligible impact on molecular uptake but significantly increase model computational demands. Because the model presented here is 2-D, the cells are effectively treated as cylindrical rather than spherical.

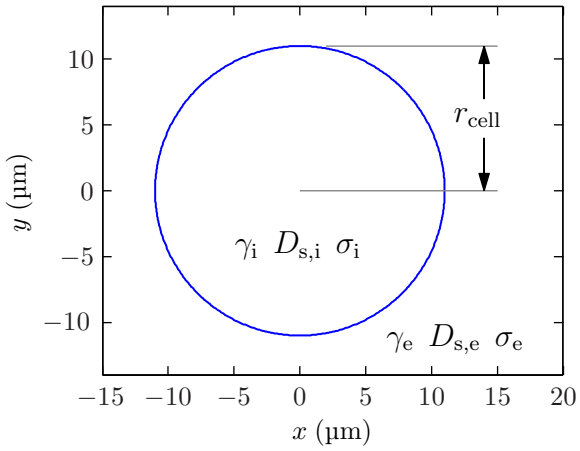

Figure 7.1: Model cell system. The circular cell is centered in a 1 mm × 1 mm region of electrolyte. Only the vicinity of the cell is shown. The cell has radius $r_{\text{cell}} = 11\,\mu\text{m}$ and corresponds to the Canatella system. The Puc system has the same layout but $r_{\text{cell}} = 8.55\,\mu\text{m}$. The system transport properties differ between the intracellular and extracellular regions. The solute concentration γ, solute diffusivity D_{s}, and electrical conductivity σ are shown, with subscript "i" indicating intracellular quantities and parameters and subscript "e" indicating extracellular quantities and parameters.

(Our basic methods extend to 3-D, but the computational demands of 3-D models are prohibitive.) Canatella et al. [49] reported an average cell radius $r_{\text{cell}} = 11\,\mu\text{m}$, and Puc et al. [50] reported an average cell radius $r_{\text{cell}} = 8.55\,\mu\text{m}$. We use these reported values of r_{cell} in the respective model systems here.

In both model systems, the cell is centered in a 1 mm × 1 mm region of electrolyte. The large system size (relative to the cell size) ensures that concentration of solute in the region of the cell remains relatively constant during a pulse, as expected in typical in vitro experiments. If a smaller system were used (e.g., several multiples of r_{cell} in size), then all solute would drift past the cell during a sufficiently long pulse, resulting in zero extracellular concentration. Moreover, using the meshed approach described here, placing the boundaries far from the cell has minimal impact on the model computation time.

To represent an applied, spatially uniform field, the anode is located along the $y = 0.5$ mm system boundary and the cathode is located along the $y = -0.5$ mm system boundary (creating two ideal

Table 7.1: Model System Parameters

Symbol	Canatella et al. System Value	Puc et al. System Value	Description and Source
r_{cell}	11 μm	8.55 μm	Cell radius [49, 50]
$\Delta\phi_{\text{m,rest}}$	−50 mV	−50 mV	Membrane resting potential [68]
σ_{e}	1.29 S/m	1.58 S/m	Extracellular conductivity [49, 73]
σ_{i}	0.3 S/m	0.3 S/m	Intracellular conductivity [74–78]
σ_{m}	9.5×10^{-9} S/m	9.5×10^{-9} S/m	Membrane conductivity [68]
ϵ_{e}	$72\epsilon_0 = 6.38 \times 10^{-10}$ F/m	$72\epsilon_0 = 6.38 \times 10^{-10}$ F/m	Extracellular permittivity [68]
ϵ_{i}	$72\epsilon_0 = 6.38 \times 10^{-10}$ F/m	$72\epsilon_0 = 6.38 \times 10^{-10}$ F/m	Intracellular permittivity [68]
ϵ_{m}	$5\epsilon_0 = 4.43 \times 10^{-11}$ F/m	$5\epsilon_0 = 4.43 \times 10^{-11}$ F/m	Membrane permittivity [68]
$D_{\text{s,e}}$	46.6×10^{-11} m^2/s	47.7×10^{-11} m^2/s	Extracellular solute diffusivity† [55]
$D_{\text{s,i}}$	$D_{\text{s,e}}/4 = 11.7 \times 10^{-11}$ m^2/s	$D_{\text{s,e}}/4 = 11.9 \times 10^{-11}$ m^2/s	Intracellular solute diffusivity*†
r_{s}	0.58 nm	0.61 nm	Solute radius† [55]
l_{s}	1.89 nm	1.46 nm	Solute length† [55]
z_{s}	−3.61	−2	Solute charge (valence)† [55]

*Value selected or calculated as described in main text. †Calcein is the solute in the Canatella et al. system. Lucifer yellow is the solute in the Puc et al. system.

parallel plate electrodes). Thus, when a pulse is applied, the electric field points in the $-y$-direction. Accordingly, calcein and lucifer yellow drift, which are negatively charged, drift in the $+y$-direction (opposite the applied field).

7.2.2 Electrical Transport Parameters

Canatella et al. [49] reported the conductivity value $\sigma_{\text{e}} = 1.29\,\text{S/m}$ for their pulsing medium (RPMI-1640 with 25 mM HEPES buffer), and we use that value for the Canatella model here. Puc et al. [50] did not report the conductivity of their pulsing medium (SMEM) but a paper from the same research group reported [73] the conductivity value $\sigma_{\text{e}} = 1.58\,\text{S/m}$ for the same medium, and we use that value for the Puc model here.

Intracellular conductivity values reported [74–78] for several cell types are in the approximate range $\sigma_{\text{i}} \approx 0.23 - 0.37\,\text{S/m}$. Here, we use the intermediate value $\sigma_{\text{i}} = 0.3\,\text{S/m}$ for both the Canatella and Puc models.

For the unperturbed membrane, we use conductivity value $\sigma_{\text{m}} = 9.5 \times 10^{-9}\,\text{S/m}$ [68] and membrane resting potential value $\Delta\phi_{\text{m,rest}} = -50\,\text{mV}$ [68] for both models.

We use extracellular and intracellular electrolyte permittivity values $\epsilon_{\text{e}} = \epsilon_{\text{i}} = 6.38 \times 10^{-10}\,\text{F/m}$

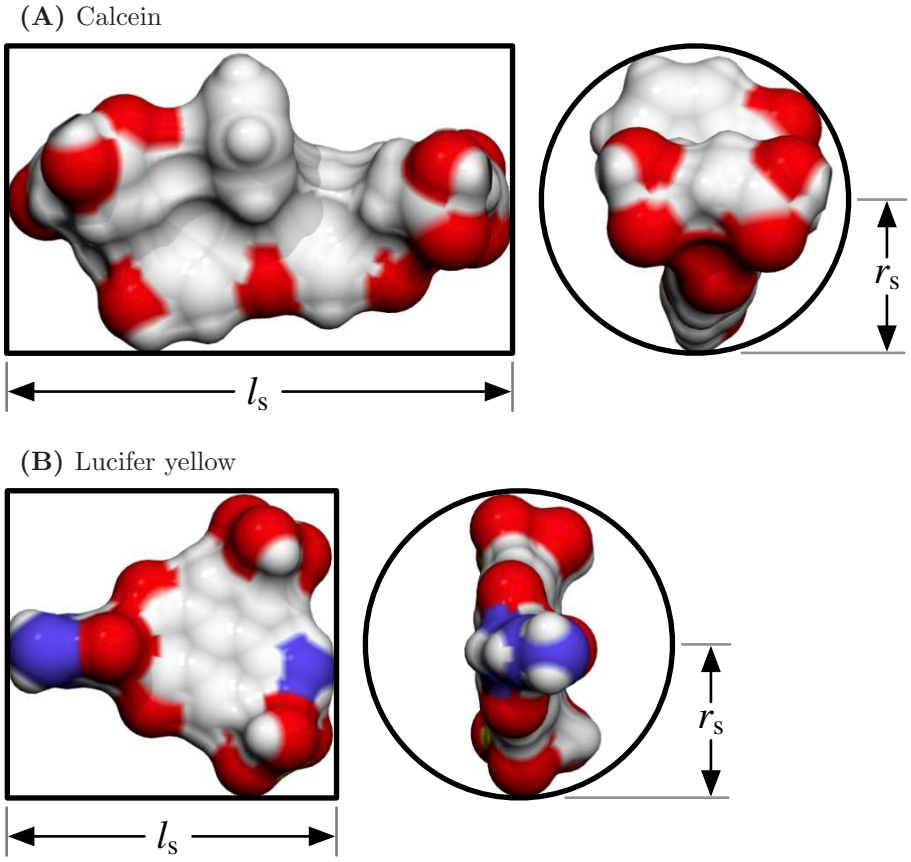

Figure 7.2: Cylindrical approximation to molecular shape. **(A)** Calcein ($r_s = 0.58\,\text{nm}$, $l_s = 1.89\,\text{nm}$) [55]. **(B)** Lucifer yellow ($r_s = 0.61\,\text{nm}$, $l_s = 1.46\,\text{nm}$) [55]. Note that the molecules are not shown to the same scale. The cylindrical approximation to molecular shape gives a more precise description of molecular shape than a spherical approximation.

and membrane permittivity value $\epsilon_m = 4.43 \times 10^{-11}\,\text{F/m}$ [68] for both models.

7.2.3 Molecular Transport Parameters

Canatella et al. [49] measured the calcein uptake. As we described previously [55], calcein can be approximated as cylindrical with radius $r_s = 0.58\,\text{nm}$ and length $l_s = 1.89\,\text{nm}$ (Fig. 7.2A). Its charge (valence) at pH 7.4 is $z_s = -3.61$ [55]. We use $D_{s,e} = 46.6 \times 10^{-11}\,\text{m}^2/\text{s}$ [55] for the extracellular (aqueous) diffusivity of calcein. The diffusivity of small molecules in the cytoplasm is typically ~25 % of the aqueous diffusivity [79–81]. Thus, we use $D_{s,i} = D_{s,e}/4 = 11.7 \times 10^{-11}\,\text{m}^2/\text{s}$ for the intracellular (cytosolic) diffusivity of calcein.

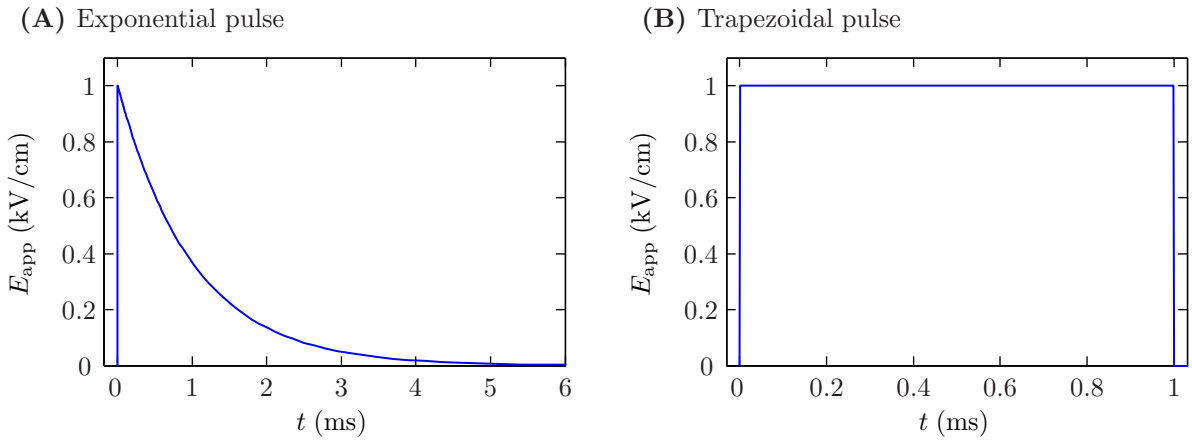

Figure 7.3: Applied electric pulses. **(A)** 1 ms, 1 kV/cm exponential pulse. The pulse has linear rise in the applied field to $E_{app} = 1\,\text{kV/cm}$ over rise-time $t_{rise} = 10\,\text{ns}$, followed by an exponential decay to zero with time constant $\tau_{pulse} = 1\,\text{ms}$. **(B)** 1 ms, 1 kV/cm trapezoidal pulse. The pulse has a linear rise in the applied field to $E_{app} = 1\,\text{kV/cm}$ over rise-time $t_{rise} = 1\,\mu\text{s}$, a plateau at E_{app} of duration $t_{plat} = 998\,\mu\text{s}$, and a linear fall to zero over fall-time $t_{fall} = 1\,\mu\text{s}$.

Puc et al. [50] measured the lucifer yellow uptake. Lucifer yellow can be approximated as cylindrical with radius $r_s = 0.61\,\text{nm}$ and length $l_s = 1.46\,\text{nm}$ [55] (Fig. 7.2B). The charge (valence) of lucifer yellow at pH 7.4 is $z_s = -2$ [55]. We use $D_{s,e} = 47.7 \times 10^{-11}\,\text{m}^2/\text{s}$ [55] for the extracellular diffusivity of lucifer yellow and $D_{s,i} = D_{s,e}/4 = 11.9 \times 10^{-11}\,\text{m}^2/\text{s}$ for the intracellular (cytosolic) diffusivity.

7.2.4 Applied Electric Pulses

In their respective experiments, Canatella et al. [49] applied decaying exponential pulses (Fig. 7.3A) and Puc et al. [50] applied trapezoidal pulses (Fig. 7.3B). Exponential pulses are characterized by a linear rise in the applied field to E_{app} over rise-time t_{rise}, followed by an exponential decay to zero with time constant τ_{pulse} (Fig. 7.3A). Trapezoidal pulses are characterized by a linear rise in the applied field to E_{app} over rise-time t_{rise}, a plateau at E_{app} of duration t_{plat}, and a linear fall to zero over fall-time t_{fall} (Fig. 7.3B). Thus, if the pulse has total duration t_{pulse}, then $t_{plat} = t_{pulse} - t_{rise} - t_{fall}$.

Neither study reported the pulse rise-time. Canatella et al. [49] used a BTX pulser that generates

an exponential pulse by means of a simple capacitor discharge [82]. Thus, in accordance with the analysis of Pliquett et al. [83], we assume an extremely small value $t_{\text{rise}} = 10\,\text{ns}$ for the Canatella pulses. Puc et al. used a Jouan square wave generator that uses complex circuitry to generate trapezoidal pulses, and this results in a longer rise-time. Using the same pulser as Puc et al. [50], Cukjati et al. [84] reported rise-time range $t_{\text{rise}} = 0.6 - 2.1\,\mu\text{s}$. Accordingly, for the Puc pulses, we use an intermediate value $t_{\text{rise}} = 1\,\mu\text{s}$. We also use fall-time value $t_{\text{fall}} = 1\,\mu\text{s}$.

Here we define E_{app} to be the applied electric field as experienced by the cells in the pulsing medium. It is often assumed that $E_{\text{app}} = V_{\text{app}}/L_{\text{elec}}$, where V_{app} is the applied voltage (at the electrodes) and L_{elec} is the distance between the electrodes. However, as Pliquett et al. [83] reported, electrochemical reactions at the electrodes can result in $E_{\text{app}} < V_{\text{app}}/L_{\text{elec}}$, particularly for aluminum electrodes. Canatella et al. [49] used aluminum electrodes but took measurements to account for this effect and reported electric field values as experienced by cells (i.e., consistent with how we have defined E_{app}). Puc et al. [50] reported V_{app}, rather than E_{app}. However, because they used stainless steel electrodes, which do not exhibit the same voltage drops at the electrode-electrolyte interface [85], we assume $E_{\text{app}} = V_{\text{app}}/L_{\text{elec}}$, where $L_{\text{elec}} = 2\,\text{mm}$ [50].

Canatella et al. [49] applied exponential pulses with $\tau_{\text{pulse}} = 50\,\mu\text{s}$, $90\,\mu\text{s}$, $0.5\,\text{ms}$, $1.1\,\text{ms}$, $2.8\,\text{ms}$, $5.3\,\text{ms}$, $10\,\text{ms}$, and $21\,\text{ms}$ with applied field E_{app} up to $3.1\,\text{kV/cm}$. Here, we examine all of these pulses except $\tau_{\text{pulse}} = 0.5\,\text{ms}$ because the associated data were too difficult to discern in the crowded Canatella et al. [49] plots. Puc et al. [50] applied trapezoidal pulses with durations $t_{\text{pulse}} = 100\,\mu\text{s}$ and $1\,\text{ms}$ with applied field E_{app} up to $2\,\text{kV/cm}$, and we consider all of these pulses.

7.2.5 Experimental Data

The Canatella experiments [49] measured calcein uptake using flow cytometry, a single cell method that yields cell population distributions that enable average behavior to be computed. They reported data in a series of plots, specifically Figs. 2 and 3 of Ref. [49]. These figures show molecular uptake plotted against E_{app} for a range of τ_{pulse}. Molecular uptake was presented as both number of

molecules taken up per cell and the corresponding relative intracellular concentration $\hat{\gamma}_i \equiv \gamma_i/\gamma_e$, where γ_i is average intracellular concentration and γ_e is initial extracellular concentration. $\hat{\gamma}_i$ was determined using the number of molecules per cell and the volume of a cell with the average radius $r_{cell} = 11\,\mu m$ [49].

The Puc experiments [50] measured lucifer yellow uptake using spectrofluorometry, a total population determination yielding average behavior. The data of Fig. 6 of Ref. [50] shows the number of molecules taken up per cell plotted against V_{app} for both t_{pulse} used.

We digitized both sets of reported data using the open-source Engauge Digitizer software (version 4.1, 2008, http://digitizer.sourceforge.net). Specifically, for the Canatella experiments [49] we digitized the relative concentration data. For the Puc experiments [50], we digitized the average number of molecules taken up per cell and converted this to relative concentration using the volume of a cell with the reported average radius $r_{cell} = 8.55\,\mu m$ [50].

Canatella et al. [49] reported data for both single and multiple pulses (1, 2, 4, 10 pulses). For the pulses with $\tau_{pulse} = 50\,\mu s$ and $100\,\mu s$ we use the 10 pulse data (divided by 10 to give the uptake per pulse) rather than the single pulse data. There is a clear trend in the data showing uptake in proportion to the number of pulses, and the amount and quality of the multiple pulse data for the $50\,\mu s$ and $100\,\mu s$ pulses is significantly better than the single pulse data.

7.2.6 System Discretization

The systems are discretized (Fig. 7.4A) using a modified version of an open-source meshing algorithm [86]. The algorithm generates very high-quality meshes with triangular elements that may vary widely in size. The system nodes are defined by the intersections of the edges of the triangular mesh elements. Here, the membrane for each system is lined by 600 node pairs. As a result, the spacing between nodes along the membrane is 115 nm for the Canatella model and 89.5 nm for the Puc model.

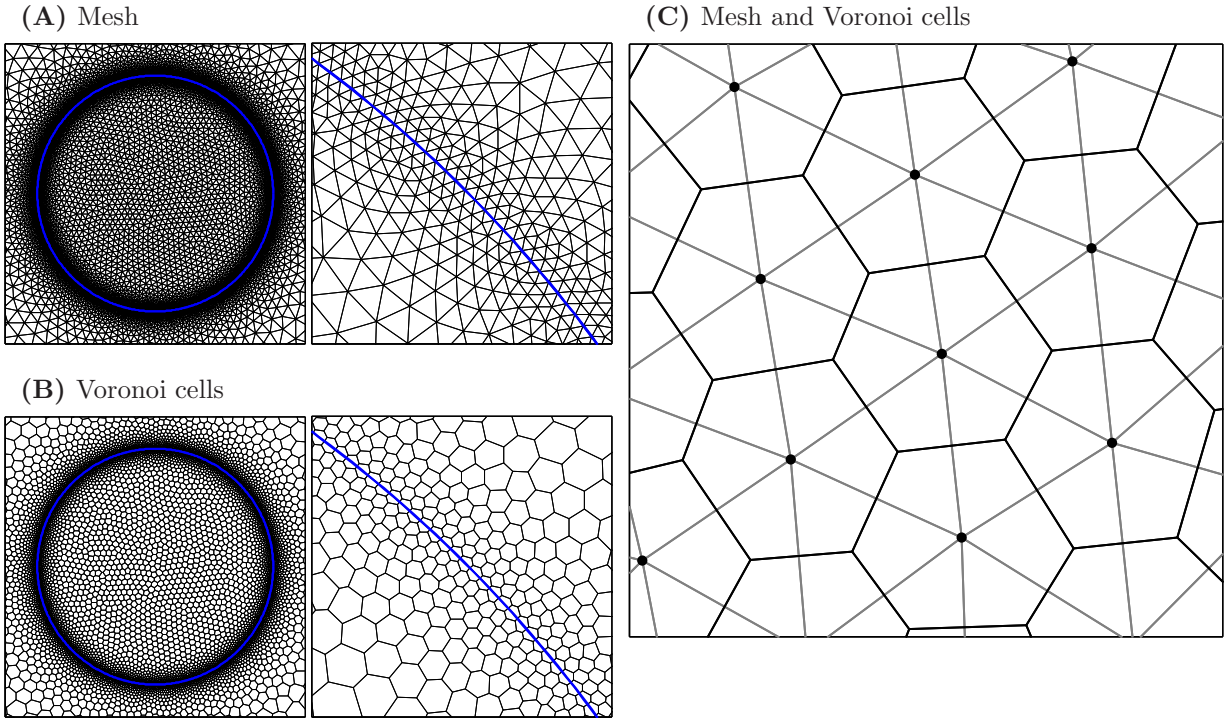

Figure 7.4: System mesh and Voronoi cells. **(A)** The system mesh is shown at the level of the cell (*left*) and the membrane (*right*). The edges of the triangular mesh elements represent the connections between adjacent system nodes. The elements are small near the membrane and expand in size with distance from the membrane. **(B)** The system Voronoi cells (VCs) associated with the mesh in (**A**) are shown using the same fields of view. Each VC defines the region of physical space represented by its associated node. **(C)** The VC edges bisect the edges of the triangular mesh elements at right angles. This is an important property that simplifies the description of transport between adjacent nodes.

A Voronoi cell (VC) (Fig. 7.4B) is associated with each node in the discretized system. Each VC defines the region of physical space represented by its associated node. Thus, while the mesh (Fig. 7.4A) determines the connections between nodes, the VCs determine the small volumes into which the system is discretized. Each node is taken to be representative of the behavior of the region represented by its associated VC. Note that VC edges bisect the edges of the triangular mesh elements at right angles (Fig. 7.4C). This is an important property that simplifies the description of transport between adjacent nodes [68].

Table 7.2: Electroporation Parameters

Symbol	Value	Description and Source
d_m	5 nm	Membrane thickness [87]
d_p	2.5 nm	Pore thickness (internal region) [57]
r_*	0.65 nm	Pore radius at local energy maximum [57]
$r_{p,min}$	1.0 nm	Pore radius at local energy minimum [57]
$r_{p,max}$	12 nm	Maximum pore radius*
W_*	45 kT	Energy at local maximum‡ [87]
W_m	28.341 kT	Energy at local minimum†‡
W_d	24.729 kT	Energy barrier to pore destruction†‡
B	1.6301×10^{-19} J	Steric repulsion constant†‡
b	3.5341	Steric repulsion constant†‡
C	-5.9522×10^{-20} J	Steric repulsion constant†‡
γ	2.0×10^{-11} J/m	Pore line tension‡ [59]
Γ	1×10^{-5} J/m^2	Membrane tension‡ [88]
Γ'	20×10^{-3} J/m^2	Hydrocarbon-water interface tension‡ [89]
F_{max}	6.9×10^{-10} N/V^2	Maximum electric force for $\Delta\phi_m = 1$ V‡ [90]
r_h	0.95 nm	Electric force constant‡ [90]
r_t	0.23 nm	Electric force constant‡ [90]
D_p	2×10^{-13} m^2/s	Pore diffusion coefficient*
a	1×10^9 /(m^2 s)	Pore creation rate density [91]
β	18 kT/V^2	Symmetric pore creation constant*
α	11 kT/V	Asymmetric pore creation constant*
τ_p	4 s	Pore resealing time constant*
f_{prot}	0.5	Membrane protein fraction [66]
r_s	0.19 nm	Radius of charge carrier‖§ [55]
n	0.25	Pore relative entrance length‖ [57]

*Optimal parameter. See Table 7.3 and main text for details. †Parameter value determined by values of other parameters. The listed values are consistent with parameter values listed in this table. See Ref. [58] for details. ‡Parameter used in the pore energy equation, as given in Ref. [58]. ‖Parameter used in hindrance or partitioning equation, as given in Ref. [57]. §Average of corrected Stokes radii of sodium, potassium, and chloride, as given in Ref. [55].

7.2.7 Pore Radius Space

The model presented here uses fixed pore radii r_p and accounts for pore expansion and contraction through the transport of pore density n between adjacent radii in radius space [58]. The minimum hydrophilic pore radius, at which pores are created and destroyed, is r_*, and the maximum pore radius is $r_{p,max}$. Slightly larger than r_* is $r_{p,min}$, the radius at which the pore energy W has a minimum at zero transmembrane voltage ($\Delta\phi_m = 0$ V). Here, we use values $r_* = 0.65$ nm and $r_{p,min} = 1$ nm [58]. The value of $r_{p,max}$ is varied in our results.

The pore radii are distributed non-uniformly in radius space to increase computational efficiency. Specifically, between r_* and $r_{p,min}$ we used discretization size $\Delta r_p = 0.025$ nm, and between $r_{p,min}$ and $r_{p,max}$ we linearly increased the discretization size Δr_p from 0.025 nm to 0.25 nm.

7.2.8 Transport in the Discretized Model System

The discretized system represents three types of transport: (1) electrical and (2) molecular transport in 2-D physical space and (3) pore transport in 1-D radius space. Below we address each type of transport in turn.

Electrical Transport

The electrical flux $J_e^{i,j}$ from node i to adjacent node j is described by [68]

$$J_e^{i,j} = -\frac{\sigma_{i,j}}{l_{i,j}}(\Delta\phi)_{i,j} - \frac{\epsilon_{i,j}}{l_{i,j}}\frac{d}{dt}(\Delta\phi)_{i,j}, \tag{7.1}$$

where $(\Delta\phi)_{i,j} \equiv \phi_j - \phi_i$ is the electric potential difference between nodes i and j, $\sigma_{i,j}$ is the conductivity between nodes i and j, and $\epsilon_{i,j}$ is the permittivity between nodes i and j. $\sigma_{i,j} = \sigma_e$, σ_i, or σ_m, as appropriate for the system region, and $\epsilon_{i,j} = \epsilon_e$, ϵ_i, or ϵ_m, as appropriate for the system region (e.g., if nodes i and j are in the extracellular region, then $\sigma_{i,j} = \sigma_e$ and $\epsilon_{i,j} = \epsilon_e$). If the connection between nodes lies along a boundary (e.g., the membrane), then the flux associated with each side of the connection is calculated independently [68].

The electrical current $i_e^{i,j}$ from node i to node j is simply the flux $J_e^{i,j}$ (Eq. 7.1) scaled by the area $A_{i,j} = w_{i,j}d$ of the interface shared by VCs i and j (Fig. 7.5):

$$i_e^{i,j} = A_{i,j}J_e^{i,j}. \tag{7.2}$$

For node pairs i and j that span the membrane (i.e., node i on the extracellular side of the membrane and adjacent node j on the intracellular side of the membrane, or vice versa), the passive current $i_e^{i,j}$ (Eq. 7.2) only accounts for the ionic and displacement current through the membrane lipid. In addition to this current, there is ionic current $i_{e,p}^{i,j}$ through pores.

Consider a pair of nodes i and j that span the membrane, with node i on the extracellular side and node j on the intracellular side. The interface shared by VCs i and j represents a small region, or

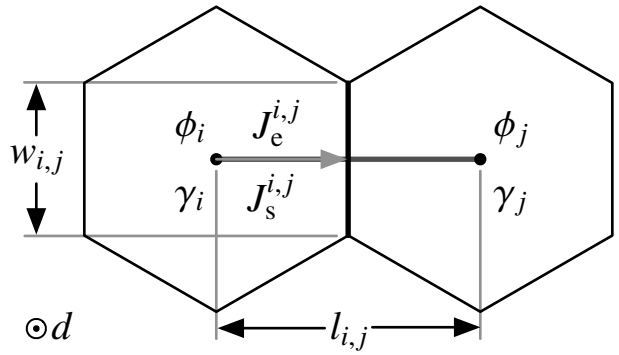

Figure 7.5: Electrical and molecular transport between adjacent system nodes. Adjacent nodes i and j are shown with their associated VCs. Node i has electric potential ϕ_i and solute concentration γ_i, and node j has electric potential ϕ_j and solute concentration γ_j. The distance between the nodes is $l_{i,j}$. The VCs share an interface with width $w_{i,j}$ and area $A_{i,j} = w_{i,j}d$, where d is the system depth. The VC associated with node i has volume V_i, and the VC associated with node j has volume V_j. Using the system transport parameters and the local mesh geometry, the electrical flux $J_e^{i,j}$ and molecular flux $J_s^{i,j}$ from nodes i to node j can be calculated.

patch, of membrane with area $A_{i,j}$. The membrane patch has transmembrane voltage $\Delta\phi_m^{i,j}$ and a radius space with discretized pore radii r_p^k with discretization $(\Delta r_p)_k$. The pore density associated with each r_p^k and $(\Delta r_p)_k$ is $n_{i,j,k}$. Note that all membrane patches have a radius space described by the same r_p^k and $(\Delta r_p)_k$, but the pore density $n_{i,j,k}$ associated with each radius in each patch is different.

The total current $i_{e,p}^{i,j}$ through pores in the membrane patch associated with nodes i and j is the sum of the currents through pores of each radius r_p^k:

$$i_{e,p}^{i,j} = A_{i,j}\,\Delta\phi_m^{i,j} \sum_k n_{i,j,k}\,(\Delta r_p)_k\, g_p(r_p^k, \Delta\phi_m^{i,j}). \tag{7.3}$$

Here, the function $g_p(r_p, \Delta\phi_m)$ describes the conductance associated with a single pore, accounting for the resistance of both the internal pore region and the pore access region [92, 93]. It is given by [57]

$$g_p(r_p, \Delta\phi_m) = \left(\frac{d_p}{\sigma_p \pi r_p^2\, H(r_p)\, K(r_p, \Delta\phi_m)} + \frac{1}{2\sigma_p r_p} \right)^{-1}. \tag{7.4}$$

Here, d_p is the thickness of the internal region of the pore, $\sigma_p = 2\sigma_i\sigma_e/(\sigma_i + \sigma_e)$ is the average conductivity of the electrolyte within the pore, $H(r_p)$ is the hindrance factor, and $K(r_p, \Delta\phi_m)$ is the partition coefficient. $H(r_p)$ and $K(r_p, \Delta\phi_m)$ are described in detail in Ref. [57].

The total current $i_{e,tot}^{i,j}$ between nodes i and j is the sum of the $i_e^{i,j}$ (Eq. 7.2) and $i_{e,p}^{i,j}$ (Eq. 7.3):

$$i_{e,tot}^{i,j} = i_e^{i,j} + i_{e,p}^{i,j}. \tag{7.5}$$

(Note that $i_{e,p}^{i,j} = 0$ for node pairs i and j that do not span the membrane.)

The current $i_{e,tot}^{i,j}$ describes the transport between nodes, but does not specify how the electric potential at the nodes changes as a result. This is provided by imposing continuity. Continuity requires that for every node i with adjacent nodes j

$$\sum_j i_{e,tot}^{i,j} = 0. \tag{7.6}$$

In other words, the sum of the currents flowing out of each node must equal zero (Kirchhoff's Current Law).

Molecular Transport

In bulk electrolyte, the molecular (electrodiffusive) flux $J_s^{i,j}$ from node i to adjacent node j is described by [56]

$$J_s^{i,j} = \begin{cases} -D_s^{i,j}\frac{(\Delta\gamma)_{i,j}}{l_{i,j}} & \text{if } (\Delta\psi)_{i,j} = 0, \\ -D_s^{i,j}\frac{(\Delta\psi)_{i,j}}{l_{i,j}}\left(\frac{\gamma_i}{1-e^{(\Delta\psi)_{i,j}}} + \frac{\gamma_j}{1-e^{-(\Delta\psi)_{i,j}}}\right) & \text{if } (\Delta\psi)_{i,j} \neq 0. \end{cases} \tag{7.7}$$

Here, ψ is the dimensionless potential $\psi \equiv q_e z_s \phi/kT$, $(\Delta\psi)_{i,j} \equiv \psi_j - \psi_i$ is the difference in dimensionless potential between nodes i and j, γ_i and γ_j are the solute concentrations at nodes i and j, and $D_s^{i,j}$ is the solute diffusivity between nodes i and j. $D_s^{i,j} = D_{s,e}$ or $D_{s,i}$, as appropriate for the system region.

In bulk electrolyte, the flow of solute $i_{\mathrm{s}}^{i,j}$ (units: molecules/s with concentration γ in units molecules/m^3) from node i to node j is simply the flux $J_{\mathrm{s}}^{i,j}$ (Eq. 7.7) scaled by the area $A_{i,j}$ of the interface shared by VCs i and j (Fig. 7.5):

$$i_{\mathrm{s}}^{i,j} = A_{i,j}\, J_{\mathrm{s}}^{i,j}. \tag{7.8}$$

Note that while $i_{\mathrm{s}}^{i,j}$ is analogous to electric current, both drift and diffusion contribute, and therefore it applies to both charged and neutral solutes.

Like electrical transport (charge carried by small ions) through pores, molecular transport through pores is also affected by hindrance and partitioning. For nodes i and j that span the membrane, the flow of solute $i_{\mathrm{s,p}}^{i,j}$ through pores is

$$i_{\mathrm{s,p}}^{i,j} = A_{i,j}\, J_{\mathrm{s}}^{i,j} \sum_k n_{i,j,k}\, (\Delta r_{\mathrm{p}})_k\, \pi (r_{\mathrm{p}}^k)^2\, H(r_{\mathrm{p}}^k)\, K(r_{\mathrm{p}}^k, \Delta\phi_{\mathrm{m}}^{i,j}). \tag{7.9}$$

Here, the relevant diffusivity of Eq. 7.7 that determines $J_{\mathrm{s}}^{i,j}$ is the average diffusivity within the pores $D_{\mathrm{s,p}} = 2D_{\mathrm{s,i}}D_{\mathrm{s,e}}/(D_{\mathrm{s,i}} + D_{\mathrm{s,e}})$. $H(r_{\mathrm{p}})$ and $K(r_{\mathrm{p}}, \Delta\phi_{\mathrm{m}})$ are described in Ref. [57].

Noting that Eq. 7.8 describes the flow between nodes i and j that do not span the membrane and that Eq. 7.9 describes the flow between nodes i and j that do span the membrane, the total flow $i_{\mathrm{s,tot}}^{i,j}$ between nodes i and j is

$$i_{\mathrm{s,tot}}^{i,j} = \begin{cases} i_{\mathrm{s}}^{i,j} & \text{if } i \text{ and } j \text{ do not span membrane,} \\ i_{\mathrm{s,p}}^{i,j} & \text{if } i \text{ and } j \text{ do span membrane.} \end{cases} \tag{7.10}$$

Unlike small ion charge, this means that solutes only pass through the membrane via pores.

The rate at which concentration changes as a result of solute flux is determined by continuity,

which requires that for every node i with adjacent nodes j,

$$\frac{\partial \gamma_i}{\partial t} = -\frac{1}{V_i} \sum_j i_{\mathrm{s,tot}}^{i,j}, \tag{7.11}$$

where V_i is the volume of VC i (Fig. 7.5). In other words, a net flow of solute out of or into a node must result in a corresponding decrease or increase in the concentration of the node.

Pore Transport

Expansion and contraction of pores is treated by behavior in pore radius space. Transport of pores in radius space is analogous to 1-D electrodiffusion in physical space [56, 58]. Just as solute is transported in response to gradients in concentration and electric potential (Eq. 7.7), pores are transported in response to gradients in pore density n and pore energy W (Fig. 7.6), with the pore energy landscape [58].

The flux of pores $J_{\mathrm{p}}^{i,j}$ from node i to adjacent node j (in radius space) is described by [58]

$$J_{\mathrm{p}}^{i,j} = \begin{cases} -\frac{D_{\mathrm{p}}}{kT} \frac{(\Delta n)_{i,j}}{(\Delta r_{\mathrm{p}})_{i,j}} & \text{if } (\Delta W)_{i,j} = 0, \\ -\frac{D_{\mathrm{p}}}{kT} \frac{(\Delta W)_{i,j}}{(\Delta r_{\mathrm{p}})_{i,j}} \left(\frac{n_i}{1-\mathrm{e}^{(\Delta W)_{i,j}/kT}} + \frac{n_j}{1-\mathrm{e}^{-(\Delta W)_{i,j}/kT}} \right) & \text{if } (\Delta W)_{i,j} \neq 0. \end{cases} \tag{7.12}$$

Here, $(\Delta W)_{i,j} \equiv W_j - W_i$ is the difference in pore energy between nodes i and j, n_i and n_j are the pore densities at nodes i and j, D_{p} is the diffusivity of pores in radius space, k is the Boltzmann constant, and T is the absolute temperature.

The pore energy $W(r_{\mathrm{p}}, \Delta\phi_{\mathrm{m}})$ is described in detail in Ref. [58]. Briefly, the pore is given by

$$W(r_{\mathrm{p}}, \Delta\phi_{\mathrm{m}}) = W_{\mathrm{steric}}(r_{\mathrm{p}}) + W_{\mathrm{edge}}(r_{\mathrm{p}}) + W_{\mathrm{surf}}(r_{\mathrm{p}}) + W_{\mathrm{polar}}(r_{\mathrm{p}}, \Delta\phi_{\mathrm{m}}) + W_{\mathrm{dipole}}(r_{\mathrm{p}}, \Delta\phi_{\mathrm{m}}). \tag{7.13}$$

Here, $W_{\mathrm{steric}}(r_{\mathrm{p}})$ is the energy that results from the steric repulsion of lipid head groups, $W_{\mathrm{edge}}(r_{\mathrm{p}})$ is the energy that results from the bending of lipid around the interior edge of a pore, $W_{\mathrm{surf}}(r_{\mathrm{p}})$ is the interfacial energy of lipid molecules, $W_{\mathrm{polar}}(r_{\mathrm{p}}, \Delta\phi_{\mathrm{m}})$ accounts for the polarization energy that re-

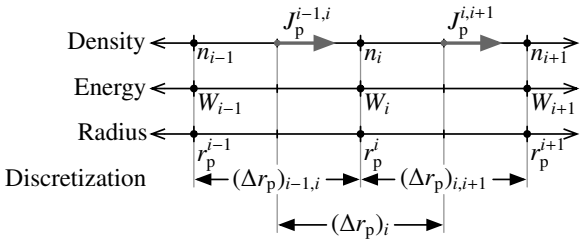

Figure 7.6: Pore transport between adjacent nodes in radius space (evolution of pore populations). Node i has adjacent nodes $i-1$ and $i+1$. The pore radius r_p, energy W, and density n for each node is indicated by its subscript or superscript. Nodes $i-1$ and i are separated by distance (in radius space) $(\Delta r_p)_{i-1,i}$, nodes i and $i+1$ are separated by distance (in radius space) $(\Delta r_p)_{i,i+1}$. The region of radius space associated with node i has length $(\Delta r_p)_i$. $J_p^{i-1,i}$ is the pore flux from node $i-1$ to node i, and $J_p^{i,i+1}$ is the pore flux from node i to node $i+1$. The pore flux between adjacent nodes is determined by the pore radii, energies, and densities of the nodes, as well as pore (e.g., diffusivity) and system (e.g., temperature) properties. The rate at which the pore density n_i changes is determined by the net flux $J_p^{i-1,i} - J_p^{i,i+1}$ into node i and the length $(\Delta r_p)_i$.

sults from the force exerted on the pore edge by the electric field, and $W_{\text{dipole}}(r_p, \Delta\phi_m)$ accounts for the energy associated with rotation of dipoles within the pore edge. A quantitative description of the dipole energy term is given in the *Appendix*. All other energy terms are described in Ref. [58].

A basic, established assumption is that all pore creation and destruction occurs at pore radius r_*. Thus, pore creation and destruction can be cast as additional flux terms at the r_* node. The pore creation flux is described by [58]

$$J_p^{*,c}(\Delta\phi_m) = a f_c e^{\left(\beta(\Delta\phi_m)^2 + \alpha\Delta\phi_m\right)/kT}. \tag{7.14}$$

Here, a is the pore creation rate density, β is the symmetric pore creation constant, α is the asymmetric pore creation constant, and f_c is the fraction of the membrane available for pore creation, as discussed below.

The pore destruction flux $J_p^{*,d}$ results from applying an absorbing boundary condition at r_* [58, 61]. Specifically, $J_p^{*,d}$ is equal to the flux from r_* to a slightly smaller radius $r_* - \Delta r_p$ node with pore density $n(r_* - \Delta r_p) = 0$.

The rate at which pore density changes as a result of the pore flux is determined by continuity, which requires that for every node i with adjacent nodes j,

$$\frac{\partial n_i}{\partial t} = -\frac{1}{(\Delta r_\mathrm{p})_i} \sum_j J_\mathrm{p}^{i,j}. \tag{7.15}$$

Here, $(\Delta r_\mathrm{p})_i$ is the size (length) of the region of radius space associated with node i (Fig. 7.6). Note that for nodes i with $r_\mathrm{p}^i = r_*$, the creation flux $J_\mathrm{p}^{*,\mathrm{c}}$ and destruction flux $J_\mathrm{p}^{*,\mathrm{d}}$ are considered flux from "adjacent" nodes.

In Eq. 7.14, f_c is the fraction of the membrane available for pore creation [58]. Specifically, f_c accounts for the fact that (1) a fraction f_prot of the total membrane area is occupied by protein and (2) a fraction of the membrane is occupied by existing pores. Both are unavailable for pore creation.

Specifically, the fraction $f_\mathrm{c}^{i,j}$ of the membrane available for pore creation in the membrane patch spanned by nodes i and j is [58]

$$f_\mathrm{c}^{i,j} = 1 - f_\mathrm{prot} - \sum_k n_{i,j,k} (\Delta r_\mathrm{p})_k \pi \left(r_\mathrm{p}^k + \frac{d_\mathrm{m}}{2} \right)^2. \tag{7.16}$$

Accordingly, as the membrane becomes saturated with pores, $f_\mathrm{c}^{i,j} \to 0$, and therefore $J_\mathrm{p}^{*,\mathrm{c}} \to 0$ for the membrane patch. Thus, f_c prevents the generation of nonphysical pore density in response to very large magnitude pulses.

7.2.9 Numerical Implementation

Each of the continuity equations (Eqs. 7.6, 7.11, and 7.15) has a time derivative term that can be isolated on the left-hand side (LHS) of the equation. Let $\boldsymbol{y}$ be an array containing all ϕ and γ for the physical space nodes and n for the radius space nodes. The corresponding system of continuity equations can be constructed:

$$\boldsymbol{M} \frac{\partial \boldsymbol{y}}{\partial t} = f(t, \boldsymbol{y}), \tag{7.17}$$

where $\boldsymbol{M}$ is a sparse matrix of constants and $f(t, \boldsymbol{y})$ is a nonlinear function that evaluates the right-hand size (RHS) of the continuity equations. This system of equations can be solved numerically. We use MATLAB (version 7.8, 2009, http://www.mathworks.com) to construct, solve, and subsequently analyze the system of transport equations. The steps in this process are:

1. Define model system regions and properties.
2. Generate system mesh and find associated VCs.
3. Evaluate mesh and VC geometry.
4. Assign transport properties associated with node connections.
5. Construct system of equations (Eq. 7.17).
6. Solve system using MATLAB function *ode15s.*
7. Analyze results.

7.2.10 Determination of Optimal Electroporation Parameters

Because our model features a mechanistic description of molecular transport by electrodiffusion [56], our model results can be directly compared to quantitative experimental measurements of cellular uptake, e.g., those of Canatella et al. [49] and Puc et al. [50]. We took advantage of this to use the Canatella et al. [49] and Puc et al. [50] measurements of uptake to determine optimal values for several important electroporation parameters that have not been well-established. Specifically, we examined the asymmetric pore creation constant α, the symmetric pore creation constant β, the pore diffusion coefficient in radius space D_{p}, the maximum pore radius $r_{\mathrm{p,max}}$, and the pore resealing time constant τ_{p}. The range of values reported for these parameters in the literature, as well as the range we examined here, are shown in Table 7.3.

For each combination of electroporation parameters, we simulated the response of the Canatella model and Puc model for the specific pulses for which experimental data was provided in the experimental studies [49, 50]. Because we considered five different parameters, the total number of parameter combinations was potentially very large. Therefore, we use an approach in which we

performed successive rounds of simulations and tightened the range of parameter values considered in reach round.

Initially we chose approximately three values spanning the plausible range for each parameter (e.g., $\beta = 10\,\mathrm{kT/V^2}$, $17\,\mathrm{kT/V^2}$, and $25\,\mathrm{kT/V^2}$). We then used each combination of parameters to simulate the responses of the Canatella model and Puc model for the pulses for which molecular uptake data was provided [49, 50]. We assessed the agreement between the model results and the experimental results by calculating the average relative error and also visually by using plots like those shown in the *Results and Discussion* section (e.g., Fig. 7.7).

After each round of simulations we tightened the window of plausible parameter values. For example, using the value $D_\mathrm{p} = 1 \times 10^{-14}\,\mathrm{m^2/s}$, the transport predicted for both model systems was far smaller than the experimentally measured transport, regardless of the values of the other electroporation parameters examined. Thus, in the next round of simulations we raised the lower bound on D_p from $1 \times 10^{-14}\,\mathrm{m^2/s}$ to $5 \times 10^{-14}\,\mathrm{m^2/s}$. With each successive round of simulations, we tightened the bounds on the parameters until we arrived at the optimal set.

7.3 Results and Discussion

7.3.1 Optimal Electroporation Parameters

Using the model and the described approach for iteratively determining optimal values of select electroporation parameters, we obtained those shown in Table 7.3. Table 7.3 shows the range of values previously reported in the literature, the range of value we examined with our model, and the final optimal set of values. In general, the optimal parameters are well within the range reported in the literature.

In the sections that follow, we compare our model results with the Canatella experiments [49] and Puc experiments [50], and then vary each tested electroporation parameter to demonstrate its effect on the model results. This sensitivity testing is an important part of our overall methods,

Table 7.3: Optimal Electroporation Parameters

Symbol	Values in Literature	Values Examined	Optimal Value	Description and References
α		$0-20\,\mathrm{kT/V}$	$11\,\mathrm{kT/V}$	Asymmetric pore creation constant [94]
β	$15-20\,\mathrm{kT/V^2}$	$10-25\,\mathrm{kT/V^2}$	$18\,\mathrm{kT/V^2}$	Symmetric pore creation constant [62, 91]
D_p	$(0.001-110)\times10^{-14}\,\mathrm{m^2/s}$	$(1-110)\times10^{-14}\,\mathrm{m^2/s}$	$20\times10^{-14}\,\mathrm{m^2/s}$	Pore diffusion coefficient [59, 60, 95, 96]
$r_\mathrm{p,max}$	$3-2200\,\mathrm{nm}$	$5-50\,\mathrm{nm}$	$12\,\mathrm{nm}$	Maximum pore radius [14, 59, 60, 64, 67, 69, 89]
τ_p	$0.16-120\,\mathrm{s}$	$1-10\,\mathrm{s}$	$4\,\mathrm{s}$	Pore resealing time constant [48, 87, 97, 98]

made realistic by having sufficient computational capability to examine many versions of both the models and the applied pulses.

7.3.2 Comparison of Model Results with Experimental Results

Figure 7.7 shows a comparison of the relative intracellular concentration $\hat{\gamma}_\mathrm{i}$ predicted by our model with the experimental measurements reported by Canatella et al. [49] and Puc et al. [50]. For the Canatella experiments, the model slightly overestimates transport in response to the 2.8 ms exponential pulses, and for the Puc experiments, the model slightly overestimates transport in response to the 100 µs pulses with $E_\mathrm{app} \lesssim 1.5\,\mathrm{kV/cm}$. However, overall the model results are in excellent agreement with the experimental results, particularly considering the large range of pulses durations and magnitudes considered. Pulse durations span nearly three orders of magnitude (50 µs – 20 ms) and corresponding pulse magnitudes span about one order of magnitude (3 kV/cm – 0.3 kV/cm), viz., larger pulses pair with shorter pulses.

Several interesting results are evident in Fig. 7.7. First, transport in the Canatella experiments occurs almost entirely during the pulse (Fig. 7.7A). (For the exponential pulses applied in the Canatella experiments, we can take "during" to mean $\sim 4\tau_\mathrm{pulse}$.) Post-pulse transport is proportional to the total number of pores created (during the pulse), and the total number of pores created increases rapidly with E_app. Yet, the total transport in response to the largest pulses with $E_\mathrm{app} \approx 3\,\mathrm{kV/cm}$ is just $\hat{\gamma}_\mathrm{i} \approx 0.01$, far below equilibrium with the extracellular medium. Post-pulse transport in response to the pulses with smaller E_app is even smaller because the number of pores created by these pulses is much smaller. This is an example of the highly nonlinear nature of electroporation, but here examining the net molecular transport rather than electrical behavior.

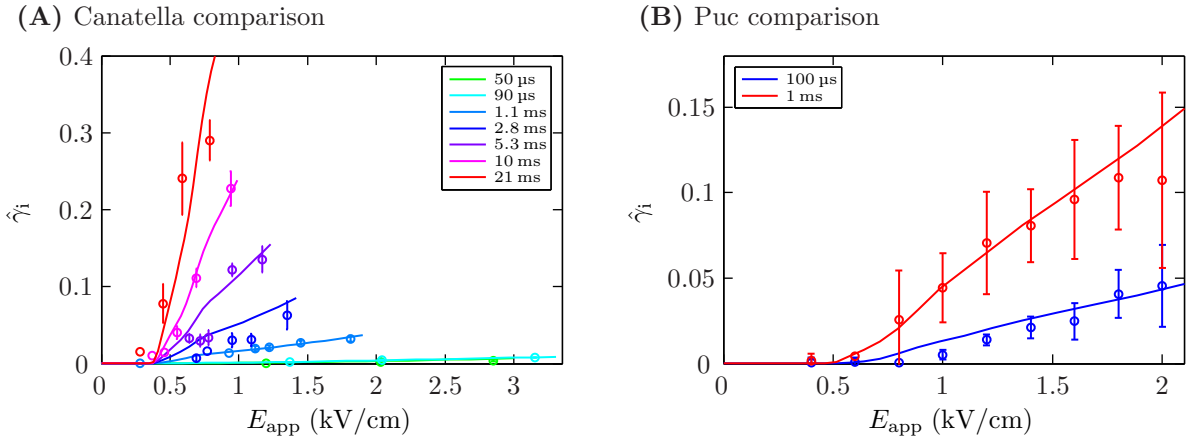

Figure 7.7: Comparison of model predictions of molecular transport with experimental measurements for the **(A)** Canatella experiments and **(B)** Puc experiments. Line color indicates the pulse duration (τ_{pulse} for the Canatella experiments and t_{pulse} for the Puc experiments) (*inset*). *Open circles* and *error bars*, where available, indicate experimental measurements [49, 50]. For the Canatella experiments, the model slightly overestimates transport in response to the 2.8 ms exponential pulses, and for the Puc experiments, the model slightly overestimates transport in response to the 100 µs pulses with $E_{app} \lesssim 1.5\,\mathrm{kV/cm}$. Otherwise, however, the overall model results are in excellent agreement with the experimental results. Note that the pulse durations span nearly three orders of magnitude (50 µs – 20 ms) and pulse magnitudes span one order of magnitude (0.3 kV/cm – 3 kV/cm)

In contrast, significant post-pulse transport occurs in the Puc experiments (Fig. 7.7B). In general, for pulses with $E_{app} \gtrsim 1\,\mathrm{kV/cm}$, essentially all pore creation occurs during the first few microseconds of a pulse. (See the companion paper [71] for an example.) Therefore, to first approximation the total transport during a pulse is proportional to pulse duration t_{pulse} and the total post-pulse transport is determined by pulse magnitude E_{app}. It follows that if all transport in the Puc experiments occurred during the pulse, then the 1 ms pulses would result in 10 times pore transport than the 100 µs pulses of the same magnitude. If all transport in the Puc experiments occurred post-pulse, then the 1 ms pulses would result in the same amount of transport as the 100 µs pulses of the same magnitude. The actual transport ratio between the 1 ms and 100 µs pulses (of the same magnitude) is ~3 – 4 for the pulses with $E_{app} \gtrsim 1\,\mathrm{kV/cm}$ (Fig. 7.7B). This implies that a significant fraction of the transport in the Puc experiments occurs post-pulse.

The reason that there is relatively little post-pulse transport of calcein but significant post-pulse

transport of lucifer yellow results from the difference in the Born energy barrier and its impact on the partition coefficient [57]. Calcein has charge $z_s = -3.61$, and lucifer yellow has charge $z_s = -2$. In our approximation, the Born energy goes as z_s^2. Therefore, the Born energy for calcein is 3.3 times larger than the Born energy for lucifer yellow, and calcein is much less likely to pass through a minimum-size pore post-pulse.

A second interesting result that is evident in Fig. 7.7 is that for any given E_{app} transport during a pulse is approximately proportional to pulse duration. This is clear for transport in the Canatella experiments (Fig. 7.7A), for which the transport during the pulse is approximately equal to the plotted total transport, but not for transport in the Puc experiments (Fig. 7.7B), for which the transport during the pulse is significantly less than the plotted total transport (due to the large amount of post-pulse transport). As previously mentioned, most pore creation and expansion occurs soon after the pulse onset (unless E_{app} is small). As a result, the rate of transport (transmembrane flux) does not depend strongly on pulse duration. Therefore, the total transport scales with pulse duration.

A final interesting result in Fig. 7.7 is that each curve has an inflection point at which transport $\hat{\gamma}_i$ shifts from superlinear (increases faster than linear) in E_{app} to sublinear (increases slower than linear) in E_{app}. For the Canatella experiments, the inflection occurs at $E_{app} \approx 0.8\,\mathrm{kV/cm}$, and for the Puc experiments, the inflection occurs at $E_{app} \approx 0.9\,\mathrm{kV/cm}$. This transition can be understood by considering the factors that influence transport and how they change with E_{app}.

For the smallest E_{app}, there is very little transport, regardless of pulse duration because E_{app} is too small to charge the membrane to a large enough transmembrane voltage $\Delta\phi_m$ to cause significant pore creation. That is, transport in response to pulses with small E_{app} is pore creation-limited [71]. When transport is creation-limited any change that increases the number of pores will result in a corresponding increase in transport. A small increase in E_{app} gives rise to a large increase in the number of pores. Therefore $\hat{\gamma}_i$ increases superlinearly in E_{app}.

In the creation-limited range of E_{app}, the pores that are created will tend to expand. (In the companion paper [71] this is described as an expansion-dominated initial trajectory in pore phase space.) This occurs because $\Delta\phi_m$ is large enough ($\gtrsim 0.5\,V$) to drive pore expansion but not large enough to cause a high rate of pore creation.

As E_{app} increases beyond the value at which $\hat{\gamma}_i$ has its inflection point, the rate of pore creation increases dramatically, and the initial pore trajectory [71] shifts from expansion-dominated to balanced. That is, pore creation and expansion are both significant in increasing the membrane conductance and thereby decreasing $\Delta\phi_m$. As a result, an increasing fraction of the pores remain small ($r_p \approx r_{p,min}$) and a decreasing fraction of the pores expand.

Due to hindrance and partitioning, transport through pores depends strongly on pore size relative to solute size [57]. Thus, as E_{app} increases, the number of pores increases but a smaller fraction of the pores become the large pores that predominate in transporting solute. As a result, the total transport $\hat{\gamma}_i$ increases sublinearly in E_{app}. In short, at the inflection point transport shifts from being creation-limited to expansion-limited.

7.3.3 Electroporation Parameters and Their Impact on Model Results

In this section, we discuss the optimal electroporation parameters (Table 7.3) and examine the impact that the value of each has on the model results.

Symmetric Pore Creation Constant

The symmetric pore creation constant β largely determines the relationship between the creation rate and transmembrane voltage $\Delta\phi_m$ (Eq. 7.14). The larger the value of β, the larger the pore creation rate for any given $\Delta\phi_m$.

Krassowska and colleagues have generally used the value (expressed in a different but equivalent form) $\beta = 15\,kT/V^2$ [61, 62, 64, 67]. According to DeBruin and Krassowska, [62], this value

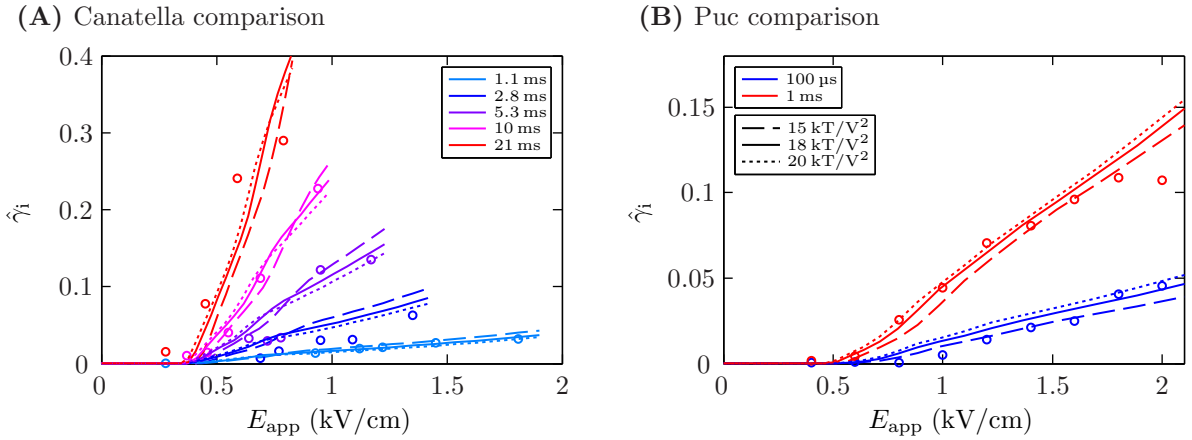

Figure 7.8: Impact of symmetric pore creation constant β on model predicted transport in the **(A)** Canatella experiments and **(B)** Puc experiments. Line color indicates the pulse duration (τ_{pulse} for the Canatella experiments and t_{pulse} for the Puc experiments) (*inset*). Line style indicates the value of β (*inset*). *Open circles* indicate experimental measurements [49, 50]. β partly determines the relationship between the creation rate and transmembrane voltage $\Delta\phi_m$. Increasing the value of β results in increased transport during pulsing over the range of E_{app} for which $\hat{\gamma}_i$ is creation-limited ($E_{app} \lesssim 0.8\,kV/cm$) and decreased transport during pulsing over the range of E_{app} for which $\hat{\gamma}_i$ is expansion-limited ($E_{app} \gtrsim 0.8\,kV/cm$). Increasing the value of β also results in increased transport post-pulse for all E_{app} by increasing total pore creation. Decreasing the value of β has the opposite effects.

was chosen to fit the experimental data of Kinosita and colleagues [34–36]. We (Weaver and colleagues) used $\beta = 15\,kT/V^2$ in Stewart et al. [99], but have subsequently [65, 68, 69, 91] used $\beta = 20\,kT/V^2$ based on a fit to the Melikov et al. [32] experimental data, as described in Vasilkoski et al. [91].

Figure 7.8 shows the impact that the value of β has on the model results. The overall impact across the range of values used in the literature ($15-20\,kT/V^2$) is relatively small. In the Canatella experiments (Fig. 7.8A), increasing the value of β from $18\,kT/V^2$ to $20\,kT/V^2$ results in increased transport over the range of E_{app} for which $\hat{\gamma}_i$ is creation-limited ($E_{app} \lesssim 0.8\,kV/cm$) and results decreased transport over the range of E_{app} for which $\hat{\gamma}_i$ is expansion-limited ($E_{app} \gtrsim 0.8\,kV/cm$). Decreasing the value of β from $18\,kT/V^2$ to $15\,kT/V^2$ has the opposite effect.

In the Puc experiments (Fig. 7.8B), increasing the value of β from $18\,kT/V^2$ to $20\,kT/V^2$ results in

slightly increased transport across all E_{app}. While the changing the value of β has the same impact on transport during a pulse as described for the Canatella experiments (Fig. 7.8A), the impact on post-pulse transport (which, as discussed, is much more significant in the Puc experiments) is larger. Specifically, increasing the value of β results in increased pore creation and therefore results in increased post-pulse transport. Decreasing the value of β results in decreased pore creation and decreased post-pulse transport.

Asymmetric Pore Creation Constant

Like β, the asymmetric pore creation constant α affects the relationship between the creation rate and transmembrane voltage $\Delta\phi_m$ (Eq. 7.14). Unlike β, the impact of α depends on the sign of $\Delta\phi_m$. For calcein and lucifer yellow, transport during a pulse occurs entirely through the cathodic side of the membrane, and most post-pulse transport also occurs through the cathodic side of the membrane because it has higher pore density than the anodic side [71]. Thus, the results presented here show the impact that the value of α has on transport through the cathodic side of the cell, specifically.

Esser et al. [94] introduced α to account for some of the experimentally observed asymmetry in transmembrane voltage [37] and transport [41, 42, 46, 48, 100, 101] during electroporation of mammalian cells. The mechanism is not yet fully understood but is hypothesized to involve the rotation of lipid and other dipoles within the edge of a pore as it is created and as it expands. Minor asymmetry is also expected from the resting potential and, for excitable cells (muscle, nerve), the conductance change due to many ion channels. Esser et al. [94] estimates additional contributions.

Figure 7.9 shows the impact that the value of α has on the model results. In the Canatella experiments (Fig. 7.9A), increasing the value of α from 11 kT/V to 18 kT/V results in a substantial decrease in transport by significantly increasing the rate of pore creation and thereby limiting pore expansion. Decreasing the value of α from 11 kT/V to 0 kT/V results in increased transport by decreasing the creation rate and thereby leading to greater pore expansion. Note that the results are more sensitive to the value of α (Fig. 7.9) than to the value of β (Fig. 7.8), particularly at small E_{app}.

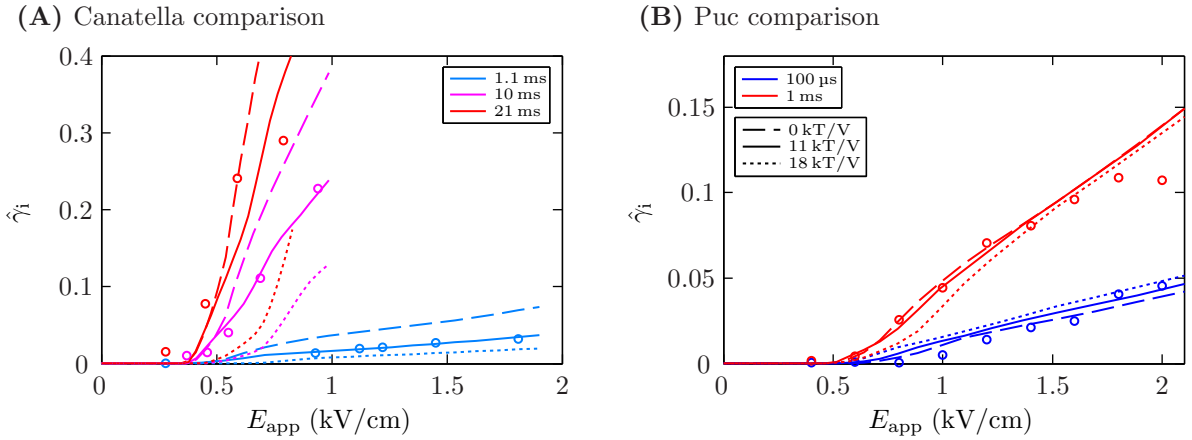

Figure 7.9: Impact of asymmetric pore creation constant α on model predicted transport in the **(A)** Canatella experiments and **(B)** Puc experiments. Line color indicates the pulse duration (τ_{pulse} for the Canatella experiments and t_{pulse} for the Puc experiments) (*inset*). Line style indicates the value of α (*inset*). *Open circles* indicate experimental measurements [49, 50]. α partly determines the relationship between the creation rate and transmembrane voltage $\Delta\phi_m$. The effect of the value of α depends on the sign of $\Delta\phi_m$. For the negatively charged solutes considered here, which predominantly enter the cell through the cathodic side [71], increasing the value of α results in decreased transport during pulsing and increased transport post-pulse. Decreasing the value of α has the opposite effects.

This is because in the pore creation rate equation (Eq. 7.14), α scales $\Delta\phi_m$ and β scales $(\Delta\phi_m)^2$. Therefore, the creation rate is more sensitive to the value of α when $\Delta\phi_m < 1\,V$.

In the Puc experiments (Fig. 7.9B), the impact of the value of α on total transport is more muted because of the significant post-pulse transport. The general effect that the value of α has on transport in response to the 1 ms pulses is the same as in the Canatella experiments (Fig. 7.9A). However, for the 100 µs pulses, the effect on transport is reversed, with increased transport for the value 18 kT/V than for the value 11 kT/V. This occurs because the increase in post-pulse transport more than compensates for the decrease in transport during the pulse.

Pore Diffusion Coefficient

The pore diffusion coefficient D_p is the perhaps the least precisely determined electroporation parameter relative to its impact on transport. Indeed, there are few values of D_p in the literature. D_p determines the rate at which pores expand and contract in response to a gradient in pore energy.

The only estimate of D_p based on fundamental physical considerations, of which we are aware, is that of Powell and Weaver [95]. By treating water as analogous to a dense ideal gas, they arrived at the order of magnitude estimate $D_p \approx 1.1 \times 10^{-12}\,\mathrm{m}^2/\mathrm{s}$. Subsequently, Barnett and Weaver [59] and Freeman et al. [60] chose to use the somewhat reduced value $D_p = 5 \times 10^{-14}\,\mathrm{m}^2/\mathrm{s}$ based on simulation results and the assumption that the viscosity of water, which was not considered in the Powell and Weaver [95] estimate, should somewhat reduce the value of D_p. The value $D_p = 5 \times 10^{-14}\,\mathrm{m}^2/\mathrm{s}$ has been widely used since, as it has been the best estimate available, but there is little reason to think that it is very accurate.

There is one other estimate of D_p in the literature [96], but the value $D_p = 1 \times 10^{-17}\,\mathrm{m}^2/\mathrm{s}$ appears much too small. If the value of D_p were $\sim 1 \times 10^{-17}\,\mathrm{m}^2/\mathrm{s}$, then under essentially all conditions pore dynamics would be creation-dominated and there would be insignificant pore expansion. This is clear from the following order of magnitude estimate of the pore expansion rate. The drift speed of pores in radius space (i.e., rate of expansion and contraction) is [58]

$$\frac{dr_p}{dt} = -\frac{D_p}{kT}\frac{\partial W}{\partial r_p}. \tag{7.18}$$

For pores with $r_p \gtrsim r_{p,\min}$, $W(r_p)$ is dominated by the edge energy and electrical energy. Assuming that the electrical contribution is equal to its asymptotic (in r_p) value $-F_{\max} r_p (\Delta\phi_m)^2$, then the drift speed may be approximated by

$$\frac{dr_p}{dt} \approx -\frac{D_p}{kT}\left(2\pi\gamma - F_{\max}(\Delta\phi_m)^2\right). \tag{7.19}$$

Generously assuming that $\Delta\phi_m$ is clamped at 1 V, we can use Eq. 7.19 to determine how much time is required for a pore to expand by 1 nm. Using the value $D_p = 2 \times 10^{-13}\,\mathrm{m}^2/\mathrm{s}$ determined here, pores expand at rate 27 mm/s. Thus, it takes 37 ns for a pore to expand by 1 nm. Using the much smaller value $D_p = 1 \times 10^{-17}\,\mathrm{m}^2/\mathrm{s}$, pores expand at rate 1.4 μm/s. Thus, it takes 0.71 ms for a pore to expand by just 1 nm. Here, we assumed that $\Delta\phi_m = 1\,\mathrm{V}$, but if pore expansion required

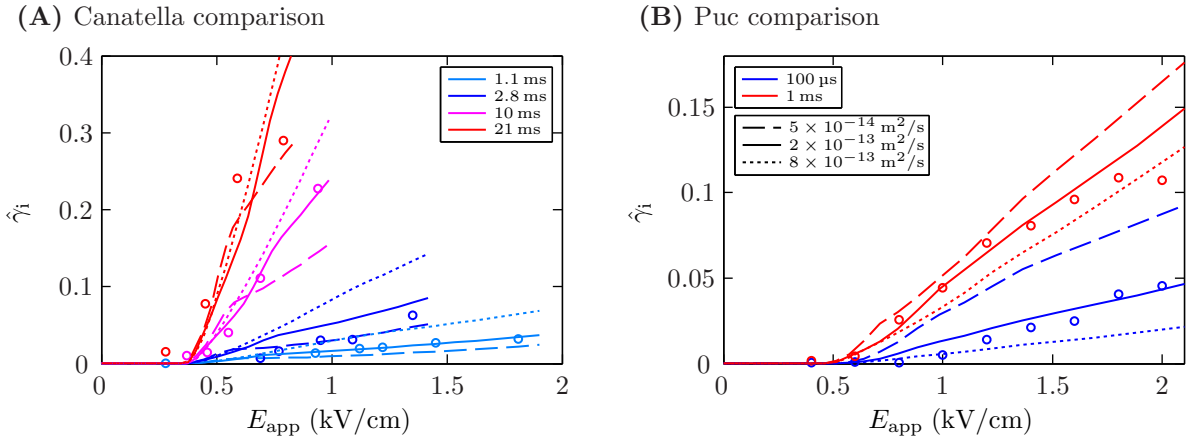

Figure 7.10: Impact of pore diffusion coefficient D_p on model predicted transport in the **(A)** Canatella experiments and **(B)** Puc experiments. Line color indicates the pulse duration (τ_{pulse} for the Canatella experiments and t_{pulse} for the Puc experiments) (*inset*). Line style indicates the value of D_p (*inset*). *Open circles* indicate experimental measurements [49, 50]. D_p determines the rate at which pores expand and contract in response to gradients in pore energy. Increasing the value of D_p results in increased transport during pulsing, particularly over the range of E_{app} for which $\hat{\gamma}_i$ is expansion-limited ($E_{app} \gtrsim 0.8\,kV/cm$). Increasing the value of D_p also results in decreased transport post-pulse for all E_{app} by decreasing total pore creation. For the Canatella experiments, the increase in transport during pulsing is greater than the decrease in transport post-pulse. For the Puc experiments, for which post-pulse transport is a much larger fraction of total transport, increase in transport during pulsing is smaller than the decrease in transport post-pulse. Decreasing the value of D_p has the opposite effects.

durations on the order of milliseconds, then pore creation would lead to a decrease in $\Delta\phi_m$ (the driving force for pore expansion) long before a pore could expand by even 1 nm. Therefore, the value $D_p = 1 \times 10^{-17}\,m^2/s$ is inconsistent with the amount of pore expansion required to explain the levels of molecular transport observed experimentally. Without the present cell system model analysis that yields quantitative new molecular transport estimates, it would have been very difficult to test D_p values.

The value $D_p = 2 \times 10^{-13}\,m^2/s$ that we determined here is well within the range of earlier estimates [59, 60, 95]. Indeed, it is approximately equal to the geometric mean of their values, and thus lies in the middle of the previous estimates in a logarithmic sense.

Figure 7.10 shows the impact that the value of D_p has on the model results. The overall impact is quite large across the range $5 \times 10^{-14} - 80 \times 10^{-14}\,\mathrm{m^2/s}$. In the Canatella experiments (Fig. 7.10A), increasing the value of D_p from $20 \times 10^{-14}\,\mathrm{m^2/s}$ to $80 \times 10^{-14}\,\mathrm{m^2/s}$ generally results in increased transport, and decreasing the value of D_p from $20 \times 10^{-14}\,\mathrm{m^2/s}$ to $5 \times 10^{-14}\,\mathrm{m/s^2}$ generally results in increased transport. The relative impact of the value of D_p on transport is larger over the range of E_{app} for which $\hat{\gamma}_i$ is expansion-limited ($E_{app} \gtrsim 0.8\,\mathrm{kV/cm}$).

In the Puc experiments (Fig. 7.10B), increasing the value of D_p from $20 \times 10^{-14}\,\mathrm{m/s^2}$ to $80 \times 10^{-14}\,\mathrm{m/s^2}$ results in slightly decreased transport across all E_{app}, and decreasing the value of D_p from $20 \times 10^{-14}\,\mathrm{m/s^2}$ to $5 \times 10^{-14}\,\mathrm{m/s^2}$ results in slightly increased transport across all E_{app}. While the changing the value of D_p has the same impact on transport during a pulse as described for the Canatella experiments, the impact on post-pulse transport (which, as discussed, is much more significant in the Puc experiments) is larger. Specifically, increasing the value of D_p results in decreased pore creation and therefore results in decreased post-pulse transport. Conversely, decreasing the value of D_p results in increased pore creation and increased post-pulse transport.

Maximum Pore Radius

In contrast to artificial membrane systems (e.g., bilayer lipid membranes and vesicles), cell membranes contain a substantial amount of protein [102]. Presumably, the protein impedes expansion and limits the size to which pores can generally grow. We recognize, however, that the distribution of protein, therefore the maximum pore radius, is likely to vary with membrane region.

Pores are clearly large enough to transport macromolecules like DNA [15, 103–109], dextran [40, 43, 54, 108], lactalbumin [44], and BSA [43–45]. Indeed, electroporation is widely used for cell transfection. That these macromolecules are transported through pores suggests that pores can grow at least as large $\sim 5 - 10\,\mathrm{nm}$.

In the context of our model, $r_{p,max}$ should be viewed as the maximum radius to which pores generally expand. That is, there may be membrane sites that permit greater pore expansion, but $r_{p,max}$

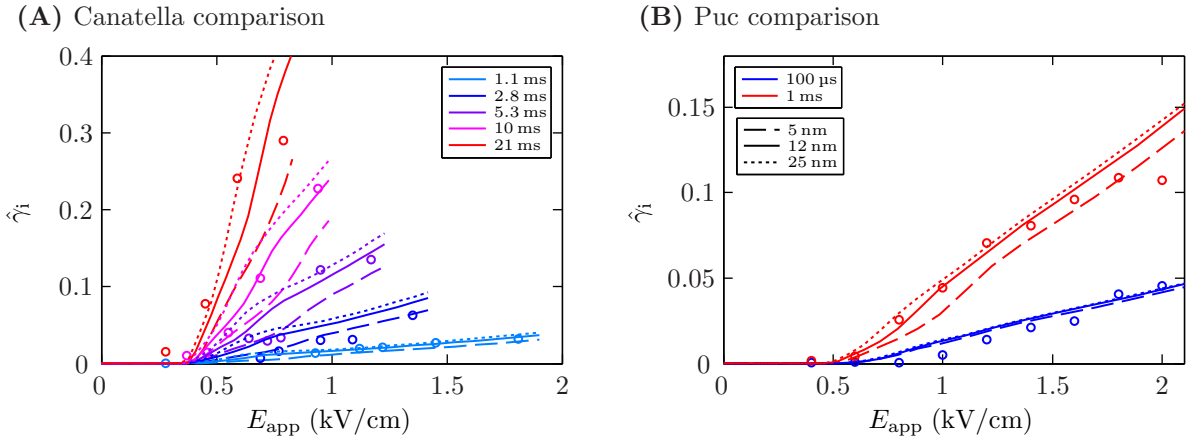

Figure 7.11: Impact of maximum pore radius $r_{p,max}$ on model predicted transport in the **(A)** Canatella experiments and **(B)** Puc experiments. Line color indicates the pulse duration (τ_{pulse} for the Canatella experiments and t_{pulse} for the Puc experiments) (*inset*). Line style indicates the value of $r_{p,max}$ (*inset*). *Open circles* indicate experimental measurements [49, 50]. $r_{p,max}$ is the maximum radius represented in the model. Large pores predominate in transporting solute during pulsing. Therefore, increasing the value of $r_{p,max}$ results in increased total transport across all E_{app} by increasing transport during pulsing. The relative impact is greater over the range of E_{app} for which $\hat{\gamma}_i$ is creation-limited ($E_{app} \lesssim 0.8\,kV/cm$). Decreasing the value of $r_{p,max}$ has the opposite effects.

is intended to capture the maximum radius to which pores expand on average. We note that the models of Krassowska and colleagues [64, 67, 89] do not require (nor do they choose to impose) a set value of $r_{p,max}$ because they represent discrete pores rather than continuum-based pore distributions. As a result, the largest pores predicted by these models range from $\sim 300\,nm$ [67] to $2.2\,\mu m$ [64, 89]. However, we are unaware of compelling evidence demonstrating that pores of this size form in cell membranes for widely used pulses.

Because we consider only small solutes here, the ability of our model to resolve an optimal value of $r_{p,max}$ is relatively weak. Using the model to analyze quantitative experimental transport results of a larger solute would provide greater insight, but that is beyond the scope of the present paper.

Figure 7.11 shows the impact that the value of $r_{p,max}$ has on the model results. Increasing the value of $r_{p,max}$ from 12 nm to 25 nm results in increased transport across all E_{app} for both the Canatella and Puc experiments. As noted above, large pores predominate in transporting solute. Therefore,

increasing the size of the largest pores results in increased transport. The relative impact is greater over the range of E_{app} for which $\hat{\gamma}_i$ is creation-limited ($E_{app} \lesssim 0.8\,kV/cm$). In this range, pores are limited in number but large in size. Thus, increasing their size results in increased transport. Increasing the value of $r_{p,max}$ also results in a slight decrease in value of E_{app} at which $\hat{\gamma}_i$ has its inflection point. Decreasing the value of $r_{p,max}$ from 12 nm to 5 nm results in decreased transport and a slight decrease in value of E_{app} at which $\hat{\gamma}_i$ has its inflection point.

Pore Resealing Time Constant

The pore resealing time constant τ_p strongly influences the amount of post-pulse transport. Specifically, post-pulse transport is proportional to τ_p. Post-pulse transport is also strongly affected by the value of $r_{p,min}$, the pore radius at which pores accumulate post-pulse ($\Delta\phi_m \approx 0\,V$). In this study, we used $r_{p,min} = 1.0\,nm$ based on our previous analysis [58] of the Melikov et al. [32] pore conductance measurements. Because post-pulse transport is very sensitive to the value of $r_{p,min}$ due to hindrance and partitioning, our $r_{p,min}$ choice necessarily affected the optimal value of τ_p determined. If we had used a smaller value of $r_{p,min}$, then we would have arrived at a larger value of τ_p, and vice versa.

Values reported for the pore resealing time constant τ_p vary widely. While Glaser et al. [87] reported $\tau_p \approx 3\,s$ and He et al. [98] reported $\tau_p \approx 0.8-2.2\,s$, Tekle et al. [97] reported a shorter $\tau_p \approx 0.16\,s$ and Djuzenova et al. [48] reported a much longer $\tau_p \approx 60-120\,s$.

Here, we found the value $\tau_p = 4\,s$ to be optimal. This value is well within the range reported in the literature but, as noted, is inextricably tied to our assumption that $r_{p,min} = 1.0\,nm$. Puc et al. reported [50] significant post-pulse transport a minute after pulsing. This suggests that the value of τ_p in their cells system was much larger than 4 s, which would also imply that $r_{p,min} < 1.0\,nm$.

Figure 7.12 shows the impact that the value of τ_p has on the model results. In both systems, increasing the value of τ_p from 4 s to 6 s results in increased post-pulse transport, and thereby results in increased total transport. Decreasing the value of τ_p from 4 s to 2 s results in decreased transport.

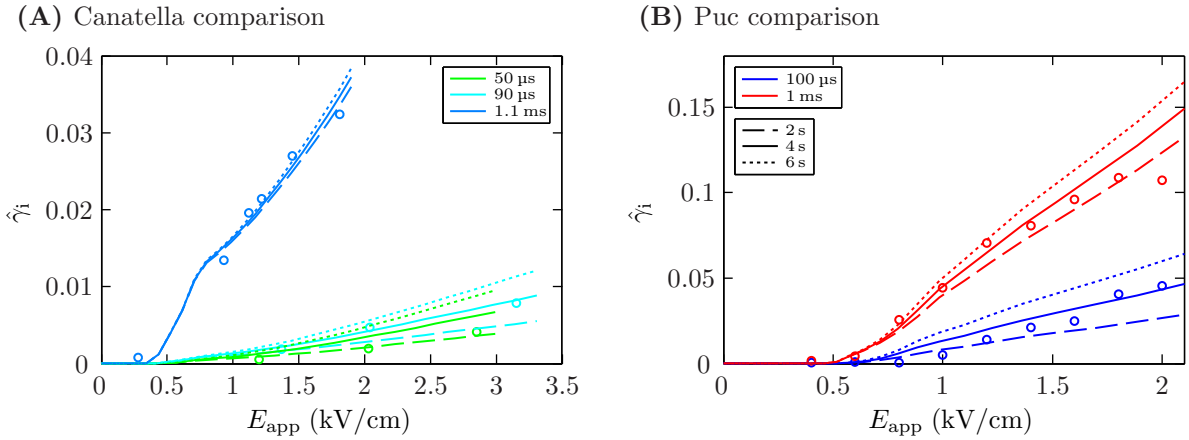

Figure 7.12: Impact of pore resealing time constant τ_p on model predicted transport in the **(A)** Canatella experiments and **(B)** Puc experiments. Line color indicates the pulse duration (τ_{pulse} for the Canatella experiments and t_{pulse} for the Puc experiments) (*inset*). Line style indicates the value of τ_p (*inset*). *Open circles* indicate experimental measurements [49, 50]. τ_p determines the time available for post-pulse transport. Increasing the value of τ_p results in increased post-pulse transport, and thereby results in increased total transport. The impact of the value of τ_p is larger for the Puc experiments, for which post-pulse transport is a significant fraction of total transport. In the Canatella experiments, post-pulse transport is a significant fraction of total transport for the shortest pulses only, as shown.

For most of the Canatella experiments (Fig. 7.12A), only a small fraction of total transport occurs post-pulse, and thus the impact of the value of τ_p is weak. The exception is for transport in response to pulses that are short in duration ($\tau_{pulse} = 50\,\mu s$ and $90\,\mu s$). Because such short pulses result in relatively little transport during the pulse, post-pulse transport comprises a larger fraction of the total transport.

In the Puc experiments (Fig. 7.12B), a large fraction of the total transport occurs post-pulse. As a result, total transport is sensitive to the value of τ_p.

7.4 Conclusions

We have described a robust, spatially distributed, mechanistic model of electroporation that features coupled quantitative descriptions of electrical transport, electrodiffusive molecular transport, and pore dynamics. The modeling approach allows the calculation of electric potential, molecular concentration, and pore density throughout the system on time scales ranging from nanoseconds

to minutes with a level of spatial and temporal resolution that cannot be achieved by typical experimental methods.

Importantly, the model enables direct comparison of model results with experimental measurements, which generally report molecular transport, not electrical behavior.

We validated the ability of the model to make accurate predictions of molecular transport at the cell level by using it to replicate (in silico) two sets of experiments in the literature that measured electroporation-mediated transport of fluorescent probes. The model predictions of molecular uptake are in excellent agreement with these experimental measurements, which collectively span nearly three orders of magnitude in pulse duration ($50\,\mu\text{s} - 20\,\text{ms}$) and an order of magnitude in pulse magnitude ($0.3 - 3\,\text{kV/cm}$).

We further exploited this comprehensive experimental data to determine the optimal values of several electroporation parameters. Included among these are the first estimate of the asymmetric pore creation constant α and perhaps the most accurate estimation to date of the pore diffusion coefficient D_p.

7.5 Appendix

7.5.1 Dipole Pore Energy Term

The pore energy term $W_\text{dipole}(r_\text{p}, \Delta\phi_\text{p})$ accounts for the energy associated with rotation of lipid dipoles within the pore edge [94]. The dipole energy scales with the number of lipid dipoles involved, which we assume to be proportional to the lipid edge area $A_\text{l,e}(r_\text{p})$, and the sine of the average lipid orientation $\bar{\Theta}_\text{l,e}(r_\text{p})$ relative to the electric field, which we assume to be parallel to the axis of the pore. Thus, the dipole energy is given by

$$W_\text{dipole}(r_\text{p}, \Delta\phi_\text{p}) = \frac{\alpha}{kT}\left(\frac{A_\text{l,e}(r_\text{p})}{A_\text{l,e}(r_*)}\right)\left(\frac{\sin(\bar{\Theta}_\text{l,e}(r_\text{p}))}{\sin(\bar{\Theta}_\text{l,e}(r_*))}\right)\Delta\phi_\text{p}, \tag{7.20}$$

where $\Delta\phi_\mathrm{p}$ is the voltage drop across the internal pore region [57]. For simplicity, the form of $W_\mathrm{dipole}(r_\mathrm{p}, \Delta\phi_\mathrm{p})$ is such that

$$W_\mathrm{dipole}(r_*, \Delta\phi_\mathrm{p}) = \frac{\alpha}{kT}\Delta\phi_\mathrm{p}. \tag{7.21}$$

The area of lipid in the pore edge is given by [58]

$$A_\mathrm{l,e}(r_\mathrm{p}) = \pi^2\left(\frac{d_\mathrm{m}}{2}\right)\left(r_\mathrm{p} + \frac{d_\mathrm{m}}{2}\right) - 2\pi\left(\frac{d_\mathrm{m}}{2}\right)^2. \tag{7.22}$$

The average orientation of lipid molecules in the pore edge can be found by taking an area-weighted integral of $\Theta_\mathrm{l,e}$ over the pore edge:

$$\bar{\Theta}_\mathrm{l,e}(r_\mathrm{p}) = \frac{2\pi\left(\frac{d_\mathrm{m}}{2}\right)}{A_\mathrm{l,e}(r_\mathrm{p})}\int_0^{\frac{\pi}{2}}\left(r_\mathrm{p} + \frac{d_\mathrm{m}}{2} - \frac{d_\mathrm{m}}{2}\sin\Theta_\mathrm{l,e}\right)\Theta_\mathrm{l,e}\,\mathrm{d}\Theta_\mathrm{l,e} \tag{7.23}$$

$$= \frac{\pi d_\mathrm{m}}{A_\mathrm{l,e}(r_\mathrm{p})}\left[\left(r_\mathrm{p} + \frac{d_\mathrm{m}}{2}\right)\frac{\Theta_\mathrm{l,e}^2}{2} - \frac{d_\mathrm{m}}{2}\left(\sin\Theta_\mathrm{l,e} - \Theta_\mathrm{l,e}\cos\Theta_\mathrm{l,e}\right)\right]_0^{\frac{\pi}{2}} \tag{7.24}$$

$$= \frac{\pi d_\mathrm{m}}{A_\mathrm{l,e}(r_\mathrm{p})}\left(\frac{\pi^2}{8}\left(r_\mathrm{p} + \frac{d_\mathrm{m}}{2}\right) - \frac{d_\mathrm{m}}{2}\right). \tag{7.25}$$

Substituting for $A_\mathrm{l,e}(r_\mathrm{p})$ and simplifying,

$$\bar{\Theta}_\mathrm{l,e}(r_\mathrm{p}) = \frac{2\pi^2 r_\mathrm{p} + \left(\pi^2 - 8\right)d_\mathrm{m}}{8\pi r_\mathrm{p} + 4\left(\pi - 2\right)d_\mathrm{m}}. \tag{7.26}$$

References

[1] Weaver, J.C. and Chizmadzhev, Y.A. Theory of electroporation: A review. *Bioelectroch Bioener*, 41(2):135–160, 1996.

[2] Weaver, J.C. Electroporation of biological membranes from multicellular to nano scales. *IEEE T*

Dielect El In, 10(5):754–768, 2003.

[3] Matsuda, T. and Cepko, C.L. Electroporation and RNA interference in the rodent retina in vivo and in vitro. *P Natl Acad Sci USA*, 101(1):16–22, 2004.

[4] Kitamura, K., Judkewitz, B., Kano, M., Denk, W., and Hausser, M. Targeted patch-clamp recordings and single-cell electroporation of unlabeled neurons in vivo. *Nat Methods*, 5(1):61–67, 2008.

[5] Voiculescu, O., Papanayotou, C., and Stern, C.D. Spatially and temporally controlled electroporation of early chick embryos. *Nat Protoc*, 3(3):419–426, 2008.

[6] Heller, R., Jaroszeski, M.J., Glass, L.F., Messina, J.L., Rapaport, D.P., DeConti, R.C., Fenske, N.A., Gilbert, R.A., Mir, L.M., and Reintgen, D.S. Phase I/II trial for the treatment of cutaneous and subcutaneous tumors using electrochemotherapy. *Cancer*, 77(5):964–971, 1996.

[7] Sel, D., Mazeres, S., Teissie, J., and Miklavcic, D. Finite-element modeling of needle electrodes in tissue from the perspective of frequent model computation. *IEEE T Bio-Med Eng*, 50(11):1221–32, 2003.

[8] Pliquett, U., Elez, R., Piiper, A., and Neumann, E. Electroporation of subcutaneous mouse tumors by rectangular and trapezium high voltage pulses. *Bioelectrochemistry*, 62(1):83–93, 2004.

[9] Davalos, R.V., Mir, I.L.M., and Rubinsky, B. Tissue ablation with irreversible electroporation. *Ann Biomed Eng*, 33(2):223–231, 2005.

[10] Smith, K.C. *Cell and Tissue Electroporation*. Master's thesis, Massachusetts Institute of Technology, Cambridge, Massachusetts, 2006.

[11] Heller, L.C., Jaroszeski, M.J., Coppola, D., McCray, A.N., Hickey, J., and Heller, R. Optimization of cutaneous electrically mediated plasmid DNA delivery using novel electrode. *Gene Ther*, 14(3):275–280, 2007.

[12] Sel, D., Lebar, A.M., and Miklavcic, D. Feasibility of employing model-based optimization of pulse amplitude and electrode distance for effective tumor electropermeabilization. *IEEE T Bio-Med Eng*, 54(5):773–781, 2007.

[13] Esser, A.T., Smith, K.C., Gowrishankar, T.R., and Weaver, J.C. Towards solid tumor treatment by irreversible electroporation: Intrinsic redistribution of fields and currents in tissue. *Technol Cancer Res T*, 6(4):261–273, 2007.

[14] Esser, A.T., Smith, K.C., Gowrishankar, T.R., and Weaver, J.C. Towards solid tumor treatment by nanosecond pulsed electric fields. *Technol Cancer Res T*, 8(4):289–306, 2009.

[15] Rols, M.P., Delteil, C., Golzio, M., Dumond, P., Cros, S., and Teissie, J. In vivo electrically mediated protein and gene transfer in murine melanoma. *Nat Biotechnol*, 16(2):168–171, 1998.

[16] Mir, L.M. and Orlowski, S. Mechanisms of electrochemotherapy. *Adv Drug Deliv Rev*, 35(1):107–118, 1999.

[17] Gothelf, A., Mir, L.M., and Gehl, J. Electrochemotherapy: Results of cancer treatment using enhanced delivery of bleomycin by electroporation. *Cancer Treat Rev*, 29(5):371–387, 2003.

[18] Goto, T., Nishi, T., Tamura, T., Dev, S.B., Takeshima, H., Kochi, M., Yoshizato, K., Kuratsu, J., Sakata, T., Hofmann, G.A., and Ushio, Y. Highly efficient electro-gene therapy of solid tumor by using an expression plasmid for the herpes simplex virus thymidine kinase gene. *P Natl Acad Sci USA*, 97(1):354–359, 2000.

[19] Hofmann, F., Ohnimus, H., Scheller, C., Strupp, W., Zimmermann, U., and Jassoy, C. Electric field pulses can induce apoptosis. *J Membrane Biol*, 169:103–109, 1999.

[20] Beebe, S.J., Fox, P.M., Rec, L.J., Willis, L.K., and Schoenbach, K.H. Nanosecond, high-intensity pulsed electric fields induce apoptosis in human cells. *FASEB J*, 17(9), 2003.

[21] Schoenbach, K.H., Joshi, R.P., Kolb, J.F., Chen, N.Y., Stacey, M., Blackmore, P.F., Buescher, E.S., and Beebe, S.J. Ultrashort electrical pulses open a new gateway into biological cells. *P IEEE*, 92(7):1122–1137, 2004.

[22] Hall, E.H., Schoenbach, K.H., and Beebe, S.J. Nanosecond pulsed electric fields induce apoptosis in p53-wildtype and p53-null HCT116 colon carcinoma cells. *Apoptosis*, 12(9):1721–1731, 2007.

[23] Nuccitelli, R., Pliquett, U., Chen, X.H., Ford, W., Swanson, R.J., Beebe, S.J., Kolb, J.F., and Schoenbach, K.H. Nanosecond pulsed electric fields cause melanomas to self-destruct. *Biochem Bioph Res Co*, 343:351–360, 2006.

[24] Garon, E.B., Sawcer, D., Vernier, P.T., Tang, T., Sun, Y., Marcu, L., Gundersen, M.A., and Koeffler, H.P. In vitro and in vivo evaluation and a case report of intense nanosecond pulsed electric field as a local therapy for human malignancies. *Int J Cancer*, 121(3):675–682, 2007.

[25] Nuccitelli, R., Chen, X., Pakhomov, A.G., Baldwin, W.H., Sheikh, S., Pomicter, J.L., Ren, W., Osgood, C., Swanson, R.J., Kolb, J.F., Beebe, S.J., and Schoenbach, K.H. A new pulsed electric field therapy for melanoma disrupts the tumor's blood supply and causes complete remission without recurrence. *Int J Cancer*, 125(2):438–45, 2009.

[26] Nuccitelli, R., Tran, K., Sheikh, S., Athos, B., Kreis, M., and Nuccitelli, P. Optimized nanosecond pulsed electric field therapy can cause murine malignant melanomas to self-destruct with a single treatment. *Int J Cancer*, 127(7):1727–36, 2010.

[27] Edd, J.F., Horowitz, L., Davalos, R.V., Mir, L.M., and Rubinsky, B. In vivo results of a new focal tissue ablation technique: Irreversible electroporation. *IEEE T Bio-Med Eng*, 53(7):1409–1415, 2006.

[28] Rubinsky, B., Onik, G., and Mikus, P. Irreversible electroporation: A new ablation modality–Clinical implications. *Technol Cancer Res T*, 6(1):37–48, 2007.

[29] Aihara, H. and Miyazaki, J. Gene transfer into muscle by electroporation in vivo. *Nat Biotechnol*, 16(9):867–870, 1998.

[30] Widera, G., Austin, M., Rabussay, D., Goldbeck, C., Barnett, S.W., Chen, M.C., Leung, L., Otten, G.R., Thudium, K., Selby, M.J., and Ulmer, J.B. Increased DNA vaccine delivery and immunogenicity by electroporation in vivo. *J Immunol*, 164:4635–4640, 2000.

[31] Rizzuto, G., Cappelletti, M., Maione, D., Savino, R., Lazzaro, D., Costa, P., Mathiesen, I., Cortese, R., Ciliberto, G., Laufer, R., La Monica, N., and Fattori, E. Efficient and regulated erythropoietin production by naked DNA injection and muscle electroporation. *P Natl Acad Sci USA*, 96(11):6417–6422, 1999.

[32] Melikov, K.C., Frolov, V.A., Shcherbakov, A., Samsonov, A.V., Chizmadzhev, Y.A., and Chernomordik, L.V. Voltage-induced nonconductive pre-pores and metastable single pores in unmodified planar lipid bilayer. *Biophys J*, 80(4):1829–1836, 2001.

[33] Kotulska, M. Natural fluctuations of an electropore show fractional Levy stable motion. *Biophys J*, 92(7):2412–2421, 2007.

[34] Kinosita, K., Ashikawa, I., Saita, N., Yoshimura, H., Itoh, H., Nagayma, K., and Ikegami, A. Electroporation of cell membrane visualized under a pulsed-laser fluorescence microscope. *Biophys J*, 53:1015–1019, 1988.

[35] Hibino, M., Shigemori, M., Itoh, H., Nagayama, K., and Kinosita, K.J. Membrane conductance of an electroporated cell analyzed by submicrosecond imaging of transmembrane potential. *Biophys J*, 59(1):209–220, 1991.

[36] Hibino, M., Itoh, H., and Kinosita, K. Time courses of cell electroporation as revealed by submicrosecond imaging of transmembrane potential. *Biophys J*, 64(6):1789–1800, 1993.

[37] Frey, W., White, J.A., Price, R.O., Blackmore, P.F., Joshi, R.P., Nuccitelli, R., Beebe, S.J., Schoenbach, K.H., and Kolb, J.F. Plasma membrane voltage changes during nanosecond pulsed electric field exposure. *Biophys J*, 90:3608–3615, 2006.

[38] Pakhomov, A.G., Shevin, R., White, J.A., Kolb, J.F., Pakhomova, O.N., Joshi, R.P., and Schoenbach, K.H. Membrane permeabilization and cell damage by ultrashort electric field shocks. *Arch Biochem Biophys*, 465(1):109–118, 2007.

[39] Pakhomov, A.G., Kolb, J.F., White, J.A., Joshi, R.P., Xiao, S., and Schoenbach, K.H. Long-lasting plasma membrane permeabilization in mammalian cells by nanosecond pulsed electric field (nsPEF). *Bioelectromagnetics*, 28(8):655–663, 2007.

[40] Bartoletti, D.C., Harrison, G.I., and Weaver, J.C. The number of molecules taken up by electroporated cells: Quantitative determination. *FEBS Lett*, 256(1-2):4–10, 1989.

[41] Tekle, E., Astumian, R.D., and Chock, P.B. Electro-permeabilization of cell membranes: Effect of the resting membrane potential. *Biochem Bioph Res Co*, 172(1):282–7, 1990.

[42] Tekle, E., Astumian, R.D., and Chock, P.B. Electroporation by using bipolar oscillating electric field: An improved method for DNA transfection of NIH 3T3 cells. *P Natl Acad Sci USA*, 88(10):4230–4, 1991.

[43] Glogauer, M. and McCulloch, C.A. Introduction of large molecules into viable fibroblasts by electroporation: Optimization of loading and identification of labeled cellular compartments. *Exp Cell Res*, 200(2):227–34, 1992.

[44] Prausnitz, M.R., Lau, B.S., Milano, C.D., Conner, S., Langer, R., and Weaver, J.C. A quantitative study of electroporation showing a plateau in net molecular-transport. *Biophys J*, 65(1):414–422, 1993.

[45] Prausnitz, M.R., Milano, C.D., Gimm, J.A., Langer, R., and Weaver, J.C. Quantitative study of molecular-transport due to electroporation – Uptake of bovine serum-albumin by erythrocyte-ghosts. *Biophys J*, 66(5):1522–1530, 1994.

[46] Tekle, E., Astumian, R.D., and Chock, P.B. Selective and asymmetric molecular transport across electroporated cell membranes. *P Natl Acad Sci USA*, 91(24):11512–6, 1994.

[47] Prausnitz, M.R., Corbett, J.D., Gimm, J.A., Golan, D.E., Langer, R., and Weaver, J.C. Millisecond measurement of transport during and after an electroporation pulse. *Biophys J*, 68(5):1864–1870, 1995.

[48] Djuzenova, C.S., Zimmermann, U., Frank, H., Sukhorukov, V.L., Richter, E., and Fuhr, G. Effect of medium conductivity and composition on the uptake of propidium iodide into electropermeabilized myeloma cells. *Biochim Biophys Acta*, 1284(2):143–52, 1996.

[49] Canatella, P.J., Karr, J.F., Petros, J.A., and Prausnitz, M.R. Quantitative study of electroporation-mediated molecular uptake and cell viability. *Biophys J*, 80(2):755–764, 2001.

[50] Puc, M., Kotnik, T., Mir, L.M., and Miklavcic, D. Quantitative model of small molecules uptake after in vitro cell electropermeabilization. *Bioelectrochemistry*, 60(1-2):1–10, 2003.

[51] Sun, Y., Vernier, P., Behrend, M., Wang, J., Thu, M., Gundersen, M., and Marcu, L. Fluorescence microscopy imaging of electroperturbation in mammalian cells. *J Biomed Opt*, 11(2), 2006.

[52] Kennedy, S.M., Ji, Z., Hedstrom, J.C., Booske, J.H., and Hagness, S.C. Quantification of electroporative uptake kinetics and electric field heterogeneity effects in cells. *Biophys J*, 94(12):5018–5027, 2008.

[53] Pucihar, G., Kotnik, T., Miklavcic, D., and Teissie, J. Kinetics of transmembrane transport of small molecules into electropermeabilized cells. *Biophys J*, 95(6):2837–2848, 2008.

[54] Zaharoff, D.A., Henshaw, J.W., Mossop, B., and Yuan, F. Mechanistic analysis of electroporation-induced cellular uptake of macromolecules. *Exp Biol Med*, 233(1):94–105, 2008.

[55] Smith, K.C. and Weaver, J.C. Compilation and computation of the size, charge, and diffusivity of fluorescent dyes and other small molecules (in preparation).

[56] Smith, K.C. and Weaver, J.C. Electrodiffusion of molecules in aqueous media: A robust, discretized description for electroporation and other transport phenomena (in preparation).

[57] Smith, K.C. and Weaver, J.C. Effects of hindrance and partitioning on ionic and molecular transport through small lipidic pores (in preparation).

[58] Smith, K.C. and Weaver, J.C. The energy landscape and dynamics of electropores (in preparation).

[59] Barnett, A. and Weaver, J.C. Electroporation – A unified, quantitative theory of reversible electrical breakdown and mechanical rupture in artificial planar bilayer-membranes. *Bioelectroch Bioener*, 25(2):163–182, 1991.

[60] Freeman, S.A., Wang, M.A., and Weaver, J.C. Theory of electroporation of planar bilayer membranes: Predictions of the aqueous area, change in capacitance, and pore-pore separation. *Biophys J*, 67(1):42–56, 1994.

[61] Neu, J.C. and Krassowska, W. Asymptotic model of electroporation. *Phys Rev E*, 59(3):3471–3482, 1999.

[62] DeBruin, K.A. and Krassowska, W. Modeling electroporation in a single cell. I. Effects of field strength and rest potential. *Biophys J*, 77(3):1213–1224, 1999.

[63] DeBruin, K.A. and Krassowska, W. Modeling electroporation in a single cell. II. Effects of ionic concentrations. *Biophys J*, 77(3):1225–1233, 1999.

[64] Smith, K.C., Neu, J.C., and Krassowska, W. Model of creation and evolution of stable electropores for DNA delivery. *Biophys J*, 86(5):2813–2826, 2004.

[65] Smith, K.C., Gowrishankar, T.R., Esser, A.T., Stewart, D.A., and Weaver, J.C. The spatially distributed dynamic transmembrane voltage of cells and organelles due to 10-ns pulses: Meshed transport networks. *IEEE T Plasma Sci*, 34:1394–1404, 2006.

[66] Gowrishankar, T.R., Esser, A.T., Vasilkoski, Z., Smith, K.C., and Weaver, J.C. Microdosimetry for conventional and supra-electroporation in cells with organelles. *Biochem Bioph Res Co*, 341:1266–1276, 2006.

[67] Krassowska, W. and Filev, P.D. Modeling electroporation in a single cell. *Biophys J*, 92(2):404–417, 2007.

[68] Smith, K.C. and Weaver, J.C. Active mechanisms are needed to describe cell responses to submicrosecond, megavolt-per-meter pulses: Cell models for ultrashort pulses. *Biophys J*, 95(4):1547–1563, 2008.

[69] Esser, A.T., Smith, K.C., Gowrishankar, T.R., Vasilkoski, Z., and Weaver, J.C. Mechanisms for the intracellular manipulation of organelles by conventional electroporation. *Biophys J*, 98(11):2506–14, 2010.

[70] Talele, S., Gaynor, P., Cree, M.J., and van Ekeran, J. Modelling single cell electroporation with bipolar pulse parameters and dynamic pore radii. *J Electrostat*, 68(3):261–274, 2010.

[71] Smith, K.C. and Weaver, J.C. A unified model of electroporation and molecular transport II: Dynamics of electrical, molecular, and pore transport (in preparation).

[72] Smith, K.C. and Weaver, J.C. An in silico study of potential mechanisms by which extremely large pulsed electric fields induce apoptosis in cells (in preparation).

[73] Pavlin, M., Kanduser, M., Rebersek, M., Pucihar, G., Hart, F.X., Magjarevic, R., and Miklavcic, D. Effect of cell electroporation on the conductivity of a cell suspension. *Biophys J*, 88:4378–4390, 2005.

[74] Archer, S., Morgan, H., and Rixon, F.J. Electrorotation studies of baby hamster kidney fibroblasts infected with herpes simplex virus type 1. *Biophys J*, 76(5):2833–42, 1999.

[75] Labeed, F.H., Coley, H.M., and Hughes, M.P. Differences in the biophysical properties of membrane and cytoplasm of apoptotic cells revealed using dielectrophoresis. *Biochim Biophys Acta*, 1760(6):922–9, 2006.

[76] Chin, S., Hughes, M.P., Coley, H.M., and Labeed, F.H. Rapid assessment of early biophysical changes in K562 cells during apoptosis determined using dielectrophoresis. *Int J Nanomed*, 1(3):333–7, 2006.

[77] Coley, H.M., Labeed, F.H., Thomas, H., and Hughes, M.P. Biophysical characterization of MDR breast cancer cell lines reveals the cytoplasm is critical in determining drug sensitivity. *Biochim Biophys Acta*, 1770(4):601–8, 2007.

[78] Duncan, L., Shelmerdine, H., Hughes, M.P., Coley, H.M., Hübner, Y., and Labeed, F.H. Dielectrophoretic analysis of changes in cytoplasmic ion levels due to ion channel blocker action reveals underlying differences between drug-sensitive and multidrug-resistant leukaemic cells. *Phys Med Biol*, 53(2):N1–7, 2008.

[79] Kao, H.P., Abney, J.R., and Verkman, A.S. Determinants of the translational mobility of a small solute in cell cytoplasm. *J Cell Biol*, 120(1):175–84, 1993.

[80] Seksek, O., Biwersi, J., and Verkman, A.S. Translational diffusion of macromolecule-sized solutes in cytoplasm and nucleus. *J Cell Biol*, 138(1):131–42, 1997.

[81] Verkman, A.S. Solute and macromolecule diffusion in cellular aqueous compartments. *Trends Biochem Sci*, 27(1):27–33, 2002.

[82] Puc, M., Corović, S., Flisar, K., Petkovsek, M., Nastran, J., and Miklavcic, D. Techniques of signal generation required for electropermeabilization. Survey of electropermeabilization devices. *Bioelectrochemistry*, 64(2):113–24, 2004.

[83] Pliquett, U., Gift, E.A., and Weaver, J.C. Determination of the electric field and anomalous heating caused by exponential pulses with aluminum electrodes in electroporation experiments. *Bioelectroch Bioener*, 39(1):39–53, 1996.

[84] Cukjati, D., Batiuskaite, D., André, F., Miklavcic, D., and Mir, L.M. Real time electroporation control for accurate and safe in vivo non-viral gene therapy. *Bioelectrochemistry*, 70(2):501–7, 2007.

[85] Loste, F., Eynard, N., and Teissie, J. Direct monitoring of the field strength during electropulsation. *Bioelectroch Bioener*, 47(1):119–127, 1998.

[86] Persson, P.O. and Strang, G. A simple mesh generator in MATLAB. *SIAM Rev*, 46(2):329–345, 2004.

[87] Glaser, R.W., Leikin, S.L., Chernomordik, L.V., Pastushenko, V.F., and Sokirko, A.I. Reversible electrical breakdown of lipid bilayers: Formation and evolution of pores. *Biochim Biophys Acta*, 940(2):275–287, 1988.

[88] Dai, J. and Sheetz, M.P. Regulation of endocytosis, exocytosis, and shape by membrane tension. *Cold Spring Harb Sym*, 60:567–71, 1995.

[89] Neu, J.C. and Krassowska, W. Modeling postshock evolution of large electropores. *Phys Rev E*, 67(2), 2003.

[90] Neu, J.C., Smith, K.C., and Krassowska, W. Electrical energy required to form large conducting pores. *Bioelectrochemistry*, 60(1–2):107–114, 2003.

[91] Vasilkoski, Z., Esser, A.T., Gowrishankar, T.R., and Weaver, J.C. Membrane electroporation: The absolute rate equation and nanosecond time scale pore creation. *Phys Rev E*, 74(2), 2006.

[92] Newman, J. Resistance for flow of current to a disk. *J Electrochem Soc*, 113(5):501–502, 1966.

[93] Hall, J.E. Access resistance of a small circular pore. *J Gen Physiol*, 66(4):531–2, 1975.

[94] Esser, A.T., Smith, K.C., Son, R.S., Gowrishankar, T.R., and Weaver, J.C. Asymmetric cell electroporation: A quantitative model (in preparation).

[95] Powell, K.T. and Weaver, J.C. Transient aqueous pores in bilayer-membranes – A statistical-theory. *Bioelectroch Bioener*, 15(2):211–227, 1986.

[96] Bier, M., Chen, W., Gowrishankar, T.R., Astumian, R.D., and Lee, R.C. Resealing dynamics of a cell membrane after electroporation. *Phys Rev E*, 66(6 Pt 1):062905, 2002.

[97] Tekle, E., Astumian, R.D., Friauf, W.A., and Chock, P.B. Asymmetric pore distribution and loss of membrane lipid in electroporated DOPC vesicles. *Biophys J*, 81(2):960–8, 2001.

[98] He, H., Chang, D.C., and Lee, Y.K. Nonlinear current response of micro electroporation and resealing dynamics for human cancer cells. *Bioelectrochemistry*, 72(2):161–168, 2008.

[99] Stewart, D.A., Gowrishankar, T.R., and Weaver, J.C. Transport lattice approach to describing cell electroporation: Use of a local asymptotic model. *IEEE T Plasma Sci*, 32(4):1696–1708, 2004.

[100] Gabriel, B. and Teissie, J. Mammalian cell electropermeabilization as revealed by millisecond imaging of fluorescence changes of ethidium bromide in interaction with the membrane. *Bioelectroch Bioener*, 47(1):113–118, 1998.

[101] Gabriel, B. and Teissié, J. Time courses of mammalian cell electropermeabilization observed by millisecond imaging of membrane property changes during the pulse. *Biophys J*, 76(4):2158–65, 1999.

[102] Engelman, D.M. Membranes are more mosaic than fluid. *Nature*, 438(7068):578–580, 2005.

[103] Neumann, E., Schaefer-Ridder, M., Wang, Y., and Hofschneider, P.H. Gene transfer into mouse lyoma cells by electroporation in high electric fields. *EMBO J*, 1(7):841–5, 1982.

[104] Wong, T.K. and Neumann, E. Electric field mediated gene transfer. *Biochem Bioph Res Co*, 107(2):584–7, 1982.

[105] Klenchin, V.A., Sukharev, S.I., Serov, S.M., Chernomordik, L.V., and Chizmadzhev, Y.A. Electrically induced DNA uptake by cells is a fast process involving DNA electrophoresis. *Biophys J*, 60(4):804–811, 1991.

[106] Sukharev, S.I., Klenchin, V.A., Serov, S.M., Chernomordik, L.V., and Chizmadzhev, Y.A. Electroporation and electrophoretic DNA transfer into cells – The effect of DNA interaction with electropores. *Biophys J*, 63(5):1320–1327, 1992.

[107] Heller, R., Jaroszeski, M., Atkin, A., Moradpour, D., Gilbert, R., Wands, J., and Nicolau, C. In vivo gene electroinjection and expression in rat liver. *FEBS Lett*, 389(3):225–8, 1996.

[108] Rols, M.P. and Teissie, J. Electropermeabilization of mammalian cells to macromolecules: Control by pulse duration. *Biophys J*, 75(3):1415–1423, 1998.

[109] Canatella, P.J. and Prausnitz, M.R. Prediction and optimization of gene transfection and drug delivery by electroporation. *Gene Ther*, 8(19):1464–1469, 2001.

Chapter 8

A Unified Model of Electroporation and Molecular Transport II: Dynamics of Electrical, Molecular, and Pore Transport

Abstract

Cell membrane electroporation involves complex interactions among electrical transport, molecular transport, and pore dynamics. In a companion paper, we describe and validate a quantitative, mechanistic model of cell electroporation with concomitant molecular transport. Here, we use this model to examine in detail the electrical transport, molecular transport, and pore dynamics that result from the application of electric pulses. First, we discuss pore dynamics in general terms and demonstrate that the membrane electroporation response in a local membrane region may be creation-dominated, expansion-dominated, or balanced (neither dominates). This has important implications for molecular transport: If the response is creation-dominated, then resulting molecular transport is expansion-limited because pores are large in number but small in size. Conversely, if the response is expansion-dominated, then resulting molecular transport is creation-limited because pores are large in size but few in number. Second, we describe the response of our model of the Canatella et al. (Biophys. J., 80:755–764, 2001) experimental system to a 1 ms, 1 kV/cm exponential pulse. Similarly, we describe the response of our model of the Puc et al. (Bioelectrochemistry, 60:1–10, 2003) experimental system to a 1 ms, 1 kV/cm trapezoidal pulse. Specifically, we examine the spatiotemporal evolution of the electric potential, solute concentration, and pore density distribution throughout the systems during and after pulsing. The model results are in good agreement with experimental studies of electroporation-mediated molecular uptake and theoretical studies of the electrical and dynamic pore responses to applied electric pulses. While this study focuses on the transport of fluorescent probes, our basic approach can be used to investigate and optimize delivery of bioactive solutes, such as drugs and oligonucleotides.

8.1 Introduction

In a companion paper [1], we describe the design and validation of a model of electroporation and concomitant molecular transport. Here we consider in detail the electrical transport, molecular transport, and pore dynamics that result from two pulses. Specifically, we examine the response of the Canatella et al. [2] system [1] to a 1 ms, 1 kV/cm exponential pulse and the response of the Puc et al. [3] system [1] to a 1 ms, 1 kV/cm trapezoidal pulse.

Previously, spatially distributed, mechanistic models with dynamic pores [4–8] have been used to examine the electrical transport and pore dynamics that result from the application of pulsed electric fields. However, to our knowledge, this is the first model to couple a spatially distributed model of electrodiffusive molecular transport [9] with a mechanistic model of electroporation assigned to curved membranes [10]. Using this model we can thus begin to address fundamental issues, such as which regions of the membrane contribute most significantly to transmembrane molecular transport, as well as total (cumulative) transport, which is needed for molecular dose (amount delivered per mass cell or mass tissue).

Here we consider the fluorescent probes calcein and lucifer yellow, which were used in the Canatella et al. experiments [2] and Puc et al. experiments [3]. However, essentially any solute of interest can be characterized [11] and used in the model. As a result, the model may produce new insights into electroporation-mediated applications, such as drug delivery [12–21], nucleic acid delivery [22–40], and tissue ablation [5, 41–48]. Thus, the model opens the possibility of screening cell, molecule, and pulse combinations for specific applications.

8.2 Methods

As described in the companion paper [1], we designed and validated a mechanistic, 2-D model of cell electroporation using quantitative measurements [2, 3] of total transport (during and after pulsing) for which the applied electric pulses collectively span a wide range of durations (50 μs –

20 ms) and magnitudes (3 kV/cm – 0.3 kV/cm) and include two different waveforms (trapezoidal and exponential). The model characterizes electrical transport and molecular (electrodiffusive) transport in physical space and pore transport in radius space.

Here, we describe in detail the spatiotemporal dynamics of electrical, molecular, and pore evolution (transport in radius space) for two pulses. Specifically, we examine the response of the Canatella model system [1] to an exponential pulse with peak magnitude $E_{app} = 1\,\text{kV/cm}$ and time constant $\tau_{pulse} = 1\,\text{ms}$, and we examine the response of the Puc model system [1] to a trapezoidal pulse with magnitude $E_{app} = 1\,\text{kV/cm}$ and duration $t_{pulse} = 1\,\text{ms}$.

Both model systems characterize mammalian cells in vitro but are somewhat different. The Canatella model system [1] has a cell with radius $r_{cell} = 11\,\mu\text{m}$, extracellular conductivity $\sigma_e = 1.29\,\text{S/m}$, and contains the (initially extracellular) fluorescent probe calcein, which has radius $r_s = 0.58\,\text{nm}$, length $l_s = 1.89\,\text{nm}$, and charge (valence) $z_s = -3.61$ [11]. The Puc model system [1] has a cell with radius $r_{cell} = 8.55\,\mu\text{m}$, extracellular conductivity $\sigma_e = 1.58\,\text{S/m}$, and contains the (initially extracellular) fluorescent probe lucifer yellow, which has radius $r_s = 0.61\,\text{nm}$, length $l_s = 1.46\,\text{nm}$, and charge (valence) $z_s = -2$ [11].

The basic modeling approach [1] involves discretizing (meshing) the cell system and describing electrical and molecular transport between adjacent nodes in terms of the mesh geometry, transport parameters, and the electric potential ϕ and solute concentration γ of the nodes. In addition, for the node connections that span the membrane, a discretized radius space is used to determine the evolution (transport) of pore density n between the discretized radii. This creation, expansion, contraction, and destruction of pores is largely determined by the local transmembrane voltage $\Delta\phi_m(t)$, and electrical and molecular transport through the membrane is largely determined by the local pore density $n(r_p, t)$. Thus, the electrical, molecular, and pore transport are closely linked, but with electrical and pore behavior governing molecular transport that does not alter electrical and pore behavior.

The time-dependent system behavior is determined from the transport relations by imposing continuity [1]. That is, solute, charge, and pores must be conserved (except for pores at the creation and destruction boundary radius r_*). These continuity equations are assembled into a large system of nonlinear equations and solved using MATLAB (version 7.8, 2009, http://www.mathworks.com). MATLAB is also used for analysis of the results.

Presently a typical cell model with a curved plasma membrane contains ~ 11 000 nodes, with ~30 000 local models for passive aqueous media regions and 600 local membrane models that account for (1) a resting potential source, (2) a passive (fixed) component of the membrane resistance and (3) a highly nonlinear and hysteretic local membrane electroporation response with dynamic, heterogeneous pore populations.

For more details on the basic methods and system parameters, please see the companion paper [1].

8.3 Results and Discussion

Electroporation involves complex interaction among electrical transport, pore dynamics, and molecular transport. Thus, before considering in detail the results of the simulations of the Puc and Canatella model systems, it is instructive to consider in general terms how these transport phenomena interact. Specifically, we consider the interaction between electrical transport and pore dynamics and how both of these influence molecular transport. As noted above, molecular transport is assumed not to affect electrical transport or pore dynamics.

8.3.1 Interaction Between Electrical Transport and Pore Dynamics

Electrical transport and local pore populations (pore density and size distribution) affect one another through the transmembrane voltage $\Delta\phi_m$. (Unless otherwise noted, $\Delta\phi_m$ should be taken to mean $|\Delta\phi_m|$.) $\Delta\phi_m$ arises as the result of spatially distributed voltage division between the membrane (including pores) and the bulk electrolyte [49]. Because the conductance of the electrolyte

is time-invariant (fixed), $\Delta\phi_m$ is determined by the magnitude of the electric field applied to the system and the spatially distributed conductances of the membrane, which in turn are determined by the local distribution (size and number) of pores in the membrane.

The pore density distribution $n(r_p)$ in a local membrane region is the result of the transmembrane voltage $\Delta\phi_m(t)$ that the local region has experienced [10]. Note that the pore distribution is hysteretic: it depends not only on the instantaneous $\Delta\phi_m$, but also the on the history of $\Delta\phi_m$. Specifically, $\Delta\phi_m$ is the driving force for both pore creation and expansion. That is, as $\Delta\phi_m$ increases, the rate of pore creation increases and the tendency of pores to expand also increases. However, pore creation and expansion both increase conductance of the membrane, and therefore decrease $\Delta\phi_m$. Thus, pore creation and expansion tend to diminish the driving force for further creation and expansion. As a result of this negative feedback, electroporation is self-limiting.

Because pore creation and expansion are driven by elevated $\Delta\phi_m$ but then diminish $\Delta\phi_m$, a competitive process is involved. In other words, $\Delta\phi_m$ may be diminished predominantly by pore creation, pore expansion, or a mix of both. Electrical and molecular transport through pores is strongly affected by pore size, and therefore the particular combination of pore creation and expansion that results from a given pulse has a large effect on net transport.

The interpretation of that electrical transport and pore dynamics can most clearly be explained in the context of pore phase space [10], as shown in Fig. 8.1. In our model, the rate of pore expansion dr_p/dt is fully determined by the pore radius r_p and transmembrane voltage $\Delta\phi_m$. For clarity, Fig. 8.1 was constructed with simplification that the electroporation parameter $\alpha = 0\,\mathrm{kT/V}$ such that dr_p/dt is independent of the sign of $\Delta\phi_m$. Therefore, all pores lie somewhere on the phase plot (Fig. 8.1).

As described above, pore creation and expansion are related processes that compete to lower $\Delta\phi_m$ to a level at which pore creation and expansion are slowed. Figure 8.1 only shows the rate of pore

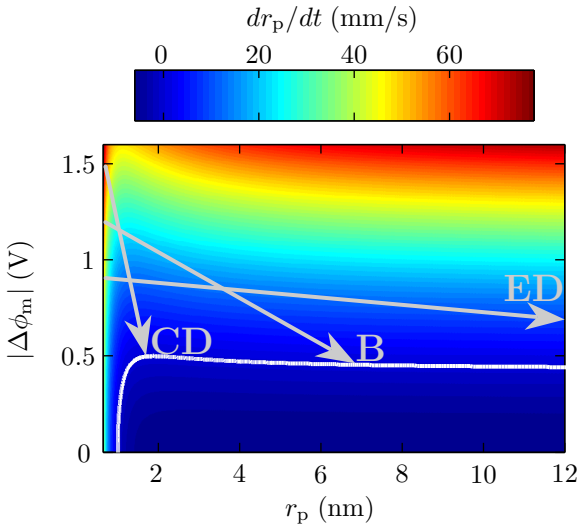

Figure 8.1: Pore dynamics phase space. The rate of pore expansion dr_p/dt is shown as a function of pore radius r_p and transmembrane voltage magnitude $|\Delta\phi_m|$. (For simplicity, this plot was created with $\alpha = 0\,\mathrm{kT/V}$ such that the results are independent of the sign of $\Delta\phi_m$.) The *white curve* indicates $dr_p/dt = 0$. Note that the unit of the rate of pore expansion, mm/s, is equivalent to μm/ms, nm/μs, and pm/ns. Elevated $\Delta\phi_m$ is the driving force for both pore creation and expansion, and both pore creation and expansion diminish $\Delta\phi_m$. These the two processes compete to push the system toward a quasi-steady state for which all pores are distributed along the *white curve* ($dr_p/dt = 0$). Whether pore creation or expansion is dominant depends on the rate of the increase in $\Delta\phi_m$. When $\Delta\phi_m$ rises very quickly to a large value, the response is creation-dominated (CD), and the pores follow the CD initial trajectory. When $\Delta\phi_m$ rises slowly, the response is expansion-dominated (ED), and the pores follow the ED initial trajectory. Intermediate between these responses is a balanced (B) response that exhibits significant pore creation and expansion. The balanced response is indicated by the B initial trajectory.

expansion. Therefore, a little imagination is required to account for the impact of pore creation. The key is that the rate of pore creation is highly nonlinear in $\Delta\phi_m$ [1, 10, 50], much more so than the rate of pore expansion [10]. Thus, the rate of pore creation increases much more dramatically with $\Delta\phi_m$ than does the rate of pore expansion.

Nevertheless, whether by pore creation or expansion, time is required for the pores be become sufficient in number or size to significantly diminish $\Delta\phi_m$. Therefore, the faster $\Delta\phi_m$ rises at the beginning of a pulse, the larger the peak $\Delta\phi_m$. The larger the peak $\Delta\phi_m$, the larger the total number of pores created because, as noted, the rate of pore creation is highly nonlinear in $\Delta\phi_m$. It follows

from these considerations that the faster $\Delta\phi_m$ rises, the more dominant pore creation is, relative to pore expansion, in reducing $\Delta\phi_m$. On the other hand, if $\Delta\phi_m$ rises slowly, the pore creation rate remain smalls, but provided $\Delta\phi_m$ is large enough to drive pore expansion ($\Delta\phi_m \gtrsim 0.5\,\mathrm{V}$), then the pores that are created expand to $r_p \approx r_{p,max} = 12\,\mathrm{nm}$. (This maximum pore radius $r_{p,max} = 12\,\mathrm{nm}$ is a construct of the present model. The value was determined in the companion paper [1] and appears reasonable given the 50 % protein in the plasma membrane [51].) Thus, when $\Delta\phi_m$ rises slowly, pore expansion is dominant in reducing $\Delta\phi_m$.

These basic principles are demonstrated by the initial pore trajectories shown in Fig. 8.1. Whether by pore creation or expansion, the pores tend to evolve toward the quasi-steady state indicated by the *white curve.* Along the *white curve*, $dr_p/dt = 0$ and the pore creation rate is small, though nonzero. Note that (1) pores assume a distribution of radii r_p as the result of thermal fluctuations (diffusion in radius space), (2) all pores in a local membrane region experience the same $\Delta\phi_m$, and (3) the *white curve* indicating dr_p/dt has a slight negative slope (for $r_p \gtrsim 2\,\mathrm{nm}$). Thus, in a pore distribution that lies along the *white curve,* the smaller pores in the distribution lie *below* the *white curve* ($dr_p/dt < 0$) and the larger pores in the distribution lie *above* the *white curve* ($dr_p/dt > 0$).

This leads to a striking expectation: the smaller pores contract and the larger pores expand, thereby resulting in the formation of two pore subpopulations, one with large pores and the other with small pores. The combined effect is such that the $\Delta\phi_m$ remains approximate at the approximate value $\Delta\phi_m \approx 0.5\,\mathrm{V}$. This outcome, in which there the rates of pore creation and expansion are relatively balanced (insofar as they diminish $\Delta\phi_m$), and result in subpopulations of small and large pores is illustrated by the balanced (B) initial trajectory shown in Fig. 8.1.

The other possible initial pore trajectories are creation-dominated (CD) and expansion-dominated (ED) (Fig. 8.1). The CD initial trajectory results from a very rapid rise in $\Delta\phi_m$ such that pores are created in a rapid burst that diminishes $\Delta\phi_m$ to a level for which the driving force for expansion is small and over such a short duration that expansion during the burst of pore creation is negligi-

bly small. The CD initial trajectory describes the response of the membrane to submicrosecond, megavolt-per-meter pulses [52].

The ED initial trajectory (Fig. 8.1) results from a very slow rise in $\Delta\phi_m$ such that rate of pore creation is too slow to appreciably diminish $\Delta\phi_m$ on the time scale required for pores to expand to the maximum pore radius $r_{p,max}$. In other words, pores are created slowly but every pore that is created expands to $r_{p,max}$. The expansion of these pores diminishes $\Delta\phi_m$, but until a sufficiently large number of pores are created and expand, $\Delta\phi_m$ remains elevated above the level (~ 0.5 V) required for pores to expand. If the pulse is long enough, then eventually a sufficient number of pores is created to diminish $\Delta\phi_m$ to a level at which a subpopulation of the pores contracts.

It is important to recognize that a full spectrum of pore trajectories is possible (Fig. 8.1). The CD and ED initial trajectories lie at the extremes of the spectrum, and B trajectory lies in the middle.

The initial trajectories (Fig. 8.1) characterize the general response of a local region of membrane. However, the initial pore trajectory, and pore behavior more generally, varies with location in a membrane (e.g., plasma membrane). This arises because the rates of charging are location dependent. Specifically, the poles of a cell charge faster than the lateral regions [53]. Therefore, the response of the polar membrane regions tends to be relatively more creation-dominated and the response of the lateral membrane regions tends to be relatively more expansion-dominated.

8.3.2 Impact of Electrical Transport and Pore Dynamics on Molecular Transport

Molecular transport through the membrane (via pores) depends strongly on (1) the number of pores and (2) the size of pores. The number of pores is important because, all else being equal, total transport is proportional to the number of pores. The size of the pores, and in particular the size of the pores relative to the size of the transported solute, is important because steric hindrance and partitioning [49] are highly nonlinear in pore radius such that larger pores permit a much larger

solute flux than smaller pores.

Thus, the initial pore trajectories, which characterize the balance between pore creation and expansion in a region of membrane, have significant implications for net molecular transport. In general, neither extreme maximizes transport for typical solutes. (An exception: small, uncharged molecules that are predominately transported through small ($r_p \approx r_{p,min}$) pores post-pulse are transported in greater amounts when the pulse results in a CD initial pore trajectory because the total number of pores available for post-pulse transport is larger.)

When the membrane response is CD, molecular transport is expansion-limited (EL). There are many pores available to transport solute, but because the pores are small they do not transport significant amounts of solute due to hindrance and partitioning. Thus, transport is limited by the minimal amount of pore expansion.

When the membrane response is ED, molecular transport is creation-limited (CL). The pores are large enough to transport solute without significant hindrance or partitioning, but because the pores are so few in number they do not collectively transport significant amounts of solute.

The overall implication is that the membrane response that results in maximal molecular transport lies somewhere in between the CD and ED responses. The solute properties (size, shape, and charge) are then important. As noted, the local membrane response varies with location. Therefore, somewhere between the more CD response of the cell pole and the ED response of the more lateral regions lies a region of membrane with just the right balance of creation and expansion to maximize transport. By examining the responses of the Puc and Canatella model systems, we show where this membrane region lies.

8.3.3 Puc Model System Response to a 1 ms, 1 kV/cm Trapezoidal Pulse

The response of the Puc model system [1] to a 1 ms, 1 kV/cm trapezoidal pulse is shown in Figs. 8.2 and 8.3. Figure 8.2 shows the electrical and pore response and Fig. 8.3 shows the molecular response.

Upon application of the electric field pulse (Fig. 8.2C), the membrane begins to charge (Fig. 8.2D), with similar charging rates for both the anodic ($\Theta = 90°$) and cathodic ($\Theta = 270°$) sides of the cell. However, due to electroporation asymmetry, the anodic side of the cell must overcome a larger energy barrier to create pores than the cathodic side. Thus, the burst of pore creation (Fig. 8.2B) commences earlier for the cathodic side and at a lower peak $\Delta\phi_m$ than the burst of pore creation on the anodic side (Fig. 8.2D). Specifically, the cathodic pole $\Delta\phi_m$ reaches a peak value of 1.02 V at $t = 0.93\,\mu s$, and the anodic pole $\Delta\phi_m$ reaches a peak value of 1.58 V at $t = 1.24\,\mu s$.

$\Delta\phi_m$ is the driving force for pore expansion with larger $\Delta\phi_m$ driving faster expansion (Fig. 8.1). Thus, because the cathodic pole electroporates at a lower peak value of $\Delta\phi_m$ than the anodic pole, the response of the cathodic pole is more CD than the response of the anodic pole. As a result, a greater fraction of the pores on the cathodic pole remain small ($r_p \approx r_{p,min}$) than on the anodic pole (Fig. 8.2B). However, the total number of pores (of any size) created on the cathodic pole is ~ 7 larger ($1.2 \times 10^{14}/m^2$ vs. $1.8 \times 10^{13}/m^2$).

As each side of the cell electroporates, the increased penetration of the electric field into that that side of the cell is manifest in the electric potential ϕ (Fig. 8.2A). An interesting aspect of the electrical behavior is that it permits behavior of one region of the system to affect another. All regions are coupled. Specifically, the burst of pore creation on the cathodic pole results in a decrease in the cathodic $\Delta\phi_m$ from its peak. Slightly later, the burst of pore creation and expansion on the anodic pole results in a decrease in the anodic $\Delta\phi_m$ from its peak. Note that as the anodic pole $\Delta\phi_m$ decreases, the cathodic pole $\Delta\phi_m$ increases (Fig. 8.2D). Thus, spatially distributed voltage division links the behavior on the two sides of the cell.

The charging rates of the lateral membrane regions are slower than at the poles (Fig. 8.2E and F). As a result, electroporation of the lateral regions occurs slightly later and at a smaller peak $\Delta\phi_m$ than at the poles. Therefore, the lateral membrane regions feature an ED response, with relatively few pores created but all pores expanding to $r_{p,max}$ (Fig. 8.2B). In the lateral regions, $\Delta\phi_m$ remains elevated relative to the poles (Fig. 8.2E and F) because, though all pores maximally expand, the rate at which they are created is too small to appreciably decrease $\Delta\phi_m$ on the time scale of the pulse.

After $\sim$10 μs, the changes in the pore density distribution and electric potential are small, and these components of the total system response settle into a quasi-steady state. However, the time scale for molecular transport is much longer. Thus, as the electrical transport and pore dynamics are settling into a quasi-steady state, the uptake of solute is just beginning.

During the pulse, essentially all molecular transport occurs through the cathodic side of the cell (Fig. 8.3A) because lucifer yellow molecules drift in the $+y$-direction. Uptake begins immediately after electroporation of the cathodic side (Fig. 8.3E), and the rate of uptake is approximately constant for the duration of the pulse (Fig. 8.3C, D, and E) because, as described, the pore density and transmembrane voltage change very little following a transient at the beginning of the application of the pulse.

The transmembrane flux $J_{s,m}$ during the pulse (Fig. 8.3D and E) is largest at Θ = 240° and 300°. These Θ correspond exactly to the positions of the transitions from CD to ED in shown in Fig. 8.2B. It is in this transition region that pores are large in size relative to in the CD region and large in number relative to in the ED region. Thus, the transition region has the optimal pore density distribution for maximal transmembrane flux.

Post-pulse, all pores contract to $r_p \approx r_{p,min}$ (Fig. 8.2B) and $\Delta\phi_m \approx 0$ V for many multiples of the

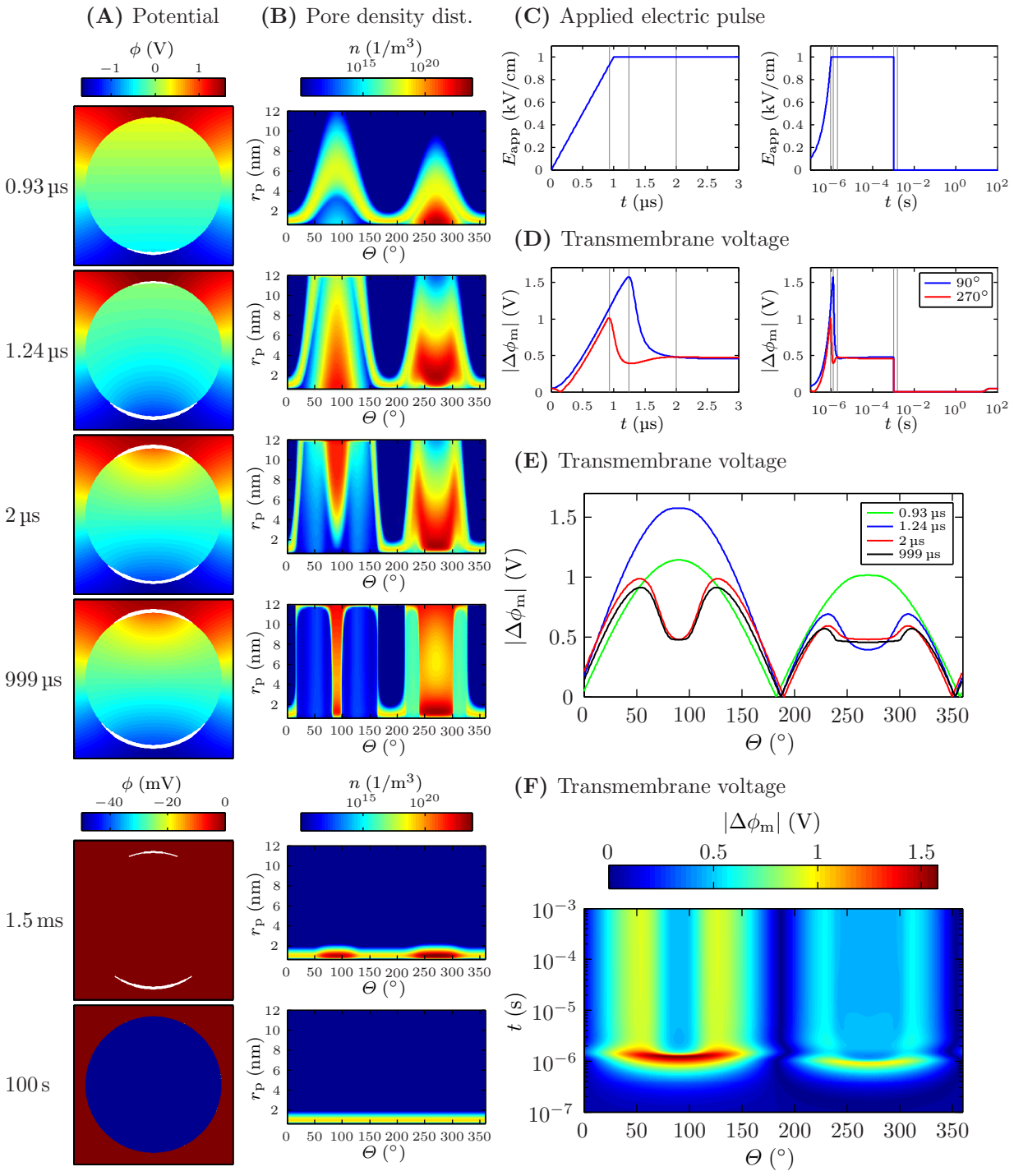

Figure 8.2: Electrical transport and pore dynamics in the Puc model system in response to a 1 ms, 1 kV/cm trapezoidal pulse. **(A)** The electric potential $\phi(x, y)$ at select time points. *White lines* indicate membrane regions with fractional aqueous area $f_{A_p} > 10^{-5}$, with thicker lines corresponding to larger f_{A_p}. **(B)** The pore density distribution $n(r_p, \Theta)$ (pores per area per dr_p) at select time points. **(C)** The applied electric field $E_{app}(t)$ on two time scales: the first 3 µs of the pulse (*left*) and the entire simulation (*right*). **(D)** The transmembrane voltage $|\Delta\phi_m(t)|$ at $\Theta = 90°$ (facing anode) and 270° (facing cathode) on time scales corresponding to those in **(C)**. **(E)** $|\Delta\phi_m(\Theta)|$ at select time points (*inset*). **(F)** $|\Delta\phi_m(\Theta, t)|$ during the pulse.

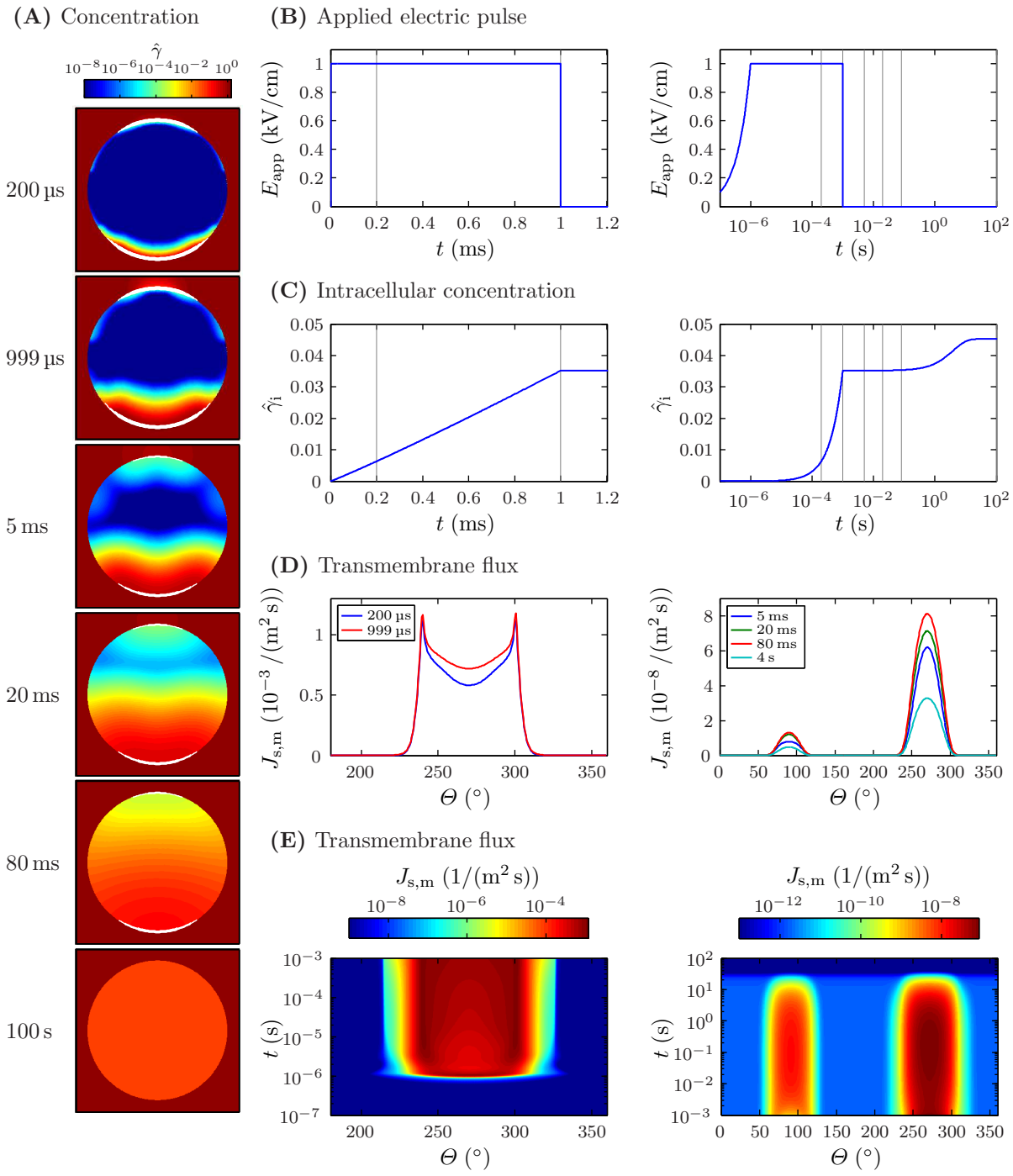

Figure 8.3: Molecular transport in the Puc model system in response to a 1 ms, 1 kV/cm trapezoidal pulse. **(A)** The relative concentration $\hat{\gamma}(x,y)$ at select time points. *White lines* indicate membrane regions with fractional aqueous area $f_{A_p} > 10^{-5}$, with thicker lines corresponding to larger f_{A_p}. **(B)** The applied electric field $E_{app}(t)$ on two time scales: the duration of the pulse (*left*) and the entire simulation (*right*). **(C)** The relative intracellular concentration $\hat{\gamma}_i(t)$ on time scales corresponding to those in **(C)**. **(D)** The transmembrane flux of solute $J_{s,m}(\Theta)$ at select time points (*insets*) during (*left*) and after (*right*) the pulse. **(E)** $J_{s,m}(\Theta, t)$ during (*left*) and after (*right*) the pulse.

pore resealing time constant ($\tau_p = 4\,s$) (Fig. 8.2A and D) as the membrane pores shunt the resting potential sources. As pores reseal, the resting potential is slowly re-established. $\Delta\phi_m$ reaches 90 % of its resting potential ($\Delta\phi_{m,rest} = -50\,mV$) value in 36 s.

Post-pulse, molecular transport occurs through both the cathodic and anodic sides of the cell (Fig. 8.3D and E). Post-pulse transport into the cell is predominantly diffusive, and the transmembrane flux $J_{s,m}$ is smaller than during the pulse by $\sim$4 orders of magnitude (Fig. 8.3D and E). Because all pores have radii $r_p \approx r_{p,min}$ post-pulse, the transmembrane flux $J_{s,m}$ through a region of membrane is proportional to its pore density. As a result, the $J_{s,m}$ is substantially larger on the cathodic side of the cell than on the anodic side.

Post-pulse transport continues until all pores reseal. The time scale for resealing is much longer than the characteristic time for diffusion on the size scale of the cell (Fig. 8.3C and E). Therefore, the concentration within the cell becomes approximately uniform (Fig. 8.3A) long before the end of post-pulse uptake (Fig. 8.3C and E).

The total amount of post-pulse transport of lucifer yellow is quite large. At the end of the pulse, the relative intracellular concentration is $\hat{\gamma}_i = 0.035$. Post-pulse, $\hat{\gamma}_i$ increases to 0.045. Thus, 22 % of the total transport occurs post-pulse.

8.3.4 Canatella Model System Response to a 1 ms, 1 kV/cm Exponential Pulse

The response of the Canatella model system [1] to a 1 ms, 1 kV/cm exponential pulse is shown in Figs. 8.4 and 8.5. Figure 8.4 shows the electrical and pore response and Fig. 8.5 shows the molecular response. Broadly, the response of the Canatella model system is similar to that described for the Puc model system. Therefore, we emphasize how the Canatella model system response is different.

Because the rise-time of the Canatella pulse is 10 ns [1] (Fig. 8.4C), significantly shorter than the 1 μs rise-time of the Puc pulse [1], the membrane charges more quickly (Fig. 8.4D), which results in a burst of pore creation somewhat earlier in the pulse (Fig. 8.4B). The cathodic pole $\Delta\phi_m$ reaches a peak value of 1.04 V at $t = 0.29\,\mu s$, and the anodic pole $\Delta\phi_m$ reaches a peak value of 1.61 V at $t = 0.50\,\mu s$.

The much faster rise in $\Delta\phi_m$ in the Canatella model system (Fig. 8.4D) also results in a more CD response (Fig. 8.4B) than that of the Puc model system. The total number of pores (of any size) created on the cathodic pole is $2.7 \times 10^{14}/m^2$, and the total number of pores created on the anodic pole is a smaller (by a factor ~ 6) $4.5 \times 10^{13}/m^2$). These pore densities are ~ 2.5 times larger than those in the Puc model system. Because of the large pore density, there is little pore expansion on the cathodic pole (Fig. 8.4B), relative to both the anodic pole (Fig. 8.4B) and both poles of the Puc model system (Fig. 8.2B).

As in the Puc model system response, the lateral membrane regions charge more slowly than the poles (Fig. 8.4E and F), electroporate at smaller peak $\Delta\phi_m$, and exhibit a more ED response. However, only narrow bands of the lateral membrane regions experience significant pore expansion on the cathodic side of the cell (Fig. 8.4B). The lateral membrane regions on the anodic side of the cell experience greater pore expansion (Fig. 8.4B).

Because the Canatella pulse is exponential (Fig. 8.4C), it does not have a well-defined end. Rather, the applied field decays to zero with time constant $\tau_{pulse} = 1$ ms. As a result, the pore density distribution and electric potential do not settle in to a quasi-steady state, as they do in the Puc model system. Instead, they experience slow, but continual downward changes on the time scale of the pulse time constant τ_{pulse}.

In each local region of membrane, the pore density distribution shifts to smaller pores in order to maintain $\Delta\phi_m \approx 0.5$ V (Fig. 8.4B) as the applied field decreases (Fig. 8.4C). Because the anodic

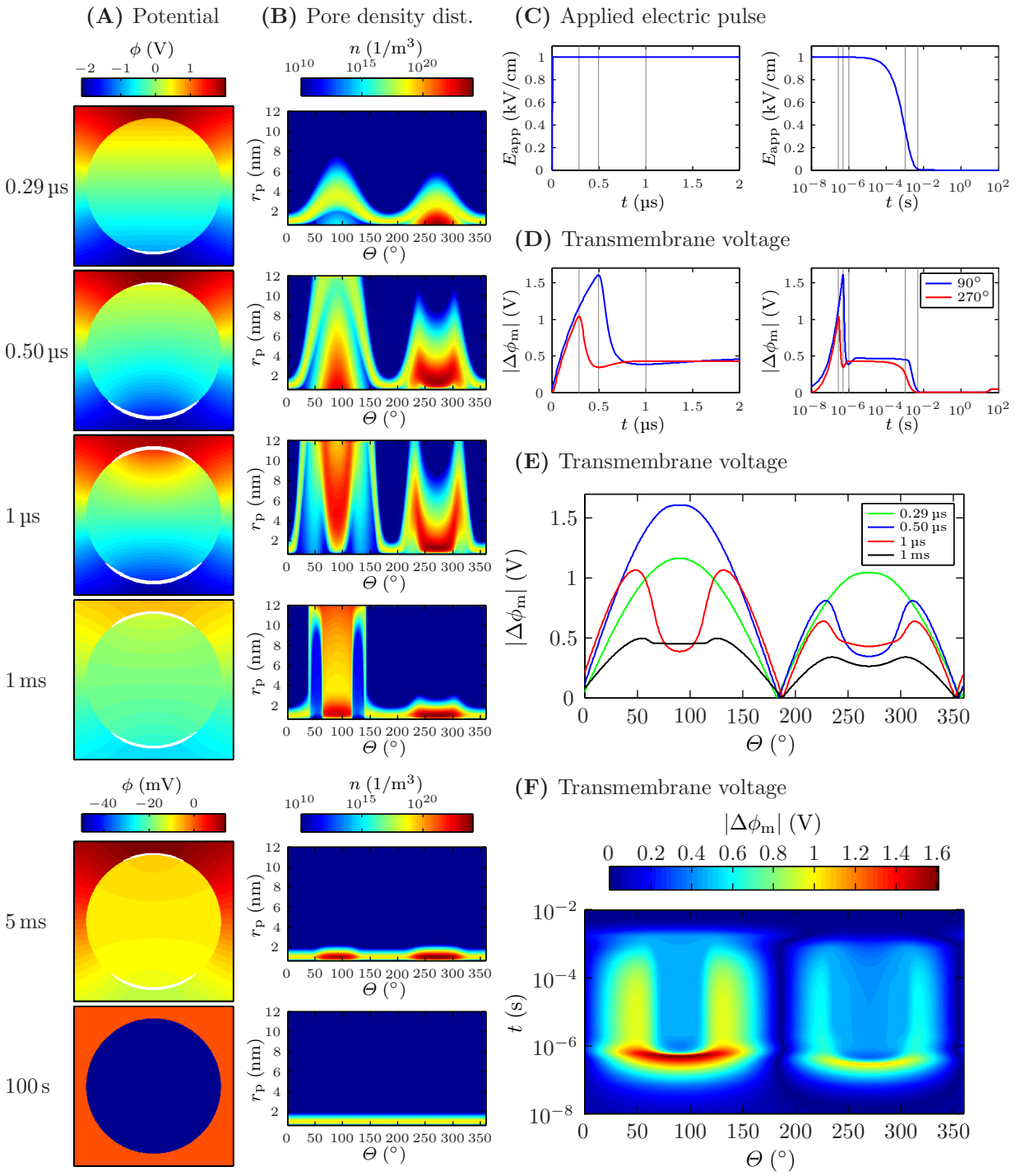

Figure 8.4: Electrical transport and pore dynamics in the Canatella model system in response to a 1 ms, 1 kV/cm exponential pulse. **(A)** The electric potential $\phi(x, y)$ at select time points. *White lines* indicate membrane regions with fractional aqueous area $f_{A_p} > 10^{-5}$, with thicker lines corresponding to larger f_{A_p}. **(B)** The pore density distribution $n(r_p, \Theta)$ (pores per area per dr_p) at select time points. **(C)** The applied electric field $E_{app}(t)$ on two time scales: the first 2 µs of the pulse (*left*) and the entire simulation (*right*). **(D)** The transmembrane voltage $|\Delta\phi_m(t)|$ at $\Theta = 90°$ (facing anode) and 270° (facing cathode) on time scales corresponding to those in **(C)**. **(E)** $|\Delta\phi_m(\Theta)|$ at select time points (*inset*). **(F)** $|\Delta\phi_m(\Theta, t)|$ during the pulse.

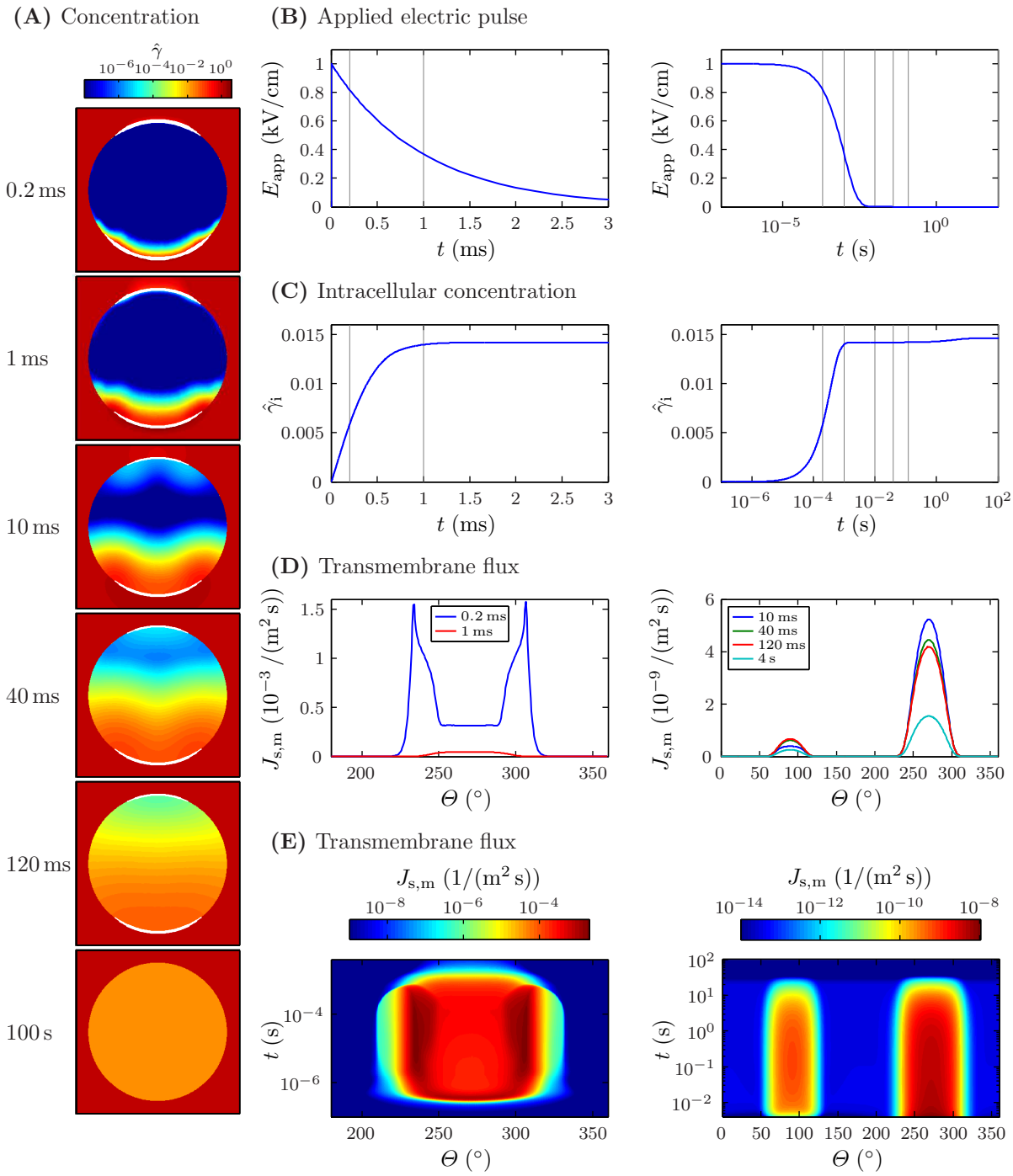

Figure 8.5: Molecular transport in the Canatella model system in response to a 1 ms, 1 kV/cm exponential pulse. **(A)** The relative concentration $\hat{\gamma}(x, y)$ at select time points. *White lines* indicate membrane regions with fractional aqueous area $f_{A_p} > 10^{-5}$, with thicker lines corresponding to larger f_{A_p}. **(B)** The applied electric field $E_{app}(t)$ on two time scales: the duration of the pulse (*left*) and the entire simulation (*right*). **(C)** The relative intracellular concentration $\hat{\gamma}_i(t)$ on time scales corresponding to those in **(C)**. **(D)** The transmembrane flux of solute $J_{s,m}(\Theta)$ at select time points (*insets*) during (*left*) and after (*right*) the pulse. **(E)** $J_{s,m}(\Theta, t)$ during (*left*) and after (*right*) the pulse.

side of the cell has fewer but on average larger pores than the cathodic side, the anodic side has a greater ability to "buffer" $\Delta\phi_m$ through the contraction of large pores [10]. In contrast, the cathodic has predominantly small pores, which cannot contract below $r_p \approx r_{p,min}$, and therefore the cathodic side has a more limited ability to buffer $\Delta\phi_m$ as the applied field decreases. As a result, the cathodic $\Delta\phi_m$ begins to decrease long before the anodic $\Delta\phi_m$. Specifically, the cathodic $\Delta\phi_m$ reaches (decreases to) 0.25 V (half of the plateau $\Delta\phi_m \approx 0.5$ V) at $t = 1.1$ ms, whereas the anodic $\Delta\phi_m$ reaches (decreases to) 0.25 V much later at $t = 2.4$ ms. Thus, $\Delta\phi_m$ remains elevated on the cathodic side for nearly twice as long as on the anodic side.

Note the significant changes in the pore density distribution associated with this electrical behavior. By $t = \tau_{pulse}$, the pore density distribution on the cathodic side, including both the polar and lateral regions, collapses to $r_p \approx r_{p,min}$ (Fig. 8.4B). In contrast, at $t = \tau_{pulse}$, the anodic side, including both the polar and later regions, still has many large pores with $r_p \approx r_{p,max}$ (Fig. 8.4B).

During the Canatella pulse, which we may take to mean $\sim 4\tau_{pulse}$, essentially all molecular transport occurs through the cathodic side of the cell (Fig. 8.5A) because the calcein molecules drift in the $+y$-direction. Uptake begins immediately after electroporation of the cathodic side (Fig. 8.5E). In contrast to the Puc model system, for which the rate of uptake is approximately constant (Fig. 8.3C, D, and E), the rate of uptake in the Canatella system decreases rapidly in time (Fig. 8.5C, D, and E), as the cathodic $\Delta\phi_m$ decreases (Fig. 8.4D, E, and F) and the pore density distribution collapses to $r_{p,min}$ (Fig. 8.4B). Additionally, as the applied field decreases (Fig. 8.5B), the drift speed of calcein decreases, and thus the rate at which calcein reaches the cathodic side of the cell decreases.

The transmembrane flux $J_{s,m}$ during the pulse (Fig. 8.5D and E) is largest at $\Theta = 234°$ and 306°. As in the Puc model system, these Θ correspond to the positions of the transitions from CD to (more) ED response shown in Fig. 8.4B. $J_{s,m}$ in these regions is much larger than at the cathodic pole (Fig. 8.5D and E). For example, at $t = 0.2$ ms, the peak value in the later regions is $J_{s,m} = 1.57/(m^2\,s)$, whereas on the cathodic pole it is a much smaller (by a factor of ~ 5)

$J_{s,m} = 0.31\ /(m^2\ s)$. The relative difference between the two is larger than in the Puc model system because the Canatella model system experiences a more CD response, and thus the pore density distribution near the pole is strongly dominated by small pores ($r_p \approx r_{p,min}$) (Fig. 8.4B) that impede molecular transport to a much greater extent than large pores.

By $t = 1\,ms$, $J_{s,m}$ is much smaller than at $t = 0.2\,ms$ (Fig. 8.5D and E) because essentially all pores on the cathodic side of the cell, including those in the lateral regions, have contracted to $r_{p,min}$ (Fig. 8.4B) and thus significantly impede the transport of solute. Because all of the pores are small, $J_{s,m}$ is approximately proportional to the pore density. Therefore, $J_{s,m}$ is largest at the cathodic pole (Fig. 8.5D and E), which has a larger pore density than the lateral membrane regions (Fig. 8.4B).

The post-pulse electrical and pore behavior in the Canatella model system is similar to that of the Puc model system. Specifically, $\Delta\phi_m \approx 0\,V$ for many multiples of the pore resealing time constant ($\tau_p = 4\,s$) (Fig. 8.4A and D). Eventually, after the vast majority of pores have resealed, the resting potential is re-established.

As in the Puc model system, post-pulse molecular transport in the Canatella model system occurs through both the cathodic and anodic sides of the cell (Fig. 8.5D and E), and the transmembrane flux $J_{s,m}$ is smaller than during the beginning of the pulse by ~ 5 orders of magnitude (Fig. 8.5D and E). Post-pulse, $J_{s,m}$ is substantially larger on the cathodic side of the cell than on the anodic side because it scales approximately with pore density. Post-pulse transport continues until essentially all pores reseal.

The total amount of post-pulse transport of calcein is quite small, much smaller than the amount of post-pulse transport of lucifer yellow in the Puc model system. At the end of the pulse, the relative intracellular concentration is $\hat{\gamma}_i = 0.0142$. Post-pulse, $\hat{\gamma}_i$ increases to 0.0146. Thus, just 2.7 % of the total transport occurs post-pulse. The reason that there is much less post-pulse transport of

calcein than lucifer yellow is that calcein has a significantly larger charge ($z_s = -3.61$) than lucifer yellow ($z_s = -2$), and thus calcein must overcome a much larger Born energy barrier to enter the cell post-pulse.

8.3.5 Comparison of Model Results with Other Results

The model results presented here are in good general agreement with experimental and theoretical results in the literature.

Several experimental studies [54–58] have examined the time course and location of molecular transport into cells using fluorescent probes. It is important to note that most of these studies have used intercalating dyes [59], like ethidium and propidium. These dyes fluoresce strongly when bound to DNA, and therefore allow intracellular dye to be easily distinguished with "washing" steps. However, because they tightly bind to DNA, the time course for transport of intercalating dyes within the cell is much slower than of typical, non-intercalating dyes and molecules, like lucifer yellow and calcein. Lucifer yellow and calcein are intrinsically fluorescent and thus extracellular dye must be washed away before the amount of intracellular dye can be determined. Therefore, they are not useful for examining the time course of transport.

Despite these differences, in most experiments the fluorescent probe is observed to predominantly enter the side of the cell into which it electrically drifts during the pulse. I.e., (positively charged) intercalating dyes predominantly enter the anodic side of the cell. This determination is made by assessing the spatial distribution of fluorescence within the cell after the pulse. However, because the time scale for post-pulse transport is relatively long based on both experiments [54–58] and our model results (Figs. 8.2C and 8.4C), this delayed measurement approach appears reasonable.

Taking the Tekle et al. studies [54, 55] of ethidium ($z_s = +1$) uptake as examples, the earliest post-pulse fluorescence images ($t \approx 0.3\,\mathrm{s}$) show fluorescence on the anodic side of the cell only, while later images ($t > 1.5\,\mathrm{s}$) show fluorescence on both sides of cell, with the fluorescence of the

cathodic side eventually approaching (qualitatively) that of the anodic side. This general timeline of events is in agreement with what we expect based on our model results. Specifically, we expect transport during the pulse to occur predominantly through the anodic side of the cell (because of the drift direction of ethidium) and later post-pulse transport to predominantly occur through the cathodic side (because it develops more pores). We expect significant post-pulse transport of ethidium because it is singly charged.

The model results are also in good general agreement with other spatially distributed models of electroporation with dynamic pores [4–8]. Krassowska and Filev [4] developed a model that represents discrete pores rather than continuum distributions of pores in radius space, as in our model. Despite this basic difference in approach, the results are broadly consistent. Specifically, the results of both models exhibit $\Delta\phi_m \approx 0.5\,\mathrm{V}$ at poles following electroporation, somewhat elevated $\Delta\phi_m$ in the lateral membrane regions, and the largest pores in the lateral membrane regions.

There are two major differences between our model results and those of Krassowska and Filev [4]. First, the largest pores in the Krassowska and Filev [4] model results are much larger ($r_p \approx 400\,\mathrm{nm}$) than the largest pores here ($r_p = r_{p,max} = 12\,\mathrm{nm}$) because we place a specific constraint on pore size [1, 10], based on the large content of protein in cell membranes [51]. Krassowska and Filev [4] did not constrain the pore size. Additionally, we include electroporation asymmetry, which was recently proposed by Esser et al. [8], and thus our model results exhibit greater asymmetry in the pore density distribution and transmembrane voltage than the results of Krassowska and Filev [4].

Esser et al. [6] used a similar modeling approach to our approach here, and the results are in good agreement. Specifically, both models exhibit $\Delta\phi_m \approx 0.5\,\mathrm{V}$ at poles following electroporation and the tendency of the membrane to buffer changes in $\Delta\phi_m$ as the applied field decreases during exponential pulses. The primary difference between the results of Esser et al. [6] and those presented here, is the inclusion of electroporation asymmetry [8] in our present model [1].

8.4 Conclusions

We have described the responses of two model cell systems to applied electric pulses. Specifically, we examined electrical transport, molecular transport, and pore dynamics in the Canatella and Puc model systems [1] during and after pulsing.

The interaction between the electrical behavior, specifically the transmembrane voltage, and the creation and evolution of pores resulted in heterogenous pore density distributions throughout the plasma membrane. The polar membrane regions exhibited a pore creation-dominated response and the lateral membrane regions exhibited a pore expansion-dominated response. The transmembrane flux of solute was largest for the balanced regions located between the creation-dominated and expansion-dominated regions, where the pores were large in size relative to the polar regions and large in number relative to the lateral regions. The exact site of maximal uptake is expected to depend on the applied electric pulse.

In this study, we examined the transport (uptake) of the fluorescent probes calcein and lucifer yellow in response to pulses used by Canatella et al. [2] and Puc et al. [3]. However, we emphasize that the basic methods [1] are general. The solute, cell system properties, and applied electric pulses can be varied. Thus, the approach opens the possibility of in silico screening of candidate electric pulses for specific applications.

References

[1] Smith, K.C. and Weaver, J.C. A unified model of electroporation and molecular transport I: Model design and validation (in preparation).

[2] Canatella, P.J., Karr, J.F., Petros, J.A., and Prausnitz, M.R. Quantitative study of electroporation-mediated molecular uptake and cell viability. *Biophys J*, 80(2):755–764, 2001.

[3] Puc, M., Kotnik, T., Mir, L.M., and Miklavcic, D. Quantitative model of small molecules uptake after in vitro cell electropermeabilization. *Bioelectrochemistry*, 60(1-2):1–10, 2003.

[4] Krassowska, W. and Filev, P.D. Modeling electroporation in a single cell. *Biophys J*, 92(2):404–417, 2007.

[5] Esser, A.T., Smith, K.C., Gowrishankar, T.R., and Weaver, J.C. Towards solid tumor treatment by nanosecond pulsed electric fields. *Technol Cancer Res T*, 8(4):289–306, 2009.

[6] Esser, A.T., Smith, K.C., Gowrishankar, T.R., Vasilkoski, Z., and Weaver, J.C. Mechanisms for the intracellular manipulation of organelles by conventional electroporation. *Biophys J*, 98(11):2506–14, 2010.

[7] Talele, S., Gaynor, P., Cree, M.J., and van Ekeran, J. Modelling single cell electroporation with bipolar pulse parameters and dynamic pore radii. *J Electrostat*, 68(3):261–274, 2010.

[8] Esser, A.T., Smith, K.C., Son, R.S., Gowrishankar, T.R., and Weaver, J.C. Asymmetric cell electroporation: A quantitative model (in preparation).

[9] Smith, K.C. and Weaver, J.C. Electrodiffusion of molecules in aqueous media: A robust, discretized description for electroporation and other transport phenomena (in preparation).

[10] Smith, K.C. and Weaver, J.C. The energy landscape and dynamics of electropores (in preparation).

[11] Smith, K.C. and Weaver, J.C. Compilation and computation of the size, charge, and diffusivity of fluorescent dyes and other small molecules (in preparation).

[12] Okino, M. and Mohri, H. Effects of a high-voltage electrical impulse and an anticancer drug on in vivo growing tumors. *Jpn J Cancer Res*, 78:1319–1321, 1987.

[13] Mir, L.M., Orlowski, S., Belehradek, J., and Paoletti, C. Electrochemotherapy potentiation of antitumor effect of bleomycin by local electric pulses. *Eur J Cancer*, 27(1):68–72, 1991.

[14] Belehradek, J., Orlowski, S., Poddevin, B., Paoletti, C., and Mir, L.M. Electrochemotherapy of spontaneous mammary-tumors in mice. *Eur J Cancer*, 27(1):73–76, 1991.

[15] Belehradek, M., Domenge, C., Luboinski, B., Orlowski, S., Belehradek, J., and Mir, L.M. Electrochemotherapy, a new antitumor treatment - 1st clinical phase-I-II trial. *Cancer*, 72(12):3694–3700, 1993.

[16] Sersa, G., Cemazar, M., and Miklavcic, D. Antitumor effectiveness of electrochemotherapy with cis-diamminedichloroplatinum(II) in mice. *Cancer Res*, 55(15):3450–3455, 1995.

[17] Heller, R., Jaroszeski, M.J., Glass, L.F., Messina, J.L., Rapaport, D.P., DeConti, R.C., Fenske, N.A., Gilbert, R.A., Mir, L.M., and Reintgen, D.S. Phase I/II trial for the treatment of cutaneous and subcutaneous tumors using electrochemotherapy. *Cancer*, 77(5):964–971, 1996.

[18] Hofmann, G.A., Dev, S.B., and Nanda, G.S. Electrochemotherapy: Transition from laboratory to the clinic. *IEEE Eng Med Biol*, 15:124–132, 1996.

[19] Mir, L.M. and Orlowski, S. Mechanisms of electrochemotherapy. *Adv Drug Deliv Rev*, 35(1):107–118, 1999.

[20] Gothelf, A., Mir, L.M., and Gehl, J. Electrochemotherapy: Results of cancer treatment using enhanced delivery of bleomycin by electroporation. *Cancer Treat Rev*, 29(5):371–387, 2003.

[21] Soden, D.M., Larkin, J.O., Collins, C.G., Tangney, M., Aarons, S., Piggott, J., Morrissey, A., Dunne, C., and O'Sullivan, G.C. Successful application of targeted electrochemotherapy using novel flexible electrodes and low dose bleomycin to solid tumours. *Cancer Lett*, 232:300–310, 2006.

[22] Neumann, E., Schaefer-Ridder, M., Wang, Y., and Hofschneider, P.H. Gene transfer into mouse lyoma cells by electroporation in high electric fields. *EMBO J*, 1(7):841–5, 1982.

[23] Wong, T.K. and Neumann, E. Electric field mediated gene transfer. *Biochem Bioph Res Co*, 107(2):584–7, 1982.

[24] Klenchin, V.A., Sukharev, S.I., Serov, S.M., Chernomordik, L.V., and Chizmadzhev, Y.A. Electrically induced DNA uptake by cells is a fast process involving DNA electrophoresis. *Biophys J*, 60(4):804–811, 1991.

[25] Sukharev, S.I., Klenchin, V.A., Serov, S.M., Chernomordik, L.V., and Chizmadzhev, Y.A. Electroporation and electrophoretic DNA transfer into cells – The effect of DNA interaction with electropores. *Biophys J*, 63(5):1320–1327, 1992.

[26] Heller, R., Jaroszeski, M., Atkin, A., Moradpour, D., Gilbert, R., Wands, J., and Nicolau, C. In vivo gene electroinjection and expression in rat liver. *FEBS Lett*, 389(3):225–8, 1996.

[27] Aihara, H. and Miyazaki, J. Gene transfer into muscle by electroporation in vivo. *Nat Biotechnol*, 16(9):867–870, 1998.

[28] Rols, M.P., Delteil, C., Golzio, M., Dumond, P., Cros, S., and Teissie, J. In vivo electrically mediated protein and gene transfer in murine melanoma. *Nat Biotechnol*, 16(2):168–171, 1998.

[29] Rols, M.P. and Teissie, J. Electropermeabilization of mammalian cells to macromolecules: Control by pulse duration. *Biophys J*, 75(3):1415–1423, 1998.

[30] Mir, L.M., Bureau, M.F., Gehl, J., Rangara, R., Rouy, D., Caillaud, J.M., Delaere, P., Branellec, D., Schwartz, B., and Scherman, D. High-efficiency gene transfer into skeletal muscle mediated by electric pulses. *P Natl Acad Sci USA*, 96(8):4262–4267, 1999.

[31] Rizzuto, G., Cappelletti, M., Maione, D., Savino, R., Lazzaro, D., Costa, P., Mathiesen, I., Cortese, R., Ciliberto, G., Laufer, R., La Monica, N., and Fattori, E. Efficient and regulated erythropoietin production by naked DNA injection and muscle electroporation. *P Natl Acad Sci USA*, 96(11):6417–6422, 1999.

[32] Widera, G., Austin, M., Rabussay, D., Goldbeck, C., Barnett, S.W., Chen, M.C., Leung, L., Otten, G.R., Thudium, K., Selby, M.J., and Ulmer, J.B. Increased DNA vaccine delivery and immunogenicity by electroporation in vivo. *J Immunol*, 164:4635–4640, 2000.

[33] Goto, T., Nishi, T., Tamura, T., Dev, S.B., Takeshima, H., Kochi, M., Yoshizato, K., Kuratsu, J., Sakata, T., Hofmann, G.A., and Ushio, Y. Highly efficient electro-gene therapy of solid tumor by using an expression plasmid for the herpes simplex virus thymidine kinase gene. *P Natl Acad Sci USA*, 97(1):354–359, 2000.

[34] Canatella, P.J. and Prausnitz, M.R. Prediction and optimization of gene transfection and drug delivery by electroporation. *Gene Ther*, 8(19):1464–1469, 2001.

[35] Andre, F. and Mir, L.M. DNA electrotransfer: Its principles and an updated review of its therapeutic applications. *Gene Ther*, 11:S33–S42, 2004.

[36] Heller, L.C., Jaroszeski, M.J., Coppola, D., McCray, A.N., Hickey, J., and Heller, R. Optimization of cutaneous electrically mediated plasmid DNA delivery using novel electrode. *Gene Ther*, 14(3):275–280, 2007.

[37] Guignet, E.G. and Meyer, T. Suspended-drop electroporation for high-throughput delivery of biomolecules into cells. *Nat Methods*, 5(5):393–395, 2008.

[38] Hojman, P., Gissel, H., Andre, F., Cournil-Henrionnet, C., Eriksen, J., Gehl, J., and Mir, L. Physiological effects of high and low voltage pulse combinations for gene electrotransfer in muscle. *Hum Gene Ther*, 2008.

[39] André, F.M., Gehl, J., Sersa, G., Préat, V., Hojman, P., Eriksen, J., Golzio, M., Cemazar, M., Pavselj, N., Rols, M.P., Miklavcic, D., Neumann, E., Teissié, J., and Mir, L.M. Efficiency of high- and low-voltage pulse combinations for gene electrotransfer in muscle, liver, tumor, and skin. *Hum Gene Ther*, 19(11):1261–71, 2008.

[40] Cemazar, M., Golzio, M., Sersa, G., Hojman, P., Kranjc, S., Mesojednik, S., Rols, M., and Teissie, J. Control by pulse parameters of DNA electrotransfer into solid tumors in mice. *Gene Ther*, 2009.

[41] Davalos, R.V., Mir, I.L.M., and Rubinsky, B. Tissue ablation with irreversible electroporation. *Ann Biomed Eng*, 33(2):223–231, 2005.

[42] Nuccitelli, R., Pliquett, U., Chen, X.H., Ford, W., Swanson, R.J., Beebe, S.J., Kolb, J.F., and Schoenbach, K.H. Nanosecond pulsed electric fields cause melanomas to self-destruct. *Biochem Bioph Res Co*, 343:351–360, 2006.

[43] Edd, J.F., Horowitz, L., Davalos, R.V., Mir, L.M., and Rubinsky, B. In vivo results of a new focal tissue ablation technique: Irreversible electroporation. *IEEE T Bio-Med Eng*, 53(7):1409–1415, 2006.

[44] Garon, E.B., Sawcer, D., Vernier, P.T., Tang, T., Sun, Y., Marcu, L., Gundersen, M.A., and Koeffler, H.P. In vitro and in vivo evaluation and a case report of intense nanosecond pulsed electric field as a local therapy for human malignancies. *Int J Cancer*, 121(3):675–682, 2007.

[45] Esser, A.T., Smith, K.C., Gowrishankar, T.R., and Weaver, J.C. Towards solid tumor treatment by irreversible electroporation: Intrinsic redistribution of fields and currents in tissue. *Technol Cancer Res T*, 6(4):261–273, 2007.

[46] Rubinsky, B., Onik, G., and Mikus, P. Irreversible electroporation: A new ablation modality–Clinical implications. *Technol Cancer Res T*, 6(1):37–48, 2007.

[47] Nuccitelli, R., Chen, X., Pakhomov, A.G., Baldwin, W.H., Sheikh, S., Pomicter, J.L., Ren, W., Osgood, C., Swanson, R.J., Kolb, J.F., Beebe, S.J., and Schoenbach, K.H. A new pulsed electric field therapy for melanoma disrupts the tumor's blood supply and causes complete remission without recurrence. *Int J Cancer*, 125(2):438–45, 2009.

[48] Nuccitelli, R., Tran, K., Sheikh, S., Athos, B., Kreis, M., and Nuccitelli, P. Optimized nanosecond pulsed electric field therapy can cause murine malignant melanomas to self-destruct with a single treatment. *Int J Cancer*, 127(7):1727–36, 2010.

[49] Smith, K.C. and Weaver, J.C. Effects of hindrance and partitioning on ionic and molecular transport through small lipidic pores (in preparation).

[50] Vasilkoski, Z., Esser, A.T., Gowrishankar, T.R., and Weaver, J.C. Membrane electroporation: The absolute rate equation and nanosecond time scale pore creation. *Phys Rev E*, 74(2), 2006.

[51] Engelman, D.M. Membranes are more mosaic than fluid. *Nature*, 438(7068):578–580, 2005.

[52] Smith, K.C. and Weaver, J.C. Transmembrane molecular transport during versus after nanosecond electric pulses (in preparation).

[53] Stewart, D.A., Gowrishankar, T.R., Smith, K.C., and Weaver, J.C. Cylindrical cell membranes in uniform applied electric fields: Validation of a transport lattice method. *IEEE T Bio-Med Eng*, 52:1643–1653, 2005.

[54] Tekle, E., Astumian, R.D., and Chock, P.B. Electro-permeabilization of cell membranes: Effect of the resting membrane potential. *Biochem Bioph Res Co*, 172(1):282–7, 1990.

[55] Tekle, E., Astumian, R.D., and Chock, P.B. Electroporation by using bipolar oscillating electric field: An improved method for DNA transfection of NIH 3T3 cells. *P Natl Acad Sci USA*, 88(10):4230–4, 1991.

[56] Tekle, E., Astumian, R.D., and Chock, P.B. Selective and asymmetric molecular transport across electroporated cell membranes. *P Natl Acad Sci USA*, 91(24):11512–6, 1994.

[57] Djuzenova, C.S., Zimmermann, U., Frank, H., Sukhorukov, V.L., Richter, E., and Fuhr, G. Effect of medium conductivity and composition on the uptake of propidium iodide into electropermeabilized myeloma cells. *Biochim Biophys Acta*, 1284(2):143–52, 1996.

[58] Sun, Y., Vernier, P., Behrend, M., Wang, J., Thu, M., Gundersen, M., and Marcu, L. Fluorescence microscopy imaging of electroperturbation in mammalian cells. *J Biomed Opt*, 11(2), 2006.

[59] Wilson, W.D., Krishnamoorthy, C.R., Wang, Y.H., and Smith, J.C. Mechanism of intercalation: Ion effects on the equilibrium and kinetic constants for the interaction of propidium and ethidium with DNA. *Biopolymers*, 24(10):1941–61, 1985.

Chapter 9

An In Silico Study of Potential Mechanisms by Which Extremely Large Pulsed Electric Fields Induce Apoptosis in Cells

Abstract

Large magnitude pulsed electric fields have been shown to induce apoptosis in cells, but the basic mechanisms remain poorly understood. Here we use a quantitative, mechanistic computational model of cell electroporation to investigate two candidate mechanisms: (1) release of calcium from the endoplasmic reticulum (ER) into the cytoplasm through electropores in the ER and (2) release of pro-apoptotic proteins from the mitochondrial intermembrane space (IMS) through electropores in the outer mitochondrial membrane (OMM). First, we present the model cell system, which includes realistic representations of the ER and mitochondria. Second, we describe the supra-electroporation response, in which a large number of small pores (~ 1 nm radius) form in membranes throughout the cell, including both the plasma membrane and organelle membranes. Third, we examine the release of calcium from the ER through electropores, and show that the release is large, occurs predominantly post-pulse, and results in a large increase in cytoplasmic calcium concentration. Fourth, we examine the release of cytochrome *c* from mitochondria through electropores, and show that the release is small, occurs entirely during pulsing, and is highly sensitive to pulse duration. Experimental studies have shown that a large number ($\sim 10^2 - 10^3$) of pulses is required to reliably induce apoptosis. Thus, our model results and interpretation of experimental results in the literature suggest that calcium release alone is unlikely to be the sole mechanism leading to apoptosis. Instead, the large number of pulses required to induce apoptosis is consistent with the need to transport a large species through OMM electropores. A solely calcium-based mechanism of apoptosis induction is inconsistent with this observation, as the model results and experimental results in the literature both support a long duration (minutes) increase in cytoplasmic calcium concentration from just a single pulse. However, a pro-apoptotic protein-based mechanism of apoptosis is consistent with experimental observations, as our model describes a small release per pulse and therefore the need for many pulses to achieve a total release of the magnitude required to induce apoptosis.

9.1 Introduction

Within the past decade, extremely large magnitude pulsed electric fields have been shown to induce apoptosis in cells in vitro [1–8] and in vivo [9–12]. Not surprisingly, there is considerable interest in both elucidating the basic mechanisms by which these pulses lead to cell death and in potential clinical applications of these pulses, such as tumor treatment [9–12].

Here, we use a quantitative, mechanistic model of electroporation with concomitant molecular transport [13] to investigate two possible mechanisms by which large magnitude electric pulses may induce apoptosis: (1) release of calcium from the endoplasmic reticulum (ER) and resulting increase in cytoplasmic calcium concentration and (2) direct release of pro-apoptotic proteins from mitochondria into the cytoplasm. Here, we focus on the release of cytochrome *c* while noting that there are other pro-apoptotic proteins that may be released from mitochondria, such as SMAC/DIABLO and OMI/HTRA2 [14]. That is, we take cytochrome *c* to approximately represent these proteins ("death molecules"). Importantly, each of these candidate mechanisms, increased cytoplasmic calcium concentration and release of pro-apoptotic proteins from mitochondria, is involved in natural, biochemically controlled apoptosis, though the basic details and pathways involved differ.

The fundamental response of cell membranes to large magnitude electric pulses is hypothesized to involve the creation of a large number of small pores (radius $r_p \approx 1\,\text{nm}$) in cell membranes (plasma membrane (PM) and organelle membranes), in a process termed supra-electroporation [15–22]. What is striking about supra-electroporation is that its effects mimic several important aspects of natural apoptosis.

First, calcium, which plays an important role in apoptosis [23–29], is released from the intracellular stores in response to large magnitude electric pulses [4, 30, 31, 31–35], and the increase in cytoplasmic calcium concentration can persist for a time scale of minutes [32].

Second, a critical step in apoptosis is mitochondrial outer membrane permeabilization (MOMP) [14, 36, 37] and the subsequent release of pro-apoptotic proteins into the cytoplasm. Indeed, in their comprehensive review article, Kroemer et al. [36] state that "mitochondrial membrane permeabilization is frequently the decisive event that delimits the frontier between survival and death". The underlying mechanisms of MOMP remains unclear [14, 37]. Candidate mechanisms include the formation of protein channels [38, 39] or lipidic pores [40–42] in the outer mitochondrial membrane (OMM). That the OMM pores may be lipidic is particularly intriguing, as it implies a pore structure similar to the electropores that models have shown to form in mitochondrial membranes in response to large pulsed electric fields [15, 16, 18, 20].

Third, loss of the inner mitochondrial membrane (IMM) resting potential during apoptosis interferes with the ability of mitochondria to perform their basic biological functions [14, 43]. Electroporation models have shown that pore formation in mitochondrial membranes results in a loss of the resting potential as pores shunt resting potential sources [15, 16, 18, 20].

Given these fundamental similarities, we hypothesize that large magnitude electric pulses may induce apoptosis by causing a supra-electroporation response that replicates critical features of natural apoptosis and thereby triggers downstream apoptotic pathways.

9.2 Methods

9.2.1 Basic Methods

In a previous study [13], we developed a mechanistic, 2-D model of cell electroporation with concomitant molecular transport and demonstrated that the model predictions are in excellent agreement with quantitative experimental measurements [44, 45] of total molecular uptake (during and after pulsing), for which the applied electric pulses collectively span a wide range of durations ($50\,\mu s - 20\,ms$) and magnitudes ($3\,kV/cm - 0.3\,kV/cm$).

Here, we use the same basic modeling approach [13] to describe the response of a model cell system with organelles to applied electric pulses. The basic approach involves discretizing (meshing) the system and describing electrical and molecular transport between adjacent nodes in terms of the mesh geometry, transport parameters, and the electric potential ϕ and solute concentration γ of the nodes. For node connections that span the membrane, a discretized pore radius space is used to describe the dynamic behavior of pores (pore creation, expansion, contraction, and destruction) in terms of the pore density distribution $n(r_p)$. The dynamic behavior of pores is largely determined by the local transmembrane voltage $\Delta\phi_m$, and in turn, the electrical and molecular transport through the membrane is largely determined by the local pore density $n(r_p)$. Thus, the electrical, molecular, and dynamic pore responses are coupled.

The transport relations are assembled into a large system of nonlinear equations and solved using MATLAB (version 7.8, 2009, http://www.mathworks.com). MATLAB is also used for subsequent analysis of the simulation results (model solutions).

9.2.2 Model Cell System

The model cell system includes a nucleus, ER, and four mitochondria (Fig. 9.1). The 2-D cell is centered in a $200\,\mu m \times 200\,\mu m$ region of electrolyte. The anode is located along the $y = 100\,\mu m$ boundary, and the cathode is located along the $y = -100\,\mu m$ boundary. Thus, when a pulse is applied, the electric field points in the $-y$-direction.

The cell has radius $r_{cell} = 8\,\mu m$ and the system has depth $d = (4/3)r_{cell} = 10.67\,\mu m$, such that the cylindrical cell has the same volume as a spherical cell of the same radius. The nucleus is circular with $3\,\mu m$ radius. The ER has large membrane area and a spatial extent that is similar to that of the nucleus. The mitochondria are elliptical with $1\,\mu m$ length and $0.5\,\mu m$ width. Each mitochondrion has an OMM that is elliptical and an IMM with cristae. Note that while the system has only 4 mitochondria, each one has system depth ($d = 10.67\,\mu m$). Thus, assuming mitochondria have an actual depth equal to their width ($0.5\,\mu m$), each of the mitochondria effectively represents $\sim$21 mi-

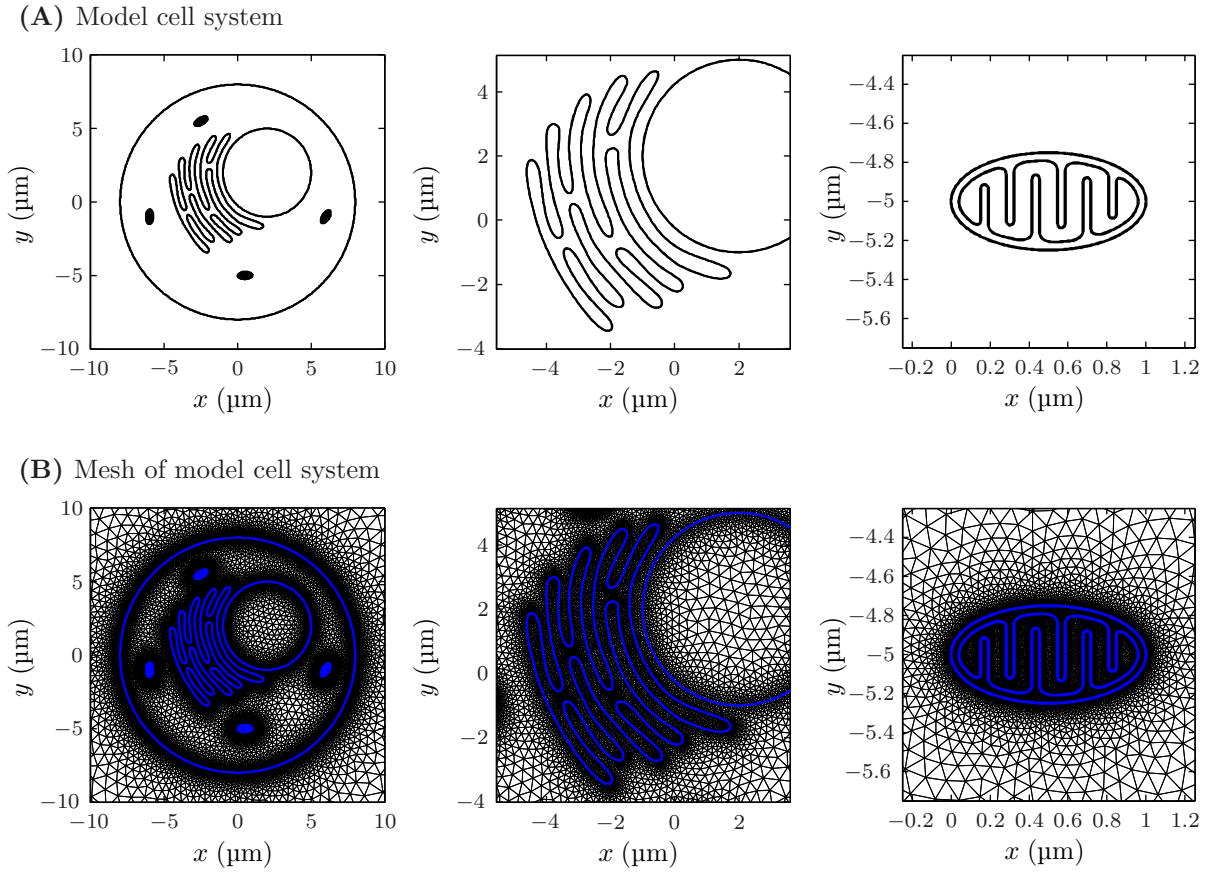

Figure 9.1: Model cell system and mesh. **(A)** The model cell system is shown at level of the cell (*left*), ER (*center*), and a mitochondrion (*right*). The cell has radius $r_{\text{cell}} = 8\,\mu\text{m}$ and is centered in a $200\,\mu\text{m} \times 200\,\mu\text{m}$ region of electrolyte. Only the vicinity of the cell is shown. **(B)** Mesh of the model cell system with fields of view corresponding to those in **(A)**.

tochondria, for ∼84 total. Nonetheless, this still underestimates the total number of mitochondria in a typical cell. Taking 0.045 to be a typical volume density of mitochondria [46, 47], a cell of the size considered here has ∼500 mitochondria. This underrepresentation of the number of mitochondria is unlikely to significantly affect the main conclusions of this study because we correct for this by appropriately scaling the amount of cytochrome *c* per mitochondrion, as described below.

The initial concentrations of calcium in the cytoplasm and organelles are set in accordance with published values, as indicated in Table 9.1. Here the initial concentration of calcium in the extracellular medium is zero. Calcium is assumed to have radius $r_{\text{s}} = 0.34\,\text{nm}$ [48], charge

Table 9.1: Model System Parameters

Symbol		Value					Description and Source
		PM	NM	ERM	OMM	IMM	
$\Delta\phi_{m,rest}$		−90	0	90	0	−200	Membrane resting potential (mV) [18]
σ_m		9.5	950	9.5	950	47.5	Membrane conductivity (nS/m) [18]
f_{prot}		0.5	0.5	0.5	0.5	0.75	Membrane protein fraction [18]
	ECF	C	N	ER	IMS	MM	
$\gamma_{Ca,0}$	0	0.2	0.2	500	0.31	0	Initial calcium concentration (μM) [53, 54]
$\gamma_{Cytc,0}$	0	0	0	0	905	0	Initial cytochrome *c* concentration* (μM)

*Value selected or calculated as described in main text. PM: plasma membrane. NM: nuclear membrane. ERM: endoplasmic reticulum membrane. OMM: outer mitochondrial membrane. IMM: inner mitochondrial membrane. ECF: extracellular fluid. C: cytoplasm. N: nucleus. ER: endoplasmic reticulum. IMS: intermembrane space of mitochondria. MM: mitochondrial matrix.

(valence) $z_s = +2$, extracellular diffusivity $D_{s,i} = 79.2\,m^2/s$ [49], and intracellular diffusivity $D_{s,i} \approx D_{s,e}/4 = 19.8\,m^2/s$. (The diffusivity of small species in the cytoplasm is typically ∼25 % of the aqueous diffusivity [50–52].)

Cells contain ∼ 70 fg cytochrome *c* [55, 56]. Because the molecular mass of cytochrome *c* is 12.2 kg/mol [48], this amounts to 5.7×10^{-18} mol per cell. We distributed this amount of cytochrome *c* evenly among the intermembrane spaces (IMS) of the four mitochondria in the system, which equates to an initial IMS concentration of 905 μM cytochrome *c.* The cytochrome *c* molecules were approximated as cylindrical with radius $r_s = 2.04$ nm, length $l_s = 4.27$ nm, and charge $z_s = +9$ [48]. We use extracellular diffusivity $D_{s,i} = 13.5 \times 10^{-11}\,m^2/s$ [48], and intracellular diffusivity $D_{s,i} \approx D_{s,e}/4 = 3.38 \times 10^{-11}\,m^2/s$. The structure of cytochrome *c* is shown in Fig. 9.2.

All electroporation parameters are the same as in our previous study [13], except as noted below. We assume that the PM exhibits asymmetric electroporation [57], characterized by the asymmetric pore creation constant $\alpha = 11\,kT/V$, as determined in our previous study [13]. However, we assume $\alpha = 0\,kT/V$ for the organelle membranes (i.e., no asymmetry), as the orientation and degree of asymmetric electroporation has not been determined for these membranes. In contrast to our previous model [13], we assume for simplicity that the membrane tension is constant, rather than a function of pore density. This assumption is reasonable, because under the conditions considered here (low membrane tension and small pores), the effect of membrane tension on pore dynamics is

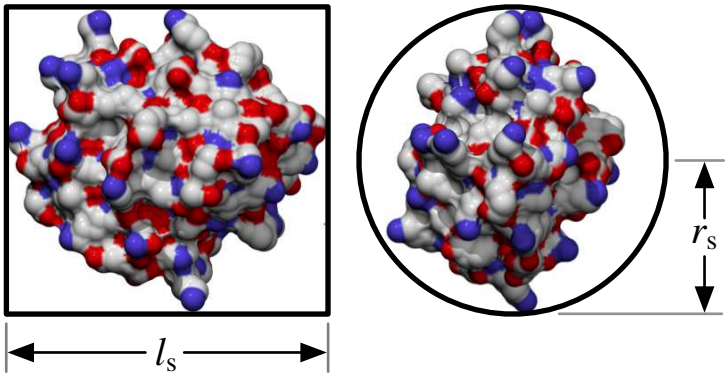

Figure 9.2: Cytochrome *c* structure. Cytochrome *c* is approximated as cylindrical with radius $r_s = 2.04\,\text{nm}$ and length $l_s = 4.27\,\text{nm}$ [48]. The radius of cytochrome *c* is significantly larger than the minimum-size pore radius ($r_{p,min} \approx 1\,\text{nm}$) and is highly charged ($z_s = +9$) [48]. As a result, it is only transported through pores during pulsing, when a small fraction of pores expand sufficiently to accommodate its size.

negligible [58].

9.2.3 Applied Electric Pulses

Trapezoidal pulses with durations $t_{pulse} = 100\,\text{ns}$, 300ns, and $1000\,\text{ns}$ and magnitude $E_{app} = 3\,\text{MV/m}$ were applied to model cell system (Fig. 9.3). All three pulses have the same rise-time $t_{rise} = 30\,\text{ns}$ and fall-time $t_{fall} = 30\,\text{ns}$. Note that these pulses, with the exception of the 1000 ns pulse, are typical of the pulses that Nuccitelli et al. [9, 11, 12] have used to treat melanomas.

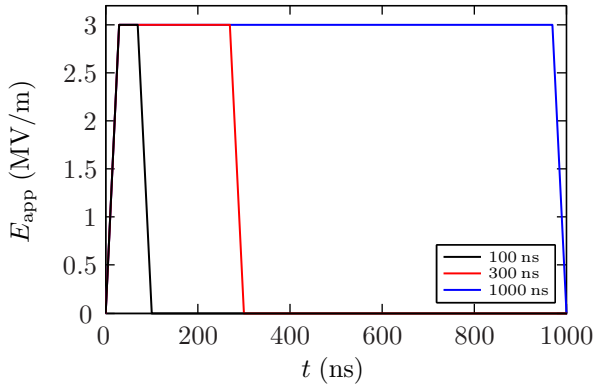

Figure 9.3: Trapezoidal electric pulses. Trapezoidal pulses with durations $t_{pulse} = 100\,\text{ns}$, 300ns, and 1000 ns (*inset*) and magnitude $E_{app} = 3\,\text{MV/m}$. All three pulses have the same rise-time $t_{rise} = 30\,\text{ns}$ and fall-time $t_{fall} = 30\,\text{ns}$.

9.2.4 Simplifying Assumptions

Our model has two important simplifying assumptions. First, we assume that binding can be neglected. Under normal physiologic conditions most intracellular calcium is bound because the cytoplasm has a large calcium binding capacity [59]. The calcium binding capacity of the ER is also large, though much smaller than that of the cytoplasm [59]. However, the ER can release the majority of its calcium into the cytoplasm on a time scale of seconds [60]. This implies that binding of calcium within the ER does not significantly affect total calcium release, the subject of this study.

Cytochrome *c* electrostatically interacts with cardiolipin on the outer side of the IMM [14, 43, 61]. However, the ionic strength in the IMS following permeabilization of the OMM is hypothesized to be sufficient to disrupt these electrostatic interactions [61]. The large magnitude electric fields here may also disrupt these interactions. Other pro-apoptotic proteins, like SMAC/DIABLO and OMI/HTRA2, do not exhibit similar interaction with the IMM [61]. Given these considerations, it is reasonable to neglect cytochrome *c* binding here.

The second simplifying assumption is that active transport mechanisms (e.g., ions pumps) can be ignored. Intracellular calcium concentration oscillations are a well known mechanism of intracellular signaling that results from active and passive transport of calcium within the cell [53]. The frequency of these oscillations is typically $\sim 10^{-3} - 1\,\text{Hz}$. Thus, the shortest characteristic time of oscillations is $\sim 1\,\text{s}$. This is approximately the upper limit of the durations we consider here. Thus, to first order it is reasonable to neglect the impact of active transport mechanisms here.

9.3 Results and Discussion

9.3.1 Supra-electroporation of Cell Membranes

Supra-electroporation is the creation of many small pores ($r_\text{p} \approx r_\text{p,min} = 1\,\text{nm}$) in cell membranes (PM and organelle membranes) in response to large pulsed electric fields [15–22]. The supra-electroporation response is in marked contrast to the conventional electroporation response, in

which pores predominantly form in the PM and may expand significantly [13, 62–67].

Elevated transmembrane voltage $\Delta\phi_m$ is the driving force for both pore creation and pore expansion [58]. As pores are created and expand, they cause $\Delta\phi_m$ to decrease by increasing the membrane conductance. As a result, both pore creation and pore expansion tend to diminish the driving force ($\Delta\phi_m$) for both process. Pore creation and expansion can thus be seen as competing to reduce $\Delta\phi_m$. Whether pore creation or pore expansion predominates in decreasing $\Delta\phi_m$ depends on the applied pulse.

When the increase in the applied field magnitude is very fast, as it is for the pulses considered here, the cell membranes charge rapidly and the membrane response is dominated by pore creation [58, 67]. Pore creation occurs in a quick burst that causes the transmembrane voltage $\Delta\phi_m$ to reach its peak and then plunge to $\sim 0.5\,\mathrm{V}$ on a time scale much too short for pore to expand. Moreover, after reaching $\Delta\phi_m \approx 0.5\,\mathrm{V}$, the driving force for pore expansion disappears and there is little subsequent pore expansion [58].

Post-pulse, $\Delta\phi_m \approx 0\,\mathrm{V}$ until the large majority of pores reseal because pores shunt resting potential sources. Pores remain minimum-size with radius $r_p \approx r_{p,min} = 1\,\mathrm{nm}$ until resealing. The process of resealing is characterized by an assumed exponential time constant $\tau_p = 4\,\mathrm{s}$ [13]. Thus, $\Delta\phi_m$ remains small and pores persist for long after the pulse.

The essential features of supra-electroporation are illustrated in Fig. 9.4, which shows the PM pore density distribution (pores per area per dr_p) (Fig. 9.4A), spatial extent of electroporation (Fig. 9.4B, C), and the concentration of calcium (Fig. 9.4B) and cytochrome *c* (Fig. 9.4C) throughout the cell system at select time points in response to a 1000 ns, 3 MV/m applied pulse. Note that the 1000 ns pulse shown in some sense "includes" the 100 ns and 300 ns pulses (minus their fall-times).

Most pore creation occurs within $20-50\,\mathrm{ns}$ of the pulse onset (not shown). The spatial extent of

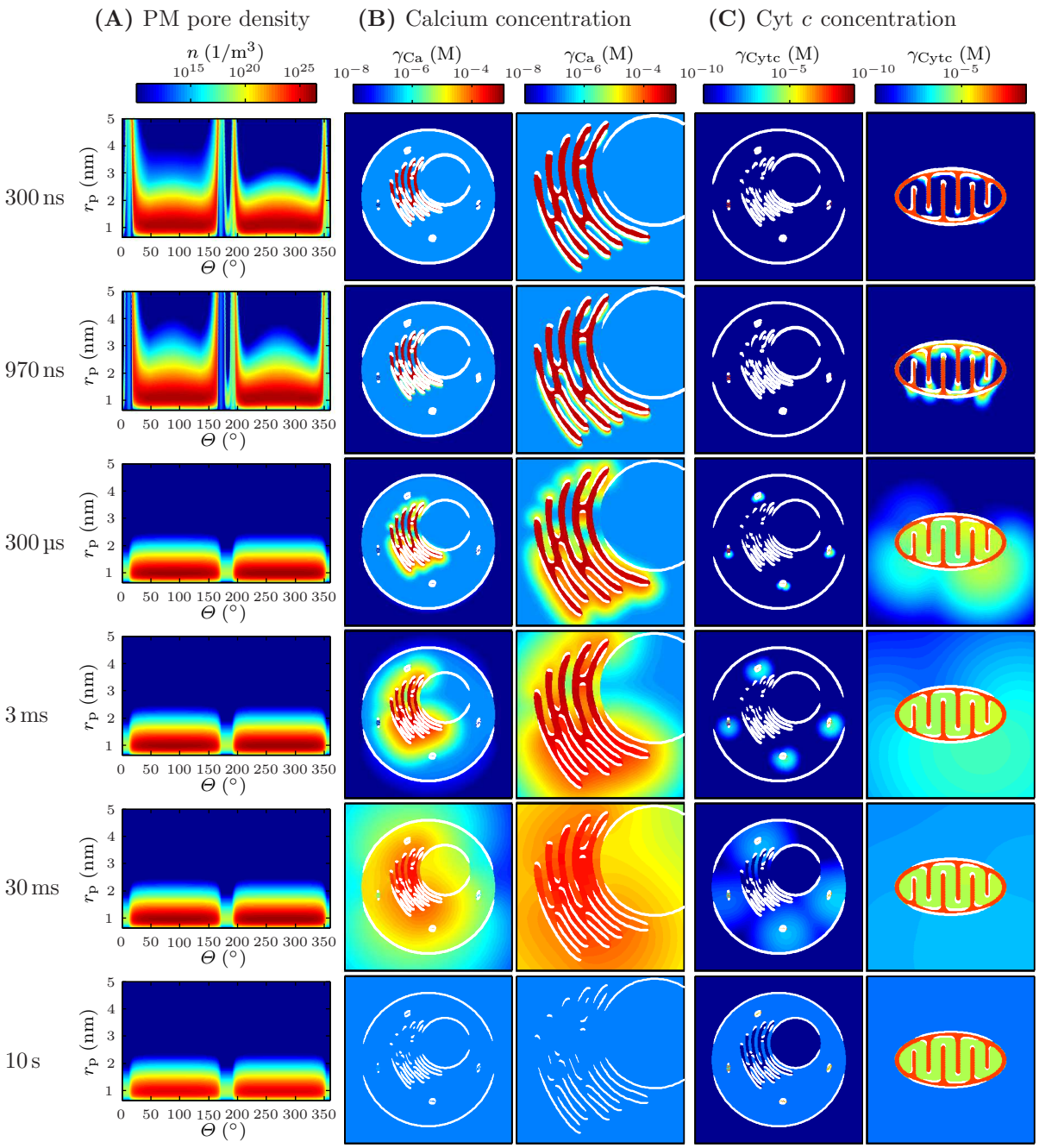

Figure 9.4: Cell system response to a 1000 ns, 3 MV/m electric pulse. **(A)** The PM pore density distribution (pores per area per dr_p) at select time points. Note that the anodic pole has $\Theta = 90°$ and the cathodic pole has $\Theta = 270°$. **(B)** Concentration of calcium at select time points shown at the level of the cell (*left*) and the ER (*right*). **(C)** Concentration of cytochrome *c* at select time points shown at the level of the cell (*left*) and a mitochondrion (*right*). *White lines* indicate membrane regions with fractional aqueous area $f_{A_p} > 10^{-5}$, with thicker lines corresponding to larger f_{A_p}.

pore formation is considerable, with significant pore formation in nearly all membrane regions (Fig. 9.4B, C). The only membrane regions without pores are those that are parallel to the electric field. In these regions, the membrane does not charge significantly, and thus pores are not created. Regions of membrane that are nearly (but not quite) parallel to applied field charge slowly and electroporate later than other membrane regions. Indeed, these slowly charging regions are the only regions that exhibit significant pore expansion (Fig. 9.4A). (Note that these larger pores contribute little to molecular transport because they are few in number and oriented nearly parallel to the applied field. Thus, drift-dominated transport during pulsing is not directed through these membrane regions as it is in membrane regions that are perpendicular to the applied field.)

Pore expansion is minimal in most membrane regions, with nearly all pores distributed around $r_p \approx 1\,\text{nm}$. Only an extremely small fraction of pores expand beyond $\sim 2\,\text{nm}$ (Fig. 9.4A). Note that only the PM pore density distribution is shown in Fig. 9.4A, but it is representative of the response of organelle membranes as well. That the pores remain small has significant implications for the transmembrane (transpore) transport that results from large magnitude pulses [22].

9.3.2 Calcium Release from the Endoplasmic Reticulum

The model results show that supra-electroporation of the ER (Fig. 9.4B) facilitates a large efflux of calcium. Essentially all of this transport occurs post-pulse through minimum-size pores ($r_p \approx 1\,\text{nm}$). While the rate of calcium transport is greater during the pulse than after, the total time available during the pulse is much smaller than the time available post-pulse. As result only a small fraction of the total transport occurs during the pulse.

Figure 9.5 shows how the concentration of calcium in the ER $\gamma_{Ca,ER}$ and cytoplasm $\gamma_{Ca,c}$ change with time for the three pulses. The change in$\gamma_{Ca,ER}$ is minimal during the pulse. Indeed the $\gamma_{Ca,ER}$ differences among the three pulses are barely perceptible (Fig. 9.5). However, post-pulse $\gamma_{Ca,ER}$ decreases tremendously. Concomitant with decrease in $\gamma_{Ca,ER}$ is the initial increase in $\gamma_{Ca,c}$. However, $\gamma_{Ca,c}$ increases only transiently because the influx into the cytoplasm from the ER is eventually

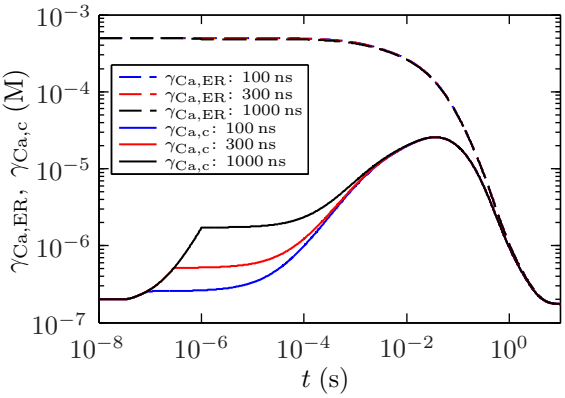

Figure 9.5: Calcium concentration in the ER and cytoplasm. Supra-electroporation of the cell membranes by 100 ns, 300 ns, and 1000 ns, 3 MV/m pulses leads to a predominantly post-pulse efflux of calcium from the ER into the cytoplasm and from the cytoplasm into the extracellular space. By $t \approx 10$ s, the calcium concentration is uniform across the three compartments. The rate and total amount of calcium release is independent of pulse duration (*inset*).

exceeded by the efflux of calcium from the cytoplasm to extracellular space. By ~10 s post-pulse, the concentration of calcium in the ER, cytoplasm, and extracellular space reach equilibrium (uniformity) (Figs. 9.4B and 9.5).

Thus, supra-electroporation enables calcium to transport between the ER and cytoplasm and between the cytoplasm and extracellular space. This has important implications. Here, we assume that the extracellular concentration of calcium is zero. However, in vivo, the typical concentration of calcium in the extracellular fluid is ~2.5 mM [68]. Therefore, these results suggest that in vivo $\gamma_{Ca,c}$ would increase as a result of influx from the ER and influx from the extracellular fluid. In that case, the initial increase in $\gamma_{Ca,c}$ shown in Fig. 9.5 would not be followed by a rapid decrease. Rather, $\gamma_{Ca,c}$ would continue to increase in the short term, until reaching an equilibrium with ER and extracellular fluid. Longer term, active cell mechanisms that are not represented in our model would be expected reduce $\gamma_{Ca,c}$.

The model calcium release results are broadly consistent with the experimental measurements of White et al. [32]. They measured the concentration of calcium in the cytoplasm following the ap-

plication of 60 ns pulsed electric fields with magnitudes in the range $0.4-1.5\,\mathrm{MV/m}$. Importantly, they performed these experiments both with and without extracellular calcium. For both cases, they reported [32] an immediate post-pulse increase in $\gamma_{\mathrm{Ca,c}}$. When the experiment was performed without extracellular calcium (and with extracellular chelating agent EGTA), the initial increase in $\gamma_{\mathrm{Ca,c}}$ was followed by a relatively rapid decrease in $\gamma_{\mathrm{Ca,c}}$ and an asymptotic approach to zero concentration. The decay in $\gamma_{\mathrm{Ca,c}}$ appears approximately exponential with a time constant $\sim 30\,\mathrm{s}$. When the experiment was performed with extracellular calcium, $\gamma_{\mathrm{Ca,c}}$ remained significantly elevated (much higher than the initial $\gamma_{\mathrm{Ca,c}}$), decreasing only slightly from its peak over the $\sim 100\,\mathrm{s}$ time scale of the measurements.

The primary differences between our model results (Fig. 9.5) and the white et al. [32] experimental results are in the magnitude and time scale of the changes in $\gamma_{\mathrm{Ca,c}}$. Specifically, the peak $\gamma_{\mathrm{Ca,c}}$ predicted by our model is much larger than the peak measured by White et al. [32] and the time scale of the subsequent depletion of $\gamma_{\mathrm{Ca,c}}$ is significantly shorter in our model results. These differences likely result from the absence of calcium binding and buffering in our model. We expect that the inclusion of these effects would blunt changes in concentration and slow the rate which calcium is transported.

Nonetheless, both the model results and the White et al. experimental results are consistent with significant transmembrane transport of calcium in response to large applied electric fields. In the absence of extracellular calcium, the increase in $\gamma_{\mathrm{Ca,c}}$ is transient as the stores of calcium initially released from the ER eventually find there way into the extracellular fluid. In the presence of extracellular calcium (e.g., in vivo), the increase in $\gamma_{\mathrm{Ca,c}}$ is long-lived as the ER and extracellular calcium both contribute to the increase in $\gamma_{\mathrm{Ca,c}}$. We speculate that active transport mechanisms may eventually restore $\gamma_{\mathrm{Ca,c}}$ to normal physiologic levels, though this may be difficult on the time scale for which pores remain in the membranes because they enable passive calcium transport (i.e., down transmembrane concentration gradients) that counteract the action of active transport mechanisms (i.e., transporting calcium into the ER and extracellular space against the transmembrane

concentration gradients).

9.3.3 Cytochrome *c* Release from Mitochondria

The model results show that supra-electroporation of the mitochondria (Fig. 9.4C) facilitates a small amount of cytochrome *c* release into the cytoplasm. In contrast to the release of calcium from the ER, which occurs predominantly post-pulse and in large amounts, the release of cytochrome *c* from mitochondria occurs entirely during pulsing and in small amounts. Unlike calcium, which is relatively small and weakly charged, cytochrome *c* is large and highly charged. As a result, it cannot pass through the small pores that exist in the membrane post-pulse. Therefore, the total release of cytochrome *c* is limited to the small amount that occurs during the applied pulse (Fig. 9.6).

Figure 9.6 shows how the concentration of cytochrome *c* in the cytoplasm $\gamma_{\text{Cytc,c}}$ changes with time for the longer two of the three pulses applied (i.e., 300 ns and 1000 ns). The 100 ns pulse was also examined, but the resulting $\gamma_{\text{Cytc,c}} < 1\,\text{pM}$. Figure 9.6A shows $\gamma_{\text{Cytc,c}}$ for 10 ns to 10 s, and Fig. 9.6B shows $\gamma_{\text{Cytc,c}}$ during (and slightly after) the pulses. It is clear from Fig. 9.6A that there is no post-pulse release of cytochrome *c.* Because of its size and charge, all cytochrome *c* releases occurs during the applied pulses.

The model results show that pulse duration has a large impact on the amount of cytochrome *c* released. $\gamma_{\text{Cytc,c}}$ is 5.4×10^{-11} M after the 300 ns pulse and 9.3×10^{-9} M after the 1000 ns pulse (Fig. 9.6). Thus, while the 1000 ns pulse is ~3.3 times longer than the 300 ns pulse, the amount of cytochrome *c* released is 170 times larger.

There are two primary reasons why longer duration pulses result in a highly nonlinear increase in cytochrome *c* release. First, pore creation and (very limited) expansion requires a finite amount of time to occur (for a given applied field magnitude). Second, cytochrome *c* requires time to drift to the inner side of the OMM. Upon reaching the OMM, only a small fraction of the cytochrome *c* is transported through the OMM pores into the cytoplasm. The rest of cytochrome *c* accumulates

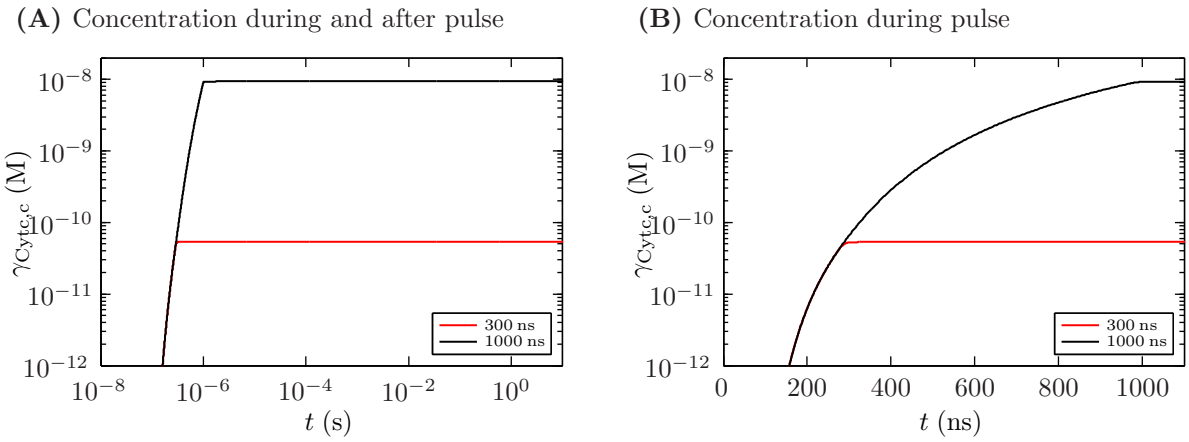

Figure 9.6: Cytochrome *c* concentration in the cytoplasm **(A)** during and after pulsing and **(B)** during pulsing. Supra-electroporation of the OMM by 300 ns and 1000 ns, 3 MV/m pulses leads to release of cytochrome *c* during pulsing only (no post-pulse transport). The total amount of cytochrome *c* released is highly dependent on pulse duration (*inset*), with the 1000 ns pulse resulting in much more cytochrome *c* release than the 300 ns pulse.

on the inner side of the OMM. As time passes, more cytochrome *c* reaches the inner side of the OMM and accumulates. This accumulation leads to an increase in the gradient in cytochrome *c* concentration across the OMM, which in turn results in a larger rate of cytochrome *c* transport through the pores in the OMM. Thus, the accumulation of solute on the inner side of the OMM increases the local supply concentration for transmembrane transport. Because the concentration on the inner side of the OMM continues to increase during the pulse [69], the rate of cytochrome *c* transport also continues to increase. Note that this local interfacial accumulation is general and applies to all solutes, not just cytochrome *c*.

That cytochrome *c* is not transported post-pulse is consistent with experimental observations that short pulses results in minimal (i.e., less than measurement threshold) uptake of fluorescent probes [6, 31, 35, 70, 71], such as propidium. These probes are far smaller and much less charged than cytochrome *c* [48]. Thus, we expect that the post-pulse transport of cytochrome *c* is even less than that of these probes.

The release of cytochrome *c* into the cytoplasm has been reported in response to large magnitude

pulses [5, 8], observed long after pulsing. It is thus unclear whether the release occurs through electropores in the OMM or as a downstream step in apoptosis.

If cytochrome *c* release does occur through electropores, then the model results suggest that many pulses would be required to release an amount sufficient to induce apoptosis. Experiments have shown that microinjection of cytochrome *c* into cells can result in apoptosis [55, 56, 72, 73]. The required cytoplasmic concentration of cytochrome *c* is $\sim 10-20\,\mu$M [72, 73], which amounts to most of the cytochrome *c* in a cell. However, given the simultaneous electroporation-mediated release of calcium from the ER, it is conceivable that the total release of cytochrome *c* through electropores required to induce apoptosis is somewhat smaller because of an amplification loop between calcium and cytochrome *c* [43].

9.3.4 Implications for Apoptosis Induction

Calcium is well-known to play an important role in apoptosis induction generally [23–29]. Some studies have speculated [6, 10] that increases in cytoplasmic calcium concentration may contribute to the induction of apoptosis in cell exposed to large pulsed electric fields. Such increases in intracellular calcium have been reported in a number of experimental studies [4, 30, 31, 31–35]. In an early study, Beebe et al. [4] reported that calcium is not required for large magnitude pulses to induce apoptosis. In their experiments [4], they found no significant difference in caspase activation between cells that had and had not been preloaded with the calcium chelating agent BAPTA before pulsing. We agree with their assessment. Based on our results here and interpretation of experimental observations that have been reported since the Beebe et al. study [4], it appears unlikely that pulsed electric fields induce apoptosis by elevating cytoplasmic calcium concentration alone.

The model results (Fig. 9.5) exhibit a large release of calcium that is independent of duration for the pulses considered here, consistent with experimental observations of significantly elevated cytoplasmic calcium concentration persisting for > 100 s when cells are electroporated in the presence of extracellular calcium [31, 32], as in in vivo conditions. Yet a number of studies have reported

that extremely large numbers of pulses (of order $10-1000$) are required to achieve significant effects [7–9, 11, 12, 71]. For example, in their 2006 study, Nuccitelli et al. [9] found that applying 100 pulses (300 ns, 2 MV/m (nominal) each) to tumors in vivo led to a much larger reduction in tumor size than applying 10 pulses. In their more recent 2010 study, Nuccitelli et al. [12] applied 2000 pulses (100 ns, 3 MV/m each). Given that the time scale for elevated cytoplasmic calcium concentration following a single pulse is on the order of minutes [32], the need for such a large number of pulses is inconsistent with induction of apoptosis resulting from elevated cytoplasmic calcium concentration alone. Moreover, Nuccitelli et al. [12] reported greater efficacy when applying pulses at 7 Hz than at 1 Hz. Yet, applying 2000 pulses at 1 Hz takes seven times longer than applying 2000 pulses at 7 Hz (2000 s vs. 286 s), which implies that the total duration of elevated cytoplasmic calcium should be much longer for the 1 Hz treatment than for the 7 Hz treatment. Thus, if calcium is the primary actor in inducing apoptosis, we would expect that the 1 Hz treatment would be more effective, but it is not.

Our results here suggest that the need to apply large numbers of pulses to achieve maximal efficacy is consistent with a larger solute being involved in inducing apoptosis induction in response to pulsed electric fields. That solute could be cytochrome *c*, another pro-apoptotic protein, or some other solute altogether. Given available results, it is simply not clear.

What is clear is that transmembrane (transpore) transport (release) of larger solutes due to short duration, large magnitude pulses (1) occurs entirely during pulsing (Fig. 9.6) and (2) occurs in small amounts. (This basic conclusion is consistent with experimental observations of minimal transport of fluorescent probes in response to these pulses.) Thus, to achieve significant transmembrane (transpore) transport of large solutes using large magnitude, short duration pulses requires many pulses.

There is a straightforward means of testing the hypothesis that the release of a larger solute is involved in apoptosis induction by pulsed electric fields. Figure 9.6 shows that the relationship

between cytochrome *c* release and pulse duration is highly nonlinear, and we expect that this basic relationship holds for other large solutes, i.e., larger than the minimum-size pores characteristic of supra-electroporation. Thus, if a large solute is involved in apoptosis induction, then far fewer pulses of longer duration (e.g., 1000 ns) should be required than pulses of shorter duration (e.g., 300 ns) to induce apoptosis.

As yet, experimental support for this hypothesis is somewhat mixed and incomplete. In a 2003 paper, Beebe et al. [4] reported greater caspase activation (20 minutes after pulsing) in both Jurkat and HL60 cells in response to a single 300 ns, 2.6 MV/m pulse than in response to a single 60 ns, 6 MV/m pulse or a single 10 ns, 15 MV/m pulse. Similarly, in a 2004 paper, Beebe et al. [31] reported much greater caspase activation (1 hour after pulsing) in response to 5 300 ns, 2.6 MV/m pulses than in response to 5 60 ns, 6 MV/m pulses. However, Hall et al. [8] reported similar caspase activation (45 minutes after pulsing) in response to 10 300 ns, 6 MV/m pulses and 50 60 ns, 6 MV/m pulses. We suspect that experiments that examine the response to pulses that differ more significantly in duration would yield clearer results.

A final potential mechanism by which large magnitude pulses may induce apoptosis is by contributing to osmotic rupture of mitochondria and concomitant release of pro-apoptotic proteins. According to Garrido et al. [74] and Kroemer et al. [36], permeabilization of the IMM may contribute to water influx into the mitochondrial matrix, leading to distention, OMM rupture, and release of pro-apoptotic proteins into the cytoplasm. It is plausible that large magnitude pulses could lead to apoptosis by a similar mechanism since such pulses do electroporate the IMM, as shown in Fig. 9.4. However, as in the case of calcium release, it is unclear why hundreds or thousands of pulses would be required to achieve membrane rupture, as even a single pulse results in supra-electroporation of the mitochondrial membranes (Fig. 9.4).

9.4 Conclusions

We have described the response of a model cell system with organelles to 3 MV/m pulsed electric fields with durations of 100 ns, 300 ns, and 1000 ns. These pulses cause supra-electroporation of the plasma and organelle membranes. This leads to a large post-pulse release of calcium from the endoplasmic reticulum and a concomitant increase in cytoplasmic calcium concentration that is independent of pulse duration. These pulses and the resulting supra-electroporation also lead to a small amount of cytochrome *c* release from mitochondria during pulsing and concomitant increase in cytoplasmic cytochrome *c* concentration that depends strongly on pulse duration, with the 1000 ns pulse resulting in the most cytochrome *c* release, by far.

Our model results suggest that the increase in cytoplasmic calcium resulting from the application of large magnitude pulses is unlikely to be the sole cause of apoptosis induction by these pulses. Rather, our model results, coupled with the experimental observation that large numbers of pulses are required to achieve significant cell killing, are consistent with apoptosis involving the electroporation-mediated release of a larger solute, such as cytochrome *c* or other pro-apoptotic proteins.

References

[1] Hofmann, F., Ohnimus, H., Scheller, C., Strupp, W., Zimmermann, U., and Jassoy, C. Electric field pulses can induce apoptosis. *J Membrane Biol*, 169:103–109, 1999.

[2] Schoenbach, K.H., Beebe, S.J., and Buescher, E.S. Intracellular effect of ultrashort electrical pulses. *Bioelectromagnetics*, 22(6):440–448, 2001.

[3] Beebe, S.J., Fox, P.M., Rec, L.J., Somers, K., Stark, R.H., and Schoenbach, K.H. Nanosecond pulsed electric field (nsPEF) effects on cells and tissues: Apoptosis induction and tumor growth inhibition. *IEEE T Plasma Sci*, 30(1):286–292, 2002.

[4] Beebe, S.J., White, J., Blackmore, P.F., Deng, Y.P., Somers, K., and Schoenbach, K.H. Diverse effects of nanosecond pulsed electric fields on cells and tissues. *DNA Cell Biol*, 22(12):785–796, 2003.

[5] Beebe, S.J., Fox, P.M., Rec, L.J., Willis, L.K., and Schoenbach, K.H. Nanosecond, high-intensity pulsed electric fields induce apoptosis in human cells. *FASEB J*, 17(9), 2003.

[6] Schoenbach, K.H., Joshi, R.P., Kolb, J.F., Chen, N.Y., Stacey, M., Blackmore, P.F., Buescher, E.S., and Beebe, S.J. Ultrashort electrical pulses open a new gateway into biological cells. *P IEEE*, 92(7):1122–1137, 2004.

[7] Pakhomov, A.G., Phinney, A., Ashmore, J., Walker, K., Kolb, J.F., Kono, S., Schoenbach, K.H., and Murphy, M.R. Characterization of the cytotoxic effect of high-intensity, 10-ns duration electrical pulses. *IEEE T Plasma Sci*, 32(4):1579–1586, 2004.

[8] Hall, E.H., Schoenbach, K.H., and Beebe, S.J. Nanosecond pulsed electric fields induce apoptosis in p53-wildtype and p53-null HCT116 colon carcinoma cells. *Apoptosis*, 12(9):1721–1731, 2007.

[9] Nuccitelli, R., Pliquett, U., Chen, X.H., Ford, W., Swanson, R.J., Beebe, S.J., Kolb, J.F., and Schoenbach, K.H. Nanosecond pulsed electric fields cause melanomas to self-destruct. *Biochem Bioph Res Co*, 343:351–360, 2006.

[10] Garon, E.B., Sawcer, D., Vernier, P.T., Tang, T., Sun, Y., Marcu, L., Gundersen, M.A., and Koeffler, H.P. In vitro and in vivo evaluation and a case report of intense nanosecond pulsed electric field as a local therapy for human malignancies. *Int J Cancer*, 121(3):675–682, 2007.

[11] Nuccitelli, R., Chen, X., Pakhomov, A.G., Baldwin, W.H., Sheikh, S., Pomicter, J.L., Ren, W., Osgood, C., Swanson, R.J., Kolb, J.F., Beebe, S.J., and Schoenbach, K.H. A new pulsed electric field therapy for melanoma disrupts the tumor's blood supply and causes complete remission without recurrence. *Int J Cancer*, 125(2):438–45, 2009.

[12] Nuccitelli, R., Tran, K., Sheikh, S., Athos, B., Kreis, M., and Nuccitelli, P. Optimized nanosecond pulsed electric field therapy can cause murine malignant melanomas to self-destruct with a single treatment. *Int J Cancer*, 127(7):1727–36, 2010.

[13] Smith, K.C. and Weaver, J.C. A unified model of electroporation and molecular transport I: Model design and validation (in preparation).

[14] Tait, S.W.G. and Green, D.R. Mitochondria and cell death: Outer membrane permeabilization and beyond. *Nat Rev Mol Cell Bio*, 11(9):621–32, 2010.

[15] Smith, K.C. *Cell and Tissue Electroporation*. Master's thesis, Massachusetts Institute of Technology, Cambridge, Massachusetts, 2006.

[16] Smith, K.C., Gowrishankar, T.R., Esser, A.T., Stewart, D.A., and Weaver, J.C. The spatially distributed dynamic transmembrane voltage of cells and organelles due to 10-ns pulses: Meshed transport networks. *IEEE T Plasma Sci*, 34:1394–1404, 2006.

[17] Vasilkoski, Z., Esser, A.T., Gowrishankar, T.R., and Weaver, J.C. Membrane electroporation: The absolute rate equation and nanosecond time scale pore creation. *Phys Rev E*, 74(2), 2006.

[18] Gowrishankar, T.R., Esser, A.T., Vasilkoski, Z., Smith, K.C., and Weaver, J.C. Microdosimetry for conventional and supra-electroporation in cells with organelles. *Biochem Bioph Res Co*, 341:1266–1276, 2006.

[19] Gowrishankar, T.R. and Weaver, J.C. Electrical behavior and pore accumulation in a multicellular model for conventional and supra-electroporation. *Biochem Bioph Res Co*, 349:643–653, 2006.

[20] Smith, K.C. and Weaver, J.C. Active mechanisms are needed to describe cell responses to submicrosecond, megavolt-per-meter pulses: Cell models for ultrashort pulses. *Biophys J*, 95(4):1547–1563, 2008.

[21] Esser, A.T., Smith, K.C., Gowrishankar, T.R., and Weaver, J.C. Towards solid tumor treatment by nanosecond pulsed electric fields. *Technol Cancer Res T*, 8(4):289–306, 2009.

[22] Smith, K.C. and Weaver, J.C. Transmembrane molecular transport during versus after nanosecond electric pulses (in preparation).

[23] Oshimi, Y., Oshimi, K., and Miyazaki, S. Necrosis and apoptosis associated with distinct Ca2+ response patterns in target cells attacked by human natural killer cells. *J Physiol*, 495 (Pt 2):319–29, 1996.

[24] Rizzuto, R., Pinton, P., Ferrari, D., Chami, M., Szabadkai, G., Magalhães, P.J., Di Virgilio, F., and Pozzan, T. Calcium and apoptosis: Facts and hypotheses. *Oncogene*, 22(53):8619–27, 2003.

[25] Mattson, M.P. and Chan, S.L. Calcium orchestrates apoptosis. *Nat Cell Biol*, 5(12):1041–3, 2003.

[26] Orrenius, S., Zhivotovsky, B., and Nicotera, P. Regulation of cell death: The calcium-apoptosis link. *Nat Rev Mol Cell Bio*, 4(7):552–65, 2003.

[27] Pinton, P., Giorgi, C., Siviero, R., Zecchini, E., and Rizzuto, R. Calcium and apoptosis: ER-mitochondria Ca2+ transfer in the control of apoptosis. *Oncogene*, 27(50):6407–18, 2008.

[28] Norberg, E., Gogvadze, V., Ott, M., Horn, M., Uhlén, P., Orrenius, S., and Zhivotovsky, B. An increase in intracellular Ca2+ is required for the activation of mitochondrial calpain to release AIF during cell death. *Cell Death Differ*, 15(12):1857–64, 2008.

[29] Roy, S.S. and Hajnoczky, G. Calcium, mitochondria and apoptosis studied by fluorescence measurements. *Methods*, 46(3):213–223, 2008.

[30] Vernier, P.T., Sun, Y.H., Marcu, L., Salemi, S., Craft, C.M., and Gundersen, M.A. Calcium bursts induced by nanosecond electric pulses. *Biochem Bioph Res Co*, 310:286–295, 2003.

[31] Beebe, S.J., Blackmore, P.F., White, J., Joshi, R.P., and Schoenbach, K.H. Nanosecond pulsed electric fields modulate cell function through intracellular signal transduction mechanisms. *Physiol Meas*, 25(4):1077–93, 2004.

[32] White, J.A., Blackmore, P.F., Schoenbach, K.H., and Beebe, S.J. Stimulation of capacitative calcium entry in HL-60 cells by nanosecond pulsed electric fields. *J Biol Chem*, 279(22):22964–22972, 2004.

[33] Vernier, P.T., Sun, Y.H., Marcu, L., Craft, C.M., and Gundersen, M.A. Nanoelectropulse-induced phosphatidylserine translocation. *Biophys J*, 86:4040–4048, 2004.

[34] Vernier, P.T., Sun, Y., Wang, J., Thu, M.M., Garon, E., Valderrabano, M., Marcu, L., Koeffler, H.P., and Gundersen, M.A. Nanoelectropulse intracellular perturbation and electropermeabilization technology: Phospholipid translocation, calcium bursts, chromatin rearrangement, cardiomyocyte activation, and tumor cell sensitivity. *Conf Proc IEEE Eng Med Biol Soc*, 6:5850–5853, 2005.

[35] Sun, Y., Vernier, P., Behrend, M., Wang, J., Thu, M., Gundersen, M., and Marcu, L. Fluorescence microscopy imaging of electroperturbation in mammalian cells. *J Biomed Opt*, 11(2), 2006.

[36] Kroemer, G., Galluzzi, L., and Brenner, C. Mitochondrial membrane permeabilization in cell death. *Physiol Rev*, 87(1):99–163, 2007.

[37] Parsons, M.J. and Green, D.R. Mitochondria in cell death. *Essays Biochem*, 47:99–114, 2010.

[38] Muchmore, S.W., Sattler, M., Liang, H., Meadows, R.P., Harlan, J.E., Yoon, H.S., Nettesheim, D., Chang, B.S., Thompson, C.B., Wong, S.L., Ng, S.L., and Fesik, S.W. X-ray and NMR structure of human Bcl-xL, an inhibitor of programmed cell death. *Nature*, 381(6580):335–41, 1996.

[39] Suzuki, M., Youle, R.J., and Tjandra, N. Structure of Bax: Coregulation of dimer formation and intracellular localization. *Cell*, 103(4):645–54, 2000.

[40] Basañez, G., Nechushtan, A., Drozhinin, O., Chanturiya, A., Choe, E., Tutt, S., Wood, K.A., Hsu, Y., Zimmerberg, J., and Youle, R.J. Bax, but not Bcl-xL, decreases the lifetime of planar phospholipid bilayer membranes at subnanomolar concentrations. *P Natl Acad Sci USA*, 96(10):5492–7, 1999.

[41] Basañez, G., Zhang, J., Chau, B.N., Maksaev, G.I., Frolov, V.A., Brandt, T.A., Burch, J., Hardwick, J.M., and Zimmerberg, J. Pro-apoptotic cleavage products of Bcl-xL form cytochrome c-conducting pores in pure lipid membranes. *J Biol Chem*, 276(33):31083–31091, 2001.

[42] Basañez, G., Sharpe, J.C., Galanis, J., Brandt, T.B., Hardwick, J.M., and Zimmerberg, J. Bax-type apoptotic proteins porate pure lipid bilayers through a mechanism sensitive to intrinsic monolayer curvature. *J Biol Chem*, 277(51):49360–5, 2002.

[43] Ow, Y.L.P., Green, D.R., Hao, Z., and Mak, T.W. Cytochrome c: Functions beyond respiration. *Nat Rev Mol Cell Bio*, 9(7):532–42, 2008.

[44] Canatella, P.J., Karr, J.F., Petros, J.A., and Prausnitz, M.R. Quantitative study of electroporation-mediated molecular uptake and cell viability. *Biophys J*, 80(2):755–764, 2001.

[45] Puc, M., Kotnik, T., Mir, L.M., and Miklavcic, D. Quantitative model of small molecules uptake after in vitro cell electropermeabilization. *Bioelectrochemistry*, 60(1-2):1–10, 2003.

[46] Blouin, A., Bolender, R.P., and Weibel, E.R. Distribution of organelles and membranes between hepatocytes and nonhepatocytes in the rat liver parenchyma: A stereological study. *J Cell Biol*, 72(2):441–55, 1977.

[47] Lorentzon, R. and Boquist, L. Stereological study of B-cell mitochondria in alloxan-treated mice. *Virchows Arch B*, 31(3):227–33, 1979.

[48] Smith, K.C. and Weaver, J.C. Compilation and computation of the size, charge, and diffusivity of fluorescent dyes and other small molecules (in preparation).

[49] Lide, D.R., editor. *CRC Handbook of Chemistry and Physics*. CRC Press, Boca Raton, FL, 2005.

[50] Kao, H.P., Abney, J.R., and Verkman, A.S. Determinants of the translational mobility of a small solute in cell cytoplasm. *J Cell Biol*, 120(1):175–84, 1993.

[51] Seksek, O., Biwersi, J., and Verkman, A.S. Translational diffusion of macromolecule-sized solutes in cytoplasm and nucleus. *J Cell Biol*, 138(1):131–42, 1997.

[52] Verkman, A.S. Solute and macromolecule diffusion in cellular aqueous compartments. *Trends Biochem Sci*, 27(1):27–33, 2002.

[53] Schuster, S., Marhl, M., and Höfer, T. Modelling of simple and complex calcium oscillations. From single-cell responses to intercellular signalling. *Eur J Biochem*, 269(5):1333–55, 2002.

[54] Gerencser, A.A. and Adam-Vizi, V. Mitochondrial Ca2+ dynamics reveals limited intramitochondrial Ca2+ diffusion. *Biophys J*, 88(1):698–714, 2005.

[55] Li, F., Srinivasan, A., Wang, Y., Armstrong, R.C., Tomaselli, K.J., and Fritz, L.C. Cell-specific induction of apoptosis by microinjection of cytochrome c. Bcl-xL has activity independent of cytochrome c release. *J Biol Chem*, 272(48):30299–305, 1997.

[56] Khodjakov, A., Rieder, C., Mannella, C.A., and Kinnally, K.W. Laser micro-irradiation of mitochondria: Is there an amplified mitochondrial death signal in neural cells? *Mitochondrion*, 3(4):217–227, 2004.

[57] Esser, A.T., Smith, K.C., Son, R.S., Gowrishankar, T.R., and Weaver, J.C. Asymmetric cell electroporation: A quantitative model (in preparation).

[58] Smith, K.C. and Weaver, J.C. The energy landscape and dynamics of electropores (in preparation).

[59] Mogami, H., Gardner, J., Gerasimenko, O.V., Camello, P., Petersen, O.H., and Tepikin, A.V. Calcium binding capacity of the cytosol and endoplasmic reticulum of mouse pancreatic acinar cells. *J Physiol*, 518 (Pt 2):463–7, 1999.

[60] Mogami, H., Tepikin, A.V., and Petersen, O.H. Termination of cytosolic Ca2+ signals: Ca2+ reuptake into intracellular stores is regulated by the free Ca2+ concentration in the store lumen. *EMBO J*, 17(2):435–42, 1998.

[61] Uren, R.T., Dewson, G., Bonzon, C., Lithgow, T., Newmeyer, D.D., and Kluck, R.M. Mitochondrial release of pro-apoptotic proteins: electrostatic interactions can hold cytochrome c but not Smac/DIABLO to mitochondrial membranes. *J Biol Chem*, 280(3):2266–74, 2005.

[62] Smith, K.C., Neu, J.C., and Krassowska, W. Model of creation and evolution of stable electropores for DNA delivery. *Biophys J*, 86(5):2813–2826, 2004.

[63] Krassowska, W. and Filev, P.D. Modeling electroporation in a single cell. *Biophys J*, 92(2):404–417, 2007.

[64] Esser, A.T., Smith, K.C., Gowrishankar, T.R., and Weaver, J.C. Towards solid tumor treatment by irreversible electroporation: Intrinsic redistribution of fields and currents in tissue. *Technol Cancer Res T*, 6(4):261–273, 2007.

[65] Esser, A.T., Smith, K.C., Gowrishankar, T.R., Vasilkoski, Z., and Weaver, J.C. Mechanisms for the intracellular manipulation of organelles by conventional electroporation. *Biophys J*, 98(11):2506–14, 2010.

[66] Talele, S., Gaynor, P., Cree, M.J., and van Ekeran, J. Modelling single cell electroporation with bipolar pulse parameters and dynamic pore radii. *J Electrostat*, 68(3):261–274, 2010.

[67] Smith, K.C. and Weaver, J.C. A unified model of electroporation and molecular transport II: Dynamics of electrical, molecular, and pore transport (in preparation).

[68] Koeppen, B.M. and Stanton, B.A. *Renal Physiology*. Mosby, 2001.

[69] Smith, K.C. and Weaver, J.C. Electrodiffusion of molecules in aqueous media: A robust, discretized description for electroporation and other transport phenomena (in preparation).

[70] Deng, J.D., Schoenbach, K.H., Buescher, E.S., Hair, P.S., Fox, P.M., and Beebe, S.J. The effects of intense submicrosecond electrical pulses on cells. *Biophys J*, 84(4):2709–2714, 2003.

[71] Vernier, P.T., Sun, Y.H., and Gundersen, M.A. Nanoelectropulse-driven membrane perturbation and small molecule permeabilization. *BMC Cell Biol*, 7:37, 2006.

[72] Brustugun, O.T., Fladmark, K.E., Doskeland, S.O., Orrenius, S., and Zhivotovsky, B. Apoptosis induced by microinjection of cytochrome c is caspase-dependent and is inhibited by Bcl-2. *Cell Death Differ*, 5(8):660–668, 1998.

[73] Zhivotovsky, B., Orrenius, S., Brustugun, O.T., and Doskeland, S.O. Injected cytochrome c induces apoptosis. *Nature*, 391(6666):449–450, 1998.

[74] Garrido, C., Galluzzi, L., Brunet, M., Puig, P.E., Didelot, C., and Kroemer, G. Mechanisms of cytochrome c release from mitochondria. *Cell Death Differ*, 13:1423–1433, 2006.

Chapter 10

Conclusions

In this thesis, we developed a robust, mechanistic model of cell electroporation with concomitant molecular transport. The model yields quantitative, mechanistic descriptions of electrical transport, electrodiffusive molecular transport, and pore creation, evolution, and destruction. The comprehensive cell electroporation model, which integrates these basic mechanisms, provides new methods and insights into the complex processes of electroporation and electroporation-mediated transport.

The key advantages of the model:

- **The model features robust mathematical characterizations of electrical and molecular transport.** Thus, direct comparisons can be made between model results and experimental results. This is essential for model validation and generation of experimentally testable predictions.
- **The model has been validated against quantitative experimental results in the literature.** Specifically, the descriptions of pore conductance and pore energy have been validated against the individual pore conductance measurements of Melikov et al. [1], and the comprehensive cell model predictions of net molecular transport have been validated against the many experimental uptake measurements of Canatella et al. [2] and Puc et al. [3].
- **The model simulates electroporation dynamics that are difficult to assess experimentally.** Many interesting and important aspects of electroporation occur on time scales and length scales that are extremely difficult to investigate experimentally. The model enables calculation of electric potential, solute concentration, and pore density throughout the sys-

tem on time scales ranging from nanoseconds to minutes with a level of spatial and temporal resolution that cannot be achieved by experimental methods. As a result, the model results provide new insights into the underlying dynamics that lead to experimentally observable endpoints.

- **The model enables screening of electric pulse waveforms for particular applications.** Systems and solutes of interest for a particular application can be represented in silico. The model can then be used to find optimal electric pulse waveforms for the application, e.g., maximal delivery of a biologically active solute. This approach does not replace experiments but enhances planning, guiding, and interpreting experiments.

It is our sincere hope that the theoretical framework provided by this model will further understanding, development, and optimization of both existing and emerging applications of electroporation.

References

[1] Melikov, K.C., Frolov, V.A., Shcherbakov, A., Samsonov, A.V., Chizmadzhev, Y.A., and Chernomordik, L.V. Voltage-induced nonconductive pre-pores and metastable single pores in unmodified planar lipid bilayer. *Biophys J*, 80(4):1829–1836, 2001.

[2] Canatella, P.J., Karr, J.F., Petros, J.A., and Prausnitz, M.R. Quantitative study of electroporation-mediated molecular uptake and cell viability. *Biophys J*, 80(2):755–764, 2001.

[3] Puc, M., Kotnik, T., Mir, L.M., and Miklavcic, D. Quantitative model of small molecules uptake after in vitro cell electropermeabilization. *Bioelectrochemistry*, 60(1-2):1–10, 2003.

Chapter 11

Appendix

11.1 Temperature Rise in Electrolyte

The temperature T of the electrolyte in a system places a fundamental bound on the duration of pulse at a given field strength. Beyond $\sim 42\,^{\circ}\mathrm{C}$, cells are irreparably damaged .

The temperature rise ΔT in response to a field with duration t and magnitude E is

$$\Delta T = \frac{\sigma}{s} E^2 t, \tag{11.1}$$

where σ and s are the conductivity and volumetric heat capacity of the electrolyte, respectively.

Note that it is the maximum temperature reached that limits the pulse duration at a given applied electric field strength, not the temperature rise. If the initial electrolyte temperature is $37\,^{\circ}\mathrm{C}$, then the maximum allowable temperature rise is $5\,^{\circ}\mathrm{C}$. However, if the initial electrolyte temperature is $17\,^{\circ}\mathrm{C}$, then the maximum allowable temperature rise is $25\,^{\circ}\mathrm{C}$.

The temperature rise (Eq. 11.1) depends on the conductivity and volumetric heat capacity of the electrolyte. For the purposes of making calculations, we use typical conductivity value $\sigma = 1\,\mathrm{S/m}$ and volumetric heat capacity value $s = 4.18 \times 10^6\,\mathrm{J/(m\,K)}$.

Figure 11.1 shows the temperature rise ΔT calculated using these parameters for pulse durations t_{pulse} ranging from 1 ns to 1 s and pulse electric field magnitudes ranging from $10^3\,\mathrm{V/m}$ to $10^7\,\mathrm{V/m}$.

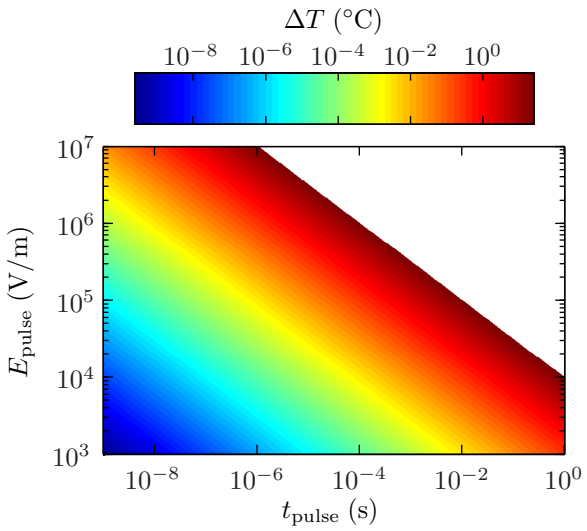

Figure 11.1: Temperature rise resulting from rectangular electric pulses. The temperature rise ΔT is shown for a range of pulse durations t_{pulse} and magnitudes E_{pulse} for electrolyte with conductivity $\sigma = 1\,\mathrm{S/m}$ and volumetric heat capacity $s = 4.18 \times 10^6\,\mathrm{J/(m\,K)}$. The maximum temperature rise shown is $\Delta T = 25\,^{\circ}\mathrm{C}$. For pulses resulting in $\Delta T > 25\,^{\circ}\mathrm{C}$, ΔT is shown as *white*.

This spans the full range typically used for electroporation.